Development and application of NMR methods to study biomolecular dynamics

Dissertation zur Erlangung des Doktorgrades
der Naturwissenschaften (Dr. rer. nat.) der Fakultät für
Biologie und Vorklinische Medizin der Universität Regensburg

vorgelegt von
Jan Overbeck

aus
Wedel

im Jahr
2021

Development and application of NMR methods to study biomolecular dynamics

Dissertation zur Erlangung des Doktorgrades
der Naturwissenschaften (Dr. rer. nat.) der Fakultät für
Biologie und Vorklinische Medizin der Universität Regensburg

vorgelegt von
Jan Overbeck

aus
Wedel

im Jahr
2021

Das Promotionsgesuch wurde eingereicht am:
17.12.2021

Die Arbeit wurde angeleitet von:
Prof. Dr. Remco Sprangers

Unterschrift:

Acknowledgements

I would like to thank everybody who contributed to the becoming of this thesis in one way or another.

Prof. Dr. Remco Sprangers – thank you for being a great boss. Your enthusiasm for NMR and your openness to discuss new ideas, your relaxed attitute, honest interest and constant support created a space, in which I could grow: from an undergrad, who was amazed and overwhelmed by NMR, to someone, who still is. I learned a lot from you and I am deeply grateful for the freedom I had.

Many thanks to Prof. Dr. Werner Kremer – for coming up with the cold shock protein, for explaining spectrometer stuff und fürn büschen Klönschnack in between. Some north deep down in Bavaria! I would also like to thank Jenny Vögele and Prof. Dr. Jens Wöhnert for the very pleasant riboswitch collaboration.

Johanna Stöfl, thank you for the constant support in the lab and in the office. You are doing a great job! But could we open the window for a second? I would also like to thank Mira Schütz-Stoffregen, the secret master of lab relocation, as well as Janina Petters, Iris Holdermann and Nadine Stefan, for keeping the labs running in the past. Simon Grunert, thanks a lot for taking care of the magnets with Werner, and thanks to Vincent Truffault in Tübingen for maintaining the NMR infrastructure. Birgit Moldovan and Patricia Albrecht - thanks for taking care of so much office stuff!

Many thanks to the whole present and past Sprangers and Wiesner labs! For good and bad coffee and probably some thousand tischkicker games, for sharing biochemistry knowledge, cakes and breaks, for joint conferences and of course for bearing bad jokes and puns and teaching me some bavarian words. Special thanks to everybody who listened to me between 11 am and 1 pm. I particularly thank Anna Fuchs, Stefan Schütz and Carsten Stollmaier for quite a long time of scientific coevolution as well as on- and off-topic talks. I also specifically thank my colleagues Daniela Lazzaretti, David Stelzig, Jobst Liebau and Philip Wurm, who proof-read parts of my thesis. I appreciate all the scientific discussions that we had in the lab over the years, and in particular I want to

thank Philip Wurm for many discussions on NMR. I had the pleasure to overview two great master students during my PhD work, and I thank David Stelzig and Lena Thurnes for all the laughs and the lab work.

I thank Kinga Ay and Carolin Apfel for great support in the RIGeL programm, and I thank Prof. Dr. Reinhard Sterner and Prof. Dr. Christine Ziegler for RIGeL mentoring.

I am thankful to all my friends. I am deeply indebted to all of you, and I am really looking forward to what lies ahead of us. Special thanks to Antonio, Fritz, Kalle, Rosa and Wladi. Ari – the future is yours. Franzi, thanks a lot for everything – joining your flat was a perfect start to Regensburg! Lily, thank you for your support at the beginning of my PhD.

All my love to my family, to my parents and sisters and their loved ones, to my niece and my nephew. Your unconditional support, mostly from far away, cannot be replaced.

Dear Feli, I thank you with all my heart for your support and your faith in me.

Summary

Structural biology has generated profound insights into biomolecular machines. The molecular basis of processes like binding, folding, catalysis and regulation, which underlie the inner working of living organisms would have largely remained unexplored without the thousands of structures that have been solved over the years. But these machines, formed by proteins and nucleic acids, are inherently dynamic, and information about this fourth dimension, the modulation of their structure with time, is often lacking. Nuclear magnetic resonance (NMR) is exquisitely suited to characterize dynamics over a wide timescale, from picoseconds, where amplitudes and correlation times can be extracted, to microsecond, milliseconds and seconds, where in favourable cases information about the kinetics, the thermodynamics and the structure of an excited state can be retrieved. With increasing size of the molecular system under consideration, however, this characterization is progressively challenging for NMR, and the analysis often focuses on $^{13}CH_3$ spin systems in a perdeuterated background. As an alternative approach, fluorine NMR has grown in popularity. The ^{19}F isotope can be introduced site-specifically, it gives rise to background-free one-dimensional spectra and the technique bypasses the need for perdeuteration. In my disseration, I expanded the existing toolkit of ^{19}F NMR, applied ^{19}F experiments that report on dynamics to high-molecular weight systems and combined their advantages with established methyl group NMR techniques.

Development of ^{19}F relaxation dispersion experiments
To develop ^{19}F relaxation dispersion (RD) experiments, I used a 7.5 kDa cold shock protein from the thermophilic organism *Thermotoga maritima* as a protein folding/unfolding model system. The global analysis of three RD experiments showed consistent results for the two-state exchange process. Our new rotating frame relaxation pulse sequences allowed to extract the absolute chemical shift of the unfolded state and significantly extended the range of timescales that can be assessed experimentally. Employing a 360 kDa double heptameric complex, I validated the applicability of the experiments on a highly challenging assembly.

Conformational changes in the exoribonuclease Xrn2
The 5′-3′ exoribonuclease Xrn2 operates in the nucleus in RNA processing and RNA

turn-over pathways. Static structures of its cytoplasmic homologue Xrn1 in the presence of substrates implicate that the enzymes undergo conformational changes to progress through the catalytic cycle. Here, I solved the X-ray structure of Xrn2 from the thermophilic organism *Chaetomium thermophilum* to 3 Å resolution and combined methyl group and fluorine relaxation dispersion to characterize the exchange in a 100 kDa apo protein core construct in solution. Upon binding of a substrate, the conformational equilibrium is substantially shifted towards the active state. Importantly, the ^{19}F experiments allowed to characterize dynamics in these unstable samples and I could show that the exchange of the enzyme:substrate complex are largely suppressed.

Multi-site exchange in a neomycin-sensing riboswitch
The existence of multiple sparsely populated states complicates the characterization of an exchanging system. Using a synthetic neomycin-binding riboswitch bound to different aminoglycoside ligands, I demonstrated that fluorine NMR can be employed to study exchange topologies with up to four states. To this end, I take advantage of an additional off-resonance technique, ^{19}F chemical exchange saturation transfer. Combined with ^{19}F RD and longitudinal exchange experiments, the results support the notion of a modular impact of aminoglycoside functional groups on the riboswitch dynamics.

Taken together, these results expand and complement the NMR toolbox to study exchanging systems, with an emphasis on high-molecular weight systems and intricate exchange topologies involving more than two states. Furthermore, they elucidate the molecular dynamics in the 5'-3' exoribonuclease Xrn2 and provide a conceptional framework to study dynamics in related systems such as Xrn1.

Zusammenfassung

Die Strukturbiologie hat bemerkenswerte Einblicke in biomolekulare Maschinen hervorgebracht. Die molekulare Basis von Prozessen wie Bindungsvorgängen, Faltung, Katalyse und Regulation, die den inneren Funktionsweisen von lebenden Organismen zugrundeliegen, blieben größtenteils verborgen ohne die tausenden Strukturen, die im Laufe der Jahre gelöst wurden. Diese Maschinen, die von Proteinen und Nukleinsäuren gebildet werden, sind allerdings inhärent dynamisch, und oft mangelt es an Information über diese vierte Dimension, die Modulation ihrer Struktur mit der Zeit. Die Kernresonanzspektroskopie (NMR) ist hervorragend dafür geeignet, dynamische Vorgänge über eine Breite von Zeitskalen zu charakterisieren, beginnend bei Dynamiken auf der Pikosekundenskala, für welche Amplituden und Korrelationszeiten extrahiert werden können, bis zu Dynamiken im Mikrosekunden-, Millisekunden- oder Sekundenbereich, für welche in günstigen Fällen Informationen über die Kinetik und die Thermodynamik des Austauschs sowie über die Struktur des angeregten Zustands gewonnen werden können. Mit zunehmender Größe der betrachteten Systeme wird ihre Charakterisierung mittels NMR allerdings auch zunehmend anspruchsvoll und muss in der Regel über $^{13}CH_3$ Spinsysteme in einem vollständig deuterierten Hintergrund erfolgen. Eine Alternative stellt die Fluor-NMR dar, die an Popularität gewonnen hat. Das ^{19}F Isotop kann ortsspezifisch eingebaut werden, ermöglicht die Messung von eindimensionalen Spektren ohne störende Hintergrundsignale und umgeht die Notwendigkeit der Deuterierung. In meiner Dissertation habe ich den bestehenden Werkzeugkasten der ^{19}F NMR-Dynamikexperimente ausgebaut, diese Experimente auf Systeme mit hohem Molekulargewicht angewendet und ihre Vorteile mit etablierten Methylgruppen-NMR Techniken kombiniert.

Entwicklung von ^{19}F Relaxationsdispersionsexperimenten
Um ^{19}F Relaxationsdispersionsexperimente (RD-Experimente) zu entwickeln habe ich ein 7.5 kDa Kälteschockprotein aus dem thermophilen Organismus *Thermotoga maritima* als Modellsystem verwendet. Die globale Analyse von drei RD-Experimenten zeigte konsistente Resultate für den Austauschprozess zwischen zwei Zuständen. Unsere neuen Pulsesequenzen zur Messung von Relaxation im rotierenden Bezugssystem erlaubten es, die absolute chemische Verschiebung des ungefalteten Zustandes zu ermitteln und

erweiterten die Spannbreite an Austauschzeiten, die experimentell zugänglich ist. Die Anwendbarkeit der Experimente wurde an einem 360 kDa schweren doppelheptameren Komplex validiert.

Konformationsänderungen in der Exoribonuklease Xrn2
Die 5′-3′ Exoribonuklease Xrn2 ist im Zellkern in die Prozessierung und den Abbau von RNA involviert. Statische Strukturen des zytoplasmatischen homologen Proteins Xrn1 mit gebundenem Substrat implizieren, dass die Enzyme Konformationsänderungen während des katalytischen Zyklus durchlaufen. In dieser Arbeit habe ich die Kristallstruktur von Xrn2 aus dem thermophilen Organismus *Chaetomium thermophilum* mit einer Auflösung von 3 Å gelöst und Methylgruppen- und Fluor-RD-Experimente kombiniert um den Austausch in einem 100 kDa Kernkonstrukt von Xrn2 in Lösung zu charakterisieren. Es wird gezeigt, dass die Bindung eines Substrats das Konformationsgleichgewicht erheblich auf die Seite des aktiven Zustandes verschiebt. Die ^{19}F Experimente erlauben es, die Dynamik auch in den instabilen Proben mit gebundenem Substrat zu untersuchen und in der Arbeit wird nachgewiesen, dass der Austausch im Enzym:Substrat-Komplex größtenteils unterdrückt ist.

Austausch mehrere Zustände in einem Neomycin-bindenden Riboswitch
Die Existenz mehrerer niedrigpopulierter Zustände erschwert die Charakterisierung des austauschenden Systems. Mithilfe eines synthetischen Neomycin-bindenden Riboswitches, welcher verschiedene Aminoglykosidliganden bindet, zeige ich, dass Fluor-NMR dazu verwendet werden kann, Austauschtopologien mit bis zu vier Zuständen zu studieren. Hierfür wurde eine zusätzliche Offresonanztechnik verwendet, der ^{19}F Sättigungstransfer. In Kombination mit ^{19}F Relaxationsdispersion und longitudinalen Austauschexperimenten unterstützen die Resultate die Hypothese eines modularen Einflusses verschiedener funktionaler Gruppen in den Aminoglykosidliganden auf die Dynamik im Riboswitch.

Zusammengenommen erweitern und komplementieren die hier vorgestellten Experimente und Resultate den NMR-Werkzeugkasten, um austauschende Systeme zu studieren, insbesondere mit Blick auf hochmolekulare Komplexe und komplizierte Austauschtopologien mit mehr als zwei Zuständen. Darüber hinaus wird die Dynamik in der 5′-3′ Exoribonuklease Xrn2 aufgeklärt und der konzeptuelle Rahmen für das Studium verwandter Systeme wie Xrn1 etabliert.

Publications

Published

J. P. Wurm, I. Holdermann, **J. H. Overbeck**, P. H. O. Mayer, and R. Sprangers. Changes in conformational equilibria regulate the activity of the Dcp2 decapping enzyme. Proceedings of the National Academy of Sciences, 114(23):6034–6039, June 2017. ISSN 0027-8424, 1091-6490. doi: 10.1073/pnas.1704496114. URL `http://www.pnas.org/lookup/doi/10.1073/pnas.1704496114`

> *Author contributions: J.P.W., I.H., J.H.O., and R.S. designed research; J.P.W., I.H., J.H.O., P.H.O.M., and R.S. performed research; J.P.W., I.H., J.H.O., and R.S. analyzed data; and J.P.W. and R.S. wrote the paper.*

J. H. Overbeck, W. Kremer, and R. Sprangers. A suite of ^{19}F based relaxation dispersion experiments to assess biomolecular motions. Journal of Biomolecular NMR, 74(12):753–766, Dec. 2020. ISSN 0925-2738, 1573-5001. doi: 10.1007/s10858-020-00348-4. URL `http://link.springer.com/10.1007/s10858-020-00348-4`

> *All authors conceived the project. J.H.O. and R.S. designed the experiments. J.H.O. performed the experiments. J.H.O. and R.S. analyzed and interpreted the experiments. J.H.O. and R.S. wrote the paper, all authors commented on the manuscript.*

In preparation

J. H. Overbeck, D. Stelzig, A.-L. Fuchs, J. P. Wurm, and R. Sprangers. Investigating conformational changes that underlie the catalytic cycle of the 5′-3′ exoribonuclease Xrn2. In preparation for submission to *Proceedings of the National Academy of Sciences*

> *J.H.O and R.S. designed experiments. J.H.O. performed experiments, analyzed and interpreted data. D.S. measured turnover rates, A.L.F helped with solving the crystal structure of Xrn1 and J.P.W. helped with recording and analyzing NMR data and with the NMR structure calculations. J.H.O. and R.S. wrote the manuscript.*

J. H. Overbeck, J. Vögele, J. Wöhnert, and R. Sprangers. Multi-site exchange in the neomycin-sensing riboswitch studied by ^{19}F NMR. In preparation.

All authors conceived the project. J.V. prepared RNA. J.H.O and R.S. designed experiments. J.H.O. performed experiments and analyzed data. All authors interpreted data. J.H.O. and R.S. wrote the manuscript.

Publications preceding PhD work

M. Mund, **J. H. Overbeck**, J. Ullmann, and R. Sprangers. LEGO-NMR Spectroscopy: A Method to Visualize Individual Subunits in Large Heteromeric Complexes. Angewandte Chemie International Edition, 52(43): 11401–11405, Oct. 2013. ISSN 14337851. doi: 10.1002/anie.201304914. URL `https://onlinelibrary.wiley.com/doi/10.1002/anie.201304914`

J. P. Wurm, **J. Overbeck**, and R. Sprangers. The S. pombe mRNA decapping complex recruits cofactors and an Edc1-like activator through a single dynamic surface. RNA, 22 (9):1360–1372, Sept. 2016. ISSN 1355-8382, 1469-9001. doi: 10.1261/rna.057315.116. URL `http://rnajournal.cshlp.org/lookup/doi/10.1261/rna.057315.116`

Contents

Acknowledgements **V**

Summary **VII**

Zusammenfassung **IX**

Publications **XI**

Abbreviations **1**

1. Eukaryotic RNA degradation by 5′-3′ exoribonucleases **3**
1.1. Cytoplasmic RNA decay 4
1.2. Nuclear RNA decay 5

2. Nuclear magnetic resonance as a technique to investigate biomolecular dynamics **9**
2.1. Molecular dynamics of proteins and nucleic acids 9
2.2. The feasibility of NMR experiments 12
2.3. Description of nuclear magnetic relaxation 15
2.4. Fluorine NMR 17
2.5. The NMR toolkit to study protein dynamics 20

3. Materials and methods **47**
3.1. Molecular biology 47
3.2. Protein expression, isotope labeling and purification 48
3.3. Cysteine fluorine labeling 50
3.4. RNA preparation 51
3.5. Xrn2 activity assays 52
3.6. NMR spectroscopy 52
3.7. Fluorescence anisotropy 59
3.8. X-ray crystallography 59
3.9. Vizualization 59

4. A suite of ^{19}F NMR experiments to study biomolecular dynamics **61**
4.1. Summary 61
4.2. Introduction 62
4.3. Results 63
4.4. Discussion and Conclusions 74

5. Investigating conformational changes that underlie the catalytic cycle of the 5′-3′ exoribonuclease Xrn2 **77**
5.1. Summary 77
5.2. Introduction 78
5.3. Results 80
5.4. Discussion 94

6. Multi-site exchange in the neomycin-sensing riboswitch studied by ^{19}F NMR **103**
6.1. Summary 103
6.2. Introduction 104
6.3. Results 106
6.4. Discussion 117

7. Discussion and Outlook **123**

A. Appendix **XLIV**

Abbreviations

1D, 2D, 3D	one-, two-, threedimensional
BTFA	3-bromo-1,1,1-trifluoroacetone
CCR	Cross-correlated relaxation
CEST	chemical exchange saturation transfer
CPMG	Carr-Purcell-Meiboom-Gill
CR	conserved region
cryo-EM	cryoelectron microscopy
CSA	chemical shift anisotropy
CSP	chemical shift perturbation
CTS	C-terminal segment
CUT	cryptic unstable transcripts
DD	Dipole-dipole
DEST	Dark-state exchange saturation transfer
EPR	electron paramagnetic resonance
ES	excited state
EXSY	exchange spectroscopy
GPCR	G protein-coupled receptor
GS	ground state
HARD	heteronuclear adiabatic relaxation dispersion
HMQC	heteronuclear multiple quantum coherence
HSQC	heteronuclear single quantum coherence
INEPT	insensitive nuclei enhanced by polarization transfer
IPTG	Isopropyl beta D-1 thiogalactopyranoside
lncRNA	long noncoding RNA
m7G	N7-methyl guanosine
MD	molecular dynamics
miRNA	micro RNA
mRNA	messenger RNA
MQ	multiple quantum
ncRNA	noncoding RNA
NEO	neomycin
Nickel-NTA	Nickel-nitrilotriacetic acid
NMR	nuclear magnetic resonance
PAGE	polyacrylamide gel electrophoresis
PAR	paromomycin
PAS	polyadenylation signal
PRE	paramagnetic relaxation enhancement
Pol II	RNA polymerase II
RD	relaxation dispersion
RDC	residual dipolar couplings
rf	radiofrequency
RIO	ribostamycin
rRNA	ribosomal RNA
SEC	size exclusion chromatography
SL	spin lock
smFRET	single molecule fluorescence resonance energy transfer
SOFAST	Band-selective optimized flip-angle short-transient
SUT	stable unannotated transcripts
SQ	single quantum
TERRA	telomeric repeat-containing RNA
TET	2,2,2-trifluoroethanthiol
TEV	tobacco etch virus
tRNA	transfer RNA
TROSY	transverse relaxation-optimized spectroscopy
WT	wild type
xrRNA	Exoribonuclease-resistant RNA
XFEL	Xray free-electron laser
XUT	Xrn1-unstable transcripts
ZnF	zinc finger

1. Eukaryotic RNA degradation by 5′-3′ exoribonucleases

The maintenance of ribonucleic acid (RNA) levels and its adaption to external stimuli is established by the coupled regulation of RNA synthesis, processing and decay, and constitutes a vital part of cellular homeostasis (Haimovich et al. 2013, Rabani et al. 2014, Shalem et al. 2008). Not only messenger RNA (mRNA), but also noncoding RNA (ncRNA) such as transfer RNA (tRNA), ribosomal RNA (rRNA), micro RNA (miRNA) and long noncoding RNA (lncRNA) exist in a dynamic equilibrium constituted by the opposing action of RNA polymerization and RNA degradation. Although RNA synthesis by RNA polymerases, transcription, is the precondition of this equilibrium, RNA degradation is by no means irrelevant or accidental, but rather enforced by evolution: the recycling of RNA building blocks partially compensates the enormous energetic costs of its biosynthesis, and the removal of RNA enables the rapid alteration of gene expression (Hui et al. 2014).

The pathways in which degradation takes place differ between bacteria, archaea and eukarya (Clouet-d'Orval et al. 2015), in accordance with the fact that the RNAs that have to be degraded have different features. Nevertheless, degradation coincides at least in two respects: first, degradation can discriminate not only between different types of RNA, but also between specific RNAs, i.e. it adds a layer of differential gene expression. Second, some degradation pathways engage endonucleases, which cut the RNA at an internal site, to initiate degradation, but both 5′-3′ and 3′-5′ exoribonucleases are known to play important roles in all domains of life. Overall, more than 30 ribonuclease families have been identified, which contrasts with only three designs for RNA polymerases (Stoecklin and Mühlemann 2013).

1.1. Cytoplasmic RNA decay

Eukaryotes use specialized degradation pathways for different RNA classes, which converge on a number of 3′-5′ exoribonucleases such as the exosome complex and Dis3L2, and 5′-3′ exoribonucleases such as Xrn1 and Xrn2. The most-studied field is cytoplasmic mRNA decay (Łabno et al. 2016), which canonically starts with the rate-limiting step of deadenylation from the 3′ end (figure 1.1). Deadenylation is predominantly carried out in the cytoplasm by the Pan2-Pan3 and the Ccr4-Not complexes, as well as the poly(A)-specific ribonuclease (PARN) which acts both in the cytoplasm and in the nucleus. Additional deadenylases such as Nocturnin, Angel1 and Angel2 are known, but less well characterized. Upon deadenylation, poly-A binding protein (PABP) dissociates from the RNA and the closed RNA loop that results from interaction of PABP with the 5′-cap binding trimeric eIF4F protein complex opens up. Several pathyways branch off at this stage: The RNA can either be further trimmed by the exosome/Ski7 complex from the 3′ end, followed by cap degradation by DcpS. Alternatively, it is decapped by the Dcp1/Dcp2 complex at the 5′-end, followed by 5′-3′ degradation via the exoribonuclease XRN1, a strategy that is often preferred in order to prevent the transcription of partially degraded RNAs that would give rise to truncated protein products (Łabno et al. 2016) .

Both pathways can be intertwined with the action of poly(U) polymerases (PUPs), also known as terminal uridyltransferases (TUTases). PUPs catalyze the non-templated addition of uridines at the 3′ end RNAs, which is sometimes a step of RNA maturation and can add to RNA stability. More often, however, polyuridylation antagonizes the stabilizing effect of polyadenylation and is linked to RNA decay (Chung et al. 2017, Zigáčková and Vaňáčová 2018). On the one hand, 3′ poly(U)-tracts induce 3′-5′ degradation by the Dis3-like exonuclease 2 (Dis3l2), a homologue of the catalytic exosome subunit Dis3 (Rrp44). On the other hand, they stimulate decapping by recruition of the Lsm1-7/Pat1 complex and in turn the decapping complex (Song and Kiledjian 2007), which again allows for 5′-3′ degradation by Xrn1. In addition to the degradation of polyadenylated mRNAs, Xrn1 functions downstream of endonucleolytic cleavage events in mRNA quality control, participates in the degradation of non-polyadenylated histone mRNAs, of tRNAs, rRNAs, small nuclear RNAs (snRNAs), miRNAs and lncRNAs such as Xrn1-unstable transcripts (XUTs) and plays an important role in the antiviral response.

Remarkably, cytoplasmic mRNA degradation is directly coupled to the translation machinery of the ribosome: when the ribosome is stalled on an aberrant mRNA, it recruits the Ski2-Ski3-Ski8 helicase complex to channel the RNA to the exosome (Schmidt et al. 2016). Xrn1, on the other hand, is involved in the co-translational degradation of mRNA

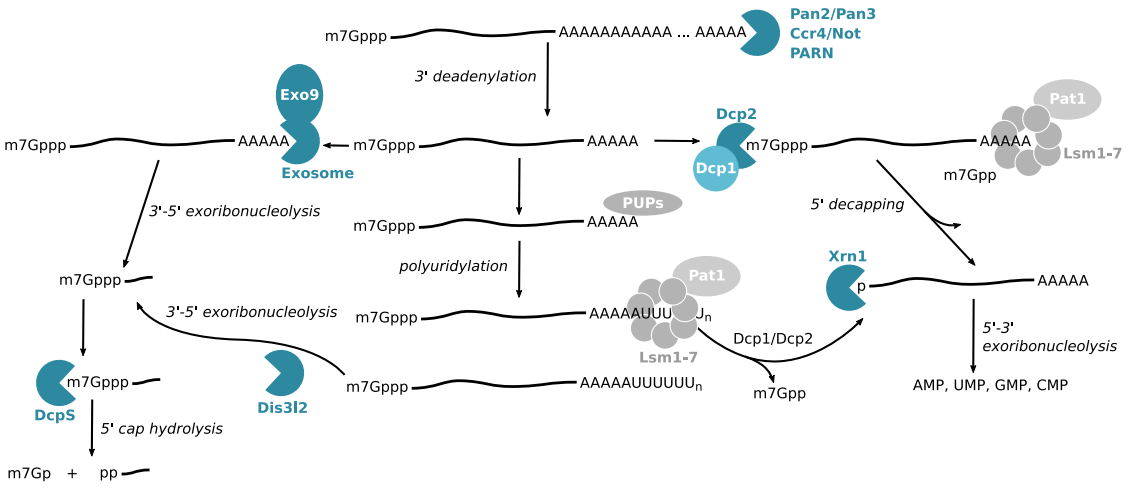

Figure 1.1.: Cytoplasmic mRNA degradation Cytoplasmic mRNA degradation is initiated by deadenylation by sucessive action of the Pan2-Pan3 and the Ccr4-Not complexes. The main pathway in the cytoplasm follows a 5′-3′ directionality, in which the 5′-cap is hydrolyzed first and the RNA is left with a 5′-monophosphate, which is prone to degradation by the 5′-3′ exoribonuclease Xrn1. Alternatively, the deadenylated RNA is degraded from the 3′ end by the exosome complex supported by the Ski helicase complex, followed by turn-over of the cap by the DcpS enzyme. As a second option, the RNA can first be polyuridylated, after which either Dis3l2 executes 3′-5′ digestion, or the Lsm1-7/Pat complex binds to the poly(U) stretch and recruits the decapping complex, followed again by Xrn1 degradation from the 5′-end.

and can directly bind to the actively translating ribosome, from which the RNA is directly directed to its final fate (Hu et al. 2009, Tesina et al. 2019).

1.2. Nuclear RNA decay

The nucleus is an inhospitable environment for RNAs: those that lack protective features such as a 5′-cap or 3′-polyadenylation will generally be cleared rapidly by the degradation machinery, but even for most RNAs that are stabilized in such a way, the decay clock is constantly ticking (Schmid and Jensen 2018). The necessity for constant RNA degradation arises from the pervasive transcription of the eukaryotic genome by RNA polymerase II (Pol II) (Jensen et al. 2013). It has been estimated, that three-quarters of the human genome can be transcribed (Djebali et al. 2012), possibly generating a plethora of RNAs that are nonfunctional and could perturb gene expression. Under normal circumstances, these transcripts are degraded promptly and therefore escape experimental detection, however, they can be classified according to their accumulation when the degradation pathyways are disturbed: cryptic unstable transcripts (CUTs) are stabilized upon loss of the catalytic exosome subunit and Xrn1-unstable transcripts (XUTs) are prone

to degradation by Xrn1, additional classes include stable unnotated transcripts (SUTs), which are related to CUTs and promoter upstream transcripts (PROMPTs), that originate from bidirectional promoter transcription.

Both 5′-3′ and 3′-5′-directional pathways play important roles in nuclear RNA metabolism, both in the productive steps of RNA processing, and in the destructive steps of RNA degradation. The nuclear 5′-3′ exoribonuclease Xrn2 shares a catalytic core domain with its cytoplasmic counterpart Xrn1 (see chapter 5 for the structural details of both enzymes) and is involved in different RNA-related processes (figure 1.2) (Miki and Großhans 2013): First, it functions in RNA quality control by degrading aberrant pre-rRNAs and pre-mRNAs as well as hypomodified tRNAs. Second, it is involved the general control of RNA levels by degrading functional pre-mRNAs (where it competes with splicing) and miRNAs. In addition, Xrn2 is involved in the degradation of telomeric repeat-containing RNA (TERRA) in *S. cerevisiae*, by which it contributes to the regulation of telomere lengths (Luke et al. 2008). Third, it plays an important role in the maturation of rRNA and small nucleolar RNA (snoRNA) by trimming 5′-extensions (Gasse et al. 2015). Fourth, Xrn2 is prominently involved in transcription termination: according to the torpedo model, Xrn2 degrades the nascent RNA transcript after cleavage of the pre-mRNA at the polyadenylation signal (PAS), thereby chasing Pol II in a torpedo-like manner. Upon encountering Pol II, Xrn2 eventually induces the dissociation of the elongation complex from the DNA. Although the exact mechanism is still under debate, the torpedo model has been integrated in the unified allosteric/torpedo model (Eaton and West 2020).

3′-5′ degradation is carried out by the nuclear exosome, a protein complex with a core of nine subunits, composed of a pseudo-hexameric ring and a trimeric cap, a catalytic subunit (Dis3/Rrp44) that has both endonuclease and exonuclease activity, and a second exonuclease (Rrp6), that distinguishes the nuclear from the cytoplasmic exosome (Januszyk and Lima 2014). A number of cofactor complexes are known to assist exosomal functions and confer helicase activity and substrate selectivity to the exosome. In metazoa these complexes comprise the Trf4/Trf5-Air1/Ar2-Mtr4 polyadenylation (TRAMP) complex, the nuclear exosome targeting (NEXT) complex and the poly(A) tail exosome targeting (PAXT) complex, both of which also include the helicase Mtr4 (Puno et al. 2019). TRAMP acts via polyadenylation of RNAs such as pre-rRNAs, aberrant tRNAs, snRNAs and snoRNAs as well as CUTs by the non-templated poly(A) polymerase Trf4 or Trf5, which promotes their turnover by the nuclear exosome . Furthermore, TRAMP is involved in rRNA processing by the exosome. NEXT acts in the degradation introns, aberrants transcripts and PROMPTS as well as related products of genome-wide transcription, whereas PAXT aids in the degradation of noncoding transcripts with long poly(A) tails.

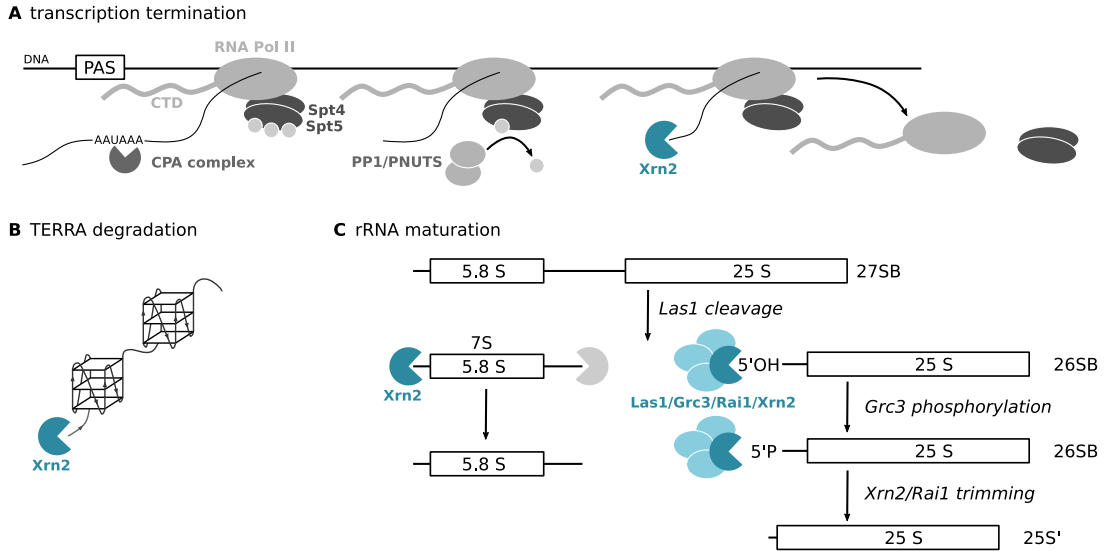

Figure 1.2.: Subset of Xrn2 functions (A) Xrn2 is involved in transcription termination. In the unified allosteric/torpedo model, protein phosphatase 1 (PP1) in complex with its nuclear targeting factor PNUTS are part of the polyadeylation signal (PAS) complexes and initiate transcription termination by dephosphorylation of the Spt5 elongation factor, tyrosine residues in the C-terminal domain (CTD) of RNA Pol II and other targets. Cooperative action of these events and sites that induce polymerase pausing or backtracking slows down Pol II. Xrn2, which digests the 3′-product of PAS cleavage, chases Pol II and acts as a molecular torpedo that displaces Pol II. The scheme is adapted from (Eaton and West 2020) (B) In *S. cerevisiae*, Xrn2 participates in the degradation of TERRA RNA and thereby promotes telomere elongation. (C) Processing of the internal trancribed spacer 2 (ITS2) is carried out by a four-subunit complex Las1-Grc3-Xrn2-Rai1 in yeast. Las1 cleaves the 27SB pre-rRNA and generates a 7S-RNA that is trimmed by Xrn2 from the 5′-end, as well as a 26SB rRNA with a 5′-OH group. Grc3 phosphorylates the 5′-end, which allows subsequent degradation by the Xrn2/Rai1 complex (Gasse et al. 2015)

1. Eukaryotic RNA degradation by 5′-3′ exoribonucleases

2. Nuclear magnetic resonance as a technique to investigate biomolecular dynamics

The aim of this chapter is fourfold: first, the importance of studying biomolecular dynamics and the specific advantages of employing NMR to do so are delineated. Second, the foundations of nuclear magnetic relaxtion are outlined. Third, fluorine NMR as a tool with great potential to study molecular dynamics is introduced. Fourth, the experiments that are used to study dynamics in a range from microseconds to seconds are described in some detail.

2.1. Molecular dynamics of proteins and nucleic acids

Matter at any level is inseparable from motion. Atomic nuclei oscillate, molecules vibrate and rotate, hearts beat, galaxies collapse. And while the perceptive organs of humans only allow direct access to a minute portion of these motions, a plethora of instruments and methods have been developed to observe, verify, analyse and make use of them.

The thermodynamic principles of physics enforce that any molecule undergoes motions at a finite temperature T. The equilibrium populations of states i with energies E_i are proportional to $\exp(-E_i/k_\mathrm{B}T)$, and it is a question of the energy barrier between these states, how fast the states interconvert, but as a rule of thumb these energy barriers are on the same scale as the energy difference between the states. At a temperature $T = 298\,\mathrm{K}$, the thermal energy is $k_\mathrm{B}T \approx 4 \times 10^{-21}\,\mathrm{J}$, which is similar to the energy differences of the lowest vibrational states of various groups such as CH or NH that are abundant in proteins and nucleic acids. It appears to be a triviality then that proteins in the liquid state are dynamic. Every single protein certainly is, due to bond vibrations on the femtosecond timescale, methyl group rotations on the picosecond-to-nanosecond timescale and rotameric jumps in side chains that range from picoseconds to microseconds (figure 2.1). Beyond these localized flucutations, however, collective motions constitute a particu-

larly interesting regime in scales of time and space, in which individual biomolecules or complexes thereof interconvert between the ground state structure and excited state structures on the order of seconds to microseconds (Henzler-Wildman and Kern 2007, Baldwin and Kay 2009, Alderson and Kay 2020). Many biochemical processes such as ligand binding and molecular recognition (Boehr et al. 2006), protein folding and unfolding (Korzhnev et al. 2004c, Neudecker et al. 2012), protein aggregation (Kotler et al. 2019, Ceccon et al. 2021), allostery (Xie et al. 2020) and catalysis (Fraser et al. 2009, Eisenmesser et al. 2005, Neu et al. 2015, Wurm et al. 2021) are connected either directely to dynamics on these timescales (i.e. to the kinetics of the exchange), to the dynamic equilibrium of the conformations that are adopted (i.e. to the thermodynamics of the exchange) or both. At the same time, protein mutations can be oncogenic by altering the relative populations of states (Xie et al. 2020), and sparsely populated states in nucleic acids with wobble base pairs hold responsible for misincorporation and fidelity checkpoint evasion (Kimsey et al. 2015, 2018). The energy landscapes of proteins and nucleic acids are thus intricately linked to their function and misfunction.

Studying conformational changes is challenging. Two workhorses of structural biology, X-ray diffraction and cryoelectron microscopy (cryo-EM) with single-particle analysis, yield static structures that can be regarded as snapshots of the conformational equilibrium and will often (but not necessarily) be close to the ground state conformation. The methods are in principle sensitive to motions: Differences in *B*-factors can be a sign of local atom displacements in X-ray structures (higher *B*-factors $\sim$ dynamics), the local density resolution in cryo-EM maps can correlate with dynamics (lower resolution $\sim$ dynamics) (Matsumoto et al. 2021), and in both cases substantially populated alternative conformers can be derived directly from the density analysis. However, care has to be taken, as high *B*-factors and local low resolution are not *necessarily* a result of motions. In addition, dedicated method developments such as time-resolved crystallography coupled to x-ray free-electron laser (XFEL) have fueled studies of mostly light-sensitive proteins, for which a reaction can be initiated by a time-controlled pump laser pulse (Brändén and Neutze 2021). Other methods to characterize biomolecular motions include hydrogen-deuterium exchange mass spectrometry that has reached sub-second resolution (Lento and Wilson 2021), ensemble and single-molecule fluoresence resonance energy transfer (FRET, smFRET) (Mazal and Haran 2019), electron paramagnetic resonance (EPR) and molecular dynamics (MD) simulations (Hollingsworth and Dror 2018).

The unique strength of NMR compared to all of these methods is its ability to experimentally characterize exchange processes with atomic resolution with a sample in the

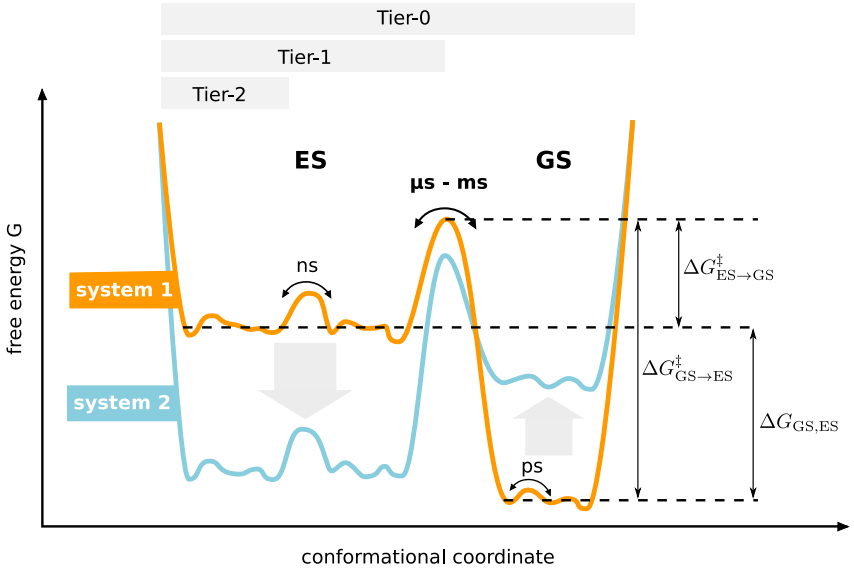

Figure 2.1.: Idealized energy landscape of a two-state exchange system Biomolecular systems have a rugged high-dimensional energy landscape that determines the populations of and exchange rates between different conformations. The energy landscape can be projected onto a one-dimensional axis for conceptual purposes, and hierarchized in a system of tiers (Frauenfelder et al. 1991). Ground state (GS) and excited state (ES) of a system that exchanges on the µs-ms timescale are thus not given by a single conformation, but by ensembles that can again be constituted by sub-ensembles which exist subsequently on ns and ps timescale. By alteration of external conditions (pH, temperature, ionic strength), upon ligand binding or by other changes to the system, the conformational equilibrium and/or the transitions between states might be changed, indicated in the figure by the energy landscapes of system 1 and system 2 (Adapted from (Henzler-Wildman and Kern 2007))

solution state[1]. It provides flexibility both regarding the spatial positioning of probes, by following a suitable isotope-labeling strategy, and regarding the timescale that is studied, by turning to appropriate experiments: Fast dynamics with excited state lifetimes of 10^{-12} to 10^{-8} s directly influence spin relaxation, and measurements of relaxation rates allow to characterize the amplitude and timescale of these local motions (Salvi et al. 2017). Measurement of residual dipolar couplings (RDCs) allow to extend this timescale up to 10^{-3} s, but require a partial alignment of the biomolecule of interest in at least five different alignment media (Kleckner and Foster 2011, Tolman and Ruan 2006). Processes on the order of 10^{-5} to 1 s can be studied by relaxation dispersion (RD), saturation transfer and magnetization transfer experiments, as well as paramagnetic relaxation enhancement (PRE) (Anthis and Clore 2015) and real-time NMR. A detailed view on a subset of

[1]Solid state NMR methods will not be discussed and applied in this thesis. The considerable progress in the field of solid-state relaxation dispersion, including Bloch-McConnell relaxation dispersion (BMRD) and near-rotary resonance relaxation dispersion (NERRD) is reviewed in Rovó (2020)

these experiments will be presented in section 2.5.

2.2. The feasibility of NMR experiments

Nuclear magnetic resonance is a spectroscopic method, in which electromagnetic fields interact with nuclear spins. It deviates from other spectroscopic methods in at least two respects (Ven 1995): First, not the electric, but the magnetic component of the electromagnetic field probes the magnetic dipole that accompanies the nuclear spin. Second, the spin eigenstates are degenerate and it is only upon placement in an external magnetic field that this degeneracy is lifted. In addition, the analysis and description of NMR experiments follows various approaches, but can typically not be restricted to the depiction of simple transitions between energy levels that is often invoked in other spectroscopic methods. In the following, the magnetization vector approach (Bloch 1946), the density matrix approach and the product operator formalism (Sørensen et al. 1984, Packer and Wright 1983, Van De Ven and Hilbers 1983) are employed, all of which are useful when it comes to the phenomenon of nuclear magnetic relaxation. The ultimate goal regarding an experiment of interest is to obtain a quantitative description of its outcome, which can subsequently be used to deduce a quantitative description of the underlying biophysical process, but also to provide a qualitative and intuitive understanding of how the experiment works.

At first sight, the molecular systems studied in biochemistry seem to be ridiculously complex: a typical biomolecular solution state NMR sample contains the target molecule with a molecular weight between kilodalton and megadalton at micromolar to millimolar concentration, corresponding to 10^{16} - 10^{17} molecules and some order of magnitudes more NMR active nuclei with spin $\frac{1}{2}$, often embedded in an aquous solution with even more NMR active ^{1}H nuclei. Even within a single molecule of interest the number of spins easily exceeds a few hundreds, all of which contribute to the full wave function that describes the molecule. Obviously, in order to analyze such a system a number of assumptions have to be made:

(1) The lattice approximation: A molecule can be thought of as being constituted by atoms, which themselves are constituted by atomic nuclei and electrons. Consequently, the quantum mechanical description of the molecule, i.e. its full Hamiltonian $\hat{H}$ and its full wave function $|\psi\rangle$ contain both electronic and nuclear contributions. The spin parts of nuclei, however, can often be treated separately to good approximation, yielding Schrödinger equations for spin Hamiltonians $\hat{H}_s$, which act on spin wave functions only and for which expectation values can be calculated

independently (Ernst et al. 2004, Cavanagh 2007). The time evolution of the spin wave function $|\psi_s(t)\rangle$ can thus in principle be calculated as

$$i\hbar\frac{\partial}{\partial t}|\psi_s(t)\rangle = \hat{H}_s|\psi_s(t)\rangle \tag{2.1}$$

where $\hat{H}_s$ contains the interactions of of the spin e.g. with the external static field $\mathbf{B}_0$ (the Zeeman Hamiltonian), with time-dependent longitudinal or transverse magnetic fields $\mathbf{B}_1$, or scalar couplings. The remaining parts of the wave function are by no means irrelevant, but constitute a surrounding that is referred to as the *lattice* in NMR spectroscopy and which can be reintroduced as a perturbation $\hat{H}_1(t)$ in order to account for relaxation. The lattice should thus not be misinterpreted as the molecular surrounding *per se*, but includes degrees of freedom from the molecule, within which the nuclear spin is situated.

(2) *The ensemble approximation:* Biomolecular NMR is an ensemble method, in which the entirety of spins gives rise to the recorded signal [2]. Accordingly, the reference to a specified spin X or spin system Y (e.g. the CH_3 group of residue X) is equivalent to referring to the statistical ensemble of this exact spin $\{X_i\}$ or spin system $\{Y_i\}$ constituted by all detected molecules i in the sample. Although all spins X_i experience an equivalent environment in their respective molecule, their wave functions $|\psi_s^i(t)\rangle$ are different, i.e. the system is not in a *pure* but in a *mixed state*, and has to be described by a *density operator* $\rho(t)$ (Cavanagh 2007), which takes on the form of a *density matrix* in a vector space. For the full quantum mechanical system with possible states $|\psi^k(t)\rangle$, the density matrix reads

$$\rho(t) = \sum_k p^k|\psi^k(t)\rangle\langle\psi^k(t)| = \sum_k p^k \sum_{n,m} c_n^k(t)c_m^{k*}(t)|n\rangle\langle m| \tag{2.2}$$

$$\equiv \sum_{n,m}\overline{c_n(t)c_m^*(t)}|n\rangle\langle m| \tag{2.3}$$

with elements

$$\rho_{nm} = \langle n|\rho(t)|m\rangle = \overline{c_n(t)c_m^*(t)} \tag{2.4}$$

[2] Notably, however, there are impressive advances in the detection and manipulation of single spins in solid state matrices (Pfender et al. 2019, Cujia et al. 2019, Abobeih et al. 2019)

Here, p^k designates the probability, that a member of the ensemble is in state k, and the wave functions have been expanded in an orthonormal basis

$$|\psi(t)\rangle = \sum_n c_n(t)\,|n\rangle \tag{2.5}$$

The real diagonal elements ρ_{nn} of the density matrix in the eigenbasis of its Hamiltonian represent the populations of the eigenstates $|n\rangle$, the off-diagonal elements $\rho_{nm,n\neq m}$ represent coherences between these states and are zero at thermal equilibrium in the absence of additional irradiation. Since NMR experiments use manipulations of the state of the spin system, it is necessary to describe the time evolution of the density matrix, and this equivalent to the Schrödinger equation is the Liouville-von Neumann equation:

$$\frac{\partial}{\partial t}\rho(t) = -i\left[\hat{H}(t), \rho(t)\right] \tag{2.6}$$

The density matrix formalism offers a straight-forward way to compute the outcome of an NMR experiment: starting from the density matrix at equilibrium ρ_{eq}, the time evolution of the density matrix through the pulse sequence is followed with the Liouville-von Neumann equation (2.6), and its final value can be converted to detectable magnetization (Cavanagh 2007):

$$\rho_{eq} \longrightarrow \rho(t) \longrightarrow M^+(t) = N\gamma\hbar\,\mathrm{Tr}\left(\rho(t)I^+\right) \tag{2.7}$$

where I^+ denotes the raising operator for spin I.

(3) *The weak coupling approximation:* In principle, the density matrix approach can be used to perform calculations on abitrary spin systems. In practice, the density matrix itself does not offer an intuitive understanding of the underlying physics, and the matrix dimensions as well as the number of eigenstates increase exponentially with the number of spins involved. An elegant approach that restricts the treatment to weakly coupled ($2\pi J_{IS} \ll |\omega_I - \omega_S|$) subsystems of the full spin system is the product operator formalism, in which the spin density operator is expanded in a set of basis operators $\{\mathbf{B}_k\}$ which span a Liouville operator space (Sørensen et al. 1984, Packer and Wright 1983, Van De Ven and Hilbers 1983, Ernst et al. 2004):

$$\sigma(t) = \sum_{k=1}^{K} b_k(t)\mathbf{B}_k \tag{2.8}$$

For a total number of N spin-$\frac{1}{2}$ nuclei, the dimension K is 4^N. The suitable choice of $\{\mathbf{B}_k\}$ depends on the case under consideration, in many situations a definition via the angular momentum operators I_α with $\alpha = x, y, z$ is advantageous:

$$\mathbf{B}_k = 2^{q-1} \prod_{j=1}^{N} \left(I_{j\alpha}\right)^{a_{jk}} \tag{2.9}$$

Here, $j = \{0 \dots N\}$ indexes the nuclei, q denotes the number of operators that are multiplied in the product and a_{jk} equals 1 for q spins and vanishes for all others. Notably, the identiy matrix divided by two, $\mathbb{1}/2$, which is derived from $j = 0$, is included in the set.

The expansion in terms of product operators greatly simplifies the analysis of how a system of weakly coupled spins evolves: First, due to the simple commutation relations of Pauli spin matrices, delays, hard radiofrequency pulses and J-couplings translate into rotations in the operator space that can be applied separately to the factors of the product. Second, in-phase operators (I_{jx},I_{jy}) and longitudinal operators (I_{jz}) can be related to I_j magnetization (M_{jx}, M_{jy}, M_{jz}). Together with visualization schemes of product operators that are reminiscent of magnetization vector diagrams, this offers some degree of intuitive understanding of complex pulse sequences. Third, the operator products present at the end of a pulse sequence directly indicate, whether they represent observable magnetization, as their product with I_j^+ has to have a non-vanishing trace (see equation 2.7). It should be noted, that some important spin systems such as CH_3 groups are not weakly coupled, since the chemical shift differences of the protons is zero, but their J-coupling has a non-zero value.

In summary, the separation of the spin system under consideration from the lattice, in conjunction with a quantum statistical mechanics treatment of the ensemble and optionally the product operator formalism pave the way to adequately analyze multi-pulse NMR experiments.

2.3. Description of nuclear magnetic relaxation

The desired perturbation of a spin system by electromagnetic radiation results in a state that deviates from the thermodynamic equilibrium. The return of the system to this equilibrium is referred to as relaxation, and the processes that drive relaxation are referred to as relaxation mechanisms. In many spectroscopic regimes, the topic of relaxation is

focused on stimulated and spontaneous emission, which represent general relaxation mechanisms that can be derived from perturbation theory. In NMR, however, spontaneous emission is completely negligible due to the relatively small energy difference between the nuclear spin ground state and excited state (Ernst et al. 2004). To illustrate this in a gedankenexperiment: An isolated excited proton nuclear spin in a perfectly stable and homogeneous external magnetic field would (with a high probability) not return to the ground state by spontaneous emission within the age of the universe. Stimulated (induced) emission and absorption, on the other hand, are constantly taking place, when transverse radiofrequency $\mathbf{B}_1$ fields are applied to the sample and lead to precession of the net magnetization around the effective field, so-called Rabi oscillations. However, in the absence of external $\mathbf{B}_1$ fields, stimulated emission is driven by thermal radiation fields with much less photons, and even if the fields were larger, the coupling would be coherent due to the long wavelengths active in NMR, and would change the direction, but not the magnitude of the magnetization (Abragam 1986). In summary, neither spontaneous emission (by coupling of the nuclear spin to vacuum field fluctuations) nor stimulated emission (by coupling to thermal radiation fields) represent significant relaxation mechanisms for nuclear spins.

In NMR, effective relaxation is instead induced by the coupling of the spin system to the lattice (a thermal bath), which is constituted by other degrees of freedom than the spin system under consideration. The lattice varies the local magnetic fields in a stochastical manner, for example by rotational motion of molecules in solution, or by collisions of molecules in a gas (Wangsness and Bloch 1953). Dependent on their frequency components and their geometric relation to the static $\mathbf{B}_0$ field, these magnetic field fluctuations can induce transitions and thus represent a driving force back to equilibrium.

In liquids, two such relaxation mechanisms prevail for nuclei with spin $\frac{1}{2}$ (Cavanagh 2007), although their relative contribution varies with the type of nucleus and other parameters such as the directly bonded atoms, the static field and the molecular weight: First, the rotation of a molecule alters the local magnetic field at the position of nuclear spins that have an anisotropic electronic environment and thus a non-zero chemical-shift anisotropy. Second, the rotation also varies the direct dipolar interaction with other spins, as can be seen from the bilinear interaction Hamiltonian of dipoles (Ernst et al. 2004). In addition, in the presence of paramagnetic molecules, the coupling to the unpaired electron can significantly enhance relaxation. Minor contributions to the relaxation of a spin I that is scalarly coupled to a spin S can also arise from the variation of scalar coupling constants J_{IS} (scalar relaxation of the first kind) or rapid longitudinal relaxation of S (scalar relaxation of the second kind) (Cavanagh 2007).

Relaxation in magnetic resonance can be theorized on different theoretical levels (Ernst et al. 2004):

(1) *Quantum-mechanical relaxation theory:* both spin system and lattice are treated as quantum mechanical objects. This model is treatable for crystalline solids and metals, for which it becomes obligatory at low temperatures, where discrete excitation of only the lowest energy states occurs (Abragam 1986).

(2) *Semi-classical relaxation theory:* the spin system is treated quantum mechanically, the lattice is described classically. This model is suitable for liquids.

(3) *Second-order perturbation theory:* Relaxation of longitudinal magnetization is treated with standard second-order perturbation theory, in which transition probabilites between different energy levels are computed from a perturbation Hamiltonian.

(4) *Phenomenological theory:* the decay of longitudinal and transverse magnetization is described phenomenologically by the Bloch equations. This macroscopic picture implicitly assumes, that the effect of the lattice is captured in two constants, the longitudinal and the transverse relaxation time (Bloch 1946)

Although a full quantum mechanical treatment of the problem is necessary to rigorously derive the random field fluctuations from the lattice, semi-classical relaxation theory is much more useful and popular for applications in liquid-state NMR spectroscopy (Ernst et al. 2004).

2.4. Fluorine NMR

Modern biomolecular NMR spectroscopy heavily relies on the spin-$\frac{1}{2}$ isotopes ^{1}H, ^{13}C and ^{15}N. This focus is rationally rooted in the atomic composition of biomolecules, and it was strenghened with the implementation of faithful coherence transfer elements such as INEPT (Morris and Freeman 1979) and the advent of advanced heteronuclear multidimensional experiments (Sattler et al. 1999). Historically, however, other nuclei have always contributed to the investigation of biomolecules with NMR and the development of new methods, amongst them ^{3}H, ^{19}F and ^{31}P. Fluorine NMR in particular has regained momentum in order to tackle specific problems, often related to protein conformational heterogeneity and dynamics. The main reasons for this revival are fivefold: first, the ^{19}F nucleus is virtually absent from protein and nucleic acids products of biosynthetic pathways occuring in nature. Although enzymatic fluorination has been reported and structurally characterized (Dong et al. 2004) it is generally rare, which is thought to be

due to the considerable electronegativity of fluorine and the need to overcome the enthalpic barrier of fluorine desolvation (Lohman et al. 2013, Agarwal et al. 2017). Second, ^{19}F has a large gyromagnetic ratio of $\gamma = 25.181 \cdot 10^7\ \mathrm{T\,s^{-1}}$, corresponding to 94.13 % of the proton value of $\gamma = 26.752 \cdot 10^7\ \mathrm{T\,s^{-1}}$, which again is seconded only by ^{3}H with $\gamma = 28.535 \cdot 10^7\ \mathrm{T\,s^{-1}}$. Not only does this high magnitude of γ translate into a high sensitivity and strong dipolar couplings, on the technical side it also frequently allows the ^{1}H-channel in the NMR probe to be matched and tuned to the ^{19}F resonance frequency. Third, the natural abundance of the ^{19}F is close to 100 %, which renders a dedicated isotope selection for labeling reagents unnecessary. Fourth, the van der Waals radius is only increased by 20 % from hydrogen to fluorine atoms and fluorine atoms can often substitute protons without inducing strong global perturbations (Kitevski-LeBlanc and Prosser 2012). Fifth, due to an anisotropic electron distribution in its $2p$ orbitals, ^{19}F is highly sensitive to its local environment and its orientation within this environment (Rastinejad et al. 1995), giving rise to a wide chemical shift distribution. The latter is advantageous for many NMR experiments that probe dynamics and where a large chemical shift difference between exchanging states facilitates the characterization of the exchange. It is, however, a mixed blessing, as it also leads to a large CSA which linearly increases with the static magnetic field strength $\mathbf{B}_0$ and often dominates relaxation.

Fluorine probes can be installed in biopolymers in various ways (Kitevski-LeBlanc and Prosser 2012). Protein labeling is achieved either during biosynthesis by incorporation of fluorinated natural or unnatural amino acids, or post-synthesis via chemical modification (figure 2.2). A large number of different fluorinated amino acid analogues or amino acid precursors has been used to introduce ^{19}F spins on a global level. Fluoroaromatics are among the most popular probes, because a variety of mono- and polyfluorinated analogues is commercially available, and aromatic residues are usually more sparse than aliphatic amino acids, which prevents excessive peak overlap in the 1D ^{19}F spectrum. On the downside, the T_2 relaxation time in fluoroaromatic systems is rather short, and can impede the application of fluorine NMR experiments especially for larger systems. Here, site-specific introduction of trifluoromethyl-groups offers an alternative and can be achieved either by repurposing amber stop codons to coding triplets for unnatural amino acids such as 4-fluorophenylalanine (Furter 1998) and 4-trifluoromethylphenylalanine (Jackson et al. 2007)(figure 2.2), or by using conventional sulfhydryl modification chemistry. Usage of a CF_3 group is advantageous in two respects: First, rapid rotation around the threefold CF_3 axis enhances the signal obtained from each probe by a factor of three. In addition, T_2 relaxation times are longer due to an methyl rotation axis order parameter $0 < S^2 < 1$. Second, signal overlap is completely abolished or can be controlled by changing the number of amber codons or accessible cysteines in the protein. Applications

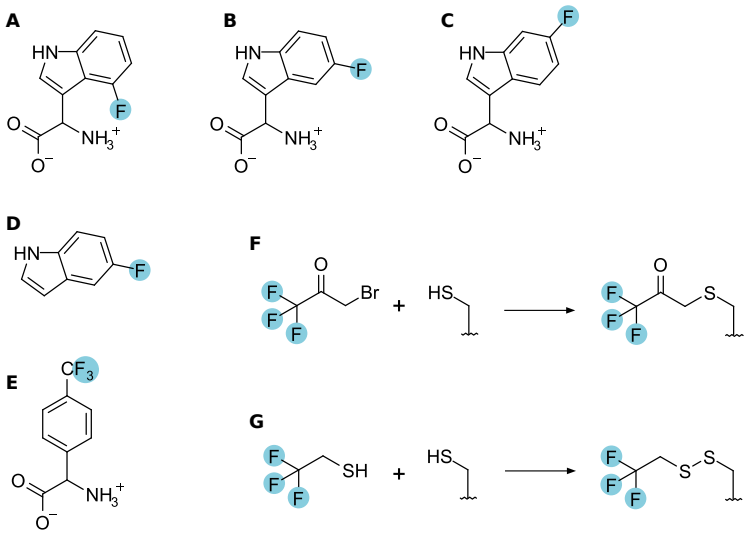

Figure 2.2.: Major ^{19}F protein-labeling strategies Biosynthetic incorporation proceeds directly by supplementation of fluorinated amino acids such as 4-fluorotryptophan (A), 5-fluorotryptophan (B) 6-fluorotryptophan (C) or by addition of the 5-fluorotryptophan precursor 5-fluoroindole (D). Site-specific labeling can be achieved by utilizing an amber-suppression system and an artificial tRNA synthetase e.g. for 4-trifluoromethylphenylalanine (E), or using covalent cysteine labeling with 3-bromo-1,1,1,-trifluoroacetone (BTFA, F) or 2,2,2-trifluoroethanthiol (TET, G). ^{19}F atoms are highlighted in blue.

of protein fluorine labeling range from protein-protein/lipid/ligand interaction studies to the characterization of folding/unfolding transitions and to the general analysis of structural dynamics and conformational heterogeneity (Gerig 1994, Danielson and Falke 1996, Kitevski-LeBlanc and Prosser 2012). Noteworthy examples of the latter include the challenging field of membrane proteins and in particular G-protein coupled receptors (GPCRs). Here, site-specific ^{19}F labeling played pivotal roles in the identification of conformational states and the influence of ligands and adaptor proteins on their equilibrium (Liu et al. 2012, Kim et al. 2013, Ye et al. 2016, Eddy et al. 2016, Horst et al. 2013, Sušac et al. 2018), the characterization of exchange dynamics between the states (Ye et al. 2016, Manglik et al. 2015, Frei et al. 2020, Huang et al. 2021) and the study of allosteric regulation of a GPCR by cations (Ye et al. 2018).

Different fluorine labeling strategies have been devised for nucleic acids, targeting the nucleobase, the sugar, or the terminal phosphate groups (figure 2.3). In particular, protocols have been established for labeling with 2-fluoroadenine (Scott et al. 2004, Sochor et al. 2016), 5-fluoropyrimidines (Horowitz et al. 1977, Hennig et al. 2007, Puffer et al. 2009), F2' ribose (Kreutz et al. 2005), terminal 5'-fluoromonophosphate and 5'-fluorodiphosphate

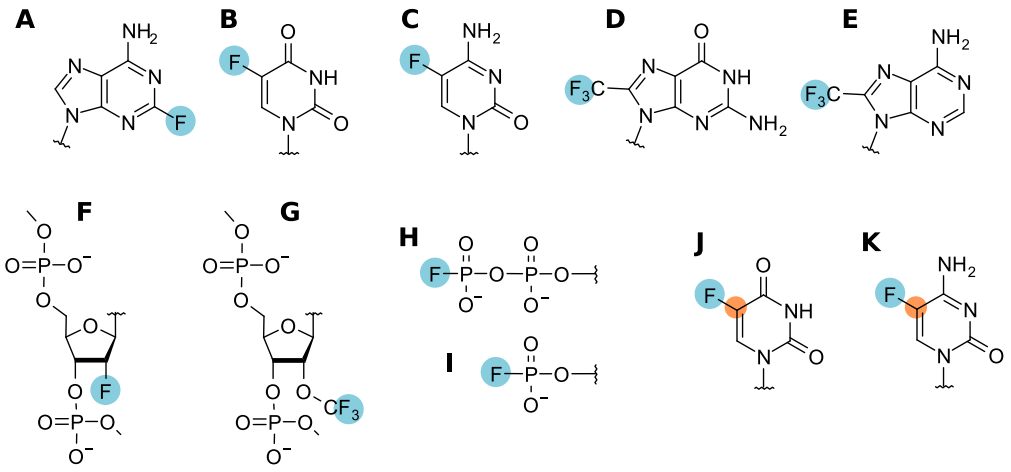

Figure 2.3.: ^{19}F nucleic acid labeling strategies Fluorine can be introduced into nucleic acids via the nucleobase, as exemplified in 2-fluoroadenosine (A), 5-fluorouridine (B), 5-fluorocytidine (C), 8-trifluoromethylguanosine (D) or 8-trifluoromethyladenosine (E). RNAs can be modified by using ribose 2′-F labeled (F) or 2′-O-trifluoromethylated (G) ribose building blocks. Synthesis of 5′-fluoromonophosphorylated (H) and 5′-difluorodiphosphorylated (I) nucleic acids has been shown to be viable for DNA fragments and can likely be transferred to RNA. Aromatic [^{19}F,^{13}C]-TROSY enhancements on the ^{13}C nucleus can be exploited in [5-^{19}F,5-^{13}C]-uridine (J) and [5-^{19}F,5-^{13}C]-cytidine labeling schemes. ^{19}F atoms are highlighted in blue, ^{13}C labels are highlighted in orange.

(Baranowski et al. 2020), trifluorothymidine (Gmeiner et al. 1991), trifluoromethylated purine ribonucleotides (Chrominski et al. 2020), 2′-O-trifluoromethylated ribonucleotides (Himmelstoß et al. 2020) and [^{19}F,^{13}C] pyrimidine for ^{19}F-^{13}C TROSY experiments (Nußbaumer et al. 2020). ^{19}F NMR has been applied to various questions in the field of nucleic acids, including RNA folding (Hammann et al. 2001), metal binding (Olejniczak 2002) and formation and exchange of secondary structures such as duplexes or G-quadruplexes (Arnold and Fisher 2000, Bao et al. 2017).

2.5. The NMR toolkit to study protein dynamics

2.5.1. Chemical exchange in NMR

An outstanding strength of NMR in comparison to other methods of structural biology is the ability to detect and quantify biomolecular dynamics. The prerequisite for an exchange process to be observable is that the states between which the exchange occurs have to be magnetically non-equivalent. Not only does that encompass chemical exchange (where atoms are transferred between molecules or the covalent structure of a molecule is altered), but it also includes internal molecular motions (where bond angles and lengths change) and binding events (where molecules are repositioned relative to

each other) [3]. Importantly, the majority of NMR methods developed to study exchange do not require a time-dependent perturbation of the chemical equilibrium of the sample, but measure the dynamical equilibrium itself. Although the spin system itself is of course perturbed in the NMR experiment, the non-equilibrium states thus generated are not significantly transferred to the lattice due to the weak coupling between system and lattice.

In section 2.1 we have seen, that dynamics in proteins and nucleic acids occur on vastly different timescales. For simplicity, we will consider a two-state exchange process between magnetically nonequivalent environments A_1 and A_2:

$$\mathrm{A}_1 \underset{\mathrm{k}_{21}}{\overset{\mathrm{k}_{12}}{\rightleftharpoons}} \mathrm{A}_2 \tag{2.10}$$

The nonequivalence of the two states can be due to a difference in relaxation rates (called R inequivalence) or, more relevant, to a difference in the chemical shifts (called C inequivalence) (Allerhand and Thiele 1966, Palmer and Koss 2019). Importantly, the appearance of an NMR spectrum is not determined by the characteristic exchange constant $k_{\mathrm{ex}} = k_{12} + k_{21}$ itself, but rather by the value of k_{ex} relative to the chemical shift difference $\Delta\omega$ between the exchanging states, as well as the populations (figure 2.4). In the limit of very slow exchange, the lifetime of each state exceeds the period of oscillation $T = 1/\Delta\nu = 2\pi/\Delta\omega$, and both states give rise to separate resonances. In the limit of very fast exchange ($k_{ex} \gg \Delta\omega$), the precession frequencies rapidly interchange and give rise to a population-averaged resonance. Due to this dependence, the exchange regimes in NMR (e.g. slow, intermediate and fast exchange) are defined on what is called an *NMR timescale*, and the regime can, ceteris paribus, change with the magnetic field strength $\mathbf{B}_0$.

Exchange phenomena arise from reversible and random processes that have irreversible consequences, and in this respect they resemble relaxation processes (Ernst et al. 2004). In line with this, the experiments used to quantify the exchange are closely linked to relaxation phenomena. Broadly speaking, the different timescales can be probed with the following experiments (figure 2.5):

- *Slow exchange ($k_{ex} \ll \Delta\omega$):* To measure slow exchange, longitudinal exchange (ZZ-exchange) and chemical exchange saturation transfer (CEST) as well as the related dark-state exchange saturation transfer (DEST) experiments can be used, all of which make use of a polarization transfer from one state to the other, reminiscent of

[3] In the following, the term *chemical exchange* will be generically used for processes, in which a nuclear spin exchanges between different environments

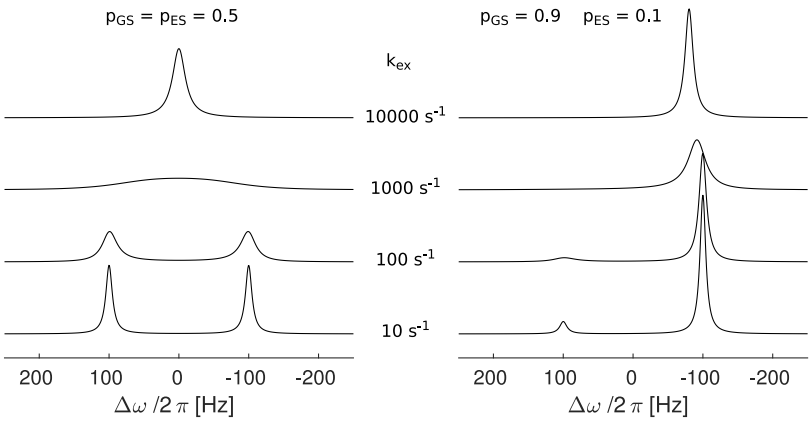

Figure 2.4.: Lineshapes modulated by chemical exchange Left: Exchange with equal populations $p_{GS} = p_{ES} = 0.5$. Right: Exchange with skewed populations $p_{GS} = 0.9$, $p_{ES} = 0.1$. All spectra were simulated with $\Delta\omega/2\pi = 200\,\text{Hz}$ and $R^0_{2,GS} = R^0_{2,GS} = 30\,\text{s}^{-1}$. The coalescence condition $k_{ex} \approx \Delta\omega/2(p_{GS}p_{ES})^{1/2}$ (Palmer et al. 2001) is fulfilled at $\sim 1257\,\text{Hz}$ (for symmetric exchange) and $\sim 2094\,\text{Hz}$ (for the skewed exchange)

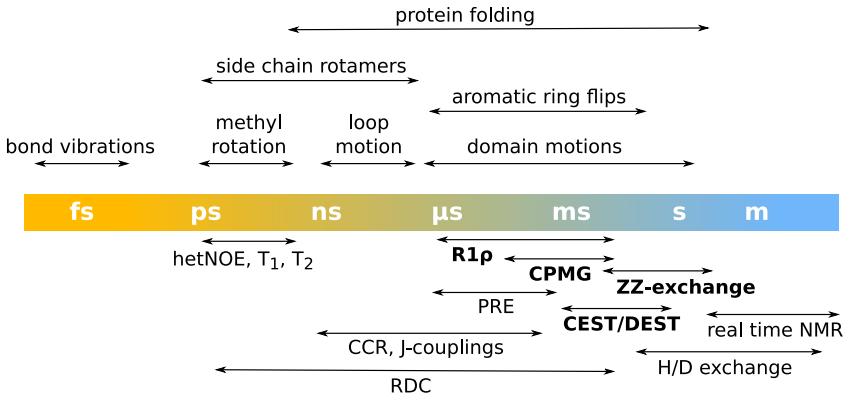

Figure 2.5.: Timescales of dynamics in biomolecules and NMR methods Biomolecules display various dynamics over a wide range of timescales, from bond vibrations over methyl rotations and aromatic ring flips to global rearrangements such as domain motions or protein folding. NMR provides a toolkit to characterize these motions, with overlapping timescale coverage. Notably, a window between the rotational correlation time $\tau_c \sim$ ns and the relaxation dispersion limit $\sim$ µs is poorly accessible: the modulation of J-couplings is generally small and averaged values can only indicate the presence of dynamics, the measurement of CCR is limited to low-molecular weight systems, and RDCs have the abovementioned drawback, that they require partial alignment in at least five alignment media.

cross-relaxation effects between different spins. At the advent of intermediate exchange, linewidth measurements can contribute to the determination of exchange parameters. For very slow processes, the fast, consecutive acquisition of NMR spectra can sometimes be applied (real time NMR).

- *Intermediate exchange ($k_{ex} \sim \Delta\omega$):* In the intermediate exchange regime, the exchange-

induced broadening of a resonance can be turned into a tool to quantify the exchange. To this end, the exchange contribution R_{ex} to the transverse relaxation rate R_2 is modulated by transverse radiofrequency (rf) fields, usually using equally spaced 180°-pulse trains (in the CPMG experiment) or constant spin-lock fields, that can be phase- or amplitude-modulated and applied on- or off-resonant (in the $R_{1\rho}$ and $R_{2\rho}$ experiments). Information can also be retrieved by the analysis of lineshapes.

- *Fast exchange ($k_{ex} > \Delta\omega$):* the fast exchange regime with lifetimes in the millisecond-to-microsecond range can be probed with both CPMG and, to slightly higher exchange rates, with $R_{1\rho}$ experiments. However, with faster exchange rates, it is increasingly difficult to separate the population of the excited state p_{ES} from the chemical shift difference $\Delta\omega$ (Ishima and Torchia 1999, Bothe et al. 2014, Korzhnev et al. 2003)

- *Very fast exchange ($k_{ex} \gg \Delta\omega$):* for exchange processes in the ns range, the exchange is on the same timescale as the Larmor frequency and the rotational correlation time τ_c. The associated motions typically alter local magnetic fields through chemical shift anisotropies and dipole-dipole interactions and can thereby influence relaxation rates such as auto-correlated relaxation rates (R_1, R_2), heteronuclear cross-relaxation rates (e.g. ^{1}H-^{15}N nuclear Overhauser effect rates σ_{HN}) and cross-correlated cross-relaxation rates η_z and η_{xy} (Salvi et al. 2017).

The dynamics investigated in this thesis span a range from sub-seconds to microseconds. The question arises, how spin relaxation (arising from very fast processes on the picosecond-nanosecond timescale) and slower exchange processes can be described simultaneously. Although both can be incorporated in the theory on the same fundamental level, the common approach is to superimpose an idealized exchange on the equation of motion for the spin system, such as given in the two-state exchange in (2.10) (Abergel and Palmer 2003). In these idealizations, the exchange occurs instantly, i.e. the transition path time that is required to migrate from state A_1 to state A_2 is always infinitely short. Obviously, this assumption is never exactly fulfilled, nevertheless, even simple two-state models are often sufficient to describe the data and can be regarded as first approximations to objective reality. In general, n-state exchange processes can be formalized as discrete Markov chains, in which transition probabilities are interpreted as exchange rates (Abergel and Palmer 2005).

The approach is exemplified *par excellence* in the BLOCH-MCCONNELL equations, which modify the vector description of magnetization by the BLOCH equations and take on the

form of a system of inhomogeneous first-order differential equations (McConnell 1958). In the next paragraphs I will briefly outline the basis of these equations, which lay the foundations for the analysis of all dynamics experiments used in this thesis. The presentation follows the clear derivation in Helgstrand et al. (2000).

We begin with the chemical configuration space: given an n-state exchange with exchange rates k_{ij} between states A_i and A_j, the rate matrix $\mathbf{K}$ reads

$$K_{ij} = \begin{cases} k_{ji}, & \text{for } i \neq j \quad (2.11) \\ -\sum_{j=1, i\neq j}^{n} k_{ij}, & \text{for } i = j \quad (2.12) \end{cases}$$

The time evolution of such a system is then given by the matrix equation

$$\frac{\mathrm{d}}{\mathrm{d}t} A(t) = \frac{\mathrm{d}}{\mathrm{d}t} \begin{pmatrix} [A_1] \\ [A_2] \\ \vdots \\ [A_n] \end{pmatrix} = \begin{pmatrix} K_{11} & k_{21} & \cdots & k_{n1} \\ k_{12} & K_{22} & \cdots & k_{n2} \\ \vdots & \vdots & \ddots & \vdots \\ k_{1n} & k_{2n} & \cdots & K_{nn} \end{pmatrix} \begin{pmatrix} [A_1] \\ [A_2] \\ \vdots \\ [A_n] \end{pmatrix} \tag{2.13}$$

with the formal solution

$$A(t) = e^{\mathbf{K}t} A(0) \tag{2.14}$$

On the other hand, we have the inhomogenous BLOCH equations that describe the time evolution of magnetization to an equilibrium magnetization M_0 in the presence of transverse relaxation with a rate R_2 and longitudinal relaxation with a rate R_1 (Bloch 1946). For magnetization at an offset Ω relative to the rf field, the equations read

$$\frac{\mathrm{d}}{\mathrm{d}t} \begin{pmatrix} M_x \\ M_y \\ M_z \end{pmatrix} = - \begin{pmatrix} R_2 & \Omega & -\omega_y \\ -\Omega & R_2 & \omega_x \\ \omega_y & -\omega_x & R_1 \end{pmatrix} \begin{pmatrix} M_x \\ M_y \\ M_z \end{pmatrix} + \begin{pmatrix} 0 \\ 0 \\ R_1 M_0 \end{pmatrix} \tag{2.15}$$

Here, an additional radiofrequency field is already included, with an amplitude B_1, a frequency ω_1 and a phase ϕ_1, such that for a nucleus with a gyromagnatic ratio γ, the fields that couple the transverse components with the longitudinal M_z magnetization are given by

$$\omega_x = -\gamma B_1 \cos \phi_1 \tag{2.16}$$

$$\omega_y = -\gamma B_1 \sin \phi_1 \tag{2.17}$$

The simple idea of the BLOCH-MCCONNELL equations is, that the transition of a protein from state A_i to state A_j includes the transfer of the current magnetization from A_i to A_j, without a change in the orientation of magnetization. Mathematically, this can be formulated by using a $3n$-dimensional product space between n-dimensional configuration space and 3-dimensional magnetization space (Helgstrand et al. 2000). The state vector is then given by

$$\mathbf{M} = \begin{pmatrix} A_1 \\ A_2 \\ \vdots \\ A_n \end{pmatrix} \otimes \begin{pmatrix} M_x \\ M_y \\ M_z \end{pmatrix} = \begin{pmatrix} M_{x1} \\ M_{y1} \\ M_{z1} \\ M_{x2} \\ \vdots \\ M_{zn} \end{pmatrix} \tag{2.18}$$

Similarly, the $3n$-dimensional rate matrix $\mathbf{K}$ in product space is obtained from the n-dimensional rate matrix $\mathbf{K}_n$ as

$$\mathbf{K} = \mathbf{K}_n \otimes \mathbb{1}_3 \tag{2.19}$$

and the Bloch evolution matrix is expanded to a block-diagonal matrix

$$\mathbf{L} = -\mathbb{1}_n \otimes \begin{pmatrix} R_2 & \Omega & -\omega_y \\ -\Omega & R_2 & \omega_x \\ \omega_y & -\omega_x & R_1 \end{pmatrix} = \begin{pmatrix} \mathbf{L}_1 & 0 & \cdots & 0 \\ 0 & \mathbf{L}_2 & \cdots & 0 \\ \vdots & \vdots & \ddots & \vdots \\ 0 & \cdots & 0 & \mathbf{L}_n \end{pmatrix} \tag{2.20}$$

with

$$\mathbf{L}_j = -\begin{pmatrix} R_{2j} & \Omega_j & -\omega_y \\ -\Omega_j & R_{2j} & \omega_x \\ \omega_y & -\omega_x & R_{1j} \end{pmatrix} \tag{2.21}$$

Here, $R_{2,j}$, $R_{1,j}$ and Ω_j refer to the transverse and longitudinal relaxation rates as well as the offset of state j, respectively. The time evolution of the system is now given by

$$\frac{\mathrm{d}}{\mathrm{d}t}\mathbf{M}(t) = (\mathbf{K} + \mathbf{L})\,\mathbf{M}(t) + \mathbf{\Theta} \tag{2.22}$$

where $\mathbf{\Theta}$ represents the inhomogeneous part

$$\mathbf{\Theta} = \begin{pmatrix} 0 \\ 0 \\ \Theta_1 \\ \vdots \\ 0 \\ 0 \\ \Theta_n \end{pmatrix} \tag{2.23}$$

with

$$\Theta_j = R_{1j} M_{0j}(t) \tag{2.24}$$

$$M_{0j} = M_0 \frac{[A_j](t)}{\sum_{i=1}^{n} [A_i](t)} \tag{2.25}$$

For the simple two-state exchange model (2.10) we obtain

$$\mathbf{K} + \mathbf{L} = \begin{pmatrix} -R_{21} - k_{12} & -\Omega_1 & \omega_y & k_{21} & 0 & 0 \\ \Omega_1 & -R_{21} - k_{12} & -\omega_x & 0 & k_{21} & 0 \\ -\omega_y & \omega_x & -R_{11} - k_{12} & 0 & 0 & k_{21} \\ k_{12} & 0 & 0 & -R_{22} - k_{21} & -\Omega_2 & \omega_y \\ 0 & k_{12} & 0 & \Omega_2 & -R_{22} - k_{21} & -\omega_x \\ 0 & 0 & k_{12} & -\omega_y & \omega_x & -R_{12} - k_{21} \end{pmatrix} \tag{2.26}$$

The inhomogeneous equations (2.22) can be casted in a homogeneous form, which are convenient for numerical purposes (Helgstrand et al. 2000). For two states the equations then read

$$\frac{\mathrm{d}}{\mathrm{d}t} \begin{pmatrix} E/2 \\ M_{x1} \\ M_{y1} \\ M_{z1} \\ M_{x2} \\ M_{y2} \\ M_{z2} \end{pmatrix} = \boldsymbol{A} \begin{pmatrix} E/2 \\ M_{x1} \\ M_{y1} \\ M_{z1} \\ M_{x2} \\ M_{y2} \\ M_{z2} \end{pmatrix} \tag{2.27}$$

with an evolution matrix

$$\boldsymbol{A} = \begin{pmatrix} 0 & 0 & 0 & 0 & 0 & 0 & 0 \\ 0 & -R_{21} - k_{12} & -\Omega_1 & \omega_y & k_{21} & 0 & 0 \\ 0 & \Omega_1 & -R_{21} - k_{12} & -\omega_x & 0 & k_{21} & 0 \\ 2\Theta_1 & -\omega_y & \omega_x & -R_{11} - k_{12} & 0 & 0 & k_{21} \\ 0 & k_{12} & 0 & 0 & -R_{22} - k_{21} & -\Omega_2 & \omega_y \\ 0 & 0 & k_{12} & 0 & \Omega_2 & -R_{22} - k_{21} & -\omega_x \\ 2\Theta_2 & 0 & 0 & k_{12} & -\omega_y & \omega_x & -R_{12} - k_{21} \end{pmatrix} \tag{2.28}$$

E is unity, chosen to conform to the product operator normalization of (2.9) (Helgstrand et al. 2000). An important simplification of the BLOCH-MCCONNELL equations arises, if transverse and longitudinal magnetization do not interconvert. In this case, their equations are independent of each other and can be solved seperately. Neglecting cross-relaxation, relaxation matrices can be defined for convenience as

$$\mathbf{R}_1^{ij} = \delta_{ij} R_{1j} \tag{2.29}$$

$$\mathbf{R}_2^{ij} = \delta_{ij} R_{2j} \tag{2.30}$$

For free precession and in the chemical equilibrium, the longitudinal magnetization $\Delta\mathbf{M}_z(t) = \mathbf{M}_z(t) - \mathbf{M}_0(t)$ then evolves according to

$$\frac{\mathrm{d}}{\mathrm{d}t}\Delta\mathbf{M}_z(t) = (-\mathbf{R} + \mathbf{K})\Delta\mathbf{M}_z(t) \tag{2.31}$$

Using the diagonal offset matrix $\boldsymbol{\Omega}$ given by

$$\Omega_{ij} = \delta_{ij}\Omega_j \tag{2.32}$$

the transverse magnetization $\mathbf{M}_+ = \mathbf{M}_x + i\mathbf{M}_y$ in the rotating frame is likewise given by

$$\frac{\mathrm{d}}{\mathrm{d}t}\mathbf{M}_+(t) = (i\boldsymbol{\Omega} - \mathbf{R} + \mathbf{K})\mathbf{M}_+(t) \tag{2.33}$$

For a two-state model, equations (2.31) and (2.33) are then two-dimensional matrix equations that can be solved analytically with conventional methods (Cavanagh 2007):

$$\frac{\mathrm{d}}{\mathrm{d}t}\begin{pmatrix} \Delta M_{z1}(t) \\ \Delta M_{z2}(t) \end{pmatrix} = \begin{pmatrix} -R_{11} - k_{12} & k_{21} \\ k_{12} & -R_{12} - k_{21} \end{pmatrix}\begin{pmatrix} \Delta M_{z1}(t) \\ \Delta M_{z2}(t) \end{pmatrix} \tag{2.34}$$

$$\frac{\mathrm{d}}{\mathrm{d}t}\begin{pmatrix} M_{+1}(t) \\ M_{+2}(t) \end{pmatrix} = \begin{pmatrix} i\Omega_1 - R_{21} - k_{12} & k_{21} \\ k_{12} & i\Omega_2 - R_{22} - k_{21} \end{pmatrix}\begin{pmatrix} M_{+1}(t) \\ M_{+2}(t) \end{pmatrix} \tag{2.35}$$

In a similar manner, the exchange can be superimposed on more difficult equations of motion for product operators in coupled spin systems, for example in $^{13}CH_3$ groups (Skrynnikov et al. 2001) and $^{15}NH_2$-groups (Mulder et al. 2001). Furthermore, BLOCH-MCCONNELL-like equations represent a starting point for the quantitative analysis of many experiments, usually by incorporating additional rf fields. Examples of such analyses will be encountered in the following sections.

2.5.2. ZZ-exchange

The transfer of longitudinal magnetization between different states by chemical exchange forms the basis of ZZ-exchange spectroscopy (also abbreviated as *EXSY*) (Jeener et al. 1979, Montelione and Wagner 1989, Farrow et al. 1994). The idea is fairly simple and applies to the slow exchange regime: if the states are sufficiently populated and sufficiently separated by a chemical shift difference $\Delta\omega$, the starting magnetization can be labeled by its chemical shift ω_i, subsequently, longitudinal spin order is allowed to exchange during a mixing period τ_{mix} and is then labeled by its final chemical shift ω_j. A crosspeak at [ω_i,ω_j] qualitatively confirms that the states exchange, a quantitative analysis of exchange rates and longitudinal decay rates can be performed by varying τ_{mix} and evaluating the intensity of the autopeaks I_{ii} and I_{jj} as well as the crosspeaks I_{ij} and I_{ji}. For a 2-state exchange, the evolution equations read (Farrow et al. 1994, Palmer et al. 2001)

$$\frac{\mathrm{d}}{\mathrm{d}t}\begin{pmatrix}\Delta M_{zA}(t)\\ \Delta M_{zB}(t)\end{pmatrix} = \begin{pmatrix}-R_{1A}^0 - p_B k_{\text{ex}} & p_A k_{\text{ex}}\\ p_B k_{\text{ex}} & -R_{1B}^0 - p_A k_{\text{ex}}\end{pmatrix}\begin{pmatrix}\Delta M_{zA}(t)\\ \Delta M_{zB}(t)\end{pmatrix} \tag{2.36}$$

$$\equiv \mathbf{E}\cdot\begin{pmatrix}\Delta M_{zA}(t)\\ \Delta M_{zB}(t)\end{pmatrix} \tag{2.37}$$

This matrix equation can be solved analytically to extract populations and transition rates. Nevertheless, a more convenient way to analyze the exchange is to solve (2.36) using a numerical calculation based on the matrix exponential (e.g. using the `expm` function in MATLAB) of the evolution matrix **E**. Turning to peak intensities I_{ij}, the solution is given by

$$\begin{pmatrix}I_{AA}(t) & I_{AB}(t)\\ I_{BA}(t) & I_{BB}(t)\end{pmatrix} = \exp\{\mathbf{E}\cdot t\}\begin{pmatrix}I_{AA}(0) & 0\\ 0 & I_{BB}(0)\end{pmatrix} \tag{2.38}$$

The advantage of equation (2.38) over the analytical solution is, that it can be extended in a straightforward manner to the general n-state exchange.

2.5.3. CEST and DEST

ZZ-exchange experiments are limited to systems, for which the exchanging states can be detected in the respective spectra, i.e. for a given signal-to-noise they have to be populated to a sufficient extent. A similar range of exchange can be probed by turning from magnetization transfer to saturation transfer, the principle of chemical exchange saturation transfer (CEST) and dark-state exchange saturation transfer (DEST) experiments. The idea is that the readout of the exchange does not have to involve both exchanging peaks, but can be restricted to the ground state (or more general to peaks of sufficient intensity), if this peak is sensitive to the selective perturbation of another state. The perturbation does not need to be a saturation, in fact, the selective inversion recovery experiment, which is closely related to the ZZ-exchange experiment can be regarded as a step from ZZ-exchange towards CEST/DEST: instead of labeling the resonances at the start of the mixing time τ_{mix} with their frequency, one of them is labeled by inverting it selectively. The generated negative longitudinal spin order is then transferred to exchanging resonances, which are correspondingly attenuated in a time-dependent manner (Robinson et al. 1985, Bain and Cramer 1993).

CEST and DEST are, however, more flexible than selective inversion: magnetization is prepared as longitudinal spin order and saturated with a weak B_1 field for a time T_{ex} at an offset Ω. Subsequently, the new equilibrium values of the visible resonances are read out. Here, the frequency of saturation $\omega_{CEST} = \gamma B_1$, the saturation/exchange time T_{ex} and the offset Ω can all be varied. Saturation transfer was first applied in a continuous wave setup (Forsén and Hoffman 1963), and subsequently used to assign broad, hyperfine-shifted signals in metalloproteins (Bertini et al. 1999, Hansen and Led 2006) and to image metabolites (Ward et al. 2000). Still, the full potential of saturation transfer in biomolecular NMR was only demonstrated in studies on the exchange of amyloid-β (Aβ) monomers with oligomers (Fawzi et al. 2010) and protofibrils (Fawzi et al. 2011) using DEST; and by the quantification of sparsely populated, "invisible" states in ^{15}N CEST experiments applied to a protein-ligand exchanging system as well as to an unfolding transition (Vallurupalli et al. 2012).

DEST makes use of different transverse relaxation rates of the states (in the nomenclature of Allerhand and Thiele (1966), it is an R inequivalence experiment). Given an excited state with a vastly increased R_2^{dark} rate, this state cannot be directly detected in conventional spectra owing to its rapid relaxation, hence the name *dark state*. Due to the corresponding line broadening, however, dark state longitudinal magnetization can be partially saturated with weak B_1 fields over a large range of offsets. The visible ground state

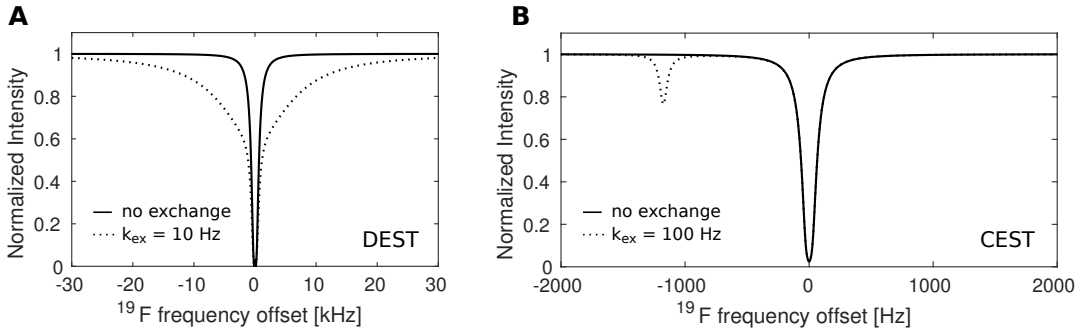

Figure 2.6.: Simulated DEST and CEST spectra (A) Simulated DEST spectrum with $p_{\mathrm{dark}} = 5\,\%$, $R_2^{\mathrm{dark}} = 10\,000\,\mathrm{s}^{-1}$, $R_1 = 3\,\mathrm{s}^{-1}$, $R_{2,\mathrm{GS}} = 10\,\mathrm{s}^{-1}$, $k_{\mathrm{ex}} = 10\,\mathrm{s}^{-1}$, $T_{\mathrm{ex}} = 1\,\mathrm{s}$. (B) Simulated CEST spectrum with $p_{\mathrm{ES}} = 5\,\%$, $R_1 = 1\,\mathrm{s}^{-1}$, $R_2 = 100\,\mathrm{s}^{-1}$, $k_{\mathrm{ex}} = 100\,\mathrm{s}^{-1}$, $\Delta\omega = 2.5 \cdot 470 \cdot 2\pi\,\mathrm{Hz}$, $T_{\mathrm{ex}} = 0.4\,\mathrm{s}$

with a low R_2^{vis} rate is not directly affected by the saturation unless it is close to its chemical shift. Exchange with the saturated excited dark state now leads to a partial saturation of the ground state, and the attenuation of the ground state signal as a function of the offset of the saturating pulse can be quantitatively analyzed (figure 2.6) (Fawzi et al. 2010, 2011, 2012, 2014, Anthis and Clore 2015). The DEST experiment is usually combined with a measurement of the lifetime line broadening R_{llb} (not to be confused with R_{ex}), defined as the difference in transverse relaxation rates in the absence and presence of exchange with a fast relaxing species, that is due to the difference in transverse relaxation rates between the states. By measuring ΔR_2, the apparent association rates $k_{\mathrm{on}}^{\mathrm{app}} \approx \Delta R_2$ can be estimated if $R_1^{\mathrm{vis}} \leq k_{\mathrm{on}}^{\mathrm{app}} \leq R_2^{\mathrm{vis}}$. This condition is frequently met if DEST profiles can be recorded, and the simultaneous fit of the data allows for better definition of the exchange parameters (Fawzi et al. 2011, Anthis and Clore 2015).

Following DEST, the original idea of utilizing the different chemical shifts of the exchanging states was picked up in biomolecular NMR (Vallurupalli et al. 2012) (in the nomenclature of Allerhand and Thiele (1966), CEST is a C inequivalence experiment). In CEST experiments, the excited state might still escape observation in a spectrum, but this time due to its low population and not because of an excessively high R_2^{ES} rate. Accordingly, saturation transfer is limited to the offsets around the chemical shift of the excited state ω_{ES}, and the existence of an excited state manifests as an additional dip in the offset-dependent saturation profile (figure 2.6).

CEST experiments have been developed for ^{15}N and ^{1}H spins in backbone amide groups (Vallurupalli et al. 2012, Yuwen and Kay 2017), ^{13}C and ^{1}H spins in $^{13}CH_3$ and $^{13}CHD_2$ groups (Bouvignies and Kay 2012, Rennella et al. 2015, Yuwen et al. 2017), $^{13}C_\alpha$ spins

(Hansen et al. 2013) and ^{13}CO spins (Vallurupalli and Kay 2013). Furthermore, pulse sequences were adapted for CEST experiments in nucleic acids on ^{13}C spins (Zhao et al. 2014), protonated and unprotonated ^{15}N spins (Zhao et al. 2020) and ^{1}H spins (Wang et al. 2021), and a nucleic acid-specific ^{1}H CEST experiment based on a novel proton-only pulse sequence was established (Schlagnitweit et al. 2018).

Analysis of DEST and CEST data follows a numerical approach, as no general analytical expression has been derived for the analysis of the profiles. Numerical calculation of CEST profiles in this thesis was performed using a recasted version of equation (2.27), in which the components are ordered by their x, y and z components and the CEST field ω_{CEST} always has a phase x:

$$\frac{\mathrm{d}}{\mathrm{d}t}\mathbf{M} = A\mathbf{M} \tag{2.39}$$

with $\mathbf{M} = [E/2, M_{x1}, M_{x2}, M_{y1}, M_{y2}, M_{z1}, M_{z2}]$ and the evolution matrix

$$A = \begin{pmatrix} 0 & 0 & 0 & 0 & 0 & 0 & 0 \\ 0 & -R_{21}-k_{12} & k_{21} & -\Omega_1 & 0 & 0 & 0 \\ 0 & k_{12} & -R_{22}-k_{21} & 0 & -\Omega_2 & 0 & 0 \\ 0 & \Omega_1 & 0 & -R_{21}-k_{12} & k_{21} & -\omega_{\mathrm{CEST}} & 0 \\ 0 & 0 & \Omega_2 & k_{12} & -R_{22}-k_{21} & 0 & -\omega_{\mathrm{CEST}} \\ 2R_{11}M_{01} & 0 & 0 & \omega_{\mathrm{CEST}} & 0 & -R_{11}-k_{12} & k_{21} \\ 2R_{12}M_{02} & 0 & 0 & 0 & \omega_{\mathrm{CEST}} & k_{12} & -R_{12}-k_{21} \end{pmatrix} \tag{2.40}$$

Here, the equilibrium magnetization M_{0i} can be identified with the population p_i of each state. The intensity of the ground state after saturation with a weak RF field ω_{CEST} at a given offset δ_{CEST} for a time T_{CEST} can then be directly calculated with a matrix exponential from the starting magnetization $\mathbf{M}_0 = [E/2, 0, 0, 0, 0, M_{z1}, M_{z2}]^\top$ and subsequent projection on the ground state $\mathbf{M}_{\mathrm{proj}} = [0, 0, 0, 0, 0, 1, 0]^\top$ as

$$I(\delta_{\mathrm{CEST}}) = \mathbf{M}_{\mathrm{proj}} \cdot e^{A \cdot T_{\mathrm{CEST}}} \mathbf{M}_0 \tag{2.41}$$

Similar equations with $(n+1) \times (n+1)$ matrices A can be formulated for $n = 3$ states (yielding a 10×10 matrix) and $n = 4$ states (yielding a 13×13 matrix). Of note, the same equations can be used to calculate the intensity of any other state i by projecting the time-evolved magnetization onto this state.

2.5.4. CPMG

CEST experiments start to fail as soon as the coalescence point of an exchange is reached and the peaks of the two states collapse into a single peak (figure 2.4). As shown above,

this event depends on the chemical shift difference $\Delta\omega$ of the two states, but it creates an approximate upper boundary for k_{ex} of $\approx 500\,s^{-1}$ (Vallurupalli et al. 2012, Anthis and Clore 2015). Fortunately, exchange-induced line broadening offers an alternative way to quantify the exchange all the way from slow to fast exchange, albeit with different restrictions concerning the parameters that can be obtained, which can in favourable cases comprise kinetic information (exchange rate k_{ex}), thermodynamic information (populations p_i) and structural information (chemical shift difference $\Delta\omega$). In general, the observed transverse relaxation rate is increased by an exchange contribution R_{ex} as (Palmer et al. 2001)

$$R_{2,obs} \equiv R_2 = R_2^0 + R_{ex} \tag{2.42}$$

The way in which R_{ex} depends on the parameters of the exchange differs with the exchange regime: in the limit of slow exchange, where two peaks are discernible, their transverse relaxation rates are increased linearly by the transition rates k_{ab} and k_{ba}, respectively:

$$R_{2a} = R_{2a}^0 + k_{ab} = R_{2a}^0 + p_b k_{ex} \tag{2.43}$$

$$R_{2b} = R_{2b}^0 + k_{ba} = R_{2b}^0 + p_a k_{ex} \tag{2.44}$$

In the limit of fast exchange, the apparent rate is obtained by the population averaged value of the individual R_2 rates plus an exchange contribution, that now depends on the populations p_j, their chemical shift difference $\Delta\omega$ as well as the exchange rate k_{ex}:

$$R_2^{av} = p_a R_{2a}^0 + p_b R_{2b}^0 + \frac{p_a p_b \Delta\omega^2}{k_{ex}} \tag{2.45}$$

From equations (2.43), (2.43) and (2.45) it follows that for both $k_{ex} \to 0$ and $k_{ex} \to \infty$ the exchange contribution vanishes.

2.5.4.1. The CPMG sequence

The increase in R_2 results from an enhanced dephasing of transverse magnetization by the flow of magnetization between different chemical environments. A similar peak broadening is induced by magnetic field inhomogeneities, which modulate the Larmor frequency in a continuous manner. In order to minimize the resulting artificial increase in R_2, several pulse schemes were developed in the early days of NMR: the 90°-90° spin echo (Hahn 1950), the 90°-$(180°)_n$ spin echo (Carr and Purcell 1954) and the improved 90°-$(180°)_n$ pulse sequence, where the 90° pulse is phase-shifted by $\pi/2$ (Meiboom and Gill 1958). The latter sequences, known by the acronyms (CP, CPMG) of their inventors,

refocus magnetization of equivalent spins by the introduction of one or more 180°-pulses, which effectively reverses phase lag and phase lead of spins that experience a higher or lower constant B_0 field. In the same way, the exchange contribution R_{ex} can be reduced to an extent that depends on the spacing τ_{CPMG}[4] in between the π-pulses or, equivalently, on the CPMG frequency

$$\nu_{CPMG} = \frac{1}{2\tau_{CPMG}} \tag{2.46}$$

The sampling of R_2^{eff} as a function of $\nu_{CPMG} = \omega_{CPMG}/2\pi$ (conventionally at a constant total CPMG time T_{CPMG}) then yields a relaxation dispersion profile. Of note, while a non-flat profile is indicative of an exchange process, a flat profile can result from the absence of exchange (on the timescale covered by the experiment), but might also arise from a vanishing chemical shift difference $\Delta\omega$, from highly skewed populations or from exchange rates that strongly differ from the applied CPMG frequencies. Generally, relaxation dispersion profiles that report on an exchange are elevated at lower frequencies, however, more complex profiles can be obtained if non-single quantum operators are used (Korzhnev et al. 2004a,b).

It is instructive to realize, that the CPMG experiment bears analogy to the CEST experiment (Vallurupalli et al. 2012): in CEST, the application of a weak ω_{CEST} field at the offset of the minor peak induces Rabi oscillations of the minor state magnetization around B_1, which translates into dephasing of the ground state magnetization by chemical exchange. In the CPMG setup, the offset $\Delta\omega$ itself corresponds to ω_{CEST} and leads to the accumulation of an additional phase in the transverse plane, if the minor state is transiently sampled.

2.5.4.2. CPMG pulse sequences

The CPMG scheme can be generalized as (Palmer et al. 2005)

$$\left\{ \left(\frac{\tau_{CPMG}}{2} - \mathbf{P}_1 - \frac{\tau_{CPMG}}{2} \right)_n - \mathbf{P}_2 - \left(\frac{\tau_{CPMG}}{2} - \mathbf{P}_1 - \frac{\tau_{CPMG}}{2} \right)_n \right\}_m \tag{2.47}$$

where $\mathbf{P}_1$ and $\mathbf{P}_2$ are pulse sequence elements (usually involving 180° pulses on different spins) and n and m are integers. Importantly, this generalized element can be incorporated into a variety of pulse sequences targeting different spin systems, thereby greatly expanding the scope of NMR methodology. Specifically, experiments targeting NH and NH_2 groups (Loria et al. 1999a,b, Tollinger et al. 2001, Ishima and Torchia 2003,

[4]The spacing is sometimes defined as $2\tau_{CPMG}$, with obvious changes in the equations for analysis

Orekhov et al. 2004, Korzhnev et al. 2004b, Yuwen and Kay 2019), $^{13}CH_3$ and $^{13}CHD_2$ methyl groups (Skrynnikov et al. 2001, Korzhnev et al. 2004a, Tugarinov and Kay 2007, Lundström et al. 2007, Baldwin et al. 2010, Otten et al. 2010, Weininger et al. 2012a, Rennella et al. 2016, Yuwen et al. 2016, Gopalan et al. 2018, Yuwen et al. 2019), ^{13}CO (Ishima et al. 2004, Lundström et al. 2008, Hansen et al. 2008) $^{13}C^{\alpha}$ (Hill et al. 2000, Hansen et al. 2008) and $^{1}H^{\alpha}$ (Lundström et al. 2009a), side chain $^{13}C^{\beta}$ (Lundström et al. 2009b) and side chain ^{1}H (Hansen et al. 2012) as well as aromatic ^{13}C (Weininger et al. 2012b) and aromatic ^{1}H probes (Raum et al. 2018, 2019) have been established. The application of these experiments have fundamentally impacted the study of conformational ensembles of biomolecules.

Special relevance can be ascribed to CPMG experiments on methyl groups in highly deuterated samples. For $^{13}CH_3$ spin systems a transverse relaxation optimized spectroscopy (TROSY) effect can be exploited, that originates from intra-methyl dipolar interactions (Tugarinov et al. 2003, Ollerenshaw et al. 2003). This methyl-TROSY effect minimizes relaxation losses so efficiently that it allows to obtain high quality ^{1}H-^{13}C HMQC datasets even for large biomolecular systems, for which transverse relaxation is otherwise prohibitive. In combination with versatile labeling strategies of Ala-β, Val-$\gamma1/\gamma2$, Thr-$\gamma2$, Ile-$\gamma2$, Ile-$\delta1$, Leu-$\delta1/\delta2$ and Met-ε methyl groups, methyl-TROSY NMR techniques have provided unique insights into protein structure, dynamics and interactions (Schütz and Sprangers 2020).

The $^{13}CH_3$ group is an AX_3 spin system for which coherences up to coherence order four can be generated. In general, the coherence $\Lambda_i = C^{k_C} H_1^{k_1} H_2^{k_2} H_3^{k_3}$ has coherence order $m_i = k_C + k_1 + k_2 + k_3$, where $k_j = \{-1, 0, 1\}$, $C^{\pm1}$ and $H_j^{\pm1}$ are shift operators and C^0 and H_j^0 can either be identiy operators $\mathbb{1}$ or longitudinal spin order C_z and H_{jz} (Palmer et al. 2005). The exchange is then associated with a frequency change of

$$\Delta\omega_i = k_C \Delta\omega_C + \sum_{i=1}^{3} k_j \Delta\omega_H \tag{2.48}$$

The selection of coherences thus opens up the possibility to perform different CPMG experiments on $^{13}CH_3$-labeled samples. The simplest methyl-CPMG experiments in terms of coherences make use of ^{1}H single-quantum (SQ) (Tugarinov and Kay 2007, Yuwen et al. 2019) or ^{13}C SQ terms (Skrynnikov et al. 2001, Lundström et al. 2007). The experiments are sensitive to a difference in either the proton ($|\Delta\omega_H|$) or carbon dimension ($|\Delta\omega_C|$) between the ground state and the excited state. $\Delta\omega_H$ and $\Delta\omega_C$ are often not correlated, thus, the experiments complement each other, as methyl groups for which the excited state is only shifted in the proton dimension would give rise to flat relaxation disper-

sion profiles in the ^{13}C SQ experiment and vice versa. In this respect, the development of a ^{1}H SQ CPMG experiment that profits from a methyl-TROSY effect is an important technical advancement that renders the experiment applicable to large biomolecular assemblies (Yuwen et al. 2019). The ^{13}C SQ CPMG experiment cannot be designed in such a way, since the transfer of in-phase (C_x, C_y) or anti-phase ($2C_xH_z$, $2C_yH_z$) carbon single-quantum coherence back to detectable proton magnetization requires the application of at least one 90°_{H} pulse, which mixes slowly and fast relaxing coherences (Tugarinov et al. 2003). Nevertheless, the improvement of the original ^{13}C$\rightarrow^{1}$H experiment (Skrynnikov et al. 2001) to the more sensitive ^{1}H$\rightarrow^{13}$C$\rightarrow^{1}$H experiment (Lundström et al. 2007) has enabled studies in large biomolecular complexes.

The full benefits of the methyl-TROSY effect can again be harnessed in the ^{1}H-^{13}C multiple-quantum (MQ) experiment (Korzhnev et al. 2004a), which is derived from the HMQC pulse sequence. Here, the CPMG element (2.47) is inserted before the ^{13}C chemical shift evolution period. During the CPMG element, zero-quantum coherences (associated with a frequency change of $\Delta\omega_H - \Delta\omega_C$) and double-quantum coherences (associated with a frequency change of $\Delta\omega_H + \Delta\omega_C$) are interconverted, which renders the relaxation dispersion profiles sensitive to chemical shift differences $|\Delta\omega_H|$ and $|\Delta\omega_C|$ in both dimensions. Difficulties can arise in the separation of these parameters in the fitting routine (see section 2.5.4.3). Still, the ^{13}C-^{1}H MQ CPMG experiment is one of the most valuable tools available to study dynamics of slowly tumbling assemblies.

Additionally, ^{1}H double quantum (DQ) (Gopalan et al. 2018) and ^{1}H triple quantum (TQ) (Yuwen et al. 2016) experiments have been established. Both experiments scale the relaxation dispersion profiles up by as much as a factor of four (DQ) and nine (TQ), as the difference in $R_{2,\text{eff}}$ is proportional to the square of $\Delta\omega$ (2.48) in the fast exchange limit, and $\Delta\omega = 2\Delta\omega_H$ (^{1}H DQ) and $\Delta\omega = 3\Delta\omega_H$ (^{1}H TQ), respectively. This is a considerable advantage that would otherwise require a twofold (DQ) or threefold (TQ) increase in $\mathbf{B}_0$. The ^{1}H TQ CPMG experiment has been successfully recorded for the 360 kDa $\alpha_7\alpha_7$ half-proteasome, nevertheless, neither the DQ nor the TQ CPMG experiment benefits from a methyl-TROSY effect and signal-to-noise ratios can be critical for applications to high molecular weight complexes.

2.5.4.3. Analysis of CPMG experiments

The informational wealth of relaxation dispersion profiles can be successfully retrieved only, if the dependence of $R_{2\text{eff}}$ on ν_{CPMG} can be accurately fit, which in turn requires an appropriate exchange model and an appropriate theory to describe the exchange. Several

analytical equations have been established for the case of a two-site exchange of an isolated spin, e.g. describing slow exchange (Tollinger et al. 2001), fast exchange (Luz and Meiboom 1963) or spanning all timescales (Carver and Richards 1972, Jen 1978, Baldwin 2014). In addition, closed-form expressions have been derived for the general n-site exchange situation (Koss et al. 2018, 2020). These equations provide useful insights into the underlying physics, support the intuitive understanding and speed up computational optimization routines. Nonetheless, a numerical calculation of relaxation dispersion profiles has several advantages: it does not make assumptions about the exchange regime, it can be extended from 2-site to n-site exchange in a straightforward manner, and it can incorporate complications like offset effects, non-ideal pulses, scalar couplings or differential relaxation of coherences.

An isolated spin 1/2 ensemble that undergoes a 2-site exchange with populations p_a and p_b has an initial magnetization vector

$$\mathbf{M}(0) = \mathbf{M}_0 = \begin{pmatrix} M_a(0) \\ M_b(0) \end{pmatrix} = \begin{pmatrix} p_a \\ p_b \end{pmatrix} \tag{2.49}$$

The magnetization now evolves during the CPMG pulse train assembled from free precession and 180° pulses:

$$\left\{ \frac{\tau_{\mathrm{CPMG}}}{2} - 180^\circ - \tau_{\mathrm{CPMG}} - 180^\circ - \frac{\tau_{\mathrm{CPMG}}}{2} \right\}_n \tag{2.50}$$

Evolution during the first $\tau_{\mathrm{CPMG}}/2$ period is described by the matrix (see equation (2.35))

$$A = \begin{pmatrix} i\Omega_a - R_{2a} - k_{ab} & k_{ba} \\ k_{ab} & i\Omega_b - R_{2b} - k_{ba} \end{pmatrix} \tag{2.51}$$

The effect of the 180° pulse is to convert magnetization $M_{+j} = M_{xj} + iM_{yj}$ to its complex conjugate $\overline{M} = M_{xj} - iM_{yj}$, or – which is equivalent due to the even number of 180° pules – to convert A to its complex conjugate

$$\overline{A} = \begin{pmatrix} -i\Omega_a - R_{2a} - k_{ab} & k_{ba} \\ k_{ab} & -i\Omega_b - R_{2b} - k_{ba} \end{pmatrix} \tag{2.52}$$

Using these two evolution matrices, and neglecting the length and non-ideal nature of pulses, the magnetization at the end of the CPMG element can be calculated from matrix exponentials as

$$\mathbf{M}(2n\tau_{\mathrm{CMPG}}) = \Big(\exp(A\tau_{\mathrm{CPMG}}/2) \exp\big(\overline{A}\tau_{\mathrm{CPMG}}\big) \exp(A\tau_{\mathrm{CPMG}}/2) \Big)^n \mathbf{M}(0) \tag{2.53}$$

The effective relaxation rate $R_{2,\mathrm{eff}}$ is then given by

$$R_{2,\mathrm{eff}}(2n\tau_{\mathrm{CPMG}}) = -\frac{1}{T_{CPMG}} \ln \frac{M_a(2n\tau_{\mathrm{CPMG}})}{M_a(0)} \tag{2.54}$$

where $T_{\mathrm{CPMG}} = 2n\tau_{\mathrm{CPMG}}$. The calculation can be adapted to an n-site exchange with arbitrary topology by using suitable evolution matrices A and starting vectors $\mathbf{M}(0)$.

Equation (2.53) applies to isolated spins. However, the calculation can often be applied to the analysis of SQ experiments probing coupled spin systems such as the ^{1}H and ^{13}C SQ CPMG described above as well, since the effects of heteronuclear J-couplings and dipole-dipole cross-correlations are taken care of in the experiment. A more complex analysis has to be used in the ^{1}H-^{13}C MQ CPMG experiment (Korzhnev et al. 2004a), for which an additional 180°_H pulse is inserted in the middle of the CPMG train in order to refocus proton chemical shift evolution:

$$\left(\frac{\tau_{\mathrm{CPMG}}}{2} - 180^\circ_{\mathrm{C}} - \frac{\tau_{\mathrm{CPMG}}}{2}\right)_n - 180^\circ_H - \left(\frac{\tau_{\mathrm{CPMG}}}{2} - 180^\circ_{\mathrm{C}} - \frac{\tau_{\mathrm{CPMG}}}{2}\right)_n \tag{2.55}$$

Here, ZQ and DQ terms are present, for which separate evolution matrices have to be applied:

$$m_{\mathrm{DQ}} = \begin{pmatrix} -R_{2a}^{\mathrm{DQ}} - k_{ab} & k_{ba} \\ k_{ab} & -i(\Delta\omega_H + \Delta\omega_C) - R_{2b}^{\mathrm{DQ}} - k_{ba} \end{pmatrix} \tag{2.56}$$

$$m_{\mathrm{ZQ}} = \begin{pmatrix} -R_{2a}^{\mathrm{ZQ}} - k_{ab} & k_{ba} \\ k_{ab} & -i(\Delta\omega_H - \Delta\omega_C) - R_{2b}^{\mathrm{ZQ}} - k_{ba} \end{pmatrix} \tag{2.57}$$

Here, the observed ground state a has been defined to have zero offset. From these matrices, the evolution can again be assembled piecewise. Defining $M_{\mathrm{DQ}} = \exp(m_{\mathrm{DQ}}\tau_{\mathrm{CMPG}}/2)$ and $M_{\mathrm{ZQ}} = \exp(m_{\mathrm{ZQ}}\tau_{\mathrm{CMPG}}/2)$ as well as

$$\mathbf{A} = \left(M_{\mathrm{DQ}}M_{\mathrm{ZQ}}M_{\mathrm{ZQ}}M_{\mathrm{DQ}}\right)^{n/2} \tag{2.58}$$

$$\mathbf{B} = \left(\overline{M}_{\mathrm{ZQ}}\overline{M}_{\mathrm{DQ}}\overline{M}_{\mathrm{DQ}}\overline{M}_{\mathrm{ZQ}}\right)^{n/2} \tag{2.59}$$

$$\mathbf{C} = \left(M_{\mathrm{ZQ}}M_{\mathrm{DQ}}M_{\mathrm{DQ}}M_{\mathrm{ZQ}}\right)^{n/2} \tag{2.60}$$

$$\mathbf{D} = \left(\overline{M}_{\mathrm{DQ}}\overline{M}_{\mathrm{ZQ}}\overline{M}_{\mathrm{ZQ}}\overline{M}_{\mathrm{DQ}}\right)^{n/2} \tag{2.61}$$

for even n and

$$\mathbf{A} = \left(M_{\mathrm{DQ}}M_{\mathrm{ZQ}}M_{\mathrm{ZQ}}M_{\mathrm{DQ}}\right)^{(n-1)/2}M_{\mathrm{DQ}}M_{\mathrm{ZQ}} \tag{2.62}$$

$$\mathbf{B} = \left(\overline{M}_{\mathrm{ZQ}}\overline{M}_{\mathrm{DQ}}\overline{M}_{\mathrm{DQ}}\overline{M}_{\mathrm{ZQ}}\right)^{(n-1)/2}\overline{M}_{\mathrm{DQ}}\overline{M}_{\mathrm{ZQ}} \tag{2.63}$$

$$\mathbf{C} = \left(M_{\mathrm{ZQ}}M_{\mathrm{DQ}}M_{\mathrm{DQ}}M_{\mathrm{ZQ}}\right)^{(n-1)/2}M_{\mathrm{ZQ}}M_{\mathrm{DQ}} \tag{2.64}$$

$$\mathbf{D} = \left(\overline{M}_{\mathrm{DQ}}\overline{M}_{\mathrm{ZQ}}\overline{M}_{\mathrm{ZQ}}\overline{M}_{\mathrm{DQ}}\right)^{(n-1)/2}\overline{M}_{\mathrm{ZQ}}\overline{M}_{\mathrm{DQ}} \tag{2.65}$$

for odd n, the effective $R_{2,\mathrm{eff}}$ is given by

$$R_{2,\mathrm{eff}}(2n\tau_{\mathrm{CPMG}}) = -\frac{1}{T_{CPMG}}\ln\left\{\mathrm{Re}\left(\frac{0.5}{p_a}\begin{bmatrix}1 & 0\end{bmatrix}(\mathbf{AB}+\mathbf{CD})\begin{bmatrix}p_a\\ p_b\end{bmatrix}\right)\right\} \tag{2.66}$$

Here the product matrix **AB** represents evolution of magnetization starting as DQ coherence, while the term **CD** represents evolution of magnetization starting as ZQ coherence. Usually, the intrinsic relaxation rates are assumed to be equal in both states a and b, such that the overall relaxation rate becomes $R_2^{\mathrm{MQ}} = 1/2(R_2^{\mathrm{DQ}} + R_2^{\mathrm{ZQ}})$ (Korzhnev et al. 2004a).

2.5.5. Rotating frame relaxation

In the CPMG experiment, the $R_{2,\mathrm{ex}}$ contribution is successively attenuated by the insertion of more and more 180° pulses in the total time T_{CPMG}, which decreases the average phase that a spin acquires between these pulses due to chemical exchange. In theory, the CPMG frequency would not be limited if infinitely short pulses and thus infinitely short spacings between theses pulses could be used. However, the power level applicable to a given NMR probe without inducing arcing establishes a lower boundary for the 180° pulse length, and care has to be taken not to overheat the probe due to a cumulative excess of power over a longer time period. In practice, ν_{CPMG} is limited to $1-2\,\mathrm{kHz}$ for ^{13}C and ^{15}N nuclei and $\sim$ 5 kHz for ^{1}H and ^{19}F nuclei, although higher frequencies have been used (Reddy et al. 2018) .

An alternative way to suppress dephasing due to chemical exchange is to apply an additional continuous RF field parallel to the magnetization vector. As the $\mathbf{B}_1$ field enforces the maintenance of alignment, this process is called a *spin-lock*. Spin-locked magnetization precesses in the laboratory frame with a frequency $\omega_1 = \omega_{\mathrm{SL}} = \gamma B_1$, where $B_1 = |\mathbf{B}_1|$. In general, application of $\mathbf{B}_1$ at an offset ω_{off} gives rise to an effective field

$\boldsymbol{\omega}_\mathrm{e}$ in the frame rotating with ω_1:

$$\boldsymbol{\omega}_\mathrm{e} = \begin{pmatrix} \omega_1 \\ 0 \\ \omega_\mathrm{off} \end{pmatrix} \tag{2.67}$$

Thus, magnetization is locked in the transverse plane in the on-resonance case, for which $\omega_\mathrm{off} = 0$, and more generally at an angle θ, a tilt angle to the z-axis given by

$$\theta = \tan^{-1} \frac{\omega_1}{\omega_\mathrm{off}} \tag{2.68}$$

In the rotating frame, the static $\mathbf{B}_0$ field vanishes in the on-resonance situation, and magnetization precesses around the effective field, reminiscent of its precession around $\mathbf{B}_0$ in the absence of $\mathbf{B}_1$. Due to this analogy, the decay of magnetization collinear to the effective field is characterized by the relaxation rate $R_{1\rho}$, whereas magnetization orthogonal to $\boldsymbol{\omega}_e$ relaxes with $R_{2\rho}$ (Palmer and Massi 2006). Notably, $R_{2\rho}$ does not provide additional information compared to $R_{1\rho}$. In the absence of exchange, the dependence of $R_{1\rho}$ on θ can be found by transforming the Bloch equations (2.15) into the θ-tilted rotating frame (Rangadurai et al. 2019):

$$\begin{aligned} \frac{\mathrm{d}}{\mathrm{d}t} \begin{pmatrix} M_x' \\ M_y' \\ M_z' \end{pmatrix} = &- \begin{pmatrix} R_2 \cos^2\theta + R_1 \sin^2\theta & (\Omega^2 + \omega_1^2)^{1/2} & (R_2 - R_1)\sin\theta\cos\theta \\ -(\Omega^2 + \omega_1^2)^{1/2} & R_2 & 0 \\ (R_2 - R_1)\sin\theta\cos\theta & 0 & R_2 \sin^2\theta + R_1 \cos^2\theta \end{pmatrix} \begin{pmatrix} M_x' \\ M_y' \\ M_z' \end{pmatrix} \\ &+ \begin{pmatrix} -R_1 M_0 \sin\theta \\ 0 \\ R_1 M_0 \cos\theta \end{pmatrix} \end{aligned} \tag{2.69}$$

Here, the spin-lock was assumed to be applied along the x-axis ($\omega_x = \omega_1, \omega_y = 0$). Often, the off-diagonal term that mixes M_x' and M_z' can be neglected, because M_x' and M_y' are rapidly mixed by $(\Omega^2 + \omega_1^2)^{1/2} \gg (R_2 - R_1)\sin\theta\cos\theta$. In this case, the evolution of M_z' decouples from M_x' and M_y' and obeys a mono-exponential decay with

$$R_{1\rho} = R_1 \cos^2\theta + R_2 \sin^2\theta \tag{2.70}$$

It should be noted, that each state i that participates in an exchange has its own offset $\omega_{\mathrm{off},i}$ and thus experiences a different effective field $\omega_{\mathrm{e},i}$ (figure 2.7). For intermediate and fast exchange, where the position of the probed resonance is shifted away from the ground state position, it is helpful to define the average effective field $\omega_\mathrm{e}^\mathrm{av}$ via the average resonance offset $\omega_\mathrm{off}^\mathrm{av}$:

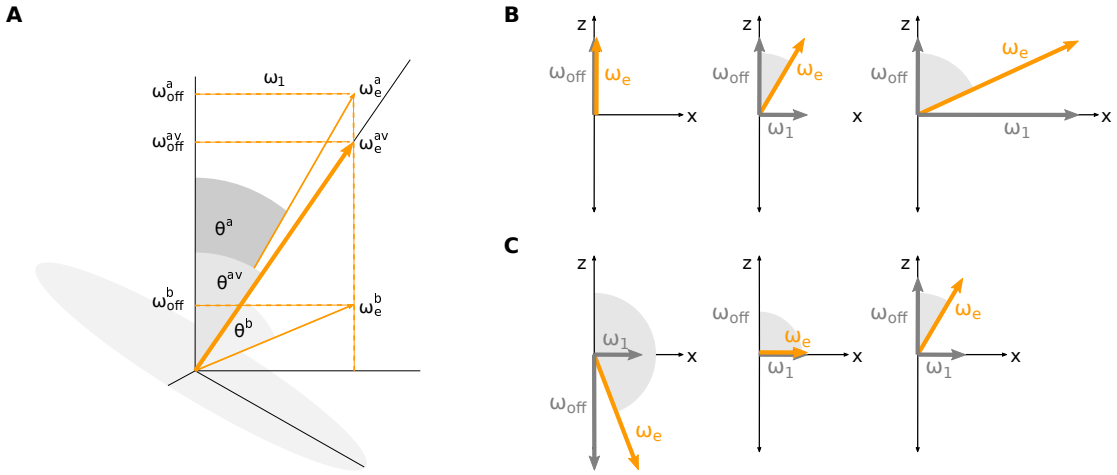

Figure 2.7.: Effective fields in the $R_{1\rho}$ setup (A) Representation of the tilted $R_{1\rho}$ reference frame (B) Variation of the effective field with different spin-lock frequencies $\omega_1 \geq 0$ (C) Variation of the effective field with different offsets ω_{off}

$$\omega_{\text{off}}^{\text{av}} = \sum_{i=1}^{n} p_i \omega_{\text{off}}^{\text{i}} \tag{2.71}$$

$$\omega_{\text{e}}^{\text{av}} = \begin{pmatrix} \omega_1 \\ 0 \\ \omega_{\text{off}}^{\text{av}} \end{pmatrix} \tag{2.72}$$

Rotating-frame spin relaxation comes in two flavors, which differ in the way that $R_{2,\text{eff}}$ is modulated and can be deduced from equation (2.68): First, by applying an on-resonant spin-lock with a varying spin-lock strength ω_1 the modulation is achieved in a manner similar to the CPMG experiment. Second, by altering the offset ω_{off} at which the spin-lock field is applied, the variation occurs by altering the effective field of the excited state, as we will see below. In principle, by changing ω_1 and ω_{off} all angles θ and amplitudes $|\boldsymbol{\omega}_{\text{e}}|$ can be sampled (figure figure 2.7).

We can now outline the basic sequence of $R_{1\rho}$ experiments (figure 2.8): The magnetization is transferred to an angle θ, which can be achieved by different means (section 2.5.5.2). Next, the spin-lock field is applied for a time T_{SL}, in which the magnetization decays with $\exp\left(-R_{1\rho}T_{\text{SL}}\right)$. Afterwards the remaining intensity is read out, the experiment is repeated with different times T_{SL} and the data is fit to an exponential decay to extract $R_{1\rho}$. Finally, the procedure is iterated with different spin-lock fields ω_1 (in the

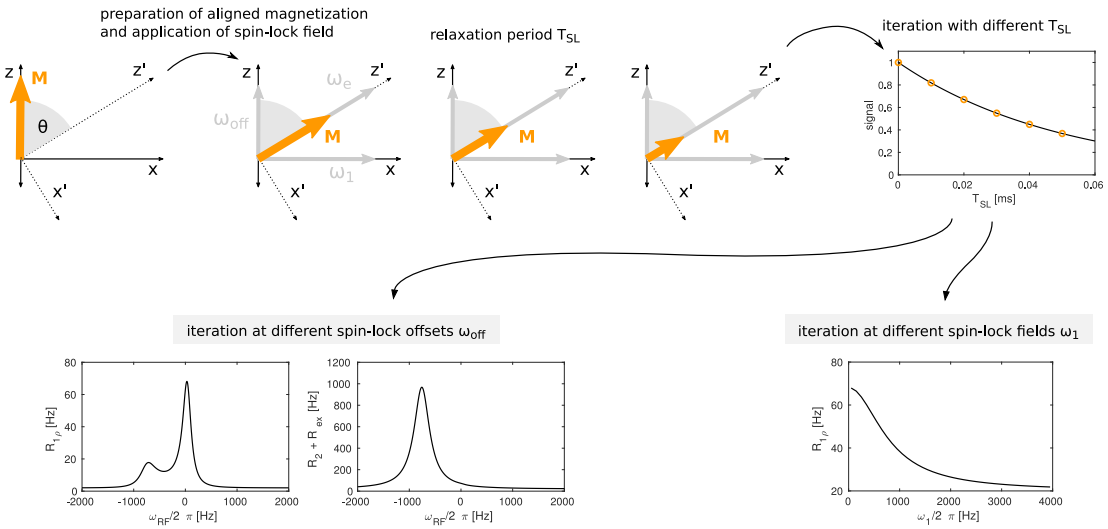

Figure 2.8.: Outline of the $R_{1\rho}$ experiment After initial preparation of magnetization, the spin-lock field ω_1 is applied. Magnetization is allowed to relax for a time T_{SL} and relative intensities from experiments with different T_{SL} are fit to an exponential decay. Finally, the experiment is repeated at either different spin-lock offsets (left) or at different spin-lock powers ω_1 (right). Off-resonance data was simulated with $\omega_1/2\pi = 100\,\text{Hz}$, on-resonance data was simulated with the spin-lock centered on the average frequency $\omega_{av} = p_a\omega_a + p_b\omega_b$. Both simulations were obtained from (2.79), with parameters used as follows: $R_{1a} = R_{1b} = 2\,\text{s}^{-1}$, $R_{2a} = R_{2b} = 20\,\text{s}^{-1}$, $k_{ab} = 50\,\text{s}^{-1}$, $k_{ba} = 950\,\text{s}^{-1}$, $\Delta\omega/2\pi = 800\,\text{Hz}$.

on-resonance $R_{1\rho}$ experiment) or different spin-lock offsets ω_{off} (in the off-resonance $R_{1\rho}$ experiment). The advantages of rotating frame relaxation compared to CPMG experiments are fourfold: First, larger effective fields can be used, which allow characterization of faster motions. Second, a full set of exchange parameters can be obtained from a single magnetic field strength $\mathbf{B}_0$ (Korzhnev et al. 2005b). Third, the sign of $\Delta\omega$ can be extracted, and fourth, experiments can be applied to uniformly labeled samples (see section 2.5.5.2).

Again, it is instructive to realize the similarity of rotating frame relaxation with other experiments: On the one hand, the $R_{1\rho}$ spin-lock can be regarded as an extension of a CPMG element, where the 180° pulses are prolonged until the duty cycle (the relative time during the CPMG train, in which pulses are applied) reaches 100 %. On the other hand, the spin-lock field ω_1 applied to magnetization aligned collinear to the effective field ω_{eff} is reminiscent of the CEST field ω_{CEST} applied to magnetization initially aligned along z. Indeed, while CEST is usually carried out at low frequencies of $\omega_{CEST}/2\pi \sim 5 - 100\,\text{Hz}$, a 'high power' CEST with frequencies up to 500 Hz can yield accurate results even in the microsecond-millisecond regime (Rangadurai et al. 2020). Since poor alignment of multiple states can limit the validity of $R_{1\rho}$ data, this extension of CEST can be of considerable advantage.

2.5.5.1. Analysis of rotating frame relaxation

Numerical analysis of rotating frame relaxation starts with the evolution equation (2.22). I will restrict the description to the two-state exchange scenario, for which evolution is governed by the matrix (2.26). Without loss of generality, the spin-lock field is again assumed to be collinear with the x-axis, $\omega_x = \omega_1$ and the components are ordered according to their x, y and z-components ($\mathbf{M} = [M_{x1}, M_{x2}, M_{y1}, M_{y2}, M_{z1}, M_{z2}]$), after which we obtain

$$\mathbf{A} = \begin{pmatrix} -R_{2a} - k_{ab} & k_{ba} & -\Omega_a & 0 & 0 & 0 \\ k_{ab} & -R_{2b} - k_{ba} & 0 & -\Omega_b & 0 & 0 \\ \Omega_a & 0 & -R_{2a} - k_{ab} & k_{ba} & -\omega_1 & 0 \\ 0 & \Omega_b & k_{ab} & -R_{2b} - k_{ba} & 0 & -\omega_1 \\ 0 & 0 & \omega_1 & 0 & -R_{1a} - k_{ab} & k_{ba} \\ 0 & 0 & 0 & \omega_1 & k_{ab} & -R_{1b} - k_{ba} \end{pmatrix} \tag{2.73}$$

Two approaches have been followed in order to extract $R_{1\rho}$ from $\mathbf{A}$, either by explicit numerical integration of the BLOCH-MCCONNELL equations (Korzhnev et al. 2005b), or by calculation of the matrix eigenvalues (Trott and Palmer 2002). In the first approach, starting magnetization $\mathbf{v}_{\text{start}}$ is integrated with the matrix exponential $\exp(\mathbf{A}T_{\text{SL}})$ and projected on the effective field axis $\mathbf{v}_{\text{proj}} = \begin{pmatrix} \sin\theta & 0 & 0 & 0 & \cos\theta & 0 \end{pmatrix}$ of the ground state magnetization:

$$M_a(T_{\text{SL}}) = \mathbf{v}_{\text{proj}} \exp(\mathbf{A}T_{\text{SL}})\mathbf{v}_{\text{start}} \tag{2.74}$$

Magnetization after a time T_{SL} is assumed to be given by the mono-exponential decay

$$M_a(T_{\text{SL}}) = e^{-R_{1\rho}T_{\text{SL}}} M_a(0) \qquad \Leftrightarrow \qquad R_{1\rho} = -\frac{1}{T_{\text{SL}}} \ln \frac{M_a(T_{\text{SL}})}{M_a(0)} \tag{2.75}$$

Expressing magnetization in terms of populations ($M_a(0) = p_a$), we obtain

$$R_{1\rho} = -\frac{1}{T_{\text{SL}}} \ln \frac{\mathbf{v}_{\text{proj}} \exp(\mathbf{A}T_{\text{SL}})\mathbf{v}_{\text{start}}}{p_a} \tag{2.76}$$

The starting magnetization is assumed to be aligned with the effective field given by the ground field offset Ω_a (in slow exchange) or with the effective field given by the average offset Ω_{av}. In certain experiments, only ground state magnetization is present before application of the spin-lock, e.g. after a Hartmann-Hahn transfer in the ^{15}N $R_{1\rho}$ experiment (Korzhnev et al. 2005b). In other situations, where magnetization is aligned

with a hard pulse (see section 2.5.5.2), all states can be present in $\mathbf{v}_{\text{start}}$. Accordingly, $\mathbf{v}_{\text{start}}$ can be written as

$$\mathbf{v}_{\text{start}} = \begin{pmatrix} p_a \sin\theta \\ 0 \\ 0 \\ 0 \\ p_a \cos\theta \\ 0 \end{pmatrix} \quad \text{or} \quad \mathbf{v}_{\text{start}} = \begin{pmatrix} p_a \sin\theta \\ p_b \sin\theta \\ 0 \\ 0 \\ p_a \cos\theta \\ p_b \cos\theta \end{pmatrix} \tag{2.77}$$

In the second approach, the general solution to the differential equation (2.22) is used, which can be written as (Trott and Palmer 2002)

$$\mathbf{M}(t) = \sum_{n=1}^{6} e^{\lambda_n t} d_n \mathbf{D}_n + \mathbf{S} \tag{2.78}$$

Here, $\mathbf{S}$ is the stationary solution, $\mathbf{D}_n$ is the n^{th} eigenvector of $\mathbf{A}$ with the proportionality factor d_n, and λ_n is the corresponding eigenvalue. Trott and Palmer (2002) found, that four of the six eigenvalues λ_n are complex under conditions encountered in rotating frame relaxation experiments, and therefore constitute oscillatory solutions. For these eigenvalues, small ω_1 inhomogeneities lead to rapid changes in the oscillatory frequency and the associated magnetization components vanish. The two real eigenvalues are negative and constitute exponential decays. Often, one of the eigenvalues is much more negative than the other, and the least negative eigenvalue λ corresponds to the dominant decay rate of $\mathbf{M}$:

$$R_{1\rho} \approx -\lambda \tag{2.79}$$

The approximation of $R_{1\rho}$ by the least negative eigenvalue of $\mathbf{A}$ can be used in a straightforward manner to yield relaxation dispersion profiles for different spin-lock fields or spin-lock offsets. It also allows to obtain analytical solutions by calculating the characteristic polynomial $|\lambda \mathbb{1}_n - \mathbf{A}|$ and using approximations to solve the characteristic equation (Trott and Palmer 2002). The solutions are of the form

$$R_{1\rho} = R_1 \cos^2\theta + \left(R_2 + R_{\text{ex}}\right) \sin^2\theta \tag{2.80}$$

An often-used expression was derived with Laguerre's method to find polynomial roots

and is thus called the Laguerre approximation (Miloushev and Palmer 2005):

$$R_{1\rho} = R_1 \cos^2\theta + R_2 \sin^2\theta \tag{2.81}$$

$$+ \frac{\sin^2\theta p_a p_b \Delta\omega_{ab}^2 k_{\mathrm{ex}}}{\frac{\omega_{\mathrm{eff},a}^2 \omega_{\mathrm{eff},b}^2}{\omega_{\mathrm{eff}}^2} + k_{\mathrm{ex}}^2 - \sin^2\theta p_a p_b \Delta\omega_{ab}^2 \left(1 + \frac{2k_{\mathrm{ex}}^2 (p_a \omega_{\mathrm{eff},a}^2 + p_b \omega_{\mathrm{eff},b}^2)}{\omega_{\mathrm{eff},a}^2 \omega_{\mathrm{eff},b}^2 \omega_{\mathrm{eff}}^2 k_{\mathrm{ex}}^2}\right)} \tag{2.82}$$

2.5.5.2. $R_{1\rho}$ experiments

$R_{1\rho}$ experiments have been developed for ^{15}N spins in ^{1}H^{15}N groups (Akke and Palmer 1996, Mulder et al. 1998, Korzhnev et al. 2002, Massi et al. 2004, Igumenova and Palmer 2006), for ^{1}H spins in ^{1}H^{15}N groups (Ishima et al. 1998, Eichmüller and Skrynnikov 2005, Lundström and Akke 2005b), for ^{13}C (Ishima et al. 1999, Brath et al. 2006) and ^{1}H (Weininger et al. 2013) spins in CHD_2 groups, for ^{13}CO (Mulder and Akke 2003) and $^{13}C^{\alpha}$ probes (Lundström and Akke 2005a), aromatic ^{13}C spins (Weininger et al. 2014) as well as ^{13}C (Hansen et al. 2009) and ^{15}N (Nikolova et al. 2012) probes in nucleic acids. In general, three problems frequently arise in these experiments: First, simultaneous measurement of multiple spin systems requires simultaneous alignment to the effective field. Hard pulses with a tip angle θ offer a fast way to transfer magnetization to a defined angle (figure 2.9), however, if the spins under consideration have different offsets, the effective field for each spin will also be tilted by individual angles θ_i and magnetization will in general be misaligned. Reasonable alignment for $68^\circ < \theta < 112^\circ$ can be achieved in an 'angle by evolution approach' by using an $90^\circ_\phi - \chi - 90^\circ_{\phi+\pi/2}$ sequence with $\chi = 1/\omega_1$ for transferring magnetization from z to θ. A third alternative is to simultaneously sweep amplitude and phase of an RF field such that the magnetization is adiabatically rotated to their individual effective field (Mulder et al. 1998). Adiabatic rotations work well over a wide range of offsets for large ω_1 fields. At lower fields, however, alignment is only partially achieved, and in order to fulfill the adiabatic condition, the pulses get prohibitively long, leading to substantial relaxation losses. Second, effects from cross-correlated relaxation and heteronuclear J-couplings have to be suppressed, which complicate the design of pulse sequences, in which low power spin-lock fields could be used (Korzhnev et al. 2002, Massi et al. 2004). Third, homonuclear couplings such as ^{13}C-^{13}C couplings in uniformly labeled proteins are detrimental, as the Hartmann-Hahn condition may be accidentally matched (Mulder and Akke 2003, Lundström and Akke 2005a). An additional problem arises for ^{1}H $R_{1\rho}$ experiments, where cross-relaxation by the nuclear Overhauser effect (NOE) and the rotating frame Overhauser effect (ROE) can generate pseudo-dispersion profiles. The problem can be addressed either by deuteration or by locking the magnetization at a constant angle of $\theta = \arctan\left(1/\sqrt{2}\right) \approx 35.3^\circ$ (Eichmüller and Skrynnikov

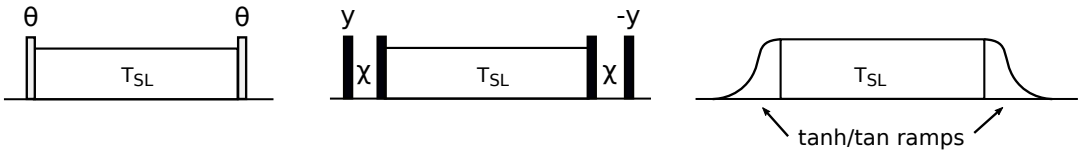

Figure 2.9.: Approaches for the alignment of magnetization at angle θ Transfer of magnetization to θ can be achieved by hard pulses with a reduced pulse length (left), by two hard 90° pulses with an evolution period $\chi = 1/\omega_1$ (middle) or by adiabatic ramps in which amplitude and frequency are modulated as tanh and tan functions, respectively (right)

2005).

An experiment designed for ^{15}N probes in protein amide groups elegantly overcomes several of the aforementioned issues (Korzhnev et al. 2005b): Instead of recording a series of 2D-experiments, the experiment selectively excites previously identified resonances via heteronuclear Hartmann-Hahn cross-polarization. Since only a single spin system is measured, magnetization can be transferred to θ with a hard pulse. Concomitant with the ^{15}N spin-lock, effects of J-coupling and DD/CSA cross-correlated relaxation are suppressed by a strong on-resonance ^{1}H continuous wave decoupling. The experiment thus focuses on resonances of interest, for which appropriate measurement times regarding the S/N ratio can be chosen. Furthermore, it allows the use of low power spin-lock fields and solves the problem of heteronuclear decoupling (Korzhnev et al. 2005b). The selective cross-polarization $R_{1\rho}$ experiment has stimulated subsequent implementations in nucleic acids using ^{15}N and ^{13}C nuclei (Hansen et al. 2009, Nikolova et al. 2012).

We have seen in section 2.5.4, that $^{13}CH_3$ methyl groups are valuable reporters on dynamics in high-mocular weight assemblies. Unfortunately, dipole-dipole cross-correlated relaxation leads to non-exponential decays in AX_3 spin systems, which cannot be rectified by the application of pulses. As a consequence, the methyl group has to be tailored to an CHD_2 group to work as an AX spin system (Brath et al. 2006, Ishima et al. 1999) and no methyl-TROSY effect can be exploited. Notably, a ^{13}C $R_{1\rho}$ experiment on ^{13}C groups can still be used to determine the sign of the carbon chemical shift $\Delta\omega_C$ (Baldwin and Kay 2012), a concept that had previously been applied to $^{1}H^{\alpha}$ probes (Auer et al. 2009).

2.5.6. Summary

To deepen our understanding of protein and nucleic acid function and misfunction, the characterization of their dynamic properties is of utmost importance. Within the existing

set of complementary methods, NMR occupies a central place with undisputed advantages, as shown in section 2.5: it allows to detect sparsely populated states, quantify populations and exchange rates between states, and make statements about the structure of these excited states. The modern NMR spectroscopist is equipped with a suite of experiments that specifically target different exchange regimes using different probes in the molecule of interest. There are, however, significant obstacles when it comes to high-molecular weight proteins. Here, a dedicated sample preparation (deuteration, specific $^{13}CH_3$ methyl-group labeling) and the use of methyl-TROSY experiments become mandatory. Fluorine-based methods have specific advantages, as outlined in section 2.4, and offer complementarity to existing methyl-probe strategies. Furthermore, the implementation of one-dimensional ^{19}F experiments is rather straight-forward, as we will see in the following result chapters.

3. Materials and methods

3.1. Molecular biology

3.1.1. Cloning of TmCsp

The protein coding sequence of Cold shock protein from Thermotoga maritima (NCBI reference sequence WP_004082199.1, hereafter referred to as TmCsp, internal reference: 2093) was codon optimized with COOL (`http://bioinfo.bti.a-star.edu.sg/COOL/`), synthesized by Integrated DNA Technologies (Coralville, USA) and cloned into a pETGB-1a vector (kindly provided by Dr Arie Geerlof, Helmholtz Zentrum München). The vector contains an N-terminal His6-GB1-tag followed by a tobacco etch virus protease (TEV protease) cleavage site constituted by the amino acid sequence ENLYFQGG. The final protein sequence therefore contains an additional GG at the N-terminus of the protein (table A.2).

3.1.2. Cloning of CtXrn2 constructs

The protein coding sequence of Xrn2 from Chaetomium thermophilum (NCBI reference sequence XP_006691410.1, internal reference 1630) was synthesized by GenScript with codon optimization for expression in E. coli and provided in a pUC57 vector. A construct with amino acids 1-875 was cloned into a pET26b+ vector (Novagen) using NdeI and XhoI restriction sites (hereafter referred to as CtXrn2, internal reference 1683, table A.2). The vector carries no additional amino acids at the N-terminus of the construct and a C-terminal His6-tag constituted by the sequence LEHHHHHH, where the amino acids LE are a remnant from the restriction site.

A construct lacking the residues 263-300, corresponding to the zinc finger loop (hereafter referred to as CtXrn2 ΔZnF, internal reference 1821) was prepared using Gibson assembly cloning. Point mutations were introduced using site directed mutagenesis with a pair of primers designed with PrimerX (`http://www.bioinformatics.org/primerx`), where the mutated sequence was typically introduced in the middle of the primers. A construct of the zinc finger (residues 265-293) was cloned using Gibson assembly into a pETGB1a vector that carried an N-terminal His6-GB1 tag followed by a TEV cleavage site (internal

reference 1820). All used constructs were validated by sequencing the full open reading frame.

3.2. Protein expression, isotope labeling and purification

3.2.1. Recombinant expression and purification of TmCsp

Plasmids were transformed into E.coli BL21(DE3) CodonPlus-RIL cells (Stratagene) and grown in LB over night. Subsequently, M9 medium was inoculated with the LB culture and grown to an optical density OD600 of 1.0 at 37°C. The medium was then supplemented with 50mg/L 5-Fluoroindole (Crowley et al. 2012) that was dissolved in DMSO at 100 mg/ml stock concentration. 45-60 minutes later protein expression was induced by addition of 1mM IPTG and the culture was shifted to 20°C. Cells were harvested by centrifugation 12-18h after induction. Cell pellets were resuspended in 10 mM Tris pH 8.0, 10 mM Imidazole pH 8.0, 1 mM EDTA, 1:1000 Triton X-100, 1 mg/L lysozyme, 0.2 U/ml DNaseI by vortexing for 30 minutes at 4°C and then lysed by sonification. After addition of 5 mM MgCl2 and 5 µg/ml RnaseA the sample was incubated for 2 hours at 37°C. The cell debris was removed by centrifugation, the supernatant was additionally cleared with a 0.45 µm syringe filter and loaded on a Nickel-NTA gravity flow column that was pre-equilibrated with buffer A (10 mM Tris, 10 mM Imidazole pH 8.0). Subsequently, the column was washed with 20-30 column volumes of buffer A and the bound protein were eluted with 10 mM Tris, 300 mM Imidazole pH 8.0. The His6-GB1-tag was cleaved by addition of a His6-tagged TEV protease and dialysis for 12-18 hours against a 10 mM Tris pH 8.0, 1 mM DTT at 20°C. In order to separate the His-tagged proteins from the target protein, the dialyzed proteins were loaded on a Nickel-NTA column pre-equilibrated with 10 mM Tris pH 8.0, 10 mM Imidazole. The column flow-through was dialyzed for 12-18 hours against 10 mM $NaHPO_4$ pH 6.8 and loaded onto a 5ml Heparin HP HiTrapTM column. The protein was eluted with a salt gradient (0 – 500 mM NaCl in the presence of 1 mM EDTA) and the target fractions were combined and concentrated to a final volume of 1-1.5 ml. Finally, the protein was purified using a 16/600 Superdex S75 column in 50 mM Tris pH 8.0, 100 mM NaCl, 1 mM EDTA. The target fractions were combined and concentrated with a simultaneous buffer exchange to 50 mM $NaHPO_4$ pH 6.5, 20 mM NaCl, 0.2 mM EDTA, 1 mM DTT. The NMR sample was supplemented with 0.03% NaN_3 and 5% D_2O, the final protein concentration was 550 µM.

3.2.2. Recombinant expression and purification of the $\alpha_7\alpha_7$ half proteasome

Plasmids were transformed into E.coli BL21(DE3) CodonPlus-RIL cells (Stratagene) and grown in LB over night. Fresh LB medium including antibiotics was inoculated from the overnight culture and grown to an optical density OD600 of 0.6-0.8 at 37ºC. The culture was shifted to 20°C and protein expression induced with 0.5 mM IPTG for 12-18h. Cell pellets were resuspended in 50 mM sodium phosphate pH 7.4, 400 mM NaCl, 10 mM Imidazole, 1 mM EDTA, 1:1000 Triton X-100, 1 mg/L lysozyme, 0.2 U/ml DNaseI by vortexing for 30 minutes at 4°C and lysed by sonification. The cell debris was removed by centrifugation, the supernatant was additionally cleared with a 0.45 μm syringe filter and loaded on a Nickel-NTA gravity flow column that was pre-equilibrated with buffer A2 (50 mM sodium phosphate pH 7.4, 400 mM NaCl, 10 mM Imidazole). In order to remove weakly bound contaminating proteins, the column was washed with 20-30 column volumes of buffer A2, after which the protein was eluted with 50 mM sodium phosphate pH 7.4, 150 mM NaCl, 300 mM Imidazole. The His6 tag was cleaved with His6-tagged TEV protease while dialyzing the elution against 50 mM sodium phosphate pH 7.4, 150 mM NaCl, 1 mM DTT at 4°C. The dialyzed sample was loaded on a second Nickel-NTA column pre-equilibrated with buffer A2. The column flow-through was concentrated to 1 ml and finally purified using a 16/600 Superdex S200 column in 25 mM HEPES pH 7.3, 125 mM NaCl, 1 mM DTT. The target fractions were combined and concentrated again to a volume of 0.5 ml. Bromotrifluoroacetone (Sigma-Aldrich) was added to a final concentration of 10 mM and incubated at 37°C for 30'. The reaction was quenched with 20 mM DTT and the sample was purified over a PD 10 column pre-equilibrated with 25 mM HEPES pH 7.3, 125 mM NaCl, 1 mM DTT. The NMR sample was supplemented with 0.03% NaN_3 and 5% D_2O, the final protein concentration was 1.3 mM (monomer concentration), corresponding to 93 μM $\alpha_7\alpha_7$ complex for the 18C mutant, and 0.75 mM (monomer concentration), corresponding to 54 μM $\alpha_7\alpha_7$ complex for the 35C mutant.

3.2.3. Recombinant expression and purification of CtXrn2

Plasmids were transformed into E.coli BL21(DE3) CodonPlus-RIL cells (Stratagene) and grown in LB over night at 37°C. For unlabeled (non isotope labeled) samples, typically one liter of LB was inoculated from an over night culture and grown to an optical density OD600 of 0.6-0.8 at 37ºC at which point the culture was cooled to 20°C and protein expression was induced by the addition of 0.5 mM IPTG. For samples with Ile-δ1 $^{13}C^{1}H_3$ methyl group labeling, an H_2O-M9 culture was inoculated from the over night LB culture and grown to OD 0.2-1.0. Cells of this culture were harvested typically in the afternoon by moderate centrifugation at 3000 rcf and resuspended in D_2O-M9 culture (containing 2 g/L $^{2}H^{12}C$-labeled glucose) to an OD of 0.1-0.15 with a volume of 1/10 of the final

D_2O culture volume. The D_2O-M9 culture was grown over night at 37°C, diluted 1:8 and grown to an OD of 0.6-0.8. A solution of the isoleucine precursor alpha-ketobutyrate in a buffered D2O solution was added to the culture, the temperature was shifted to 20°C and protein expression was induced one hour later by addition of 0.5 mM IPTG. Cells were harvested by centrifugation 14-18 hours after induction and cell pellets were stored at -20°C. Protein purification followed a two-step protocol with a Ni affinity chromatography and a gel filtration. Briefly, cell pellets were resuspended in 50 mM Na phosphate buffer pH 7.4, 400 mM NaCl, 10 mM imidazole, 1:1000 Triton X-100, 1 mg/L lysozyme, 0.2 U/ml DNase I with vortexing for 30 minutes at 4°C and lysed by sonification. The cell debris was removed by a centrifugation step at 18.000 rcf, the supernatant was cleared with a 0.45 μm syringe filter and loaded on a gravity flow Nickel-NTA column with a typical volume of 2 ml beads, that was pre-equilibrated with buffer A (50 mM Na phosphate pH 7.4, 400 mM NaCl, 10 mM imidazole). The column was subsequently washed with at least 10 column volumes buffer A, the bound protein was eluted with typically 10-15 ml buffer B (50 mM Na phosphate pH 7.4, 150 mM NaCl, 300 mM imidazole), until a Bradford test did not show significant staining any more, and 1 mM DTT was added to the elution. The elution was concentrated to a volume of 1-1.5 ml and purified using a 16/600 Superdex S200 column in GF buffer (25 mM HEPES pH 7.3, 125 mM NaCl, 1 mM DTT). The target fractions were combined and concentrated. For deuterated samples, the buffer was exchanged in this concentration step by multiple rounds of addition of D2O-GF buffer (25 mM HEPES pH 7.3, 125 mM NaCl, 1 mM DTT in D2O) and subsequent concentration. NMR samples were supplemented with 0.03% NaN_3 and 5% D_2O (for samples not in 100% D_2O).

The $^{13}C/^{15}N$-labeled ZnF was expressed in M9 medium containing 0.5 g/L $^{15}NH_4Cl$ and 2 g/L $^{1}H^{13}C$-labeled glucose. The purification followed the procedure described above, but included a dialysis step against 50 mM Na phosphate pH 7.4, 150 mM NaCl, 1mM DTT with simultaneous TEV cleavage after the Ni-affinity chromatography step. The cleaved His6-GB1 tag was removed by applying the solution to a second Ni-affinity chromatography step where the resin was equilibrated in buffer A. The flow-through of the column was collected, concentrated and purified using a 16/600 Superdex S75 column equilibrated in GF buffer. Target fractions were pooled and concentrated again, the sample was supplemented with 0.03% NaN_3 and 5% D_2O.

3.3. Cysteine fluorine labeling

Proteins were fluorine labeled after gel filtration at protein concentrations of typically 100 μM. For labeling with 3-bromo-1,1,1-trifluoroacetone (BTFA), the sample was cooled

on ice and BTFA was added to a final concentration of 10 mM. The reaction was incubated for 30 minutes on ice, quenched with 20 mM DTT and the sample was purified over a PD10 or PD Minitrap G-25 desalting column pre-equilibrated with GF buffer. NMR samples were supplemented with 0.03 % NaN_3 and 5 % D_2O. For labeling with 2,2,2-trifluoroethanethiol (TET), the sample was cooled to 4 °C, dichloro-(1,10-phenanthroline)-copper (II) (CuPh) was added to a final concentration of 20 µM and TET was added to a final concentration of 500 µM, the reaction was followed in ^{19}F spectra until free TET was depleted.

3.4. RNA preparation

5'-monophosphorylated RNAs were prepared by *in vitro* transcription in the presence of an excess of GMP over GTP. In brief, a template DNA oligonucleotide with the desired RNA sequence in reverse complement followed by a reverse complementary T7 promoter sequence at the 3' end (5'- TATAGTGAGTCGTATTACG-3') was used in equimolar amounts with an antisense T7 promoter oligonucleotide (5'-CGTAATACGACTCACTATAGG-3') in the reaction at a concentration of 1 µM. The reaction included 40 mM Tris pH 8.0, 5 mM DTT, 1 mM spermidine, 0.01% Triton X-100, 10-40 mM MgCl2 and 0.2 µM T7 RNA polymerase (prepared in house). GMP was included at a concentration of 10 mM, and the required nucleoside triphosphates were included typically at 4 mM concentrations, with the exception of GTP, which was used at concentration of 0.8 mM.
In vitro transcriptions were carried out at 37°C for 4h to over night, after which EDTA was added to dissolve apparent magnesium-pyrophosphate precipitate. Reaction products were precipitated with 0.7 reaction volumes isopropanol and 0.1 reaction volumes 3 M NaAc pH 5.3 with subsequent cooling at -20°C for at least 30 minutes. The precipitate was pelleted by centrifugation, washed with cold 70% Ethanol, air-dried, and resuspended in 5 M Urea, 20 mM Tris pH 8.0. The solution was applied to a preparative anion exchange DNAPac column (Dionex) and separated by size with a salt gradient. Fractions containing RNA were analyzed with urea polyacrylamide gel electrophoresis and the fractions of interested were pooled, precipitated with isopropanol, washed with 70% ethanol and resuspended in H_2O. If necessary, the solutions were concentrated with a SpeedVac vacuum concentrator. RNA samples were stored at -20°C.

3.5. Xrn2 activity assays

RNase assays were performed in GF buffer (25 mM HEPES pH 7.3, 125 mM NaCl, 1 mM DTT). Protein samples used for activity assays were prepared freshly and mixed with 0.01 % Triton X-100. 10 µL samples were stopped with 30 µL 8 M Urea, after which the samples were immediately heated to 90 °C for two minutes and stored at −20 °C for HPLC analysis. HPLC assays were performed at 40 °C on a DNAPacTM PA100 column (Dionex) using an HPLC system with automatic injection of 18 µL samples. Substrate and products were separated using a linear NaCl gradient from 5 M Urea, 20 mM Tris/HCl pH 8.0, 100 mM NaCl to 5 M Urea, 20 mM Tris/HCl pH 8.0, 600 mM NaCl. For qualitative assays, reactions were stopped using an equivalent volume of 2x RNA loading buffer (8 M Urea, 20 mM EDTA pH 8.0, 2 mM Tris pH 8.0, 0.025 % w/v bromophenol blue, 0.025 % w/v xylene cyanole) and analysed by urea polyacrylamide gel electrophoresis.

3.6. NMR spectroscopy

3.6.1. $^{1}H^{13}C$ HMQC SOFAST

HMQC SOFAST spectra (Schanda and Brutscher 2005) were recorded with a Bruker Avance III 800 MHz spectrometer equipped with a helium cooled TCI or probehead, unless indicated otherwise. Methyl-TROSY based SQ-CPMG and MQ-CPMG (Korzhnev et al. 2004a) experiments were recorded with Bruker Avance III 500 MHz, 600 MHz and 800 MHz spectrometers equipped with helium (800) or nitrogen (500 and 600) cooled TCI probeheads as pseudo-3D experiments, where the CPMG frequency was used as a third dimension, that was recorded in an interleaved manner. Data were recorded with a recycle delay of 1.5 s and carbon acquisition times of 24.8 ms (800 MHz),29.0 ms (600 MHz) and 29.8 ms (500 MHz) in the indirect dimension. In all CPMG experiments, the constant time T_{CPMG} was set to 24 ms and frequencies were sampled at 83.3 Hz, 166.7 Hz, 250 Hz, 333.3 Hz, 416.7 Hz, 500 Hz, 666.7 Hz, 833.3 Hz, 1000 Hz, 1166.7 Hz, 1333.3 Hz, 1666.7 Hz and 2000 Hz. All datasets were recorded either two or three times to obtain error estimates for all datapoints.

3.6.2. $^{1}H^{15}N$ TROSY

^{1}H-^{15}N TROSY: ^{1}H-^{15}N TROSY spectra of Xrn2 and Xrn2 Linker (residues 265-293) were recorded with a Bruker Avance III 600 MHz spectrometer equipped with a PATXI cryoprobe.

3.6.3. ^{19}F NMR

All NMR RD experiments of TmCsp, the $\alpha_7\alpha_7$ half proteasome and the riboswitch RNA were recorded on a 500 MHz Bruker NEO NMR spectrometer equipped with triple resonance TCI H&F-C/N-D nitrogen cooled probehead, where the proton coil was tuned and matched to the ^{19}F resonance frequency (470 MHz). Data was acquired with 1024 points in the direct dimension and a relaxation delay of 1.5 s. The 1D spectra of TmCsp (figure 4.1) were recorded at 333 K, 343 K and 373 K on a Bruker 600 MHz spectrometer equipped with a TBI 1H/19F/D probehead. Temperatures were calibrated using an ethylene glycol sample. Both the ethylene glycol sample as well as the sample of 5-fluoroindole dissolved in glycerol were locked using a capillary filled with D_2O that was inserted into the 5 mm NMR tube. ^{19}F spectra were referenced to TFA indirectly by measuring the absolute proton frequency of DSS and using a correction factor $\Xi = 0.940866982$.

The CPMG experiments for TmCsp were recorded with a relaxation delay of 40 ms and with 23 different CPMG frequencies of (50, 100, 150, 200, 250, 300, 350, 400, 450, 500, 600, 700, 800, 900, 1000, 1500, 2000, 2500, 3000, 3500, 4000, 4500 and 5000 Hz).

The CPMG experiments for the $\alpha_7\alpha_7$ complex at 303 K, 313 K and 323 K were recorded with a relaxation delay of 8 ms and with 22 different CPMG frequencies of (125, 250, 375, 500, 625, 750 875, 1000, 1125, 1250, 1500, 1750, 2000, 2250, 2500, 2750, 3000, 3250, 3500, 4000, 4500 and 5000 Hz); the experiments at 293 K were recorded with a relaxation delay of 4 ms and with 20 different CPMG frequencies of (250, 500, 750, 1000, 1250, 1500, 1750, 2000, 2250, 2500, 2750, 3000, 3250, 3500, 3750, 4000, 4250, 4500, 4750 and 5000 Hz).

The fully extended phase cycle for the ^{19}F CPMG including the aring-sequence (figure 4.2) is $\phi1$ = [0 0 0 0 0 0 0 0 0 0 0 0 0 0 0 0 0 0 2 2 2 2 2 2 2 2 2 2 2 2 2 2 2 2 1 1 1 1 1 1 1 1 1 1 1 1 1 1 1 1 1 3 3 3 3 3 3 3 3 3 3 3 3 3 3 3 3], $\phi2$ =[1 1 1 1 1 1 1 1 3 3 3 3 3 3 3 3 3 1 1 1 1 1 1 1 1 3 3 3 3 3 3 3 3 0 0 0 0 0 0 0 0 2 2 2 2 2 2 2 2 0 0 0 0 0 0 0 0 2 2 2 2 2 2 2 2], $\phi3$ =[2 2 2 2 2 2 2 2 2 2 2 2 2 2 2 2 0 0 0 0 0 0 0 0 0 0 0 0 0 0 0 0 3 3 3 3 3 3 3 3 3 3 3 3 3 3 3 3 1 1 1 1 1 1 1 1 1 1 1 1 1 1 1 1], $\phi4$ =[2 0 2 0 2 0 2 0 2 0 2 0 2 0 2 0 2 0 2 0 2 0 2 0 2 0 2 0 2 0 2 3 1 3 1 3 1 3 1 3 1 3 1 3 1 3 1 3 1 3 1 3 1 3 1 3 1 3], $\phi5$ =[0 0 2 2 1 1 3 3 0 0 2 2 1 1 3 3 2 2 0 0 3 3 1 1 2 2 0 0 3 3 1 1 1 1 3 3 2 2 0 0 1 1 3 3 2 2 0 0 3 3 1 1 0 0 2 2 3 3 1 1 0 0 2 2], ϕ_{rec} =[0 2 2 0 1 3 3 1 0 2 2 0 1 3 3 1 2 0 0 2 3 1 1 3 2 0 0 2 3 1 1 3 1 3 3 1 2 0 0 2 1 3 3 1 2 0 0 2 3 1 1 3 0 2 2 0 3 1 1 3 0 2 2 0], where [0,1,2,3] corresponds to [x,y,-x,-y].

The $R_{1\rho}$ on-resonance experiments for TmCsp were based on six different spin-lock times

T_{SL} (0, 4, 8, 16, 32 and 48 ms) and 28 different spin-lock fields (351.05, 393.88, 441.94, 495.87, 556.37, 624.26, 700.43, 785.9, 881.79, 989.38, 1110.11, 1245.56, 1397.54, 1568.07, 1759.4, 1974.08, 2214.95, 2485.22, 2788.46, 3128.71, 3510.47, 3938.81, 4419.42, 4958.67, 5563.72, 6242.59, 7004.3, 7858.96 Hz). The ^{19}F frequency carrier was centered on the respective peak maximum in the 1D ^{19}F spectrum.

The $R_{1\rho}$ on-resonance experiments for the $\alpha_7\alpha_7$ complex were based on six different spin-lock times T_{SL} (0, 2, 4, 8,12 and 16 ms) and 31 different spin-lock fields (103.54, 116.17, 130.35, 146.25, 164.10, 184.12, 206.591, 231.80, 260.08, 291.82, 327.42, 367.37, 412.20, 462.50, 518.93, 582.25, 653.29, 733.01, 822.45, 922.80, 1035.40, 1161.74, 1641.00, 2600.81, 3274.23, 4122.01, 5189.30, 5822.49, 6532.94, 7330.08, 8224.49 Hz). The ^{19}F frequency carrier was centered on the respective peak maximum in the 1D ^{19}F spectrum.

The $R_{1\rho}$ off-resonance experiments for TmCsp were based on six different spin-lock times T_{SL} (0, 4, 8, 16, 32 and 48 ms), 73 different offsets frequencies (+ and - 0, 50, 100, 150, 200, 250, 300, 350, 400, 450, 500, 600, 700, 800, 900, 1000, 1100, 1200, 1300, 1400, 1500, 1600, 1700, 1800, 1900, 2000, 2100, 2200, 2300, 2400, 2500, 2600, 2800, 3000, 3200 and 3400 Hz) and 4 different spinlock fields (100, 200, 300 and 400 Hz). The spin-lock is flanked by two hard pulses that transfer the magnetization to the spin-lock angle θ. θ is calculated from the spin-lock power and the spin-lock offset as $\theta = \tan^{-1}(\omega_1/\Delta\Omega)$, after which the length of the θ-hard pulse is calculated from the 90° hard pulse phard as $p_\theta = \theta/90° \cdot p_{\text{hard}}$. The ^{19}F frequency carrier was centered on -122.1 ppm, corresponding to the Trp7 peak maximum in the 1D ^{19}F spectrum.

All relaxation dispersion datasets were recorded in triplicate in order to obtain the indicated error estimates.

^{19}F spectra of Xrn2 were recorded with Bruker Avance III 500 MHz and 600 MHz spectrometers equipped with nitrogen cooled TCI probeheads. 1D spectra were recorded with the aring pulse sequence from Bruker. ^{19}F-CPMG and ^{19}F-$R_{1\rho}$ experiments were recorded in a pseudo-2D and pseudo-3D fashion, respectively, using the published pulse sequence described in section 4. Data were recorded with a recycle delay of 1.0 s. All ^{19}F-CPMG experiments were recorded with a constant time T_{CPMG} of 16 ms and CPMG frequencies of 62.6 Hz, 125 Hz, 187.5 Hz, 250 Hz, 312.5 Hz, 375 Hz, 437.5 Hz, 500 Hz, 562.5 Hz, 1000 Hz, 1500 Hz, 2500 Hz and 5000 Hz (experiments on the 500 MHz spectrometer) and CPMG frequencies of 62.5 Hz, 125 Hz, 187.5 Hz, 250 Hz, 312.5 Hz, 375 Hz, 437.5 Hz, 500 Hz, 625 Hz, 1000 Hz, 1500 Hz, 2000 Hz, 2500 Hz, 3000 Hz, 3500 Hz, 4000 Hz, 4500 Hz and 5000 Hz (experiments on the 600 MHz spectrometer), respectively.

^{19}F-$R_{1\rho}$ experiments were recorded with five different spinlock times T_{SL} (0, 4, 8, 16 and 32 ms) and 18 different spin-lock fields on the 500 MHz spectrometer (50 Hz, 75 Hz, 100 Hz, 125 Hz, 150 Hz, 200 Hz, 250 Hz, 300 Hz, 400 Hz, 500 Hz, 600 Hz, 700 Hz, 800 Hz, 1000 Hz, 2500 Hz, 3000 Hz, 5000 Hz, 8000 Hz) as well as 18 different spin-lock fields on the 600 MHz spectrometer (50 Hz, 75 Hz, 100 Hz, 125 Hz, 150 Hz, 200 Hz, 250 Hz, 300 Hz, 400 Hz, 500 Hz, 600 Hz, 800 Hz, 1000 Hz, 1500 Hz, 2000 Hz, 3000 Hz, 5000 Hz, 8000 Hz). The ^{19}F frequency carrier was centered on the respective peak maximum in the 1D ^{19}F spectrum. All relaxation dispersion datasets were recorded in triplicates in order to obtain experimental errors for all datapoints. NMR spectra were processed with the NMRPipe/ NMRDraw software suite (Delaglio et al. 1995).

All ^{19}F ZZ-exchange, CEST, CPMG, on-resonance $R_{1\rho}$ and off-resonance $R_{1\rho}$ experiments on the riboswitch RNA were recorded on a 500 MHz Bruker NEO NMR spectrometer equipped with a triple resonance TCI H&F-C/N-D nitrogen cooled probehead, with the proton coil tuned and matched to the 19F resonance frequency of 470.59 MHz. Data were acquired with a recycle delay of 1.0˜1.5 s without ^{1}H decoupling during the acquisition. The carrier frequency was -51.0 ppm for the 1D spectra and adapted to the resonance of interest for all on-resonance experiments. 90° pulse lengths were calibrated individually for all samples and temperatures and were typically between 12.8 µs and 13.2 µs. Spectra were processed with the NMRpipe software (Delaglio et al. 1995) and analyzed with Python and Matlab scripts.

^{19}F-^{19}F ZZ-exchange (EXSY) spectra were acquired as pseudo-3D experiments with an acquisition time of 8.5 ms in the indirect dimension (F1) and mixing times of 1, 2, 5, 10, 25, 50, 75, 100, 150, 200, 400 and 700 ms.

^{19}F CEST experiments were acquired as pseudo-2D experiments. In brief, a low power pulse is applied at a stepped frequency offset specified by an `fq1list`, followed by an anti-ringing element (aring). 1D spectra were extracted and converted to text format data with the NMRpipe scripts `readROI` and `pipe2txt` scripts, respectively. B_1 inhomogeneities were estimated by the method of (Guenneugues et al. 1999) and were consistently around 10 %.

^{19}F CPMG experiments were acquired with the pulse sequence described in section 4 with a relaxation delay of 6 ms and 20 CPMG frequencies (167, 333, 500, 667, 833, 1000, 1167, 1333, 1500, 1667, 2000, 2333, 2667, 3000, 3333, 3667, 4000, 4333, 4667 and 5000 Hz). To avoid offset effects in the relaxation dispersion, the ^{19}F carrier frequency was set to the maximum of the respective peak in the ^{19}F 1D spectrum.

On-resonance $R_{1\rho}$: 19F- on-resonance $R_{1\rho}$ data were collected using the pulse sequence described in section 4 with five different spin-lock times T_{SL} (0, 1, 2, 4 and 8 ms) and 31 different spin-lock fields (100, 200, 300, 400, 500, 600, 700, 800, 900, 1000, 1200, 1400, 1600, 1800, 2000, 2500, 3000, 3500, 4000, 4500, 5000, 5500, 6000, 6500, 7000, 7500, 8000, 8500, 9000, 9500 and 10000 Hz). The 19F carrier frequency was set to the respective peak maximum observed in the ^{19}F 1D spectrum.

Off-resonance $R_{1\rho}$: ^{19}F- off-resonance $R_{1\rho}$ experiments were recorded with the pulse sequence described in section 4 with seven different spin-lock times T_{SL} (0, 1, 2, 4, 8, 16 and 32 ms) and 71 different spin-lock offset frequencies. Data was acquired for spin lock fields of 50, 100, 150, 200, 300, 400, 600 and 800 Hz.

3.6.4. Data processing/analysis/fitting

Methyl-TROSY CPMG: The pseudo-3D data was processed with NMRPipe (Delaglio et al. 1995) and analyzed with in-house written Matlab scripts. In brief, peak intensities $I(\nu_{CPMG})$ corresponding to CPMG frequencies ν_{CPMG} were extracted from 2D planes with NMRPipe and normalized to a reference intensity I_0 obtained by omitting the CPMG element. The normalized intensity $I(\nu_{CPMG})/I_0$ was then converted into effective transverse relaxation rates $R_{2,eff}$ by assuming an exponential decay over the constant CPMG time T_{CPMG}:

$$R_2(\nu_{CPMG}) = -\frac{1}{T_{CPMG}} \ln \frac{I(\nu_{CPMG})}{I_0} \tag{3.1}$$

The data were fitted numerically to a global two-state model using equation (2.66) in order to extract the exchange parameters p_{GS}, k_{ex}, $\Delta\omega_C^i$ and $\Delta\omega_H^i$, $R_{2,MQ}^i$ and $R_{2,SQ}^i$ where the index i refers to the residue number. A minimum standard deviation of $0.5\,s^{-1}$ was assumed for the fit.

^{19}F CPMG: pseudo-2D datasets were processed with NMRPipe (Delaglio et al. 1995). Effective transverse relaxation rates were calculated according to equation (3.1). CPMG profiles were numerically fitted using equations (2.54) and (2.53). Here, the starting magnetization $\mathbf{M}(0)$ and the evolved magnetization $\mathbf{M}(2n\tau_{CPMG})$ were chosen according to the exchange model. Relaxation rates R_1^i and R_2^i were each assumed to be equal for all states i involved in the exchange. Minimum standard deviations of the Xrn2 ^{19}F data were set to $2\,s^{-1}$ to avoid excessive weighting of datapoints with accidentally low errors.

Rotating frame relaxation: $R_{1\rho}$ pseudo-3D datasets were processed with NMRPipe and $R_{1\rho}$ rates were extracted from the exponential fit of resonance intensities from different spin lock times T_{SL}. On-resonance $R_{1\rho}$ data was fitted numerically using the eigenvalue approximation (2.79) for $R_{1\rho}$. To avoid errors arising from approximations, the shift of the average peak was calculated as the imaginary part of the complex eigenvalues of the exchange matrix during parameter optimization for the Xrn2 data. Off-resonance $R_{1\rho}$ data was fitted with an in-house Matlab script using the Laguerre approximation (2.82) for TmCsp data, and calculated using the eigenvalue approch (2.79) in case of the riboswitch RNA. Minimum standard deviations were set to $2\,s^{-1}$ to avoid excessive weighting of datapoints with accidentally low errors.

To extract errors in the parameters extracted from the NMR relaxation data, Monte Carlo simulations with 100-200 fit iterations were carried out by random variation of R_2 rates according to their standard deviation and subsequent execution of the numerical fitting routine.

3.6.4.1. Thermodynamic and kinetic analysis

Solutions for $k_{ex} = k_F + U$ and the folded population p_F from the CPMG fits at different temperatures were used to calculate the unfolding rate k_u, the folding rate k_F and the equilibrium constant K_{eq} according to

$$p_U = 1 - p_F \tag{3.2}$$

$$k_U = p_U k_{ex} \tag{3.3}$$

$$k_F = p_F k_{ex} \tag{3.4}$$

$$K_{eq} = \frac{k_U}{k_F} \tag{3.5}$$

To obtain the thermodynamic parameters, first K_{eq} was fit according to

$$K_{eq} = e^{-\Delta G/RT} = e^{(T\Delta S - \Delta H)/RT} \tag{3.6}$$

The values obtained for the change in entropy ΔS and in enthalpy ΔH were subsequently used as constraints

$$\Delta S = \Delta S^{\ddagger F \to U} + \Delta S^{\ddagger U \to F} \tag{3.7}$$

$$\Delta H = \Delta H^{\ddagger F \to U} + \Delta H^{\ddagger U \to F} \tag{3.8}$$

in the fit equations

$$k_{\mathrm{U}} = \frac{1}{\tau_{\mathrm{TPT}}} e^{(T\Delta S^{\ddagger F\to U} - \Delta H^{\ddagger F\to U})/RT} \tag{3.9}$$

$$k_{\mathrm{F}} = \frac{1}{\tau_{\mathrm{TPT}}} e^{(T\Delta S^{\ddagger U\to F} - \Delta H^{\ddagger U\to F})/RT} \tag{3.10}$$

where τ_{TPT} is the transition path time, ΔS and ΔH are the differences in entropy and enthalpy between the folded and the unfolded state, $\Delta S^{\ddagger F\to U}$ and $\Delta H^{\ddagger F\to U}$ are the entropy and enthalpy differences between the folded and the transition state, and $\Delta S^{\ddagger U\to F}$ and $\Delta H^{\ddagger U\to F}$ are the entropy and enthalpy differences between the unfolded state and the transition state.

3.6.5. NMR structure calculations of the zinc finger

All spectra used for the structure calculation were acquired at 288 K on Bruker Avance III 500 MHz and 600 MHz spectrometers equipped with nitrogen cooled TCI probeheads. Assignment of the zinc finger (residues 265-293) backbone and sidechain resonances was obtained based on the following spectra: ^{1}H^{15}N-HSQC, ^{1}H^{13}C-HSQC, 3D-HNCACB, 3D-HN(CA)CO, 3D-H(CC)(CO)NH-TOCSY, 3D-(H)CC(CO)NH-TOCSY (Sattler et al. 1999). All assignment spectra were processed using Topspin 4.0.2 and analyzed with CARA (Keller 2004). Distance restraints for the structure calculation were obtained from 3D ^{15}N NOESY-HSQC (mixing time 150 ms), 3D ^{13}C NOESY-HSQC (mixing time 150 ms) and 2D ^{13}C$^{\mathrm{aro}}$-NOESY-HSQC spectra with automatic peak picking using NMRFAM-SPARKY (Lee et al. 2015). Torsion angle restraints were derived from chemical shift assignments using the TALOS-N web server (Shen and Bax 2013). Additional restraints were manually added for Zn^{2+} coordination, where the Zn^{2+} ion was included using a CYSZ residue. The structure was calculated with CYANA, where seven iterations were performed with 100 initial and 20 final structures (Güntert and Buchner 2015). NMR assignments are deposited in the BMRB under accession number 50997, the NMR structure is deposited in the PDB under accession number 7PVM.

3.6.6. Titration of Xrn2 with substrates

HMQC spectra of 50 µM Xrn2 with different substrates were recorded at 313 K in the presence of 5 mM MgCl2 unless indicated otherwise. 3',5'-bisphosphoadenosine (100 mM stock solution) was added to a final concentration of 500 µM. 5'-phosphorylated A5-DNA (2 mM stock solution) was added to a final concentration of 200 µM. xrRNA prepared by in vitro transcription was added to a final concentration of 100 µM.

3.7. Fluorescence anisotropy

Fluorescence Anisotropy experiments were performed in 25 mM HEPES pH 7.3, 125 mM NaCl, 0.002 % Triton with fluoresceine-labeled 5mer 5'-GGAGUFsc-3' and 10mer 5'-GGAGGAGAGUFsc-3' RNAs (where UFsc is a thiouridin covalently labeled with iodacetamido-fluorescein) generated as described above. RNA concentrations were 5 nM (5mer RNA) or 1 nM (10mer RNA), protein concentrations were 0, 5, 10, 30, 100, 400 and 1000 nM (5mer RNA) and 0, 2, 5, 10, 30, 80 and 200 nM (10mer RNA). Data was acquired with a TECAN Spark microplate reader with excitation and emission wavelengths of 485 nm and 535 nm, respectively. Fluorescence anisotropy data was analyzed with in house written Matlab scripts.

3.8. X-ray crystallography

Crystallization of *C. thermophilum* Xrn2 1-875 was carried out with vapor diffusion in sitting drops, derived from 0.3 µl of Xrn2 (36 mg/ml) in 25 mM HEPES pH 7.3, 125 mM NaCl, 0.5 mM DTT and 0.3 µl of the precipitant reservoir solution (20% w/v PEG3350, 200 mM magnesium formate). Crystals grew as thin needles within 2-4 weeks. Crystals were shortly incubated in the reservoir solution with 30% glycerol added for cryoprotection before harvesting. Diffraction data were collected at 100 K on the PXII beamline at the Swiss Light Source with a wavelength of 1Å, and processed with XDS (Kabsch 2010). S. pombe Xrn2 (Rat1, PDB entry 3FQD) was pruned with the CCP4 utility Chainsaw (Stein 2008) to serve as a search model for molecular replacement, which was performed with the CCP4 utility Phaser (McCoy et al. 2007). The final structure was obtained after performing several cycles of iterative model building and refinement with Coot (Emsley et al. 2010) and Phenix (Liebschner et al. 2019), respectively. Structure factors and coordinates have been deposited in the PDB under accession code 7OPK.

3.9. Vizualization

The helical wheel in figure 5.6 was generated with Drawcoil 1.0 (`https://grigoryanlab.org/drawcoil/`). All pictures of structures were prepared with ChimeraX (Pettersen et al. 2021), all pictures of 2D NMR spectra were prepared using NMRView (`www.onemoonscientific.com`). The sequence alignment in figure 5.4 was generated with ClustalX 2.1 (Larkin et al. 2007).

4. A suite of ^{19}F NMR experiments to study biomolecular dynamics

The results of this chapter were published in the JOURNAL OF BIOMOLECULAR NMR (Overbeck et al. 2020) [1], the chapter is therefore largely identical to the publication in both text and figures. All authors conceived the project. J.H.O. and R.S. designed the experiments. J.H.O. performed the experiments. J.H.O. and R.S. analyzed and interpreted the experiments. J.H.O. and R.S. wrote the paper, all authors commented on the manuscript.

4.1. Summary

Proteins and nucleic acids are highly dynamic bio-molecules that can populate a variety of conformational states. NMR relaxation dispersion (RD) methods are uniquely suited to quantify the associated kinetic and thermodynamic parameters. Here, we present a consistent suite of ^{19}F-based CPMG, on-resonance $R_{1\rho}$ and off-resonance $R_{1\rho}$ RD experiments. We validate these experiments by studying the unfolding transition of a 7.5 kDa cold shock protein. Furthermore we show that the ^{19}F RD experiments are applicable to very large molecular machines by quantifying dynamics in the 360 kDa half-proteasome. Our approach significantly extends the timescale of chemical exchange that can be studied with ^{19}F RD, adds robustness to the extraction of exchange parameters and can determine the absolute chemical shifts of excited states. Importantly, due to the simplicity of ^{19}F NMR spectra, it is possible to record complete datasets within hours on samples that are of very low costs. This makes the presented experiments ideally suited to complement static structural information from cryo-EM and X-ray crystallography with insights into functionally relevant motions.

4.2. Introduction

Bio-molecules are inherently dynamic and populate a number of structurally different states. NMR spectroscopy is a unique tool to experimentally investigate these bio-molecular motions with atomic resolution. When the exchange rates between the different states are on the millisecond timescale Carr-Purcell-Meiboom-Gill (CPMG) and rotating-frame relaxation experiments at different effective magnetic fields can be exploited to record relaxation dispersion (RD) profiles. These profiles directly depend on thermodynamic (populations) and kinetic (rates) parameters of the exchange process and structural information (chemical shifts) of sparsely populated (invisible), short-lived excited states can be obtained. For proteins under 20 kDa, RD experiments can be recorded on protonated ^{15}N-labeled samples, whereas deuteration and Transverse Relaxation Optimized Spectroscopy (TROSY) (Pervushin et al. 1997) are required for larger systems. In very large complexes (> 80 kDa), methyl group labeling in a fully deuterated background combined with methyl-TROSY based approaches (Tugarinov et al. 2003, Schütz and Sprangers 2020, Abramov et al. 2020) can be used to record ^{13}C single quantum (SQ) (Skrynnikov et al. 2001, Lundström et al. 2007) (Rennella et al. 2016) and ^{13}C multiple quantum (MQ) as well as ^{1}H SQ, double quantum (DQ) (Gopalan et al. 2018) and triple quantum (TQ) (Gopalan et al. 2018) RD profiles.

Recently, fluorine (^{19}F) NMR has regained attraction (Hellmich et al. 2009, Liu et al. 2012, Kim et al. 2013, Kitevski-Leblanc et al. 2013, Aramini et al. 2014, Hoang and Prosser 2014, Manglik et al. 2015, Matei and Gronenborn 2016, Lu et al. 2019, Huang et al. 2020). This spin is absent from virtually all biomolecules, however, ^{19}F probes can be artificially introduced into proteins by incorporation of fluorinated amino acids (Crowley et al. 2012) or through post-translational modification with fluorine-containing tags (Brauer and Sykes 1986). These ^{19}F labeling strategies provide a number of advantages. First, the resulting samples contain only a limited number of NMR probes and spectra can often be recorded in a simple one-dimensional (1D) manner. Second, in most cases, fluorine-based experiments can be recorded in a fully protonated background and samples can thus originate from sources where deuteration or methyl group labeling is not easily achievable (e.g. mammalian expression systems). Third, ^{19}F experiments can complement and verify information from deuterated systems, where structure, stability and dynamics can be altered due to the pervasive isotopic substitution (Korzhnev et al. 2005a). Fourth, ^{19}F shares favorable characteristics with ^{1}H with respect to RD experiments (Juen et al. 2016), including reduced sample heating on probe heads with inverse coil configuration, short pulses and an extended range of accessible effective field strengths. Finally, the ^{19}F chemical shift dispersion is large, which can result in significant chemical shift differ-

ences between the ground state and excited states and thus RD profiles that have large amplitudes.

In the past, ^{19}F RD CPMG experiments have been exploited to study dynamic protein interfaces (Aramini et al. 2014), dynamic dimer asymmetry (Kim et al. 2013), allostery (Manglik et al. 2015), ligand-bound states (Hoang and Prosser 2014), protein folding (Kitevski-Leblanc et al. 2013) and fold-switching (Liebau et al. 2020). In those experiments, a varying number of 180° pulses is applied within a fixed relaxation delay such that exchange induced line-broadening can be suppressed. Fitting of these RD profiles with analytical or numerical approaches provides insight into the exchange constant k_{ex}, the populations p_A and p_B as well as the absolute value of the chemical shift difference $|\Delta\omega|$ between the two states. However, in many cases these data are not sufficient to unambiguously and accurately determine these parameters as significantly different exchange regimes can result in similar RD profiles. In those cases $R_{1\rho}$ experiments can be used to resolve these ambiguities. In $R_{1\rho}$ experiments the effective relaxation rate is measured in the rotating frame as a function of spin-lock field strengths ("on-resonance") or as a function of spin-lock offsets ("off-resonance"). Compared to the CPMG approach, this has several advantages. First, $R_{1\rho}$ experiments can access higher frequencies and thus allow quantification of faster dynamics. Second, off-resonance experiments can provide not only the magnitude but also the sign of $\Delta\omega$. Third, the sampling of points in the frequency dimension is not restricted, as it is in CPMG experiments where only frequencies that correspond to an integer number of 180 degree pulses in the relaxation delay are possible. Motivated by these considerations, we developed a suite of one-dimensional CPMG, on-resonance $R_{1\rho}$ and off-resonance $R_{1\rho}$ pulse sequences for ^{19}F nuclei. We validate the experiments on the unfolding transition of a cold shock protein, show, that they yield consistent exchange parameters and extract thermodynamic information from a temperature series of RD datasets. Moreover, we demonstrate the applicability of ^{19}F rotating frame relaxation to a fully protonated 360 kDa protein complex.

4.3. Results

Here we introduce a suite of one-dimensional ^{19}F pulse sequences for the collection of CPMG, on-resonance $R_{1\rho}$ and off-resonance $R_{1\rho}$ data to characterize dynamics on the µs-ms timescale. We use the cold shock protein from Thermotoga maritima (TmCsp) to highlight the applicability of these sequences to accurately determine exchange parameters in biomolecules. TmCsp is a small (7.5 kDa) thermostable protein that undergoes an unfolding transition with a melting temperature of $T_m = 359\,\mathrm{K}$ (Schuler et al. 2002a).

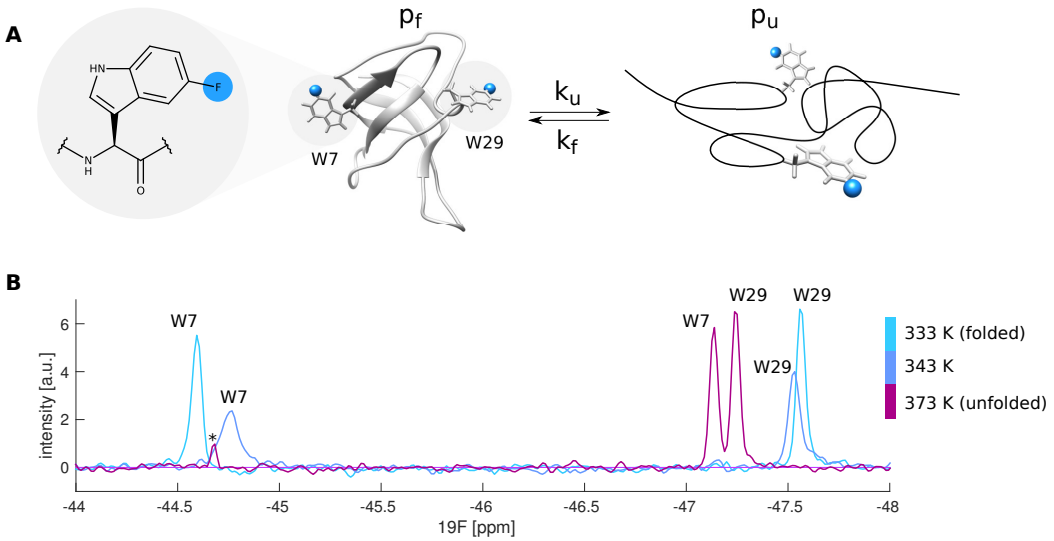

Figure 4.1.: Scheme of TmCsp unfolding with 1D ^{19}F spectra A) The chemical structure of 5-fluoro tryptophan (5FW; left) and a schematic presentation of the (un-) folding of TmCsp, which contains 5FW residues at positions 7 and 29 (Protein Data Bank (PDB) ID 1G6P (Kremer et al. 2001)). B) ^{19}F spectra of TmCsp at 333 K, 343 K and 373 K with assignments for Trp7 and Trp29. The peak labeled with an asterisk results from a small impurity in the sample. This impurity resonates outside the displayed spectral window at the two lower temperatures.

Two ^{19}F probes were introduced into the protein by replacing two natural tryptophan residues (W7 and W29) with 5-fluoro tryptophan (5FW; figure 4.1). Both the natural and the 5FW-labeled protein follow a two state unfolding transition (Perl et al. 1998, Wassenberg et al. 1999, Schuler et al. 2002a,b), which makes it a well-suited system to establish our ^{19}F RD experiments.

The ^{19}F NMR spectra of the protein show two sharp resonances at low (333 K) and high (373 K) temperatures corresponding to the fully folded (light blue) and fully unfolded (red) states (figure 4.1). Based on these spectra, the chemical shift differences between the folded and thermally unfolded protein are 2.53 ppm (W7) and 0.33 ppm (W29) respectively. Of note, at temperatures above 373 K the resonances of the unfolded state (red) continue to shift towards lower ppm values. Based on this temperature dependence of the unfolded state chemical shift we can derive that the chemical shift differences at 333 K are 2.35 ppm (W7) and 0.48 ppm (W29). At 343 K (blue) extensive line broadening is observed, which arises from the exchange ($k_{ex} = k_F + k_U$) between the folded (F) and unfolded (U) states of the protein (figure 4.1).

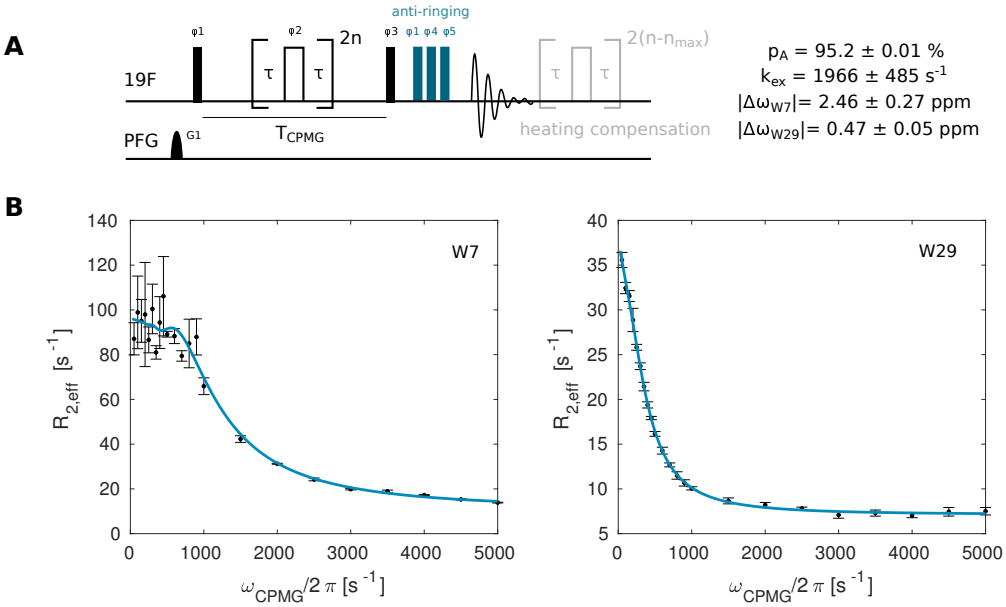

Figure 4.2.: The ^{19}F CPMG experiment. A) Pulse sequence for recording ^{19}F CPMG RD profiles. Narrow (wide) rectangles indicate 90° (180°) pulses, which are applied along the x-axis unless indicated otherwise. The phase cycle is $\phi_1 = \phi_{rec}$ = [x,x,-x,-x,y,y,-y,-y], ϕ_2 = [y,-y,y,-y,x,-x,x,-x]. The number of CPMG pulses applied during the CPMG time T_{CPMG} is given by $2n$, where n is an integer. The maximum number $n_{\max}$ is chosen so that the highest applied frequency $\nu_{CPMG} = t_{max}/T_{CPMG}$ is at or below 5 kHz. B) CPMG relaxation dispersion profiles for W7 and W29 recorded at 344 K. The size of the error-bars correspond to 1 standard deviation.

To quantify this exchange process we first recorded ^{19}F CPMG RD profiles using the pulse sequence displayed in figure 4.2. This sequence contains two elements that we found to be particularly important for obtaining high quality data. First, we included a heat compensation block such that the sample is exposed to the same total RF power independent of the CPMG frequency. This is especially important when higher ^{19}F CPMG frequencies (5 kHz) are used in combination with longer (>20 ms) CPMG times. Second, when using a probehead where the ^{1}H coil is de-tuned to record ^{19}F spectra, we found broad baseline artifacts at the on-resonance ^{19}F frequency that are due to suboptimal performance of the ^{1}H RF coil for ^{19}F experiments. These imperfections can be suppressed through the use of an "anti-ring" sequence (Gerothanassis 1987) that consists of three 90 degree pulses of different phases in combination with extensive phase cycling. We then used a sample that contains 5-fluoroindole in glycerol to show that the CPMG experiment results in flat RD profiles for a system that does not undergo chemical exchange (figure 4.3). Due to the high viscosity, the ^{19}F T_1 and T_2 times are comparable to the ^{19}F relaxation times in proteins making this a good testing system for biological samples.

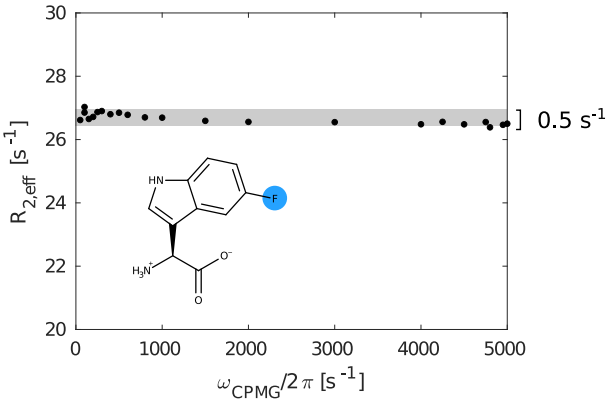

Figure 4.3.: ^{19}F CPMG experiment of 5-fluoroindole in glycerol at 298 K. The flat profile indicates, that artifacts in the ^{19}F CPMG experiment are minimized to a sufficient extent in the absence of chemical exchange

Based on the above, we recorded CPMG RD profiles on TmCsp at 11.7 T (500 MHz ^{1}H frequency) and 344 K, which is 15 K below the melting temperature of the protein. In total, we recorded a full dataset with 23 CPMG frequencies in approximately 40 minutes (64 scans, 1.5 s interscan delay), highlighting the efficiency of the 1D based ^{19}F CPMG method. The ^{19}F signals of the two ^{19}F tryptophan residues show large dispersions, indicative of chemical exchange (figure 4.2). A global numerical fit (solid line) according to a two-site exchange model gives an exchange rate of $k_{ex} = 1966 \pm 485\,s^{-1}$, populations of $p_F = 95.2 \pm 0.1\,\%$, $p_U = 4.8 \pm 0.1\,\%$ and chemical shift differences of $|\Delta\omega_{W7}| = 2.46 \pm 0.26$ ppm and $|\Delta\omega_{W29}| = 0.47 \pm 0.05$ ppm, where the errors in the extracted parameters are standard deviations calculated by Monte Carlo simulations based on three separately recorded datasets (figure 4.4). It is noteworthy that the determined chemical shift differences agree well with the values obtained from 1D spectra recorded at different temperatures (2.35 ppm and 0.48 ppm for W7 and W29 respectively; figure 4.1), especially when considering that only two peaks at a single field strength are used to fit the exchange parameters. The relatively high accuracy of the extracted parameters can be explained based on the fact, that the values of $|\Delta\omega|$ are significantly different for the two residues. The ratio between the kinetic parameter k_{ex} ($1966\,s^{-1}$) and the absolute value of $|\Delta\omega|$, which defines the exchange regime, effectively yields an intermediate exchange for W7 ($|\Delta\omega_{W7}| = 2.44$ ppm $= 2\pi \cdot 1170$ Hz), but is in fast exchange for W29 ($|\Delta\omega_{W29}| = 0.46$ ppm $= 2\pi \cdot 216$ Hz). Our data here show, that the exchange parameters can be reliably extracted from the CPMG dispersions alone. The associated standard deviations in the extracted parameters are nevertheless considerable (figure 4.4).

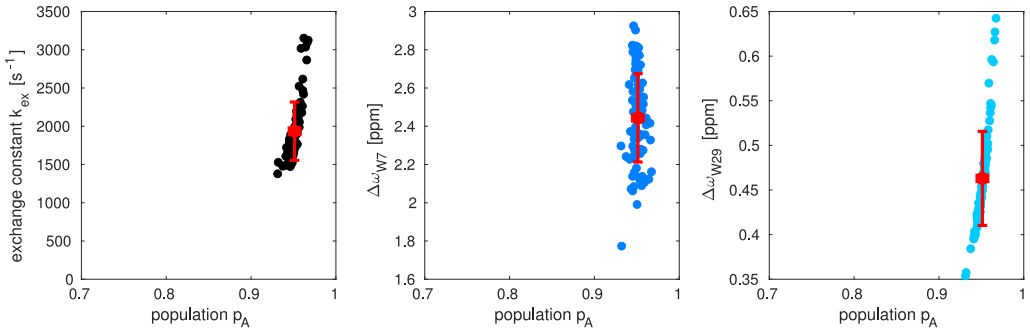

Figure 4.4.: Monte Carlo simulation for CPMG experiments of 5FW-labeled TmCsp at 344 K and 500 MHz Shown are correlation plots of the exchange constant k_{ex} with population p_A as well as the chemical shift differences $\Delta\omega_{W7}$ and $\Delta\omega_{W29}$ with p_A

To complement the CPMG RD data and to be able to study systems that exchange on faster timescales we made use of a ^{19}F on-resonance $R_{1\rho}$ pulse sequence (figure 4.5). We initially implemented the option to use adiabatic ramps with tanh/tan amplitude/phase modulation for the magnetization transfer to the transverse plane (Mulder et al. 1998). However, we found a transfer with hard pulses more convenient, as it is compatible with lower spin-lock powers, for which the adiabatic condition would otherwise be violated. As for the CPMG RD experiment, we observed significant baseline distortions in the spectra that result from acoustic ringing in the ^{1}H/^{19}F-coil at the ^{19}F resonance frequency. These artifacts could be efficiently eliminated with an anti-ringing element. In addition, the pulse sequence includes a heating compensation for different spin-lock times T_{SL} to ensure a constant rf power. We recorded separate datasets for W7 and W29 at 11.7 T and 344 K with the carrier frequency placed on-resonance (either at W7 or at W29), each with 28 spin-lock field strengths between 0.35 kHz and 7.8 kHz. Every datapoint corresponds to an $R_{1\rho} = R_2 + R_{ex}$ value that is obtained by fitting of an exponential decay recorded over six time points T_{SL}. The total experimental time for one complete $R_{1\rho}$ dataset (32 scans, 1.5 s interscan delay) is around 2.3 hours. To extract a reliable estimate of the error, we recorded three datasets for W7 and three datasets for W29. The data was simultaneously fitted using Trott's and Palmer's approach (Trott and Palmer 2002) (solid line) and yields an exchange rate of $k_{ex} = 2275 \pm 268\,s^{-1}$, populations of $p_F = 96.6 \pm 0.4\,\%$, $p_U = 3.4 \pm 0.4\,\%$ and chemical shift differences of $|\Delta\omega_{W7}| = 2.64 \pm 0.18$ ppm and $|\Delta\omega_{W29}| = 0.51 \pm 0.02$ ppm. The extracted parameters agree well with the parameters that we extracted from the RD CPMG experiments (figure 4.2) and with the chemical shift differences that we observe in the 1D NMR spectra (figure 4.1).

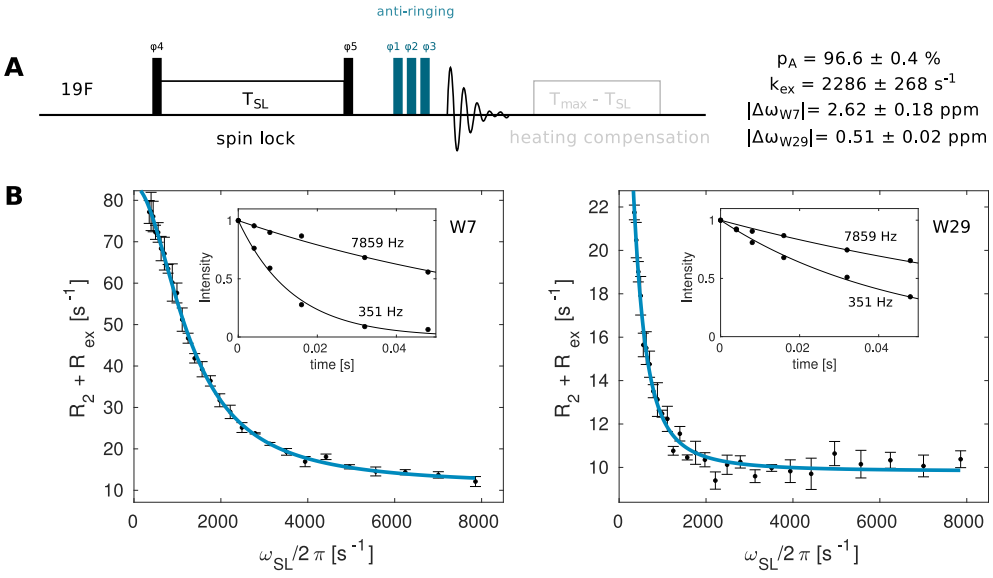

Figure 4.5.: ^{19}F on-resonance $R_{1\rho}$ experiment (A) Pulse sequence for the ^{19}F on-resonance $R_{1\rho}$ experiment. Narrow (wide) rectangles indicate 90° (180°) pulses, which are applied along the x-axis unless indicated otherwise. The phase cycle is ϕ_1 = x, ϕ_2 = [-x,x], ϕ_3 = [x,x,-x,-x,y,y,-y,-y], ϕ_4 = [y], ϕ_5 = [-y], ϕ_{rec} = [x,-x,-x,x,y,-y,-y,y]. (B) On-resonance $R_{1\rho}$ relaxation dispersion profiles for W7 and W29. The size of the error-bars correspond to 1 standard deviation.

It is noteworthy, that higher spin-lock fields up to 20 kHz have been employed in proton $R_{1\rho}$ experiments on cryoprobes (Steiner et al. 2016), which accordingly expands the range of dynamics that can be studied with the presented fluorine $R_{1\rho}$ experiment. On the other end, the lower limit of the spinlock field is dictated by the largest J-couplings present in the spin system (Zhao et al. 2014). In 5FW, the $^3J_{FH}$ coupling of $\sim$ 9.9 Hz restricts the use of spin-lock to fields below 30 Hz (Zhao et al. 2014). This limitation is eluded by the use of a dual ^{1}H-^{19}F probehead where proton-fluorine couplings can be decoupled and is also not applicable in fluorine labels where no vicinal protons are coupled to the ^{19}F spin, as is the case in bromotrifluoroacetone (BTFA; see below). We note that in CPMG experiments the $^3J_{FH}$ coupling leads to the interconversion of ^{19}F in-phase and anti-phase magnetization during the periods 2τ between the refocusing pulses. Depending on the CPMG frequency and on the difference of in-phase and anti-phase transverse relaxation, this would result in a distorted RD profile (Kay et al. 1992), a problem that could be solved by employing an explicit relaxation-compensation, where in-phase and anti-phase contributions are averaged for all CPMG frequencies (Loria et al. 1999a). In biological ^{19}F NMR, however, this problem is negligible for most practical purposes, as the anti-phase contributions only become relevant, when the periods 2τ between the refocusing pulses

become longer than $1/4J$. Even in the case of a strong three-bond H-F coupling of 10 Hz, this corresponds to 25 ms and thus to a long CPMG time of 50 ms with the minimum of two refocusing π pulses, or a CPMG frequency of $\omega_{\mathrm{CPMG}}/2\pi = 20\,\mathrm{Hz}$. Finally, it is worth mentioning that we here sampled six points of the exponential decay in order to rule out a non-exponential behavior of the spin-locked relaxation, that can arise due to inaccurate alignment of the magnetization with the spin-lock field. The experimental time can be reduced at least by a factor of 3 when only a reference and a single timepoint are measured to determine the exponential decay for each spinlock field (figure A.2), without a significant change in the values of the extracted parameters.

The CPMG and $R_{1\rho}$ RD experiments only yield the absolute value of the chemical shift difference between the two states ($|\Delta\omega_i|$). ^{19}F off-resonance $R_{1\rho}$ experiments (figure 4.6) on the other hand can be used to extract a full set of parameters (p_{F}, k_{ex}, R_2^i, $\Delta\omega_i$) from measurements at a single $\mathbf{B}_0$ field in case of a two-state exchange process (Trott and Palmer 2002, Korzhnev et al. 2005b). In that experiment the effective field, which is defined by the vector sum of the spin-lock field ω_1 and the spin-lock offset ω_{offset}, is now inclined by an angle θ. The magnetization is transferred from the $\pm$z axis to an angle θ by hard pulses of the appropriate length, which allows to use very low spin-lock fields. Again, our pulse sequence included a heating compensation for the different spin-lock lengths as well as an anti-ringing element. We recorded datasets for W7 at 11.7 T and 344 K at spin-lock fields of 100 Hz, 200 Hz, 300 Hz and 400 Hz and with 71 offsets in each experiment. The total experimental time for this complete dataset (16 scans, interscandelay 1.5 s) is 11.5 hours. To estimate the error in the data, this dataset was recorded three times.

Figure 4.6 shows the $R_{1\rho}$ data together with a global fit of all off-resonance datasets (solid line). A main peak corresponding to the observable resonance (F) is centered at zero offset, with a width determined by the spin lock power ω_1. Exchange between the folded and the unfolded state leads to the appearance of a second peak that is centered around the resonance frequency of the excited, unfolded state (U). At 100 and 200 Hz, this peak gives rise to a distinct maximum; at higher spin-lock frequencies the resonances merge, but still add up to a clearly asymmetric profile that is indicative of the exchange process. The contribution of $R_2 + R_{\mathrm{ex}}$ can be extracted from the $R_{1\rho}$ data as $R_2 + R_{\mathrm{ex}} = (R_{1\rho} - R_1 \cdot \cos^2\theta)/\sin^2\theta$ (figure 4.6). The error in $R_2 + R_{\mathrm{ex}}$ rapidly increases with the spin-lock offset, because the contribution is scaled with the inverse of $\sin^2\theta$. At the same time, the error at a given offset decreases when increasing the spin lock power, as is readily visible from the data between 100 Hz and 400 Hz power. Based on a global fit of the complete off-resonance dataset, we extract an offset $\Delta\omega_{W7}$ of $-2\pi \cdot 1097 \pm 84\,\mathrm{Hz}$

= -2.33 $\pm$ 0.18 ppm, a ground state population of $p_F = 95.0 \pm 0.2\,\%$ and an exchange constant of $k_{ex} = 1922 \pm 137\,s^{-1}$, which is close to the values obtained by the CPMG and on-resonance $R_{1\rho}$ RD experiments. We also observe that the single datasets at 100 Hz or 200 Hz can be used to obtain accurate exchange parameters. The 300 Hz data, and certainly the 400 Hz data, on the other hand fail to give well-defined results (figure A.3), because a higher spin lock field increasingly overwrites off-resonance effects (Trott and Palmer 2002).

In order to evaluate the consistency between the CPMG, the on-resonance $R_{1\rho}$ and the off-resonance $R_{1\rho}$ experiments, we used a global fit for all datasets (figure A.5, figure A.4). We expect that a global fit yields the most precise parameters, because the three experiments contain redundant information about the protein folding/unfolding transition. In the fit, we optimized the following parameters: k_{ex}, $\Delta\omega_{W7}$, $\Delta\omega_{W29}$, p_F and R_2. Because we observed small deviations on the order of $2\,s^{-1}$ in the R_2 values from the CPMG and the $R_{1\rho}$ experiments we introduced two independent R_2 variables: R_2^{CPMG} and $R_2^{R_{1\rho}}$. Based on that, we obtained a ground state population of $p_F = 94.8 \pm 0.1\,\%$, an exchange constant of $k_{ex} = 1737 \pm 54\,s^{-1}$, and chemical shift differences of $\Delta\omega_{W7} = 2\pi \cdot 1086 \pm 66\,Hz$ = 2.31 $\pm$ 0.14 ppm, $\Delta\omega_{W29} = 2\pi \cdot 202 \pm 5\,Hz$ = 0.43 $\pm$ 0.01 ppm. These parameters are in agreement with the individually fitted datasets, but have a significantly increased precision (figure A.5).

Temperature dependent RD measurements are well suited to extract thermodynamic parameters of chemical exchange processes (Mulder et al. 2001, Nikolova et al. 2011, Audin et al. 2013). Here, we measured ^{19}F CPMG RD profiles at seven different temperatures between 328 K and 343 K and determined the unfolding and folding rates (k_U, k_F) as well as equilibrium constants $K_{eq} = k_U/k_F$ (figure 4.7). The temperature-profile of K_{eq} was subsequently fit to an Arrhenius model for Gibbs free energy $\Delta G = \Delta H - T\Delta S = -RT \ln K_{eq}$, from which we obtain $\Delta H = 43.9 \pm 1.0\,kcal\,mol^{-1}$ and $T\Delta S = 40.6 \pm 1.0\,kcal\,mol^{-1}$ at 343 K, indicating an entropy-enthalpy compensation during TmCsp unfolding. Similarly, transition state theory can be used to obtain estimates of the enthalpic and entropic contributions to the energy barrier that separates the folded and the unfolded state. Because the traditional pre-exponential factor $k_B T/h$ in the Eyring equation is on the timescale of covalent bond vibrations and hence a suboptimal estimate for large-scale biomolecular dynamics (Moore 2012, Vallurupalli et al. 2016), we chose to estimate it as $1/\tau_{TPT}$, where τ_{TPT} is the transition path time. Based on MD simulations and single-molecule fluorescence studies that show that τ_{TPT} is similar even for proteins with vastly different folding rates (Shaw et al. 2010, Chung et al. 2012, Vallurupalli et al. 2016), we assumed τ_{TPT} to be 1 µs and obtained values of $\Delta H^{\ddagger} = 45.8 \pm 1.2\,kcal\,mol^{-1}$ and

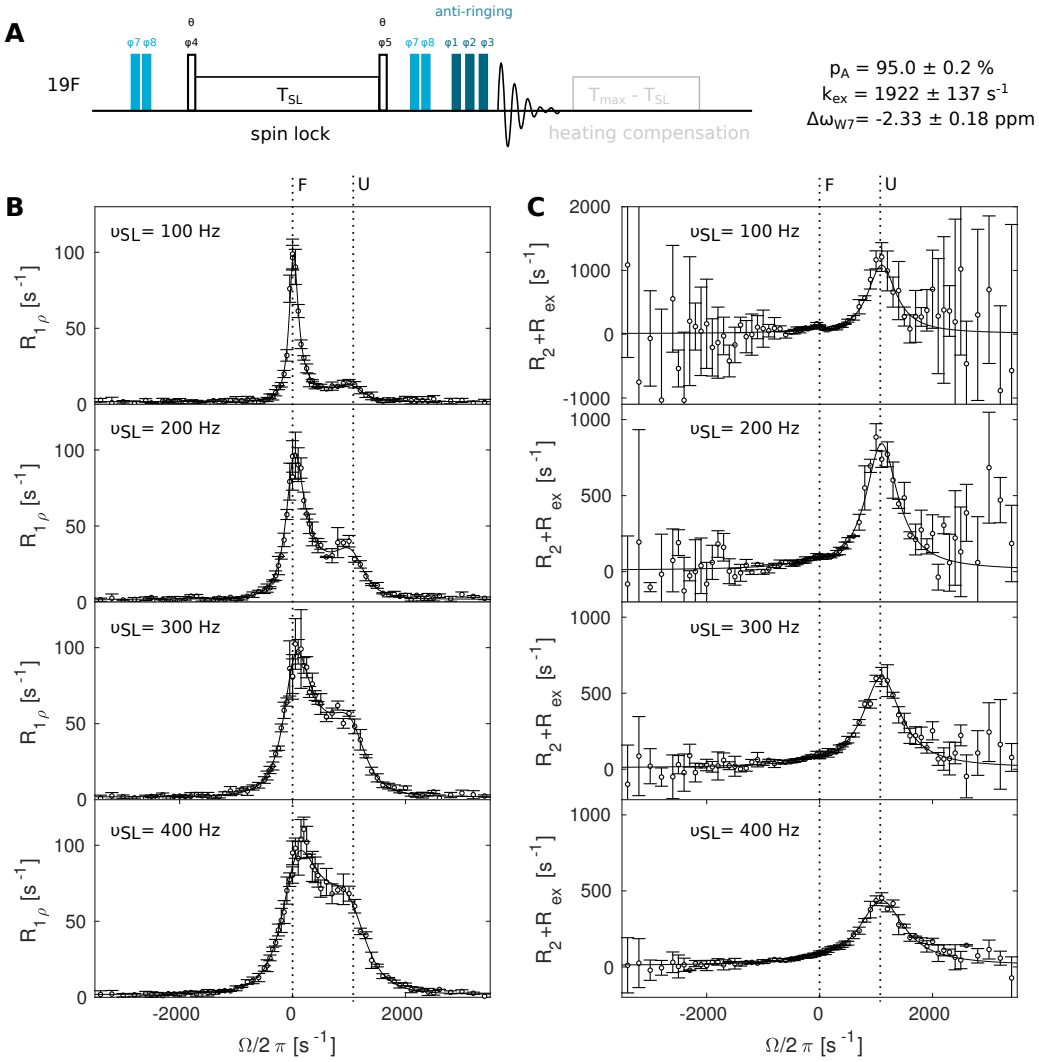

Figure 4.6.: ^{19}F off-resonance $R_{1\rho}$ experiment. (A) Pulse sequence for the ^{19}F off-resonance $R_{1\rho}$ experiment. Narrow rectangles indicate 90° pulses. The phase cycle is ϕ_1 = x, ϕ_2 = [-x,-x,x,x], ϕ_3 = [x,x,x,x,-x,-x,-x,-x,-x,y,y,y,y,-y,-y,-y,-y], ϕ_4 = [y,-y], ϕ_5 = [-y,y], ϕ_6 = [x,-x], ϕ_7 = [x], ϕ_8 = [x,-x], ϕ_{rec} = [x,-x,-x,x,x,y,-y,-y,y]. The flip-angle of pulses that flank the spinlock block is θ, which ensures that the magnetization is aligned at the angle of the effective magnetic field. This angle depends on the offset and the spinlock power. The pulse pairs with phases ϕ_7/ ϕ_8 are used to cycle the magnetization to $\pm$z before the spin lock period and back to +z after the spin lock, which ensures that the rotating frame relaxation is symmetrically measured both above and below the transverse plane at all offsets. (B) $R_{1\rho}$ off-resonance relaxation dispersion profiles and C) corresponding $R_2 + R_{ex}$ contributions for W7 at spin-lock fields of 100 Hz, 200 Hz, 300 Hz and 400 Hz. Solid lines show the best fit to a two-state Laguerre approximation. The offsets of the folded (F) and the unfolded (U) state are indicated with dotted lines. Errorbars show experimental uncertainty (one s.d.).

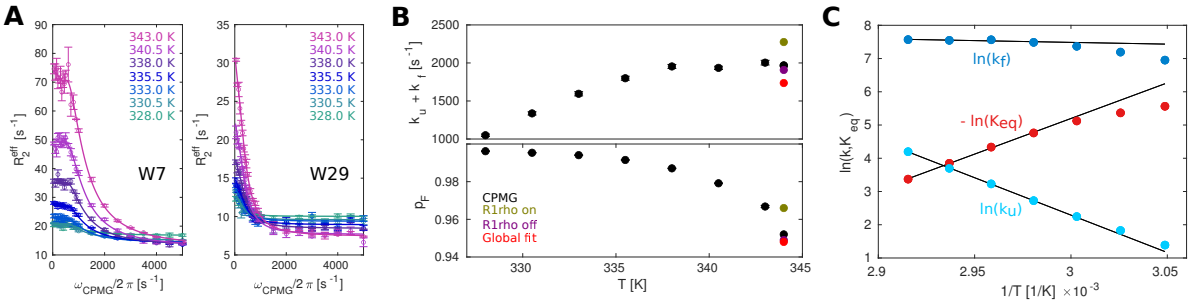

Figure 4.7.: Kinetic and thermodynamic analysis of the TmCsp folding. (A) CPMG curves with a global fit, assuming a constant chemical shift difference between the folded and the unfolded state across all temperatures (B) temperature dependence of exchange rates and populations from 328 K to 343 K. For comparison, the results from the experiments at 344 K are included (C) Temperature dependence of k_u, k_f and K_{eq} of 5FW-labeled TmCsp from 328 K to 343 K.

$T\Delta S^{\ddagger} = 39.2 \pm 1.2\,\text{kcal mol}^{-1}$ at 343 K. We note that the value of the transition path time barely affects the enthalpy of the transition state, but the entropic contribution is dependent on it and varies from $37.7 \pm 1.1\,\text{kcal mol}^{-1}$ for $\tau_{TPT} = 0.1\,\mu\text{s}$ to $40.9 \pm 1.3\,\text{kcal mol}^{-1}$ for $\tau_{TPT} = 10\,\mu\text{s}$.

Based on these findings a higher temperature prefers the unfolded state due to an entropic benefit. Likewise, but to a slightly lesser extent, a higher temperature reduces the free energy of the transition state. As a result, an increase in temperature results in a significantly increased energy barrier for the folding reaction, while the energy barrier for the unfolding rate is decreased but to a lesser degree. The consequence of this is that the folding rate (k_{U}) decreases with temperature equally fast as the unfolding rate increases. This leads to the counterintuitive situation where the folding-unfolding exchange rate ($k_{\text{ex}} = k_{\text{F}} + k_{\text{U}}$) is nearly constant between 335 K and 343 K (figure 4.7).

For high molecular weight systems, the R_2 relaxation rates will be significantly higher than the rates that we observed for TmCsp. In those cases, the CPMG relaxation time has to be shortened to such an extent, that the lower relaxation dispersion frequencies can no longer be sampled, which will hamper the faithful examination of dynamics. This limitation can be resolved with $R_{1\rho}$ experiments that are able to sample arbitrary frequencies between a lower limit given by scalar couplings and an upper limit given by the probe head power limits. To illustrate this we applied ^{19}F RD experiments to a 360 kDa double heptameric $\alpha_7\alpha_7$ complex (half proteasome) derived from the $\alpha_7\beta_7\beta_7\alpha_7$ 20S proteasome of Thermoplasma acidophilum (figure 4.8). The seven N-termini in each of

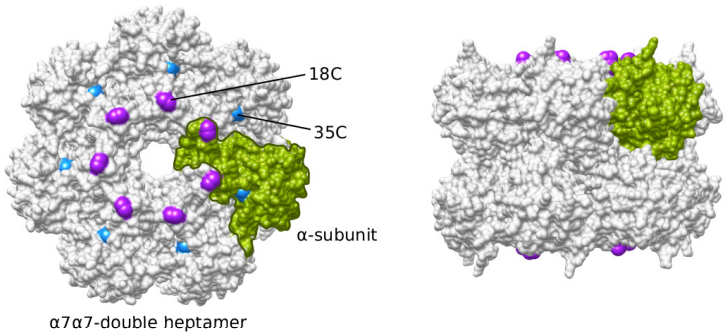

Figure 4.8.: Model of the double heptameric $\alpha_7\alpha_7$ complexes Model with 14 BTFA labeling sites at position 18C (purple) of each subunit. Position 35 that does not show exchange (figure A.6) is indicated in cyan. The model of the complex is based on the structure of the 20S proteasome from T. acidophilum (PDB ID 1PMA)

the two α-rings have been shown to sample conformations in- and outside of the ring pore, thereby forming a functionally important dynamic gate (Sprangers and Kay 2007, Religa et al. 2010). We introduced single cysteine mutations at positions 18 and 35 of the α-subunit and labeled the purified half proteasome with bromotrifluoroacetone (BTFA) to introduce a site specific ^{19}F probe. The sample with a cysteine at position 35, that is remote from the pore, showed a modest relaxation rate of 122 Hz and a flat CPMG curve (figure A.6). However, for the 18C-sample, we found that the single fluorine resonance at -84 ppm shows strongly temperature dependent peak widths between 161 Hz (293 K) and 88 Hz (323 K). To monitor the gate dynamics, we collected CPMG (figure 4.9A) and $R_{1\rho}$ (figure 4.9B) datasets at 293 K, 303 K, 313 K and 323 K. The constant time in the CPMG experiment had to be restricted to 4 ms at 293 K which results in CPMG frequencies that are multiples of 250 Hz. In the rotating frame relaxation experiments, on the other hand, we recorded 8 different $R_{1\rho}$ rates below 250 Hz, which provides essential information on the exchange process. Of note, the trifluoroacetone moiety lacks vicinal protons that couple to the ^{19}F spins and the largest scalar coupling present is a $^4J_{FH}$ coupling of around 1 Hz (Abraham et al. 1996) which eliminates the lower bound for the sampling of the frequencies. To extract exchange parameters, we simultaneously fitted the CPMG and $R_{1\rho}$ data at all temperatures with a two-state model, assuming that the $\Delta\omega$ between the ground state and the excited state is independent of the experimental temperature. Based on that, we unexpectedly observe that higher temperatures result in significantly slower exchange rates and increased populations of the ground state (figure 4.10A). In line with this, an Eyring plot of the rate constants k_1 and k_{-1} shows a linear decrease in $\ln(k)$ for both constants (figure 4.10B). These results arise from a negative entropy of the excited state ($T\Delta S = -10.1 \pm 3.0\,\mathrm{kcal\,mol^{-1}}$ at 313 K) as well as the transition state

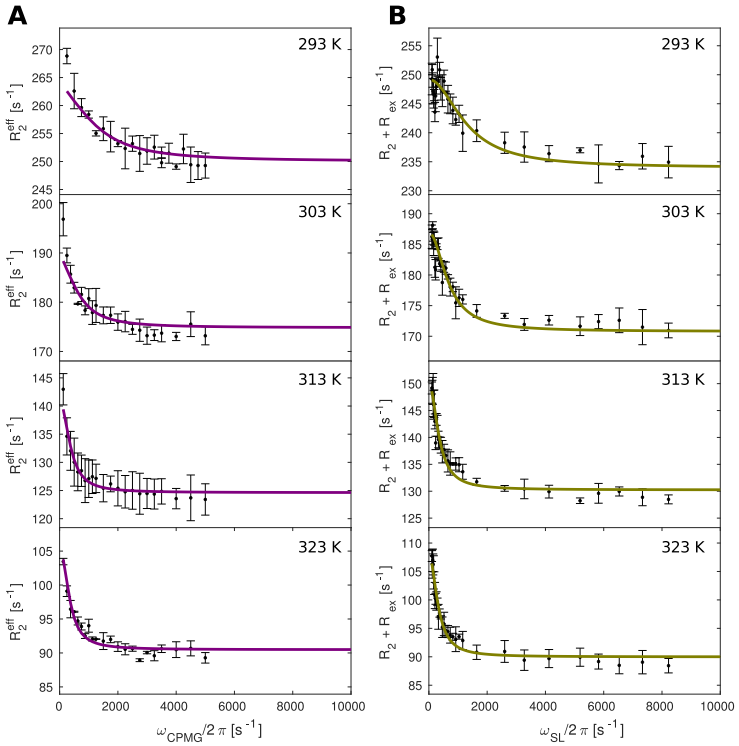

Figure 4.9.: ^{19}F relaxation dispersion experiments on the 360 kDa $\alpha_7\alpha_7$ double heptamer (A) CPMG experiments from 293 K to 323 K (B) On-resonance $R_{1\rho}$ experiments from 293 K to 323 K

($T\Delta S^{\ddagger} = -26.1 \pm 4.8$ kcal mol^{-1} at 313 K), which makes the excited state unfavorable at higher temperatures (figure 4.10C). Structurally, this behavior can be explained by a model where the N-terminal extensions are flexible in the open ground state and motionally restricted in the excited state where this region of the protein is located within the annulus pore (figure 4.10C).

4.4. Discussion and Conclusions

Taken together, we here present a suite of one-dimensional ^{19}F RD experiments, to study exchange processes in ^{19}F-labeled proteins. The on-resonance and off-resonance $R_{1\rho}$ pulse sequences provide a number of important advantages over the complementary CPMG RD experiments. First, the rotating frame experiments can make use of very low spin-lock fields, opening the possibility to obtain a full set of parameters at a single static magnetic field. The ability to sample arbitrary frequencies also allows study cases where the ^{19}F signals experience fast relaxation and where CPMG experiments are restricted to higher frequencies due to the requirement for very short (2-3 milliseconds) CPMG times

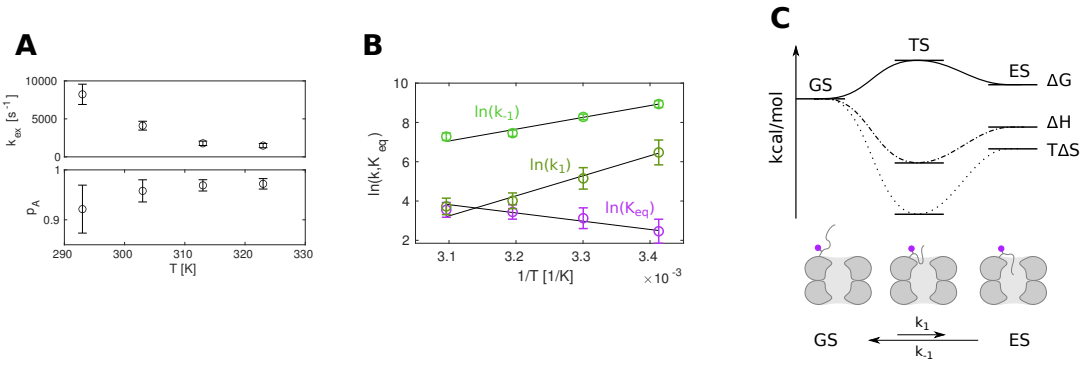

Figure 4.10.: Kinetic and thermodynamic analysis of the dynamic proteasome gate in the 18C^{BTFA} labeled half-proteasome (A) plot of exchange rates against temperatures as derived from the global fit of all RD data (B) logarithmic plot of kinetic rates against inverse temperature (C) Schematic presentation of ΔG, ΔH and $T\Delta S$ changes from the ground state GS to the excited state ES state via a transition state TS.

(Manglik et al. 2015). In this context it is noteworthy, that recent developments of two-dimensional (2D) ^{13}C-^{19}F TROSY experiments (Boeszoermenyi et al. 2019) make it attractive to collect relaxation dispersion data from a set of 2D experiments in cases where an extensive signal overlap in the fluorine dimension prevents the reliable analysis of dispersions from 1D spectra. The new pulse sequences benefit from a TROSY effect based on partial cancellation of relaxation contributions from the chemical shift anisotropy and dipole-dipole relaxation. The ^{19}F transverse relaxation nevertheless remains on the order of $200 - 1000\,\mathrm{s}^{-1}$, depending on the fluorinated amino acid and the field strength. Thus, the inclusion of an $R_{1\rho}$ instead of an CPMG element should again be advantageous. Since the TROSY effect is much more accentuated in the ^{13}C transverse relaxation, another option might be to use the carbon itself as a probe for dynamics, which is less sensitive in terms of chemical shift perturbations by structural changes, but would allow longer relaxation periods. Second, compared to CPMG RD experiments, the rotating frame approaches can expand the timescale of chemical exchange that is accessible to very fast (µs timescale) processes. Third, the off-resonance $R_{1\rho}$ experiments provide important information on the sign of the chemical shift differences, which provides direct information on the nature of the excited state.

We anticipate that fluorine NMR methods will become increasingly popular. Indeed, studies in the recent years have shown first examples of its applicability to challenging systems including GPCRs, where the possibilities for protein deuteration and methyl group labeling are limited due to the requirements of eukaryotic expression systems. Proteins from these sources can, however, be labeled with trifluoromethyl groups in a

straightforward posttranscriptional manner at very low costs. The very short experimental times of the ^{19}F based 1D experiments will further increase the applicability to systems that are not stable over time and where time intensive ^{13}C, ^{15}N or ^{1}H based RD are not feasible. In the case of our model system TmCsp, the use of ^{19}F RD approaches stood to reason by enhanced amide-proton exchange rates at our experimental conditions, a problem which is generally encountered at elevated temperatures or high pH and which significantly deteriorates the quality of standard ^{1}H-^{15}N based experiments. Finally, recent advances in labeling techniques have made RNA and DNA accessible for ^{19}F NMR (Sochor et al. 2016, Baranowski et al. 2020), thereby further expanding the applicability of the presented methodologies. In summary, our approach will strengthen the use of ^{19}F NMR to accurately quantify dynamic processes in a broad range of biological systems. The applicability of this strategy will benefit from the ^{19}F capabilities of many modern NMR probe-heads.

5. Investigating conformational changes that underlie the catalytic cycle of the 5′-3′ exoribonuclease Xrn2

The results of this chapter are in preparation for publication, the chapter is therefore largely identical to the manuscript in both text and figures. Jan H. Overbeck and Remco Sprangers designed experiments. J.H.O. performed experiments, analyzed and interpreted data. David Stelzig measured turnover rates, Anna-Lisa Fuchs helped with solving the crystal structure of Xrn2 and Jan-Philip Wurm helped with recording and analyzing NMR data and with the NMR structure calculations. J.H.O. and R.S. wrote the manuscript.

5.1. Summary

The development of nuclear magnetic resonance (NMR) methods that quantitatively probe motions on the molecular and atomic level has propelled the understanding of biomolecular processes for which static structures cannot provide a satisfactory description. Here we study the structure and dynamics of the essential 100 kDa eukaryotic 5′-3′ exoribonuclease Xrn2. A combination of complementary fluorine and methyl-TROSY NMR spectroscopy reveals that the apo enzyme is highly dynamic around the catalytic center. These observed dynamics are in agreement with a transition of the enzyme from the ground state into a catalytically competent state. We show that the conformational equilibrium in Xrn2 shifts significantly towards the active state in the presence of substrate and magnesium. Finally, our data reveal that the dynamics in Xrn2 correlate with the RNA degradation rate as a mutation that attenuates motions also impacts catalytic activity. In that light, our results stress the importance of studies that go beyond the description of static structural information.

5.2. Introduction

5′-3′ exoribonucleases are essential enzymes that processively remove nucleotides from the 5′ end of an RNA. In the nucleus, this process is carried out by the exoribonuclease Xrn2 (also called Rat1), which is important for the removal of aberrant pre-mRNAs (Davidson et al. 2012) but also plays pivotal roles in rRNA maturation and rRNA decay (Henry et al. 1994, Geerlings et al. 2000, Wang and Pestov 2011, Gasse et al. 2015), processing of small nucleolar RNA (snoRNA) (Petfalski et al. 1998, Qu et al. 1999, Lee 2003), transcription termination (West et al. 2004, Kim et al. 2004) telomere length regulation (Luke et al. 2008) and the degradation of miRNAs (Chatterjee and Großhans 2009) and hypomodified tRNAs (Chernyakov et al. 2008). This multitude of cellular functions is mirrored in the observation, that the Xrn2 gene is essential in lower eukaryotes such as *S. cerevisiae* (Amberg and Goldstein 1992, Kenna 1993) and *S.pombe* (Shobuike 2001, Sugano et al. 1994) and in *C.elegans* development (Miki et al. 2014b).

The molecular basis of RNA degradation by Xrn2 and its cytoplasmic paralogue Xrn1 has been established by a number of structural and functional studies. Both enzymes are highly selective for substrates with exposed 5′-phosphorylated ends and require divalent cations (Mg^{2+}, Mn^{2+}) to catalyze the hydrolysis of phosphodiester bridges (Stevens and Poole 1995, Langeberg et al. 2020). The Xrn1 enzymes are highly processive and remove tens of nucleotides per second from the substrate (Stevens 1980, Xiang et al. 2009, Chang et al. 2011, Jinek et al. 2011, Hoek et al. 2019). The combination of processivity and speed is biologically important, as it enables Xrn1 to closely follow ribosomes in co-translational mRNA decay (Hu et al. 2009, Antic et al. 2015, Pelechano et al. 2015, Tesina et al. 2019) and allows Xrn2 to chase RNA polymerase II in co-transcriptional RNA degradation after cleavage of the pre-mRNA at the polyadenylation signal (Eaton and West 2020). Notably, DNA can also be processed by Xrn1 and Xrn2, albeit at a strongly attenuated rate (Stevens and Poole 1995, Page et al. 1998, Solinger et al. 1999).

On a structural level, Xrn1 and Xrn2 share two conserved regions, designated CR1 and CR2, and a less conserved C-terminal segment (CTS) which together form the XRN core domain (Xiang et al. 2009, Jinek et al. 2011, Chang et al. 2011) (figure 5.1). This Xrn core domain harbors the catalytic site, which has three crucial features: First, a set of seven conserved acidic residues mediates the coordination of two divalent cations that are important for catalysis and substrate binding (Page et al. 1998, Solinger et al. 1999, Xiang et al. 2009, Chang et al. 2011, Jinek et al. 2011). Second, an adjacent basic binding pocket is responsible for the selective recognition of the 5′ phosphate of the substrate (Jinek et al. 2011). This pocket thereby rationalizes the finding that neither unphosphory-

lated (no recognition) nor 5′-triphosphorylated or 5′-capped RNAs (steric hindrance) are substrates of Xrn1 or Xrn2. As a third feature, two conserved residues (one histidine and one tryptophan), sandwich the aromatic rings of the first three nucleotides of the substrate in an extensive base stack. Especially the substrate interactions with the histidine contributes to the processivity of the enzyme (Jinek et al. 2011).

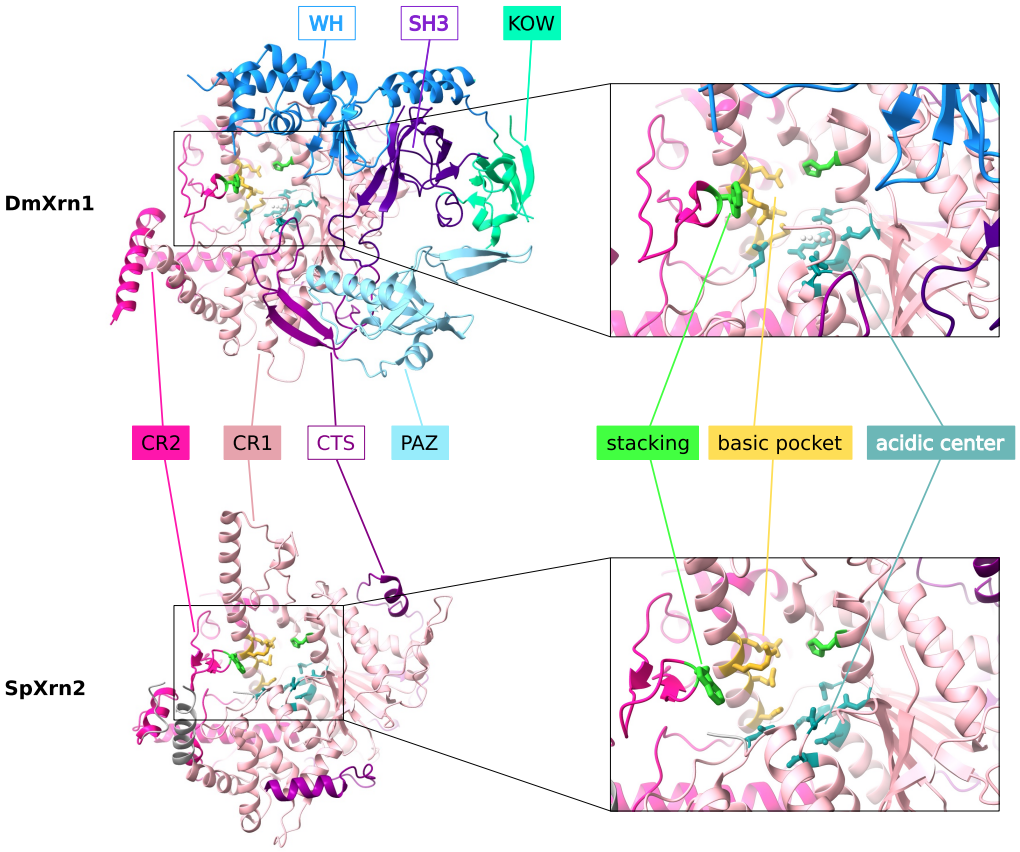

Figure 5.1.: Structure of Xrn1 from D. melanogaster (DmXrn1; PDB: 2Y35) and Xrn2 fom S. pombe (SpXrn2; PDB: 3FQD) with highlighted domains and features Xrn1 and Xrn2 share a conserved exoribonuclease core formed by the conserved regions 1 (CR1, salmon) and 2 (CR2, pink) are completed by a less-conserved C-terminal segment (CTS, purple). In the active site, both Xrn1 and Xrn2 have a conserved acidic magnesium binding site, a basic pocket that recognizes the monophosphorylated 5′-end of the RNA substrate (yellow) as well as a conserved His-Trp pair which sandwiches the substrate by aromatic stacking (green). In addition, Xrn1 features a folded C-terminal region composed of a PAZ domain (cyan), a Kyprides-Ouzounis-Woese (KOW) domain (lime), an SH3 domain (dark purple) and a winged helix (WH) domain (blue). The far C-terminal region of Xrn1 and Xrn2 is disordered, poorly conserved and not displayed here.

This static view of the enzyme:substrate complex has been expanded by the comparison of two structures that display Xrn1 in different states during the catalytic cycle (figure 5.2). First a crystal structure of the *D. melanogaster* Xrn1 enzyme in complex with a pseudosubstrate DNA displays the enzyme in a post-translocation, pre-hydrolysis metastable state. This state was stabilized by an inactivating mutation that disturbed Mg^{2+} binding as well as by the missing 2′-hydroxyl group in the substrate (Jinek et al. 2011). A second snapshot of the catalytic cycle was provided by a cryo-EM structure of *S. cerevisiae* Xrn1 stably bound to a stalled ribosome and in the presence of an mRNA substrate. In this latter structure the $\pi - \pi$ stack of the first three bases could be observed, but at the same time the terminal 5′-phosphate had yet to be translocated to the basic pocket (Tesina et al. 2019). This state was thus interpreted as a post-scission / pre-translocation state. Based on those two snapshots, it was noted that substantial conformational changes accompany the substrate translocation step, with a particularly pronounced rearrangement taking place at the very N-terminus of Xrn1 (Tesina et al. 2019). This amino-terminal α1-helix is functionally important as it has been postulated to constitute a steric hindrance for other than single-stranded substrates (Jinek et al. 2011) and as deletion of the first four residues results in reduced catalytic activity (Chang et al. 2011). Although no structural data has been reported for Xrn2 in a substrate-bound state, the conservation of CR1 and CR2 between Xrn1 and Xrn2 make it plausible, that both enzymes share a common molecular mode of action, in which the N-terminal helix can accommodate at least two functionally important conformations.

Here, we study the interplay of structure, function and dynamics of a 100 kDa Xrn2 core construct and address whether the N-terminal helix displays functionally relevant dynamics in solution. In brief, we combine X-ray crystallography with NMR relaxation dispersion measurements on $^{13}CH_3$ and ^{19}F labeled Xrn2 samples. We find that the N-terminal region of Xrn2, samples an excited state that resembles the pre-hydrolysis substrate-bound state. The functional relevance of the observed helix dynamics is emphasized by a mutant enzyme in which both the motions and catalytic activity of Xrn2 are reduced.

5.3. Results

5.3.1. Chaetomium thermophilum Xrn2 adopts a 5′-3′ exoribonuclease structure

High resolution NMR studies that address protein dynamics require isotope labeled samples that are stable over multiple days at protein concentration in the high µM range.

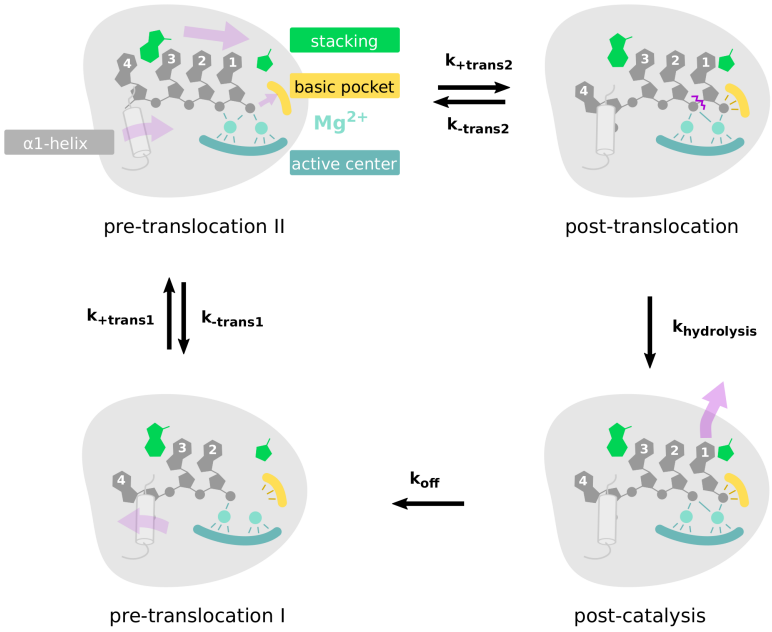

Figure 5.2.: Model of the translocation-hydrolysis mechanism in Xrn1/Xrn2 The enzyme interacts with the RNA substrate, in which the first three nucleotides are stacked between the conserved His/Trp residues (top left; pre-translocation II). Due to a conformation change (k_{trans2}) the RNA is translocated to a hydrolysis-prone position (post-translocation; top right), where hydrolysis can take place. After hydrolysis ($k_{\text{hydrolysis}}$) the bond between the terminal 5′ nucleotide and the RNA body is cleaved (post-catalysis; bottom right). Subsequently, the cleaved 5′ nucleoside monophosphate is released (k_{off}; pre-translocation I; bottom left). Finally, the conserved tryptophan residue shovels the next base into the aromatic stack (green) and brings the enzyme substrate complex into the pre-translocation II position (top left). Structures of the Xrn enzyme in the pre-translocation state II (Xrn1 in the complex with mRNA within the 80S ribosome-Xrn1 complex) as well as in the post-translocation state (Xrn1 in complex with a 5′-phosphorylated 11-mer DNA oligonucleotide) have been solved. The N-terminal α1-helix has been suggested to function as a brownian in the substrate translocation process.

Obtaining such samples is often a bottleneck for advanced NMR experiments, especially for large eukaryotic enzymes. Here, we found that the Xrn2 core from the thermophilic yeast *C. thermophilum* (CtXrn2; residues 1-875; molecular weight of 100 kDa; figure 5.3) fulfills those conditions. In order to lay the structural foundation for our NMR experiments, we first crystallized wild-type CtXrn2 and obtained crystals that diffracted up to a resolution of 3.0 Å. The structure of the enzyme (figure 5.3B) was determined based on the molecular replacement approach where the Xrn2 structure from *S. pombe* (Xiang et al. 2009) was used as a search model (Table 5.1). In agreement with the high sequence similarity between Xrn2 enzymes from different species, we found that the CtXrn2 structure closely resembles the structures of Xrn2 from *S. pombe* (Xiang et al. 2009) and *C. elegans*

(Richter et al. 2016). In addition the CtXrn2 structure is similar to the structures of the Xrn1 paralogues from *D. melanogaster* (Jinek et al. 2011), *K. lactis* (Chang et al. 2011) and *S. cerevisiae* (Tesina et al. 2019) (figure A.7).

The active site of the enzyme is positioned in a pocket in front of the 'tower' domain helix (helix α4) (figure 5.3B). Seven acidic residues (D55, D104, E209, E211, D239, D241 and D351) provide a coordination platform for the two catalytically important Mg^{2+} ions (figure 5.3C). Furthermore, we find that His61 and Trp706 are correctly positioned above the active site to form a continuous $\pi - \pi$ stack with the RNA substrate, as has been observed for Xrn1 in complex with the a pseudosubstrate DNA (Jinek et al. 2011) and the mRNA substrate in the context of a stalled ribosome (Tesina et al. 2019) (figure A.8).

5.3.2. Chaetomium thermophilum Xrn2 contains a functional Zinc Finger (ZnF)

In our structure of the CtXrn2 enzyme, electron density was lacking for the three regions: i) the top of the tower domain (residues 135-158) that is also less well defined in other Xrn2 structures, ii) the linker region between CR1 and CR2 (residues 423-568) that is highly flexible in solution, as can be judged from ^{1}H-^{15}N NMR spectra (figure A.9) and iii) a for short loop between residues 266 and 304 that harbors a putative CCHC zinc finger (ZnF) motif.

Such a CX2CX4HX4C ZnF motif (where C, H and X correspond to a cysteine, a histidine and any amino acid respectively) is present in Xrn2 homologues from higher eukaryotes (figure 5.3), including *C. elegans*, where it was deleted from the crystallization construct (Richter et al. 2016), and in a limited number of yeast species (e.g. *N. crassa* and *A. fumigatus*). The ZnF is, however, missing in Xrn2 homologues from Ascomycota (inluding *S. pombe* (Xiang et al. 2009) and *S. cerevisiae*) and is also generally absent in Xrn1. To obtain insights into the functional importance of the Xrn2 ZnF, we here solved the NMR structure of this region (*C. thermophilum* Xrn2 residues 265-293) (figure 5.3E). The structural ensemble (figure A.10) displays a well-defined core (residues 269-284) that is highly similar to other ZnFs, that are known to interact with (ribo-)nucleotides (figure A.11). In the context of the full-length protein (figure 5.3B) the ZnF finger is anchored close to the active site, (figure 5.3B), which prompted us to determine if the CtXrn2 ZnF is functionally important for substrate recruitment and/or turnover.

To test this, we first measured the binding affinity of short 5mer and 10mer RNAs to

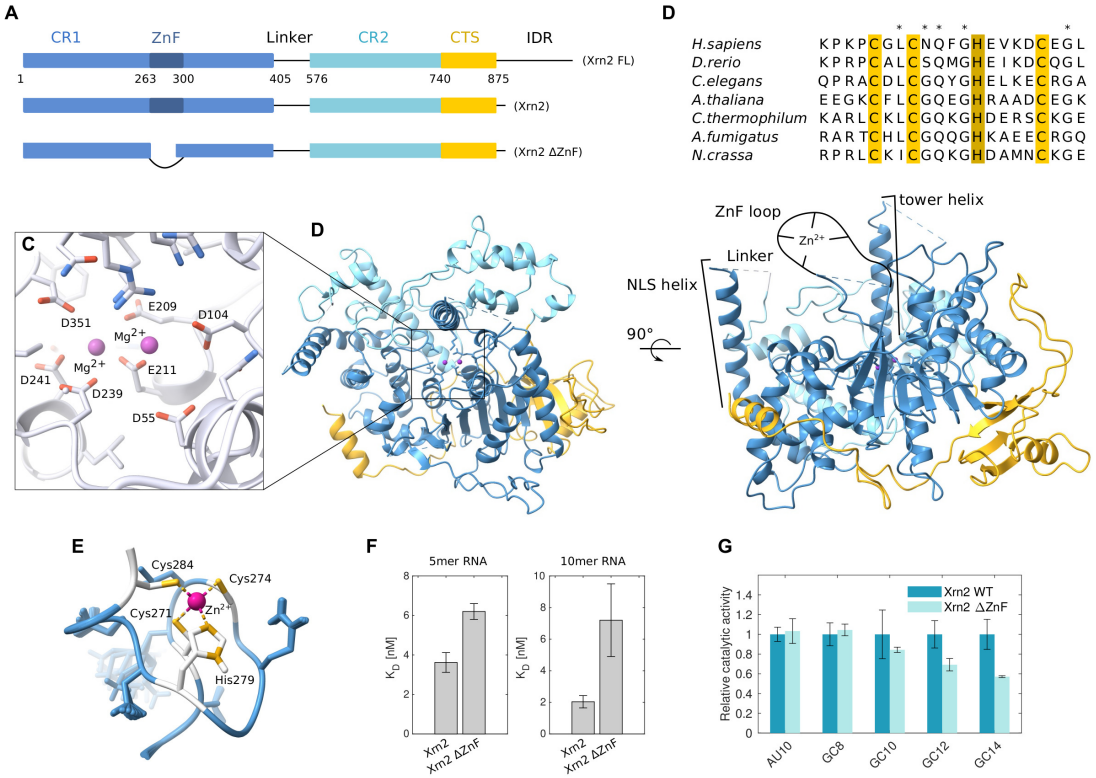

Figure 5.3.: Structure of the Xrn2 enzyme from the thermophilic eukaryote Chaetomium thermophilum (A) Schematic representation of the domain architecture of the full length Xrn2 protein (top) and two constructs (Xrn2: middle; Xrn2 ΔZnF: bottom) used in this study. Solid boxes represent folded regions, the linker region and the C-terminal intrinsically disordered region (IDR) are predicted to be unstructured and represented as lines. (B) Crystal structure of CtXrn2, color-coded according to (a). The conserved regions CR1 and CR2 together with the Xrn2-specific C-terminal segment (CTS) form a globular Xrn-core, in which the active site is accessible only from the top. (C) Close-up of the active site, where seven conserved acidic residues (shown as sticks) coordinate two Mg^{2+} ions. (D) Sequence alignment of the zinc Xrn2 finger motif. The residues that coordinate the Zn^{2+} ion are highlighted in yellow (cysteines) and brown (histidine), additional residues with partial conservation are indicated with an asterisk. (E) NMR structure of the zinc finger region. (F) Affinities of 5mer and 10mer RNA to Xrn2 to wild type Xrn2 and Xrn2 ΔZnF. Note that the binding experiments were preformed in the absence of Mg^{2+} and in the presence of Zn^{2+}. (G) Relative reaction rates of Xrn2 WT and Xrn2 ΔZnF for RNAs (table A.1) containing either a 10 nucleotide AU hairpin (AU10) or GC hairpins with 8, 10, 12 or 14 nucleotides (GC8, GC10, GC12, GC14).

Xrn2 and found that these substrates bind with low nanomolar affinities (figure 5.3F). These experiments were recorded in the absence Mg^{2+} such that rapid degradation of the RNA substrate during the measurements is prevented. We next "inactivated" the ZnF by using an Xrn2 ΔZnF construct, which lacks residues 263-300. This decreased the dissociation constant K_D by a factor of 1.5 (5mer) to 3 (10mer), corresponding to a small free energy contribution of $\Delta G < 2.7\,\mathrm{kJ\,mol^{-1}}$ at room temperature (figure 5.3F). Secondly,

we investigated if the ZnF plays a role for Xrn2 activity. To that end, we compared the degradation rates of the Xrn2 wild type (WT) protein with a version of the enzyme that lacks the ZnF. As the importance of the ZnF might depend on the extend of secondary structure in the substrate we performed degradation assays using five RNA substrates with different stem-loop stabilities (figure 5.3G). We found that RNAs with a stem-loop of low stability were degraded with similar rates in the presence or absence of the ZnF. For RNAs that contain increasingly stable stem-loop elements, we found that the deletion of the zinc finger decreased the relative degradation rate accordingly. Based on the above, we conclude, that the ZnF in Xrn2 plays a functionally important role in RNA binding and that it promotes the degradation of structured RNA substrates.

5.3.3. Free Xrn2 displays structural dynamics in solution

Structures from the Xrn2 paralogue Xrn1 indicate, that the N-terminal α1-helix adopts different conformations in the apo and substrate-bound states and that the associated motions are correlated with translocation of the RNA substrate towards the active site (figure 5.2) (Jinek et al. 2011, Tesina et al. 2019). The α1-helices from Xrn2 and Xrn1 are similar, both on a sequence and on a structural level (figure 5.4), where it should be noted that the electron density for the first residues is less well defined in all Xrn1 and Xrn2 crystal-structures in the apo-state. Although there is no direct structural data for substrate-bound Xrn2, we reasoned, that both Xrn2 and Xrn1 undergo a similar conformational change upon substrate binding and through the catalytic cycle. In this process, the N-terminal α1-helix has been suggested to function as a brownian ratchet (figure 5.2) (Jinek et al. 2011).

To elucidate these and other structural dynamics in Xrn2 we turned to methyl-TROSY NMR spectroscopy. Spectra of Ileδ1-[$^{13}CH_3$] and Metε-[$^{13}CH_3$] methyl labeling Xrn2 samples are of very high quality, especially for a 100 kDa single chain protein (figure 5.5). Based on NMR spectra of 46 Xrn2 samples that each lack a single methyl group, we assigned M704 as well as 38 of the 48 isoleucine resonances (table A.4). At 313 K, a subset of the isoleucine probes showed substantial peak broadening and could only be partially assigned at a lower temperature of 293 K (figure 5.5B and figure A.12). Importantly, we noted that the resonances that broaden at higher temperature cluster around the α1-helix, which indicates the existence of a substantially populated excited state (ES) of the protein in addition to the mainly populated ground state (GS) for this part of Xrn2. In order to verify this hypothesis, we recorded methyl group single-quantum (SQ) and multiple-quantum (MQ) Carr-Purcell-Meiboom-Gill (CPMG) relaxation dispersion (RD)

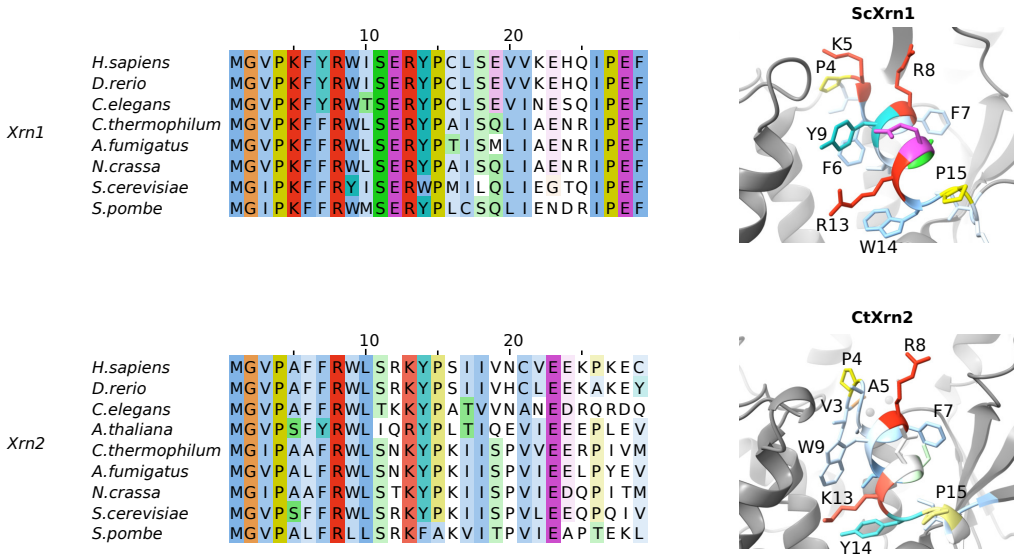

Figure 5.4.: Sequence alignments of Xrn1 and Xrn2 homologues and close-up view of the α1-helix in the ScXrn1 and CtXrn2 structures The N-termini of Xrn1 and Xrn2 are conserved from lower to higher eukaryotes (from *S. pombe* and *S. cerevisiae* to *D. rerio* and *H. sapiens*) and are similar to each other in sequence and structure. Notable differences include the presence of a positively charged residue (Lys) at position 5 and a negatively charged residue (Glu) at position 12 in Xrn1.

experiments at proton Larmor frequencies of 500, 600 and 800 MHz (figure A.14). These experiments can be used to quantify motions for which the lifetime of the excited state is on the order of milliseconds. We found strong relaxation dispersions in a number of peaks that surround the α1-helix and could fit all six datasets (MQ and SQ datasets from three field strengths) from five probes (Ile59, Ile89, Ile235, Ile850 and Ile853) simultaneously with the same exchange parameters $p_{ES} = 18.1 \pm 6.2\,\%$ and $k_{ex} = 710 \pm 63\,s^{-1}$ (where p_{ES} is the population of the ground state and k_{ex} is the exchange rate) (figure 5.5 and figure A.13). Taken together, we here establish that the α1-"ratchet"-helix of Xrn2 samples multiple states in solution in the absence of a substrate.

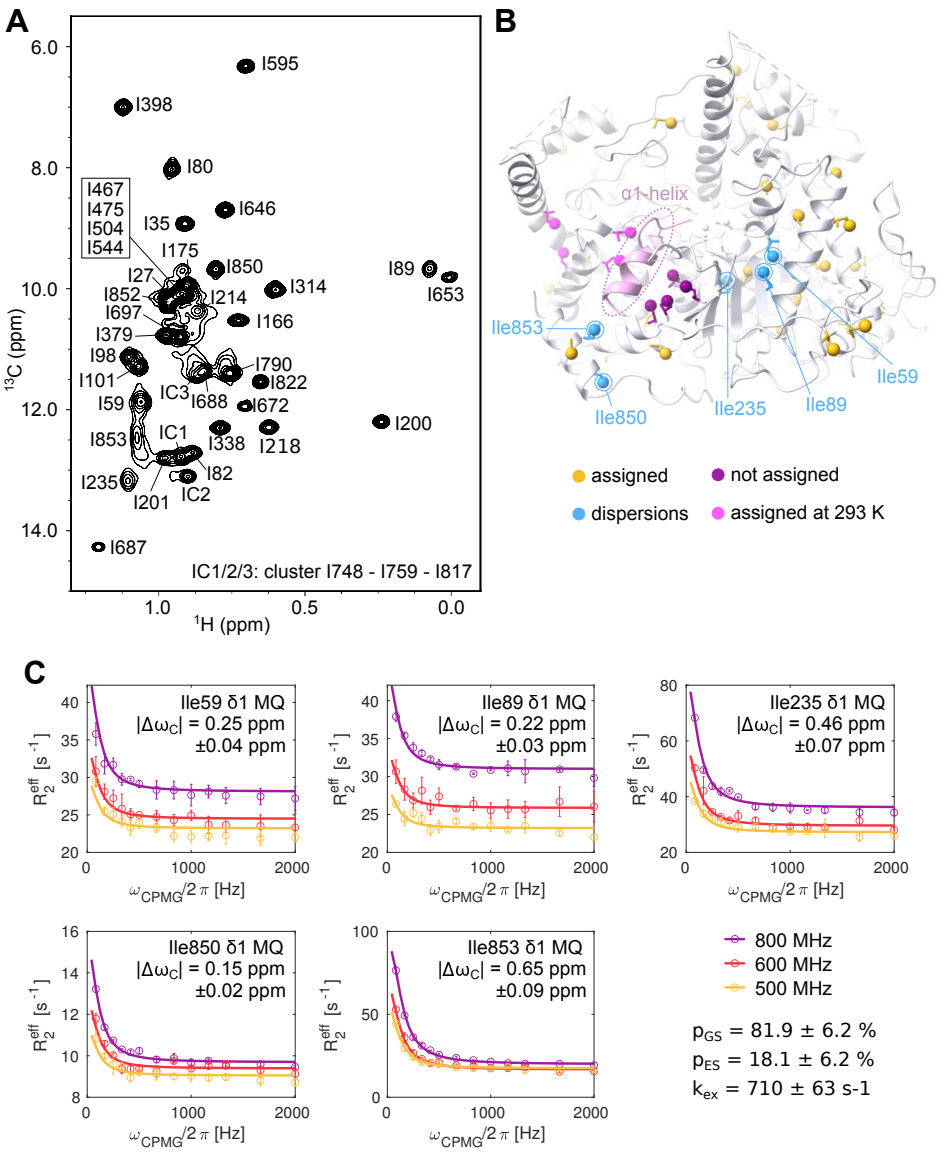

Figure 5.5.: Methyl-TROSY NMR reveals conformational dynamics located around the N-terminal α1-helix (a) ^{1}H-^{13}C HMQC methyl-TROSY spectrum of U-2H, Ile-δ1 labeled CtXrn2 recorded at 18.8 T (800 MHz 1H frequency) and 313 K with assignments. Isoleucines I467, I475, I504 and I544 are located in the flexible linker between CR1 and CR2 and were assigned by comparison of HMQC spectra from the CtXrn2 WT protein and a CtXrn2 ΔLinker construct. Isoleucines I748, I759 and I817 are in close spatial contact and lead to reciprocal chemical shift perturbations upon mutation, their isoleucine cluster (IC) was assigned to three peaks. The double resonances of I59, I89, I235 and I853 δ1-methyl groups show visible peak broadening. (b) Distribution of Isoleucine residues in the Xrn2 protein. Ile-δ1 probes are represented as spheres, where assigned probes are coloured yellow and unassigned probes are coloured purple. Residues I59, I89, I235, I850 and I853 showed relaxation dispersion, their position is explicitly indicated. I59 and I89 are in close proximity and situated above the central β-sheet opposite of I235. I850 and I853 are located in the C-terminal helix of Xrn2, with I853 directly opposite of Y14 at the rear side of the α1-helix. (c) MQ CPMG relaxation

dispersion profiles measured at 313 K and 11.7 T (500 MHz 1H frequency, yellow), 14.1 T (600 MHz 1H frequency, red) and 18.8 T (800 MHz 1H frequency, purple) as described in the methods. Data points are shown with errorbars derived from multiple measurements, the curve corresponds to the best fit of the joined analysis of MQ CPMG and 13C-SQ CPMG data from all five residues.

5.3.4. Fluorine NMR provides an independent measure of α1-helix dynamics

The methyl-TROSY CPMG RD experiments provided accurate information with a high spatial resolution. The drawback of those experiments is, however, the extended measurement time that is required to record full datasets (> 1 week). This prevents the performance of NMR measurements in the presence of substrates, as these would be turned over before the acquisition of the data is finished. Recently, we have shown that ^{19}F RD data can be recorded in significantly less time and that this approach can provide accurate insights into biomolecular exchange processes. NMR active ^{19}F groups can be conveniently introduced post-translationally through e.g. the labeling of cysteine sidechains with trifluoromethyl-containing electrophiles (Brauer and Sykes 1986, Liu et al. 2012, Manglik et al. 2015, Overbeck et al. 2020). Here, we introduced a cysteine in CtXrn2 at position 12, that is located at the end of the α1-helix and that is exposed on the surface (figure 5.6). To prevent the labeling of other cysteine residues, we made use of the Xrn2 construct that lacks the ZnF (that contains three highly accessible cysteine residues; figure A.15) and bromotrifluoroacetone (BTFA) labeling times that are sufficiently short such that the other four cysteine residues in Xrn2 (Cys63, Cys184, Cys345 and Cys620) are not labeled.

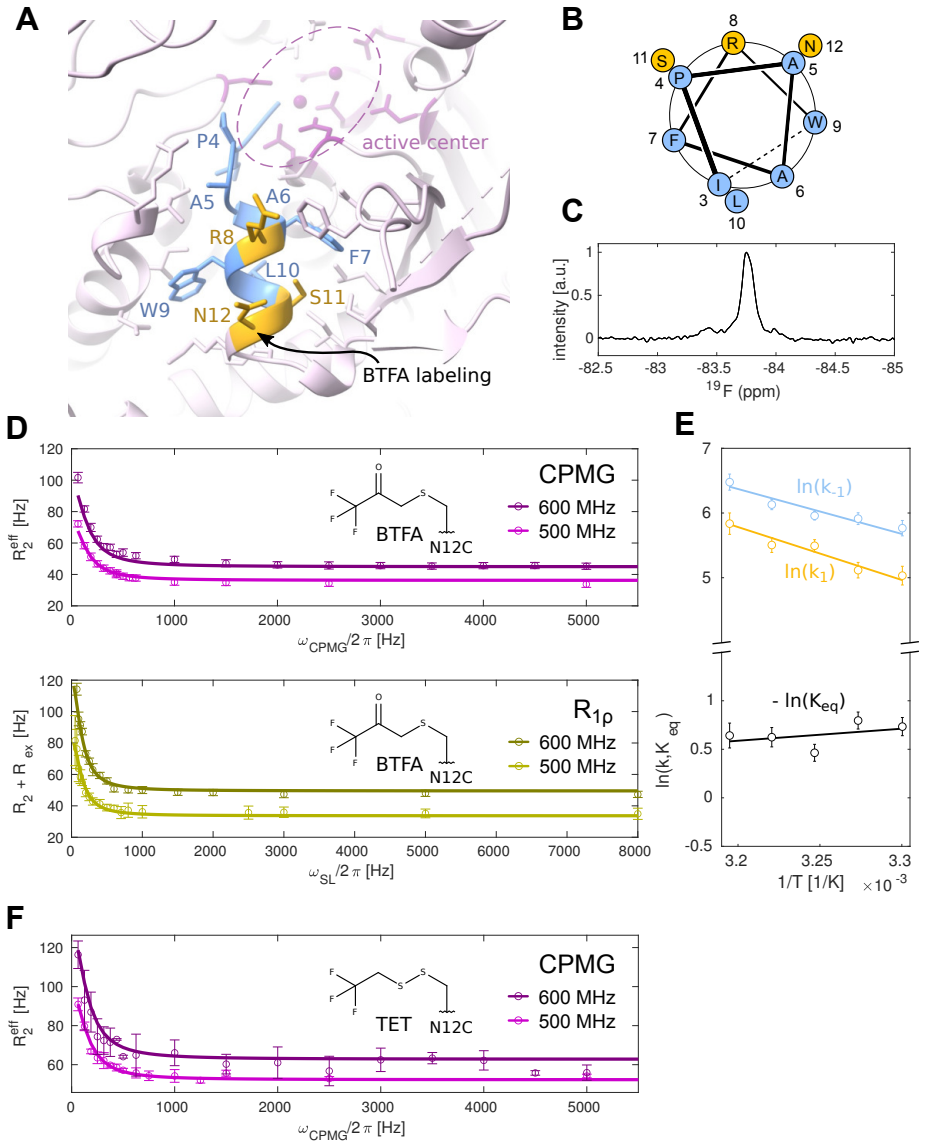

Figure 5.6.: ^{19}F NMR supports the sampling of an excited conformational state by the α1-helix (A) Close-up view of the α1-helix, where the mutation N12C was introduced at the rear side of the helix to allow for BTFA labeling. Hydrophobic residues are shown in blue, charged and polar residues are shown in yellow. (B) Helical wheel projection for residues 3 to 12 in the α1-helix. Coloring as in A. (C) ^{19}F spectrum of Xrn2 ΔZnF N12C^{BTFA}. (D) CPMG and on-resonance $R_{1\rho}$ dispersion profiles for Xrn2 ΔZnF N12C^{BTFA} samples recorded at 11.7 T (500 MHz 1H frequency) and 14.1 T (600 MHz 1H frequency) at 313 K. Datapoints are shown with errorbars derived from multiple measurements, lines show the best fit derived from the simultaneous analysis of all datasets from five temperatures with one global $\Delta\omega$. (E) Logarithmic plot of the exchange rates k_1 ($= k_{GS\rightarrow ES}$) and k_{-1} ($= k_{ES\rightarrow GS}$) , where $k_1 + k_{-1} = k_{ex}$) and the equilibrium constant $K_{eq} = k_1/k_{-1}$ against the inverse temperature. (F) CPMG dispersion profiles of Xrn2 ΔZnF N12C^{TET} at 11.7 T (500 MHz 1H frequency) and 14.1 T (600 MHz 1H frequency) at 313 K. The data was fit with the population $p_{GS} = 65.5\,\%$ and the exchange constant $k_{ex} = 992\,s^{-1}$ obtained from analysis of the BTFA data.

Based on the resulting 1-dimensional ^{19}F NMR spectra (figure 5.6), we recorded CPMG and on-resonance $R_{1\rho}$ relaxation dispersion data at ^{1}H Larmor frequencies of 500 MHz and 600 MHz and at five temperatures between 303 K and 313 K (figure 5.6 and figure A.16). For all temperatures, we observed strongly enhanced effective transverse relaxation rates at CPMG/spin lock-frequencies below 500 Hz. We fit all datasets simultaneously with a single global chemical shift difference parameter $|\Delta\omega_F|$ and temperature-dependent parameters for excited state populations $p_{\mathrm{ES}}^{\mathrm{temp}}$, exchange rates $k_{\mathrm{ex}}^{\mathrm{temp}}$ and transverse relaxation rates $R_2^{\mathrm{temp,field}}$ and determined the fit parameter uncertainties by Monte Carlo simulations (figure A.17). For the global chemical shift difference we obtained $|\Delta\omega| = 0.15 \pm 0.01$ ppm. From 303 K to 313 K, the exchange rate increase linearly from $472 \pm 52\,\mathrm{s}^{-1}$ to $992 \pm 104\,\mathrm{s}^{-1}$, while the population of the excited state stays approximately constant around 35 % over the observed temperature range. We note that separate fits of only the CPMG data or only the on-resonance $R_{1\rho}$ data result in populations and chemical shift difference that are less well defined (figure A.17). In summary, the ^{19}F RD data independently highlights that the N-terminal α1-helix in Xrn2 is involved in an exchange process. The exchange parameters at 313 K (k_{ex}, p_{ES}) that we extract from the ^{19}F data and from the methyl-TROSY data at 313 K are compatible ($k_{\mathrm{ex}}^{\mathrm{CH3}} = 710 \pm 63\,\mathrm{s}^{-1}$ and $k_{\mathrm{ex}}^{\mathrm{19F}} = 992 \pm 104\,\mathrm{s}^{-1}$) and within a factor of 2 ($p_{\mathrm{ES}}^{\mathrm{CH3}} = 18.1 \pm 6.2$ % and $p_{\mathrm{ES}}^{\mathrm{CH3}} = 34.5 \pm 4.4$ %). We attribute these deviations in the exchange equilibrium to the introduced ^{19}F label that can cause small shifts in the conformational equilibrium. This notion is corroborated by measurements on samples where the ^{19}F label has been positioned at other sites close to the N-terminal helix (position R8C or R362C), that also showed very clear RD profiles with slightly different exchange parameters (figure A.18). Importantly, a control experiment where the ^{19}F label is positioned at position V416, displays no sign of dynamics (figure A.17). It is, however, important to note that ^{19}F RD dispersion profiles that we record for a specific position are the same for BTFA and TET labeled enzymes (figure 5.6). Together, these aspects further enforce the notion that our ^{19}F RD profiles directly report on motions in the enzyme. In brief, we have established that ^{19}F NMR measurements are suitable for detecting dynamic processes of the region around the active site in Xrn2.

5.3.5. Substrate binding induces a change in the Xrn2 structure and dynamics

The fast degradation of RNA by Xrn2 hinders the NMR characterization of a complex of Xrn2 with an RNA substrate. In order to investigate the structural changes that occur in Xrn2 upon substrate interaction, we here used three substrates with strongly attenuated degradation rates: 3′,5′-bisphosphoadenosine (pAp), a 5mer DNA substrate and an exoribonuclease-resistant RNA (xrRNA) (Akiyama et al. 2016). It is important to note

that we focus on interaction studies that use catalytically active wild-type (WT) Xrn2 as versions of the enzyme that lack the catalytically important magnesium ions also likely display altered interactions and/ or motions.

First, we used pAp, which is a byproduct of the assimilatory sulfate reduction pathway and a second messenger in plants (Pornsiriwong et al. 2017) and which has been identified as an inhibitor of 5′-3′ exoribonucleases in yeast (Dichtl 1997). Here, we observe that pAp is slowly hydrolyzed to adenosine 5′-monophosphate (AMP) by Xrn2 at a rate of $0.05\,\mathrm{min}^{-1}$ (figure 5.7). Based on this slow turnover we could measure HMQC spectra of Ileδ1-[$^{13}CH_3$]-labeled Xrn2 in the presence of an excess of pAp (figure 5.7). The binding of pAp to Xrn2 resulted in significant chemical shift perturbations (CSPs) of the methyl group resonances that are in agreements with a conformational change around the active site of the enzyme (figure 5.7). Interestingly, the carbon chemical shifts of the excited apo state hat we extract from the CPMG experiments (figure 5.5) correlate linearly with the carbon chemical shifts that we measure in the presence of pAp (figure 5.7). Likewise, the ^{19}F chemical shift difference upon addition of pAp to BTFA labeled N12C labeled (0.10 ppm) is in agreement with $p_{GS} \cdot |\Delta\omega|$ ($0.655 \cdot 0.154\,\mathrm{ppm} = 0.10\,\mathrm{ppm}$) that we determined from the RD dispersion experiments in the absence of the substrate (figure 5.7). These findings support the notion that the apo enzyme transiently populates a state that is structurally similar to the substrate bound conformation. Interestingly, ^{19}F line-widths and RD experiments reveal that the dynamics in Xrn2 are significantly reduced upon substrate binding (figure 5.7). Taken together, our data reveals that Xrn2 locks into a stable active conformation upon substrate recruitment. As a consequence of the more rigid nature of the Xrn2:substrate complex we were able to assign 9 additional Xrn2 methyl resonances (Ile3, Ile17, Ile18, Ile 243, Ile308, Ile361, Ile366, Ile372, Ile409, figure 5.7, table A.4) that were broadened beyond detection in the apo state, presumably due to exchange broadening.

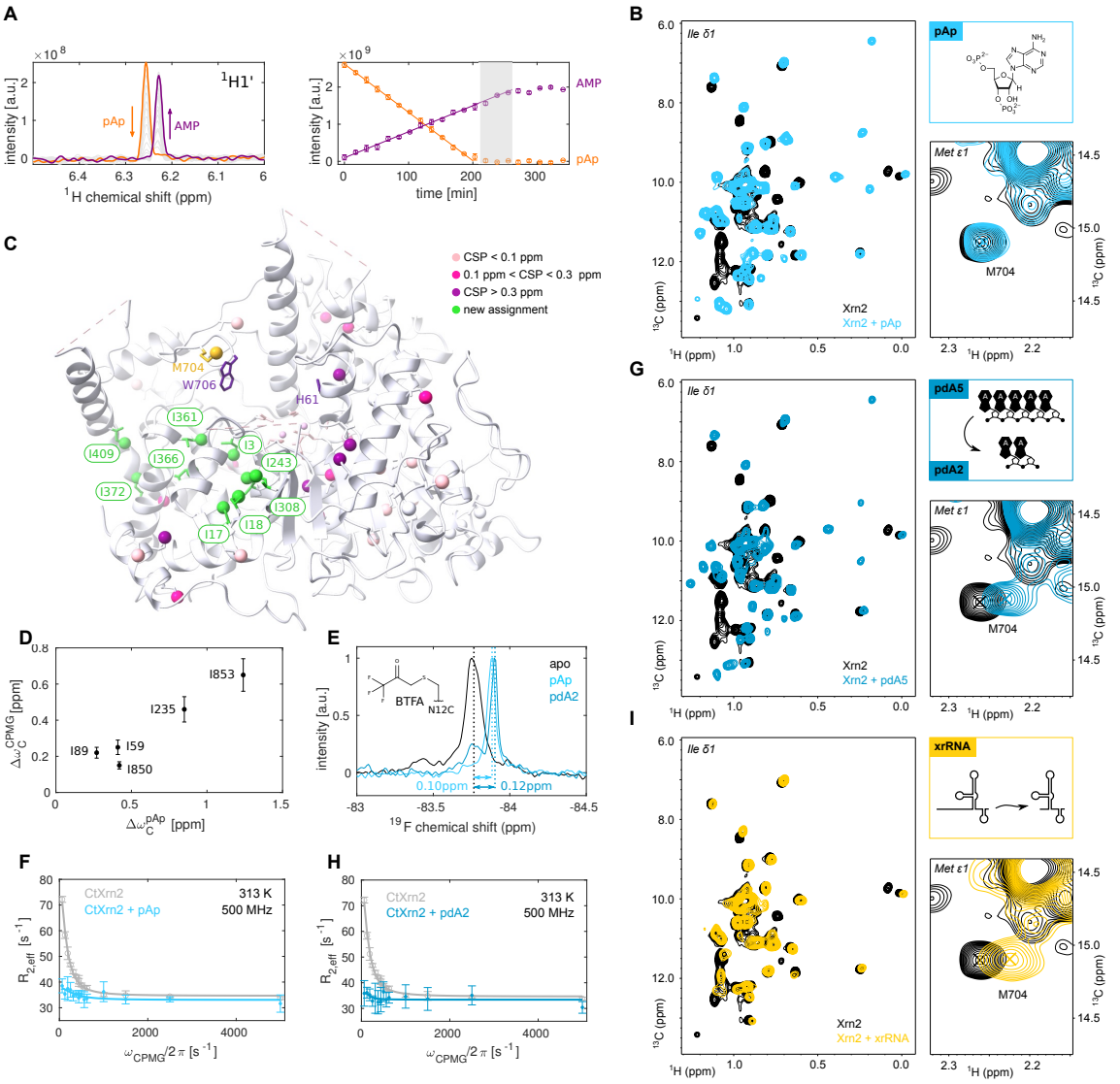

Figure 5.7.: ^{19}F NMR supports the sampling of an excited conformational state by the α1-helix (A) Left: Section of 1H spectrum showing the 1H1′ resonance of pAp/AMP. Over time pAp (orange) is fully degraded into AMP (purple). Right: Integrated peak intensities of pAp and AMP with a linear fit reveals a turnover rate of 0.05 min^{-1}. (B) Overlay of the ^{1}H-^{13}C HMQC methyl-TROSY spectra in the absence (black) and presence (light blue) of pAp, recorded at 18.8 T at 313 K. Binding of pAp leads to strong chemical shift perturbations, whereas the M704 resonance remains almost unperturbed. (G) Overlay of the ^{1}H-^{13}C HMQC methyl-TROSY spectra in the absence (black) and presence (dark blue) of pdA5, recorded at 18.8 T at 313 K. pdA5 is degraded to pdA2, which leads to strong chemical shift perturbations in the Ile region, the M704 resonance experiences a characteristic upfield shift in the 1H dimension. (I) Overlay of the ^{1}H-^{13}C HMQC methyl-TROSY spectra in the absence (black) and presence (yellow) of an xrRNA derived from the Zika virus 3′UTR, recorded at 18.8 T at 313 K. The linear leader sequence of the xrRNA is rapidly degraded, until Xrn2 encounters the Xrn-resistant pseudoknot structure. The upfield shift of M704 as well as Ile-δ1 chemical shift perturbations close to the active site and the RNA entry site show, that the RNA remains bound to

Xrn2. However, the Ile-δ1 section of the spectrum indicates, that the conformational change observed in the presence of pAp and pdA5 is not induced with the xrRNA, because the sterical pseudoknot road block prevents RNA translocation and locks the enzyme:substrate complex in a post-scission / pre-translocation conformation. (C) Close-up of RNA entry site and active site. Ile-δ1 methyl groups that could only be assigned in the pAp bound state are colored green, whereas Ile-δ1 probes which shifted upon addition of pAp were colored according to the amplitude of the CSP. H61 and W706, the residues that form a continuous $\pi - \pi$ stack with the first three nucleotides of the RNA substrate are shown as dark magenta sticks, M704 is shown in yellow. (D) Correlation of CSPs in the carbon dimension obtained upon binding of pAp (x-axis) and the chemical shift differences extracted from the CPMG data (y-axis; figure 5.5) (E) ^{19}F spectra of Xrn2 ΔZnF N12C^{BTFA} without ligand (black), with pAp (light blue) and pdA5 (dark blue). Upon interaction with the substrate the line-width of the ^{19}F signal is reduced from 55 Hz to 36 Hz (pAp) and 32 Hz (pdA5), respectively. (F) CPMG dispersion profiles of Xrn2 ΔZnF N12C^{BTFA} at 11.7 T (500 MHz 1H frequency) in the absence (grey) and presence (light blue) of pAp. (H) CPMG dispersion profiles of Xrn2 ΔZnF N12C^{BTFA} at 11.7 T (500 MHz ^{1}H frequency) in the absence (grey) and presence (dark blue) of pdA5/pdA2

To obtain additional information on the structural and conformational changes in Xrn2 upon substrate binding we next made use of a 5′-phosphorylated DNA pentanucleotide (pdA5). Addition of this substrate analogue to catalytically active Xrn2 showed that pdA5 is readily degraded into a 2mer DNA (pdA2) and free nucleotides (figure A.19). pdA2 is one nucleotide longer than pAp that we used above (figure 5.7) and induced similar chemical shift perturbations in the HMQC spectrum as pAp did (figure 5.7, figure A.20). In analogy to pAp binding, the binding of pdA2 to Xrn2 also abolished the extensive motions in the enzyme (figure 5.7). These findings reveals that pAp and pdA2 induce the same stable active conformation in Xrn2. Interestingly, in the presence of pdA2, we noticed a CSP of Met704 that was absent in the pAp bound states (figure 5.7G). As pdA2 is one base longer than pAp, we concluded that the CSP of Met704 reports on the location of the second base of the Xrn2 substrate. In the structure of Xrn2 Met704 is positioned in direct proximity to the conserved Trp706 residue, which stacks at the back of the third nucleotide base in the structure of Xrn1 bound to a 5′-phosphorylated DNA 11-mer (Jinek et al. 2011, Tesina et al. 2019). Based on that, Met704 is an excellent probe that reports on the occupancy of the RNA binding groove next to the active site.

In the absence of Mg^{2+} pdA5 is not degraded to pdA2 by Xrn2 (figure A.19). Under these conditions, pdA5 is correctly recruited to the RNA binding groove (as reported by Met704, figure A.21) but the stable formation of the active conformation in Xrn2 (as reported by the methyl-TROSY spectra; figure A.21) is not formed. This is also confirmed by ^{19}F RD measurements, that show that the binding of pdA5 to Xrn2 in the absence of magnesium has not effect on the dynamics of the N-terminal α-helix. From that we conclude the divalent ions in the active site play an important role in the transition of Xrn2 from the ground (pre-translocation) conformation to the active (post-translocation) con-

formation. This finding underscores the importance of performing experiments on the WT enzyme as the Mg^{2+} ions are required for both catalysis and the stable formation of the active conformation.

Finally, we used a modified xrRNA derived from a subgenomic flavivirus RNA from Zika virus as an Xrn2 substrate. This RNA forms a highly stable pseudoknot that is resistant to the 5′-3′ exoribonuclease activity of Xrn1 (Akiyama et al. 2016) as well as an unstructured 5′-end. The addition of Xrn2 to this xrRNA results in the rapid hydrolysis of the unstructured 5′ region and the subsequent formation of a stable complex between Xrn2 and the xrRNA pseudoknot that is one nucleotide too short to reach the active site (figure A.22). The HMQC spectrum of this complex shows overall reduced peak intensities, that are particularly pronounced at resonances that are localized between the α3-helix and the active site (figure 5.7 and figure A.23). Those reduced resonance intensities can be contributed to the increase in the molecular weight and the large number of protons from the xrRNA that come close to Xrn2 methyl groups and thereby enhance relaxation rates. Based on the methyl-TROSY spectrum of the Xrn2:xrRNA complex, it can nevertheless be concluded that the active state of the enzyme is not stably formed, as the signature chemical shifts of the active state (figure 5.7B) are not fully observed. Met704, on the other hand, shows a clear CSP, which confirms that the 5′ end of the trimmed xrRNA interacts in the substrate binding groove. Taken together, we conclude that the Xrn2 enzyme is locked at a pre-translocation state in the presence of the xrRNA product, as was observed in the cryo-EM structure of Xrn1 in the presence of a stalled ribosome.

In summary, our data reveal a situation where the apo Xrn2 enzyme is in a dynamic equilibrium between a ground (pre-translocation) conformation and a conformation that corresponds to the active (post-translocation) state. Upon recruitment of a substrate and in the presence of Mg^{2+} Xrn2 stably adopts the active (post-translocation) conformation.

5.3.6. A point mutation in α1-helix alters Xrn2 dynamics and decreases Xrn2 activity

In order to investigate how the dynamics in Xrn2 are correlated with RNA substrate degradation, we introduced single point mutations in or close to the α1-helix with the aim of changing the dynamics around the active site. We subsequently exploited ^{19}F CPMG RD experiments to assess if any of these mutations indeed displayed altered motions. Of the 22 single point mutant enzymes that we tested, we found that the A5F mutation led to drastically reduced relaxation dispersions (figure 5.8A), indicative of significant changes in the energy landscape of the enzyme. It is important to note that HMQC spectra of

the A5F mutant enzyme reveals that this mutation does not interfere with the overall structure of the enzyme or with the interaction between the substrate and the enzyme (figure A.24). These data are in agreement with an A5F induced shift in the populations of the Xrn2 enzyme away from the active (post-translocation) conformation. We reasoned that this shift in populations would manifest itself in a reduction of the catalytic activity. In order to test this hypothesis, we determined the catalytic turnover rates of the wild type enzyme (Xrn2 1-875; WT) and the enzyme with the A5F mutation (A5F) and found that the A5F mutation decrease the activity of Xrn2 by 30 %-50 %, depending on the substrate (figure 5.8B). It should be noted that the ^{19}F NMR experiments were performed in an enzyme that lacks the ZnF and that contains the additional N12C mutation that is linked to BTFA (Xrn2 1-875 Δ263-300 N12C^{BTFA}; ΔZnF N12C) and also in this background the introduction of the A5F mutation resulted in a 30 %-50 % reduction of the catalytic activity. Based on these findings, we conclude that the A5F mutation results in a destabilization of the active conformation and at the same time in a decrease in the enzymatic turnover rates.

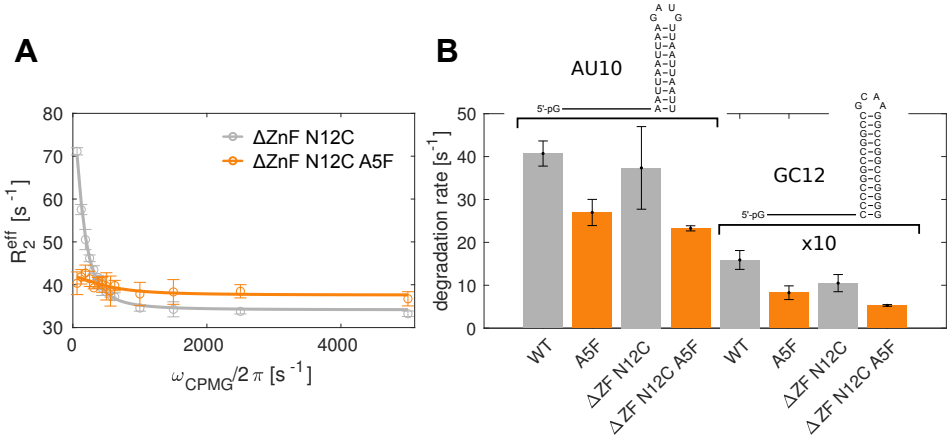

Figure 5.8.: The N-terminal helix is functionally important for RNA degradation (A) CPMG dispersion profiles of Xrn2 ΔZnF N12C^{BTFA} (grey) and Xrn2 ΔZnF A5F N12C^{BTFA} (orange) at 11.7 T (500 MHz 1H frequency). (B) Changes in the degradation rate of 5′-monophosphorylated AU10 and GC12 stem loop RNAs by Xrn2, the Xrn2 A5F mutant, Xrn2 ΔZnF N12C^{BTFA} and Xrn2 ΔZnF N12C^{BTFA} A5F. The GC12 RNA is degraded approximately 20x slower than AU10 and the degradation rates are multiplied by 10 for clarity.

5.4. Discussion

Static macromolecular structures, as experimentally obtained by X-ray crystallography or cryo-EM, provide important information about biochemical mechanisms. It is, however, important to realize that these static structures i) not necessarily represent the ground

state conformation of the macromolecule in solution (Wurm et al. 2017) and ii) fail to reveal the dynamical processes that underly allostery (Popovych et al. 2006, Tzeng and Kalodimos 2013, Wurm et al. 2021) or catalysis (Boehr et al. 2006, Neu et al. 2015, Fuchs et al. 2020). In that regard, it is thus of central importance to complement our understanding of molecular function with information regarding dynamic processes, although this can be technically highly challenging (Schütz and Sprangers 2020).

A catalytic cycle of a chemical reaction comprises multiple steps, where the overall rate of the reaction is determined by the slowest of these steps. Enzymes can increase the speed of these reactions dramatically, by significantly reducing the rate limiting step that normally involves the breaking or formation of chemical bonds. In an enzyme catalyzed chemical reaction, the slowest step can then be shifted to a conformational change in the enzyme. This has been shown for e.g. dihydrofolate reductase (DHFR) that needs to rearrange from a closed conformation where catalysis can take place to an occluded conformation that is required for product release (Boehr et al. 2006). Likewise, the opening of a lid domain was found to constitute the rate limiting step in reaction cycle of hyperthermophilic and mesophilic homologs of the enzyme adenylate kinase (Wolf-Watz et al. 2004).

The conformational heterogeneity in Xrn2 is indirectly revealed by multiple crystal structures of Xrn1 and Xrn2. In these structures two structurally distinct states have been identified: i) a catalytically incompetent pre-translocation state. This state is observed in the apo state of the enzyme and in a complex between Xrn1 and the ribosome, where the mRNA is stalled and has not moved fully into the active site and ii) a catalytically competent post-translocation state, where the substrate is located in the active site in a manner that is optimal for catalysis. This state is observed in the complex between inactivated Xrn1 and a DNA substrate mimic. Large structural differences between the two states take place at the N-terminal α1-helix that moved by $10 - 15$ Å.

In this study, we exploit methyl-TROSY (s figure 5.5 figure 5.7) and ^{19}F (figure 5.6 figure 5.7 figure 5.8) NMR techniques and combination with X-ray crystallography (figure 5.3) and degradation assays (figure 5.3 figure 5.8) to investigate the structural dynamics of the eukaryotic Xrn2 exoribonuclease. Our solution methods reveal, that the N-terminal α1-helix and the surroundings are highly dynamic in the apo enzyme. We attribute these motions to a conformational change between the structural states that resemble the pre- and post-translocation states (figure 5.2). Our methyl-TROSY and ^{19}F NMR data shows that the pre-translational state (the ground state in the apo enzyme) is occupied to around $65\,\% - 82\,\%$ at 313 K. This ground states exchanges on the ms

timescale with the post-translocation state (the excited state) that is populated to around $18 - 35\,\%$ ($p_{ES} = 0.184$; $k_{ex} = k_{GS\text{-}ES} + k_{ES\text{-}GS} = 661\,s^{-1}$; $k_{GS\text{-}ES} = p_{ES} \cdot k_{ex} = 122\,s^{-1}$; $k_{ES\text{-}GS} = p_{GS} \cdot k_{ex} = 539\,s^{-1}$). These rates are significantly faster than the catalytic turnover rate of the enzyme (AU rich RNA: turnover rate = $20 - 35\,s^{-1}$; GC rich RNA: turnover rate = $0.5 - 1.0\,s^{-1}$). This implies that the motions of the N-terminal helix, as they takes place in the absence of substrate, are not rate limiting for the exonucleolytic reaction.

The energy landscape of Xrn2 is significantly altered upon substrate binding, This is clearly observed in the reduced line-width of both $^{13}CH_3$ and ^{19}F resonances upon substrate binding and is reported by a large reduction of the amplitude of the relaxation dispersion profiles ($R_{2,eff}^{65.5\,Hz} - R_{2,eff}^{5\,kHz}$) is reduced from $> 35\,s^{-1}$ to $> 5\,s^{-1}$ upon pAp or pdA2 binding). The lack of a sizable relaxation dispersion profile in the presence of the Xrn2 substrate prevents us from obtaining direct information on the Xrn2 motions in the presence of substrates. Theoretically, the observed reduction in the amplitude of the RD profile can be explained by three scenarios. First, a reduction of k_{ex} from $950\,s^{-1}$ to $20\,s^{-1}$. This reduction in k_{ex} does not happen upon substrate binding in Xrn2, as this would shift the exchange process into the slow exchange regime, where resonances of the ground and excited state would be simultaneously visible, which is not the case (figure 5.7). Second, a reduction in the chemical shift difference between the ground and excited state from 0.15 ppm to 0.04 ppm. Also this scenario can be excluded as substrate binding takes place more than 20 Å from the site where we measure the dynamics of the N-terminal helix. Experimentally we also observe that substrate binding has no direct effect of the ^{19}F chemical shift as the ^{19}F NMR spectra of pAp and pdA2 bound Xrn2 are very similar (figure 5.7E). Thirdly, the observed reduction in the relaxation dispersion amplitude can be caused by a shift in the populations of the pre-translocation (to $\sim 2\,\%$) and post-translocation (to $\sim 98\,\%$) states. This explanation is in agreement with the observation that the chemical shifts of the excited state that we calculate for the apo protein based on $^{13}CH_3$ SQ and MQ CPMG experiments correlate with the chemical shifts that we observe in the NMR spectra of the substrate bound enzyme. Substrate binding then locks the enzyme primarily in the excited, substrate bound conformation. In case substrate binding does not simultaneously and significantly increase k_{ex}, the shift in populations would result in a situation where the k_{ES-GS} rate (the rate from the post-translocation to the pre-translocation state) is reduced to less than $20\,s^{-1}$, which is close to the turnover rate of the enzyme. In that situation the N-terminal helix dynamics become rate limiting in the presence of substrate. This finding is in agreement with the observation that k_{cat} and k_{ex} both linearly change with temperature (figure 5.9).

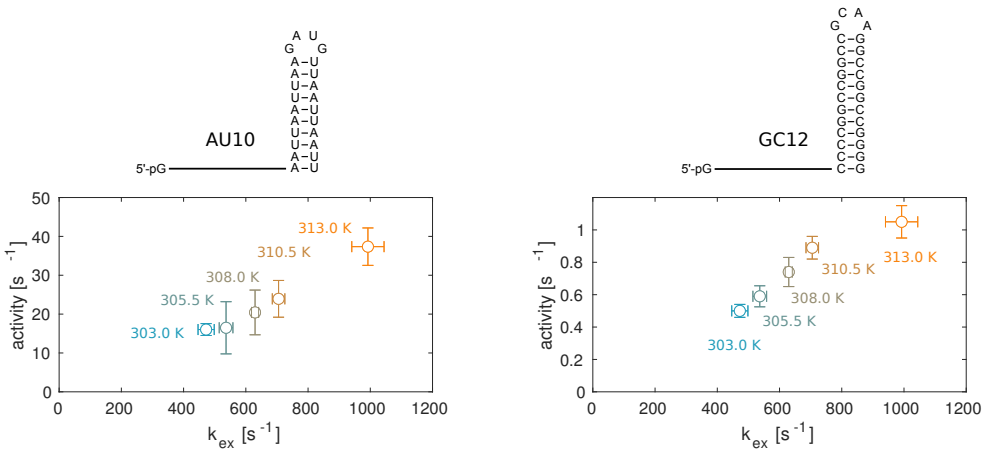

Figure 5.9.: The exchange rate k_{ex} is linearly correlated with the activity in the Xrn2 The activity (turnover rate) and exchange rates (k_{ex}) were measured with an Xrn2 ΔZnF N12C^{BTFA} sample. Activities are derived from HPLC assays, exchange rates are derived from the global fit of ^{19}F relaxation dispersion data (figure A.16). The linear correlation between k_{ex} ($k_{ex} = k_{GS\text{-}ES} + k_{ES\text{-}GS}$) and turnover rates suggests that the exchange and degradation rates are functionally linked. In that situation the rate $k_{GS\text{-}ES}$ (where $k_{GS\text{-}ES} = p_{ES} \cdot k_{ex}$) can becomes rate limiting, when p_{ES} is small.

A second indication that the motions in Xrn2 that we measure here are correlated with catalysis comes from experiments with a mutant form (A5F) of Xrn2. In this mutant the energy landscape of Xrn2 is altered significantly, as revealed by ^{19}F CPMG experiments (figure 5.8), which coincides with a reduction of the turnover rates. This degree of reduction of k_{cat} is independent of the substrate we use and also independent of the presence or absence of the ZnF region in Xrn2. Taken together, our data shows that motions in the N-terminal α-helix in Xrn2 are correlated with catalytic activity. This finding is in agreement with indirect information that can be deducted from static crystal and cryo-EM structures of Xrn1 and Xrn2 (Jinek et al. 2011, Tesina et al. 2019).

In previous studies, it has been shown that the activity of Xrn2 can be enhanced by the interaction with binding partners (Xiang et al. 2009, Miki et al. 2014a). On the one hand, Xrn2 in higher eukaryotes can recruit XTB domain (XRN2-binding domain, XTBD) containing binding partners through an Xrn2 region that is located on the back side of the tower domain (Richter et al. 2016), over 20 Å remote from the active site. This interaction results in the folding or stabilization of the XTBD binding pocket of Xrn2, which has been proposed to stabilize the Xrn2-fold in the absence of a substrate (Richter et al. 2016). In our crystal structure of CtXrn2 this segment is, however, fully folded, although neither a substrate nor an adaptor protein is present (figure A.25). Furthermore, the chemical shifts of Ile687 and Ile688 δ1-methyl groups in the ^{13}C-^{1}H HMQC spectrum at 313 K clearly de-

viate from the shift of Ileδ1-methyl groups in unstructured regions (figure 5.5A), which indicates that this Xrn2 segment is not only folded in our crystal structure, but also in solution. The finding that the unoccupied XTBD binding region in CtXrn2 is folded is in agreement with the notion that XTBD-containing proteins have only been identified in metazoa so far (Miki et al. 2014a, Richter et al. 2016), and indicated that the mechanisms that regulate the catalytic activity of Xrn2 differ between yeast and metazoa. On the other hand, yeast Xrn2 directly interacts with the pyrophosphohydrolase Rai1 through a region that is located at the bottom of the Xrn2. It has been speculated that the resulting enhancement of *S. Pombe* Xrn2 activity is due to the a stabilization of the Xrn2 fold upon interaction with Rai1, or by indirectly effecting Xrn2 catalysis (Xiang et al. 2009). Here, we show that *C. thermophilum* Xrn2 and Rai1 also form a stable complex (figure A.26). However, we observe that the recruitment of Rai1 to Xrn2 does not result in an enhancement of *C. thermophilum* Xrn2 activity (figure A.27), opposing findings for the enzymes from *S. pombe* (Xiang et al. 2009). In line with that finding, we also observe that the motions in the active site of Xrn2 are not influenced by Rai1. This implies that the CtXrn2 fold is stable without interaction partners and that Rai1 binding has no effect on the catalytic center of Xrn2. In agreement with that, we don't observe chemical shift perturbations of methyl resonances in close vicinity of the Xrn2 active site upon Rai1 binding (figure A.28). Interestingly, it has been observed that Rai1 enhances the Xrn2 activity especially for RNA substrates that contain stable secondary structure elements, indicating that Rai1 possesses an RNA unwinding activity. Here, we find that a zinc finger in the CtXrn2 enzyme is able to provide such an unwinding activity (figure 5.8). The zinc finger is predominantly found in Xrn2 enzymes from higher eukaryotes, where the interaction between Xrn2 and Rai1 (DXO, Dom3Z) has been lost. This suggests that the subsidiary unwinding activity has moved from the Xrn2 interacting protein Rai1 to the Xrn2 enzyme itself.

In summary, we here made extensive use of NMR methods to quantify and localize structural changes in Xrn2. It should be noted that Xrn2 (875 residues, 100 kDa) is among the largest single chain enzymes that have ever been studied using solution state NMR methods. As such, we exploited methyl labeling strategies that provide a higher spatial resolution and ^{19}F labeling that is able to provide information regarding protein motions in short times. It is important to note that the data from the methyl labeled samples provided direct information on where to place the fluorine label. We found that the methyl-fluorine combination is highly efficient, however, would like to stress the importance of cross-checking that the methyl and fluorine labels report on the same molecular process. Here, we ensured this by comparing the exchange parameters that were extracted from $^{13}CH_3$ and ^{19}F based relaxation dispersion measurements and by labeling the enzyme

with two independent fluorine containing compounds (BTFA and TET). Importantly, the rapid (1 hour) ^{19}F experiments allowed us to obtain information on catalytically active Xrn2 (as opposed to a version where the active site has been impaired) in the presence of substrates before those are fully turned over. We anticipate that the combination of complementary NMR labeling techniques with information on static structures will be an important approach to obtain fundamental insights into biologically important dynamics in large enzymes.

CtXrn2:Mg^{2+} (PDB 7OPK)	
Data collection	
Space group	P 3_1 2 1
Cell dimensions	
a, b, c (Å)	198.78, 198.78, 69.14
α, β, γ (°)	90, 90, 120
Resolution (Å)	47.75 – 3.0 (3.107 – 3.0)
R_{pim}	0.068 (0.455)
R_{meas}	0.309 (2.037)
$I/\sigma(I)$	14.74 (2.17)
$CC_{1/2}$	0.996 (0.786)
Completeness (%)	99.85 (99.94)
Redundancy	20.4 (19.9)
Refinement	
Resolution (Å)	
No. reflections	31580
R_{work}/R_{free} (%)	18.3 / 22.4
No. atoms	
Protein	5306
Ion (Mg^{2+})	2
Water	1
Bfactors	64.64
Protein	64.65
Ion (Mg^{2+})	49.14
Water	42.53
r.m.s. deviations	
Bond lengths (Å)	0.003
Bond angles (°)	0.57

Table 5.1.: Data collection and refinement statistics for CtXrn2 One crystal was used for the structure. Values in parentheses shown for the highest resolution shell.

CtXrn2 Zincfinger:Zn^{2+} (PDB 7PVM)	
Completeness of resonance assignments	
Backbone	91.3 %
Side chain	70.1 %
Conformationally restricting restraints	
Distance restraints	
Total	380
Short range ($\|i-j\| \leq 1$)	227 (59.7 %)
Medium range ($1 < \|i-j\| < 5$)	79 (20.8 %)
Long range ($\|i-j\| \geq 5$)	74 (19.7 %)
No. of restraints per residue	12.3
No. of long-range restraints per residue	2.4
Distance restraint violations	
Number of violations > 0.1Å	0
RMS	0.0036 ± 0.0005 Å
Ramachandran statistics (%)	
Residues in most favored regions	74.0
Residues in additionally allowed regions	25.8
Residues in generously allowed regions	0.2
Residues in disallowed regions	0.0
Model quality	
RMSD backbone atoms (residues 8-23)	0.03 ± 0.01 Å
RMSD heavy atoms (residues 8-23)	0.57 ± 0.15 Å

Table 5.2.: Structural statistics for the NMR solution structure of the CtXrn2 zinc finger The completeness of assignment was calculated with the CARA script `assignment report`, restraint statistics were obtained from CYANA `ovw`-files and the `cyanatable` command

6. Multi-site exchange in the neomycin-sensing riboswitch studied by ^{19}F NMR

The results of this chapter are in preparation for publication, the chapter is therefore largely identical to the manuscript in both text and figures. The project is conducted in collaboration with Jenny Vögele and Jens Wöhnert (Goethe Universität Frankfurt).

6.1. Summary

The synthetic neomycin-sensing riboswitch efficiently discriminates between its cognate ligand neomycin and the structurally related paromomycin. Although both aminoglycosides induce almost identical ground state structures in solution, only neomycin competently represses translation initiation upon binding to the riboswitch. The molecular origin of this difference has been traced back to the structural dynamics that accompany the different ligands, where the paromomycin-bound riboswitch displays localized dynamics in the flap lid that closes over the ligand. Using a set of fluorine-based NMR methods that probe dynamics from sub-seconds to microseconds, we characterize the energy landscape of the riboswitch in the presence of the four ring-aminoglycosides paromomycin and neomycin, and the three ring-aminoglycoside ribostamycin. The chemical shift sensitivity of the ^{19}F nucleus leverages the off-resonance advantage of chemical exchange saturation transfer (CEST) and off-resonance rotating frame relaxation (off-resonance $R_{1\rho}$) NMR experiments and allows us to directly quantify exchange processes with up to four states. Our results support a modular influence of aminoglycoside sub-motifs on the dynamics of the RNA. Furthermore, the data underscore the potential of ^{19}F NMR to characterize complex dynamics with several excited states.

6.2. Introduction

Riboswitches are RNA motifs that restructure in response to ligand binding and can thus function as molecular switches. Naturally occuring riboswitches are typically located in the 5'-untranslated regions (5'-UTR) of genes related to the sensed ligand, which ensures that a freshly transcribed riboswitch can act as a real-time cis-acting sensor for the requirement of the downstream gene product. In this manner, riboswitches can modulate gene expression on the level of transcription, translation or RNA processing without recruiting protein factors. Consequently, the need to reliably bind the ligand and translate this binding into a functional change imposes strong limitations for the sequence variability of the aptamer element. At the same time, the exact riboswitch sequence has to generate structural features that allow to discriminate between different ligands.

While naturally evolved riboswitches are usually encoded in long (> 40 nucleotides) RNAs with an intricate structure, artificial riboswitches derived from in vitro selection followed by in vivo testing can be considerably shorter and often give rise to a simpler fold (Werstuck 1998, Grate and Wilson 2001, Harvey et al. 2002, Dwidar et al. 2019). A well-studied example of such a synthetically derived RNA element is the neomycin (NEO)-sensing riboswitch (Weigand et al. 2008). It was identified by in vivo screening of an aptamer pool in a GFP-expression assay reporting on NEO-dependent changes and shows sequence similarity to the natural target of aminoglycosides, the amino acid-tRNA decoding site of the ribosome (Weigand et al. 2008, Duchardt-Ferner et al. 2010). Based on this similarity and the solution structure of a previously reported NEO-aptamer (Jiang et al. 1999), a structural model was proposed, where the terminal riboswitch loop flaps on the binding pocket formed by an internal loop (Weigand et al. 2008). This model was confirmed by the solution structures of the NEO riboswitch bound to ribostamycin (RIO) (Duchardt-Ferner et al. 2010), a close relative of NEO that lacks ring IV, and paromomycin (PAR) (Duchardt-Ferner et al. 2016), in which a hydroxy group replaces the 6' amino group of ring I (figure 6.1).

The riboswitch recognizes RIO and PAR in a modular manner, in which different RNA and ligand elements contribute to an overall clamp-like binding with a low nanomolar affinity (Duchardt-Ferner et al. 2016). In both structures, the closing stem (G1:C27 to G5:C23) coaxially stacks with the upper stem (G9:C22 to U13:U18) (figure 6.2). The resultant major groove harbors a binding pocket for ring I and II, and interactions of the amino groups at position 1 and 3 of ring II to the G5:C23 and the U10:U21 base pairs stabilize the continuous helical stem. The apical hexaloop (U13-U18) is stabilized by a U-turn motif of U14, U15 and A16, after which A17 protrudes from the loop and stacks

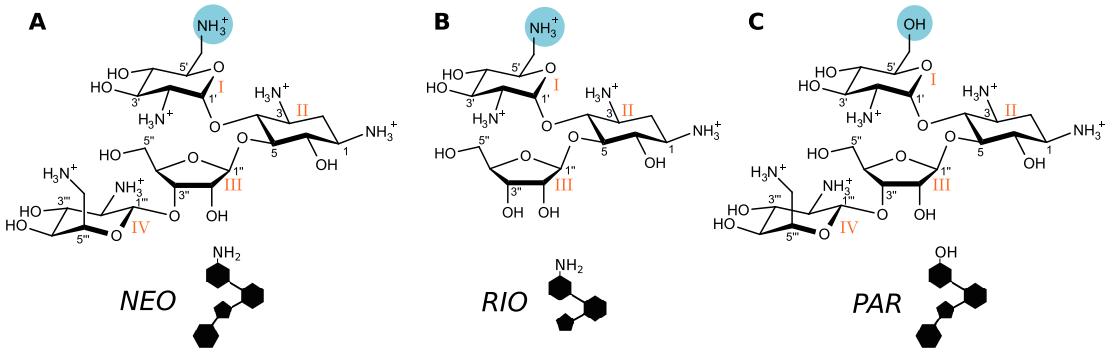

Figure 6.1.: Structures of aminoglycoside antibiotics Structures and cartoon representations of (A) neomycin (NEO) (B) ribostamycin (RIO) and (C) paromomycin (PAR). The distinguishing 6′ groups are highlighted in blue, the rings are labeled with roman numbers according to the numbering in Duchardt-Ferner et al. (2016).

against ring I. Based on the comparison of [^{1}H,^{1}H]-NOESY spectra, the same binding mode was inferred for the cognate NEO ligand (Duchardt-Ferner et al. 2010).

The structural similarity of these complexes strikingly contrasts with their regulatory effectiveness to repress translation initiation, which is highest for NEO, weakened for RIO and completely absent for PAR (Weigand et al. 2008, Duchardt-Ferner et al. 2016). The molecular basis for these differences is found in the structural dynamics of the complexes (Duchardt-Ferner et al. 2016): although PAR stabilizes the same average ground state structure as RIO, it displays greatly enhanced flexibility in the flap lid A17 in the µs regime that translates into overall enhanced dynamics of the stacked stem structure.

In this work, we investigate the dynamics of the neomycin-sensing riboswitch in the presence of NEO, RIO and PAR in a site-specific manner. To this end, we use 2-fluoroadenine labeled RNA and quantify populations and exchange dynamics ranging from sub-seconds to microseconds using five different ^{19}F NMR experiments. Our results show that aminoglycoside motifs modularly influence the energy landscape of the complex. NEO stabilizes two conformations that exchange very slowly ($k_{ex} < 1\,s^{-1}$), the minor of which is selectively stabilized by the binding of RIO due to the lack of ring IV. This is accompanied by the sampling of an excited state, that is not observed in the presence of NEO. In the presence of PAR, we detect both the slowly exchanging states from NEO, as well as the excited state sampled in the RIO-bound riboswitch, adding up to a total of three states in a dynamic equilibrium. To demonstrate the robustness and potential of ^{19}F-CEST measurements, we characterize the exchange in partially unsaturated riboswitch:RIO and riboswitch:PAR samples with three and four different states, respectively.

6.3. Results

^{19}F-measurements have emerged as a valuable approach in biomolecular NMR to study low-populated states (Manglik et al. 2015, Liebau et al. 2020, Huang et al. 2020, Overbeck et al. 2020), mainly due to three reasons: First, fluorine atoms are almost completely absent from biomolecules, allowing background-free measurements of resonances from artificially introduced fluorine probes. Second, the ^{19}F isotope has virtually 100% natural abundance and a high gyromagnetic ratio, both of which facilitates measurements with high signal-to-noise that are essential for quantitative experiments. Third, ^{19}F chemical shifts are sensitive reporters of their local environment due to an anisotropic electron distribution (Rastinejad et al. 1995). While this property allows to detect subtle molecular changes and equips ^{19}F NMR with a wide chemical shift dispersion, it inevitably comes at the cost of large chemical shift anisotropies (CSA) that dominate ^{19}F relaxation already at modest field strengths of 7.04 T.

In order to illuminate the structural dynamics of the NEO-riboswitch, we labeled the RNA with 2-fluoroadenine (Scott et al. 2004, Sochor et al. 2016) (figure 6.2A). The incorporation of ^{19}F in this way is beneficial, as only three adenine bases are present in the construct and spectral overlap is thus kept low. Importantly, the probes report on different parts of the RNA and include the flap lid A17, its direct neighbor A16, which represents the conserved purine nucleotide that completes the U-turn motif (Gottstein-Schmidtke et al. 2014), and the distant base A24, that is part of the closing stem (figure 6.2B). In the apo-state at 303 K, three main resonances are resolved, that we assigned by mutagenesis (figure 6.2C). Both A16 and A17 give rise to sharp resonances in the ^{19}F spectrum around -52 ppm, while the 2F resonance from A24 is shifted upfield. Upon addition of NEO, we observed a drastic chemical shift perturbation of A17 to -47.9 ppm and peak splitting, where the integrated peak intensity of the minor peak (excited state, ES) is 37 % relative to the major peak (ground state, GS) at 303 K, translating into relative populations of $p_{GS} = 73\,\%$ and $p_{ES} = 27\,\%$. The same peak splitting is observed after addition of PAR, where the relative minor peak intensity decreases to 26 %, and both peaks are shifted upfield by 0.47 ppm compared to the NEO-bound state. In contrast, binding of RIO yields a single resonance at -47.18 ppm.

6.3.1. Binding of NEO stabilizes two conformations that exchange very slowly

We started with the investigation of the NEO-bound riboswitch and focused on the dynamics of A17, the residue that contacts the ligand. The existence of two distinct peaks in the ^{19}F spectrum indicates, that the riboswitch samples two conformations that are

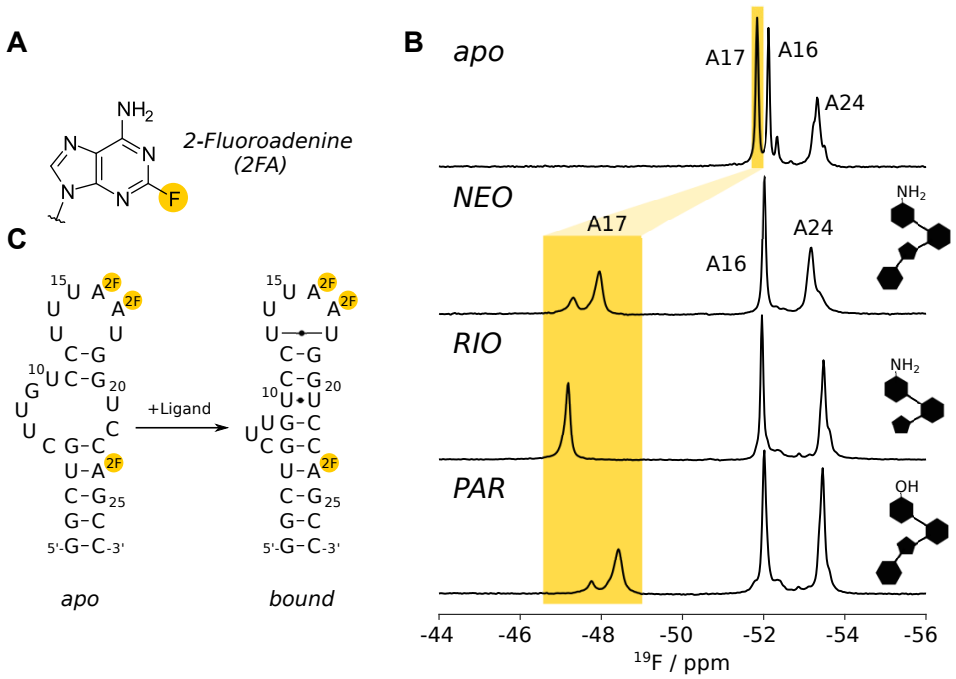

Figure 6.2.: 2FA-labeled neomycin-sensing riboswitch and ^{19}F spectra with different ligands (A) Structure of the 2-Fluoroadenine base. (B) ^{19}F spectra of the 2FA-labeled riboswitch in the absence (apo) and presence (NEO, RIO, PAR) of a ligand. The ligand structure highlighting the differences is shown as a sketch above the respective spectrum. RIO differs from NEO by the substitution of ring IV with a proton, PAR differs from NEO by the substitution of the amino group at position 6′ with an hydroxy group. (C) Changes in the secondary structure of the riboswitch upon ligand binding. 2F-labeling of adenine bases at position 16, 17 and 24 are indicated by spheres.

in slow exchange on the NMR timescale, i.e. the exchange rate $k_{ex} = k_1 + k_{-1}$ is much smaller than the chemical shift difference $\Delta\nu$. In order to quantify the exchange, we measured ZZ-exchange, but could not detect cross peaks indicative of exchange. We reasoned, that the exchange should thus be below the longitudinal relaxation rate R_1, such that no significant cross peak intensity can build up. As an alternative approach, we recorded chemical exchange saturation transfer (CEST) data and simultaneously analyzed the intensities from both GS and ES state (figure 6.3). In the CEST experiment used here, magnetization is selectively saturated at variable offsets for a time T_{CEST}, after which an anti-ringing (aring) sequence composed of three 90° pulses is used to detect the magnetization. If a nucleus samples two sites, selective perturbation at one site influences the magnetization at the other. A careful analysis showed slightly decreased intensity levels of the ES peak upon saturation of the GS resonance and vice versa (figure 6.3A, insets). The global fit with a 2-state exchange model yielded an exchange rate of $k_{\mathrm{ex}} = 0.3\,\mathrm{s}^{-1}$ and populations of $p_{\mathrm{GS}} = 67.3\,\%$ and $p_{\mathrm{ES}} = 32.7\,\%$ (figure 6.3A), in good

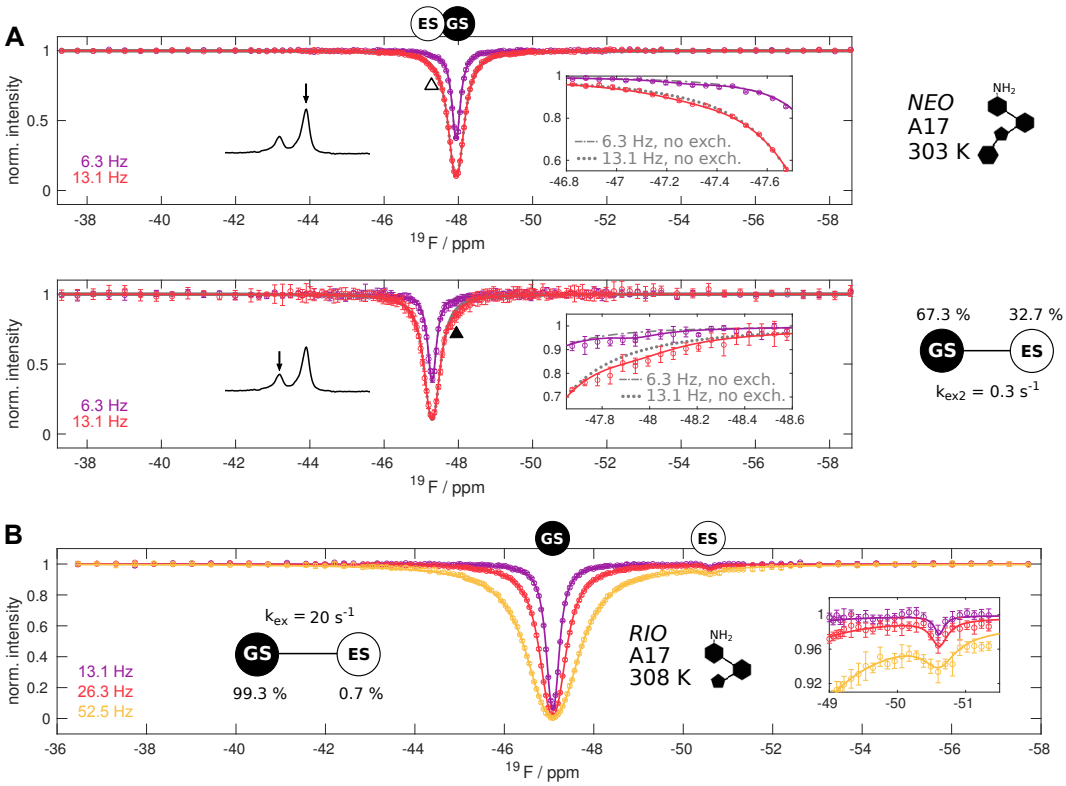

Figure 6.3.: Slow dynamics in the NEO- and RIO-bound riboswitch (A) CEST profiles from A17 major (top) and A17 minor (bottom) state at 303 K with data (circles with errorbars) and fit (solid line). The integrated peak is indicated in the left insets in each case. The right inset shows a zoom of the region where the data deviates from the no-exchange model, in line with a very slow exchange between GS and ES. (B) CEST profiles at 308 K from A17 at B1 fields of 13.1 Hz, 26.3 Hz and 52.5 Hz with data (circles with errorbars) and the fit from the 2-state exchange model (solid line). The resonance positions of GS and ES are indicated above the CEST spectra. The inset shows a zoom of the CEST profiles in the region of the ES.

agreement with the relative peak intensities.

CEST experiments report on slow exchange processes. In order to extend our analysis to faster dynamics, we collected ^{19}F Carr-Purcell-Meiboom-Gill (CPMG) and on-resonance rotating frame relaxation ($R_{1\rho}$) data (figure 6.4). The relaxation dispersion profiles from both the GS and the ES are overall flat and slightly elevated towards lower frequencies. The data could not be fit unambigously, but indicate the existence of higher energy states that exchange rapidly with GS and ES.

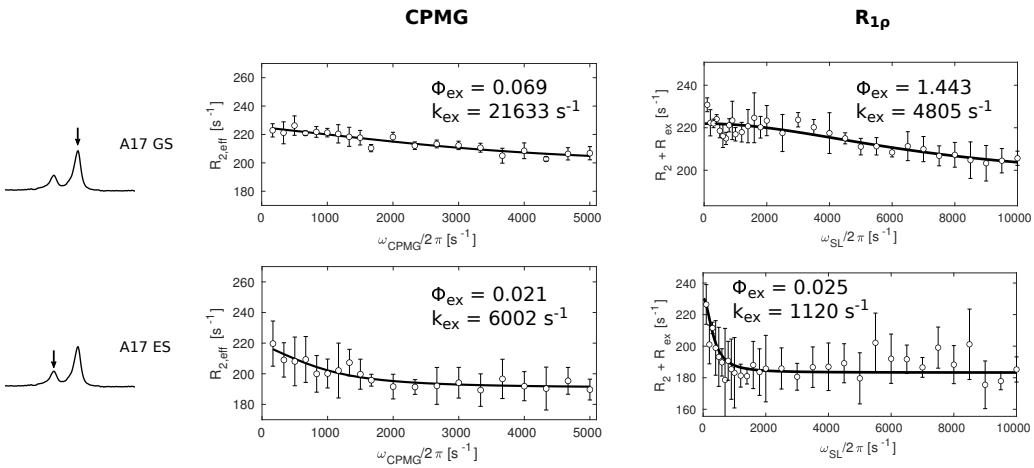

Figure 6.4.: ^{19}F relaxation dispersion data for GS and ES of the NEO-bound riboswitch at 303 K Left panels: CPMG data. Right panels: $R_{1\rho}$ data. The fast exchange does not allow to extract populations p_i and chemical shift difference $\Delta\omega_{ij}$, which are entangled in the parameter $\Phi_{\text{ex},ij} = p_i p_j \Delta\omega_{ij}^2$, where i is either the GS or the ES and j corresponds to the additional rapidly exchanging excited state.

6.3.2. RIO stabilizes a highly populated ground state conformation that samples an excited state

To gain more insight into the impact of aminoglycoside sub-motifs on the structural dynamics of the riboswitch, we measured dynamics in the RIO-bound state. F2 from A17 gives rise to a single peak at -47.18 ppm, close to the minor state in the NEO-bound state at -47.30 ppm (figure 6.2C). The CEST profiles of this resonance at 308 K showed a small minor dip at -50.6 ppm, corresponding to a marginally populated excited state (figure 6.3B). We fit the data numerically with a 2-state exchange model and obtained a population of the excited state of 0.7 %, which exchanges with the 99.3 % ground state at a rate of $k_{\text{ex}} = 20\,\text{s}^{-1}$. To gain insights into the thermodynamics of the exchange, we recorded additional datasets at 293 K, 298 K and 303 K (figure A.29). The data obtained at 303 K could again be fit to a 2-state model, where p_{ES} remained at 0.7 %, but the exchange rate decreased to $10\,\text{s}^{-1}$. For the data obtained at 293 K and 298 K, no dip could be identified at the position of the ES, which population presumably drops below our detection limit. CPMG data at 308 K indicated exchange to an excited state in the fast exchange regime, similar to the situation in the NEO-bound riboswitch (figure A.30).

6.3.3. CEST and relaxation dispersion experiments unravel a three-site exchange in the PAR-bound riboswitch

The PAR- and RIO-bound riboswitches adopt virtually identical solution structures, but PAR fails to induce a globally stabilized riboswitch structure that sterically blocks ribosomal scanning (Duchardt-Ferner et al. 2016). To illuminate the molecular basis of this observation, we collected CEST data of the PAR-bound riboswitch (figure 6.5). As noted above, the A17 2F resonance splits into two peaks in the presence of NEO and PAR, but not RIO (figure 6.2c). In agreement with this, we observe a decreased intensity of the ground state (-48.42 ppm, GS) upon saturation of this minor state (-47.76 ppm, ES1) and vice versa. We confirmed this exchange with a [^{19}F-^{19}F] ZZ-exchange experiment, in which cross peaks between GS and ES1 are clearly visible (figure 6.5E). In addition to this slow exchange contribution, the CEST profiles derived both from the GS and the ES1 resonance exhibit a dip around -51.0 ppm (ES2), which is close to the position of the excited state in the RIO-bound state at 303 K (-50.75 ppm). Initial fit results suggested, that the exchange rate between the GS and ES2 is approximately $1500 - 2000\,\mathrm{s}^{-1}$, which places the exchange in a regime, that is ideally suited for characterization by relaxation dispersion. We therefore recorded ^{19}F CPMG, ^{19}F on-resonance and ^{19}F off-resonance $R_{1\rho}$ experiments (Overbeck et al. 2020) for the GS resonance of the A17(F2) nucleus, as well as a ^{19}F CPMG experiment for the ES1 resonance (figure 6.5B-C, figure 6.6). As expected, the CPMG and on-resonance $R_{1\rho}$ profiles of the GS show elevated relaxation rates in the lower frequency range. The off-resonance $R_{1\rho}$ profiles display enhanced relaxation at the resonance offset corresponding to the ES2 dip in the CEST profile (figure 6.5D), whereas no distinct relaxation enhancement is visible at the position of the ES1 resonance. For the ES1 resonance, we find a low relaxation dispersion amplitude which we attribute to the very fast exchange process also present in the NEO-bound complex (figure 6.4).

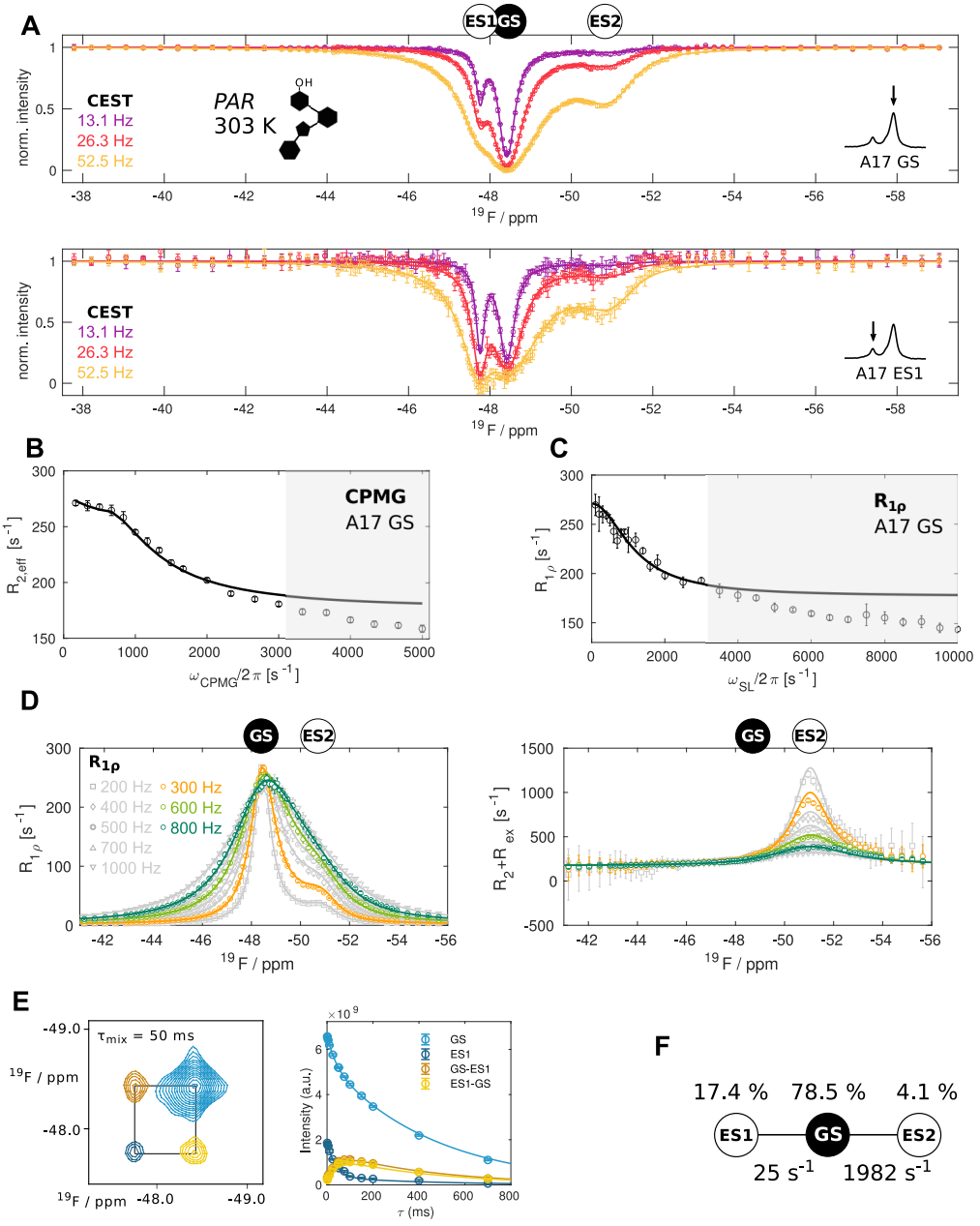

Figure 6.5.: A three-state exchange in the PAR-bound riboswitch (A) CEST profiles obtained from analysis of the GS and the ES1 resonances of the A17 2F probe. (B) CPMG relaxation dispersion profile of the GS. (C) On-resonance R1rho relaxation dispersion profile. (D) Off-resonance $R_{1\rho}$ relaxation dispersion and $R_2 + R_{ex}$ contributions. (E) Exemplary [^{19}F-^{19}F] ZZ-exchange spectrum for a mixing time of $\tau_{mix} = 50$ ms, and [^{19}F-^{19}F] ZZ-exchange data for the GS-ES1 exchange. All data in (A) to (E) were recorded for the A17 F2 nucleus at 303 K and 11.7 T. Data points are shown as open circles with errorbars corresponding to 1 standard deviation, the fit is shown as a solid line. (F) Fit parameters for the linear ES1-GS-ES2 model at 303 K.

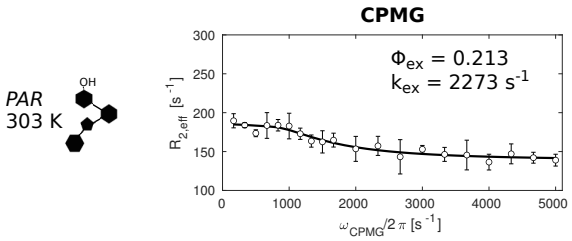

Figure 6.6.: CPMG data for the ES1 resonance of the PAR-bound riboswitch at 303 K The fast exchange does not allow to extract populations p_i and chemical shift difference $\Delta\omega_{ij}$, which are entangled in the parameter $\Phi_{\text{ex},ij} = p_i p_j \Delta\omega_{ij}^2$, where i is ES1 and j corresponds to the additional rapidly exchanging excited state.

The ZZ-exchange experiment suggests, that the GS exchanges directly with the ES1. This is consistent with the observation, that the riboswitch exchanges between two homologous conformations when it binds to NEO (figure 6.3). At the same time, the relaxation dispersion experiments indicate, that the GS, but not ES1, exchanges directly with ES2. Based on these findings, we used a linear model ES1-GS-ES2 to fit all datasets (CEST, CPMG, on-resonance $R_{1\rho}$, off-resonance $R_{1\rho}$, ZZ-exchange) simultaneously. We noted, that the CPMG and the on-resonance $R_{1\rho}$ experiment showed a linear decrease in the effective relaxation rate ($R_{2,\text{eff}}$, $R_{1\rho}$) even at high frequencies, similar to the CPMG experiments in the NEO-bound and RIO-bound riboswitch. This behaviour is likely a result of an additional, very fast process, which escapes our observation in the CEST and the off-resonance $R_{1\rho}$ experiment and can not be unambiguously fit by the experiments used here. To minimize a systematic error in our fit due to the presence of this additional process, we excluded the CPMG and on-resonance $R_{1\rho}$ data beyond frequencies ($\omega_{\text{CPMG}}/2\pi$, $\omega_{\text{SL}}/2\pi$) of 3000 Hz. The global fit with the linear ES1-GS-ES2 model yielded a ground state population of $p_{\text{GS}} = 78.5 \pm 0.3\,\%$, a population of ES1 of $p_{\text{ES1}} = 17.4 \pm 0.3\,\%$ and a population of ES2 of $p_{\text{ES2}} = 4.1 \pm 0.1\,\%$. The exchange rate between GS and ES1 is $p_{\text{GS,ES1}} = 25 \pm 1\,\text{s}^{-1}$, whereas GS and ES2 exchange on the fast timescale with $p_{\text{GS,ES2}} = 1982 \pm 43\,\text{s}^{-1}$ (figure 6.5).

Having established, that the PAR-bound riboswitch exists in a dynamic equilibrium of three conformational states, we aimed at obtaining information about the thermodynamic parameters of the states and their corresponding transition states. To this end, we measured ^{19}F CEST, CPMG and ZZ-exchange experiments at additional temperatures of 293 K, 298 K and 308 K. The data from each temperature were globally fit to the introduced linear 3-state exchange model ES1-GS-ES2 (figure A.31 figure A.32) and the retrieved exchange parameters were fit to Arrhenius and Eyring equations (figure 6.7). Both exchange processes show an enthalpy-entropy compensation and are entropically

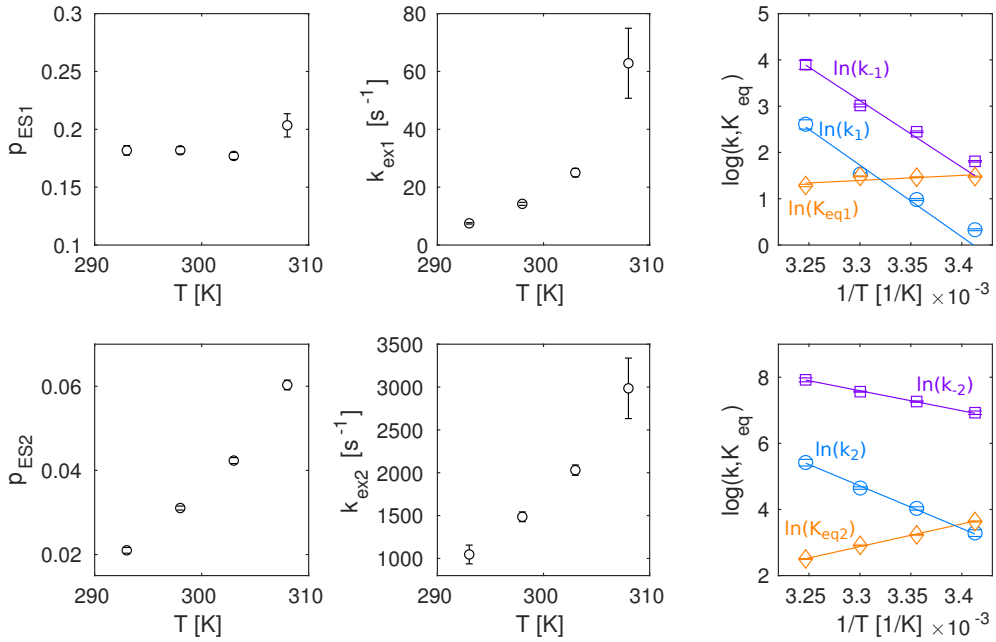

Figure 6.7.: Temperature dependence of exchange processes in the PAR-bound riboswitch Populations (p_{ES1}, p_{ES2}, left) and exchange rates (k_{ex1}, k_{ex2}, middle) as a function of temperature T. Right: Logarithmic rate constants k_1, k_2, k_{-1} and k_{-2} as well as equilibrium constants K_{eq} and K_{eq2} as a function of inverse temperature T^{-1}.

favoured, but both enthalpy and entropy changes are larger in the GS-ES2 process (GS-ES1: $\Delta H = 2.14 \pm 0.36\,\text{kcal mol}^{-1}$, $T\Delta S = 1.29 \pm 0.38\,\text{kcal mol}^{-1}$, GS-ES2: $\Delta H = 13.74 \pm 0.03\,\text{kcal mol}^{-1}$, $T\Delta S = 12.00 \pm 0.04\,\text{kcal mol}^{-1}$, both at 303 K).

Taken together, our data reveal, that the neomycin-sensing riboswitch exists in a dynamic equilibrium of three states when bound to PAR.

6.3.4. ^{19}F NMR enables the characterization of 4-state topologies

The successful characterization of the 3-state exchange prompted us to investigate whether the combination of complementary ^{19}F dynamics experiments has the potential to characterize topologies with more states. To this end, we first extended our 2-state system of the RIO-bound riboswitch by preparing a sample in which the riboswitch is not fully saturated with RIO, thus obtaining a 3-state topology, in which two states correspond to the RIO-bound riboswitch conformations described above, and one additional state

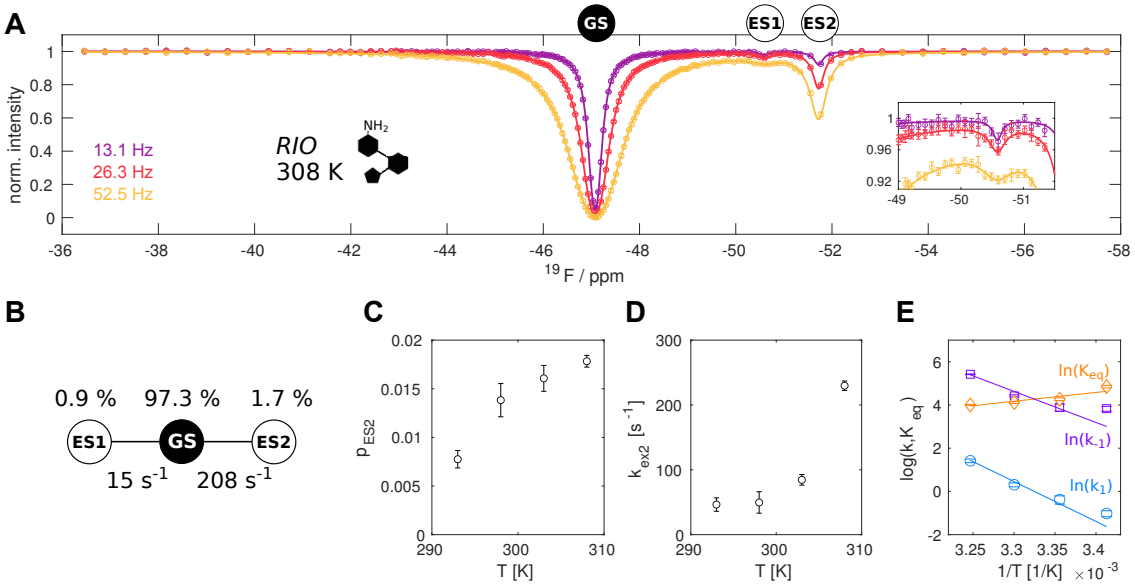

Figure 6.8.: A three-state exchange in the unsaturated RIO-bound riboswitch. (A) CEST profiles at 308 K from A17 2F at B_1 fields of 13.1 Hz, 26.3 Hz and 52.5 Hz with data (circles with errorbars) and the fit from the 2-state exchange model (solid line). The resonance positions of GS, ES1 and ES2 are indicated above the CEST spectra. The inset shows a zoom of the CEST profiles in the region of the ES1. (B) exchange parameters in the linear ES1-GS-ES2 model (C) temperature dependent populations of the unbound riboswitch (p_{ES2}) (D) temperature dependent exchange rates between the GS and ES2 (E) logarithmic plot of the rates $k_1 = k_{off}$, $k_{-1} = [RIO]_{free} \cdot k_{on}$ and $k_{eq} = k_1/k_{-1}$.

of the free riboswitch, which we designated ES2. Again, we measured ^{19}F CEST experiment for the A17 2F resonance at 293 K, 298 K, 303 K and 308 K. The population of free riboswitch is markedly visible as an additional dip at the resonance frequency of the apo state, and at 303 K and 308 K the dips originating from the excited states partially overlap (figure 6.8, figure A.33).

We fit the data using a two state model GS-ES2 at 293 K and 298 K, and a linear 3-state model ES1-GS-ES2 at 303 K and 308 K. Both the population of the free riboswitch, as well as its exchange rate with the RIO-bound GS increase significantly with temperature, in line with an entropy gain for both the transition state of the dissociating ligand, as well as its final dissociated state. From the data we obtain a $K_D = 0.27\,\mu M$ at 303 K.

Finally we turned again to the PAR-bound riboswitch, for which we aimed to extend the 3-state exchange to a 4-state exchange by measuring a non-saturated sample. We recorded a full set of ^{19}F experiments (CEST, CPMG, on-resonance $R_{1\rho}$, off-resonance $R_{1\rho}$,

ZZ-exchange) for the A17 2F resonance at 303 K, as well as reduced sets (CEST, CPMG, ZZ-exchange) at 293 K, 298 K and 308 K (figure 6.9A-E). As expected, the population of free riboswitch manifests itself in a saturation transfer from its apo resonance position around -52 ppm to both the GS and the ES1 (figure 6.9A). In line with that, we found a clear increase in the rotating frame relaxation rate $R_{1\rho}$ and its ($R_2 + R_{ex}$) contribution at the offset of the free riboswitch resonance (figure 6.9D). In contrast, both the CPMG and the on-resonance $R_{1\rho}$ experiment show minor changes compared to the fully saturated case, which suggests, that the binding exchange at the concentrations of RNA riboswitch and PAR ligand in the case under consideration is not in the intermediate-to-fast exchange limit mainly probed by on-resonance relaxation dispersion experiments. Indeed, the ZZ-exchange spectra feature weak cross peaks between GS and ES3 in addition to the strong cross peaks between GS and ES1, indicative of a slow exchange binding of PAR to the riboswitch.

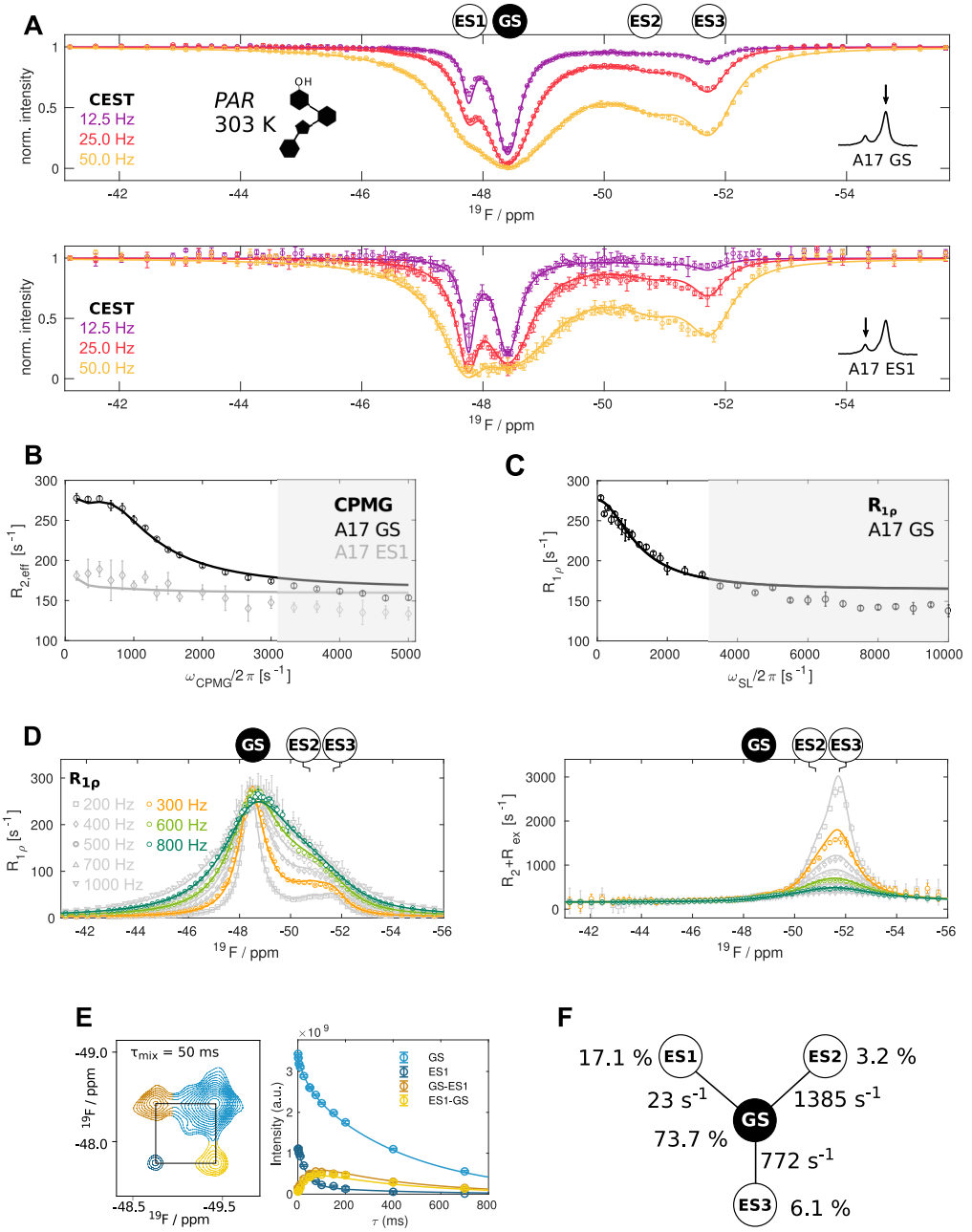

Figure 6.9.: A four-state exchange in the unsaturated PAR-bound riboswitch. (A) CEST profiles obtained from analysis of the GS and the ES1 resonances of the A17 2F probe. (B) CPMG relaxation dispersion profile of the GS and ES1. (C) On-resonance $R_{1\rho}$ relaxation dispersion profile. (D) Off-resonance $R_{1\rho}$ relaxation dispersion and $R_2 + R_{ex}$ contributions (E) Exemplary [^{19}F-^{19}F] ZZ-exchange spectrum for a mixing time of $\tau_{mix} = 50$ ms, and [^{19}F-^{19}F] ZZ-exchange data for the GS-ES1 exchange. All data in (A) to (E) were recorded for the A17 at 303 K and 11.7 T. Data points are shown as open circles with errorbars corresponding to 1 standard deviation, the fit is shown as a solid line. (F) Fit parameters for the star-like four-state model at 303 K.

Based on the linear 3-state model used above, we moved to a star-like 4-state exchange model in which all three excited states are connected to the ground state, but not with each other, to fit all datasets at 303 K simultaneously. Overall, the best fit obtained with this 4-state model explains the data well. Minor deviations are visible around ES2 and ES3 in both the CEST spectra from GS and ES1 resonances(figure 6.9A), as well as in the off-resonance $R_{1\rho}$ data (figure 6.9D). The ground state population obtained by the fit is $p_{GS} = 74.4\,\%$. The GS exchanges with a rate $k_{ex1} = 24\,s^{-1}$ with ES1, which is populated to 16.7 %, and with a rate $k_{ex2} = 1424\,s^{-1}$ with ES2, which is populated to 3.0 %. In addition to these exchange processes, which were already comprised by the 3-state model in the PAR-saturated sample, the GS also exchanges with the unbound riboswitch (ES3), which is populated to 5.9 % with a rate of $k_{ex3} = 772\,s^{-1}$. Again, we repeated the CEST, ZZ-exchange and CPMG experiments at 293 K, 298 K and 308 K (figure A.34 figure A.35) and fitted the rate constants to an Arrhenius/Eyring model (figure 6.10). As expected, the exchange from the GS to the unbound state ES3 is strongly favoured by the entropic contribution. From the fit, we obtained a dissociation constant $K_d = 4.6\,\mu M$ at 303 K.

6.4. Discussion

The starting point to generate a functional synthetic riboswitch de novo is an iterative in vitro selection of RNA molecules that bind the target ligand by SELEX (Ellington and Szostak 1990, Tuerk and Gold 1990). While the procedure opens up the possibility to engineer a switch for arbitrary molecules, and not just ligands for which a binding sequence has been found in nature, almost all aptamers obtained in this manner fall short to show regulatory activity (Weigand et al. 2008, Boussebayle et al. 2019). The reason for this failure is not simply an insufficient affinity of the ligand to the aptamer (Awwad and McKeague 2018), but rather that ligand binding does not necessarily involve a conformational change which converts binding into function. The issue can be overcome by using follow-up in vivo screening of potential riboswitch candidates (Weigand et al. 2008) or more advanced SELEX strategies (Boussebayle et al. 2019), but it points to a fundamental question: how can molecular changes in structure and dynamics of nucleic acids translate into functional changes?

The synthetic neomycin-sensing riboswitch is an attractive model system to investigate this question exemplarily. It adopts the same average structure upon binding to the aminoglycoside NEO, RIO and PAR, but the conformational flexibility of the RNA:ligand complexes differ strongly. NEO is able to stabilize the structure of two coaxially stacked stems to such a degree, that ribosomal scanning is sterically stopped, while the transient sampling of other, non-interferring states in the PAR-bound riboswitch leads to a leaky

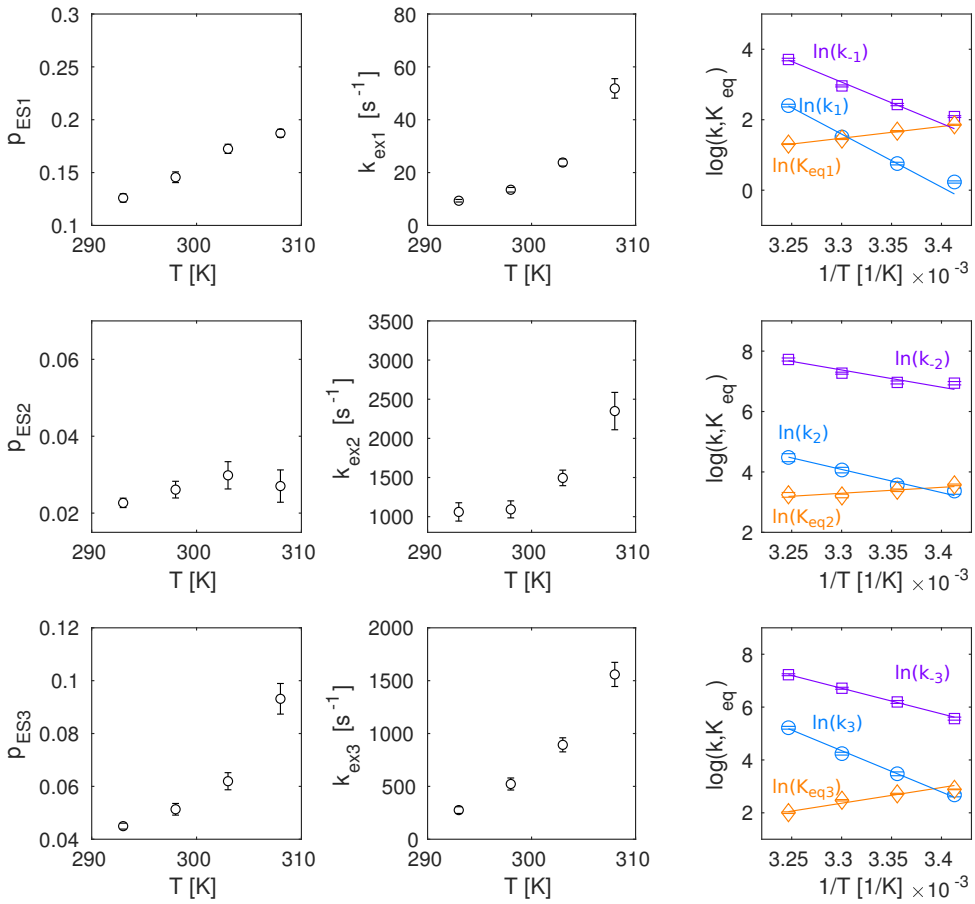

Figure 6.10.: Temperature dependence of exchange processes in the unsaturated PAR-bound riboswitch
Populations (pES1, pES2, pES3, left) and exchange rates (k_{ex1}, k_{ex2}, k_{ex3}, middle) as a function of temperature T. Right: Logarithmic rate constants k_1, k_2, k_3, k_{-1}, k_{-2} and k_{-3} as well as equilibrium constants K_{eq1}, K_{eq2} and K_{eq3} as a function of inverse temperature T^{-1}.

resistance against the small ribosomal subunit (Duchardt-Ferner et al. 2016).

Although the 27nt riboswitch is the smallest synthetic RNA-based element that functionally responds to ligand binding (Gottstein-Schmidtke et al. 2014), the dissection of its molecular basis is challenging. Insights have been obtained by mutational studies, NMR experiments, molecular dynamics (MD) and fluorescence assays (Duchardt-Ferner et al. 2010, 2016, Weigand et al. 2014, Gottstein-Schmidtke et al. 2014, Krepl et al. 2018, Kulik et al. 2018, Gustmann et al. 2019, Zhang et al. 2021, Chyży et al. 2021) . Several reports underline the importance of the apical hexaloop U13-U18 involving a canonical U-turn

motif: based on nuclease cleavage patterns, the very first study to report the synthetic riboswitch already put forward a model, in which this loop participates in a bipartite binding mode (Weigand et al. 2008), a model that was subsequently confirmed by solution NMR structures (Duchardt-Ferner et al. 2010, 2016). Interestingly, it was found that a U-to-C substitution at position 14 retained riboswitch function, while other deviations from the UNR U-turn motif were not tolerated (Weigand et al. 2014). This finding was reconciled by the discovery, that protonation of the cytosine base enables it to replace the uracil base both structurally and functionally (Gottstein-Schmidtke et al. 2014), and the results thus support the necessity of the U-turn motif. The reason for this requirement is to be found in the directly neighbouring adenosine at position 17, which is neither involved in the U-turn nor a base-pairing in the stem-loop, but which mutation moderately (A17C) or strongly (A17G, A17U) effects the regulation by the riboswitch (Weigand et al. 2014). A17 is flipped out of the hexaloop and directly contacts the ligand in a flap-like manner, a motif, which had been observed previously in a related neomycin-binding aptamer (Jiang et al. 1999). The adenine base engages in multiple interactions with the aminoglycoside, including an electrostatic interaction with the positively charged 6'-NH_3^+ group in RIO and NEO. There is no equivalent for this interaction in the presence of PAR, where the 6' amino group is replaced by an hydroxy group, and as a consequence, the A17 base is more flexible in the PAR-bound complex (Duchardt-Ferner et al. 2010).

Here, we employ A17 as a central reporter for the dynamic conformational equilibria of the riboswitch, that we probe with a combination of complementary ^{19}F NMR experiments in the presence of NEO (figure 6.3), RIO (figure 6.3, figure 6.8) and PAR (figure 6.5, figure 6.9). Upon binding to the cognate NEO ligand the complex populates two states which interconvert with an exchange rate well below 1 s^{-1}. We quantified the populations and the exchange rate based on CEST spectra recorded at low (6.3 Hz, 13.1 Hz) CEST fields, and obtained a major:minor population ratio of 68:32. However, we note that the exchange can hardly be analyzed robustly, since the exchange rate ($0.3\,s^{-1}$) is below the longitudinal relaxation rate and saturation transfer effects are accordingly relatively weak. In this regard it is noteworthy, that the relative maxima of the states in the ^{19}F 1D spectrum at 303 K indicate a ratio of 73:27 (figure 6.2).

The situation is changed in the RIO-bound riboswitch: only a single resonance is observed in the ^{19}F spectrum (figure 6.2), from which we conclude, that RIO stabilizes a single ground state. The resonance position is close to the position of the smaller peak of A17 F2 in the NEO-bound riboswitch (-47.1 ppm versus -47.3 ppm), which suggests, that the minor conformation in the NEO complex and the ground state in the RIO complex are conformationally similar. In addition, we detected a minor state at 303 K and

308 K, which is populated to less than 1 % and upfield shifted from the ground state by 3.5 ppm to -50.6 ppm (figure 6.3). This is close to the resonance of the free riboswitch and indicates, that the A17 base is less tightly bound to the ligand than in the ground state. Even though this riboswitch is therefore locked most of the time in a presumably stable state that cannot be resolved by the scanning small ribosomal subunit, it opens up transiently when it samples the excited state, and allows for the scanning subunit to pass.

The PAR-bound riboswitch has been shown to be locally and globally more dynamic than its RIO- or NEO-bound counterparts (Duchardt-Ferner et al. 2016). Specifically, the NMR experiments reveal, that the PAR 6'-OH group engages in a hydrogen bond to the G9 phosphate group. The stability of this hydrogen bond has been questioned by MD simulations, however, both studies arrive at the conclusion, that the loss of interactions at the 6' position of the aminoglycoside leads to increased dynamics in the apical loop and a more mobile A17 residue (Kulik et al. 2018). Our results support this finding, as we observe, that A17 samples three states in the presence of PAR. Two of these states exchange slowly and are homologous to the slowly exchanging states in the NEO-bound riboswitch, since both are shifted upfield by -0.48 ppm and have similar relative populations (figure 6.3, figure 6.5). The third state likely resembles the excited state found in the RIO-complex, as both have similar chemical shifts (figure 6.3, figure 6.5). However, both the population of this state as well as its exchange rate with the ground state are strongly increased, indicating a relative stabilization of the excited state as well as its corresponding transition state. Interestingly, it was reported in MD simulations that A17 can flip out of its binding to the ligand when PAR is bound (Kulik et al. 2018), an event that was not observed for NEO or RIO. The simulations were carried out for 100 ns with replica exchange and analyzed at 310.15 K and 311.13 K, which is close to the temperature of 308 K for which we found a marginal population of 0.7 % in the RIO-bound complex (figure 6.3B). It is therefore possible, that the flipping-out of A17 represents the excited state visible in our experiments with RIO and PAR, but goes undetected in the MD traces for RIO, because the event is too rare. Structurally, this interpretation is supported first by the observation, that the excited state resonance is close to the free state resonance, and second, by the large entropic contribution to the exchange process.

Taken together, our results point to a modular influence of the aminoglycoside nature on the conformational energy landscape of the bound complex: first, the aminoglycoside ring IV in NEO and PAR leads to the stabilization of two substantially populated states that exchange slowly. Ring IV is unconstrained in the NMR solution structure (Duchardt-Ferner et al. 2016), but MD simulations indicate, that it contacts the phosphate groups of U18 and G19 (Chyży et al. 2021). The two states could thus represent sub-

ensembles in which ring IV is either docked to the RNA backbone, or undocked, which is in turn sensed by the nearby A17. Second, the replacement of the 6'-NH_3^+ group by 6'-OH destabilizes key aminoglycoside:RNA interactions, which favors the flipping-out to an even larger extent than the loss of ring IV.

Our work also highlights the scope of ^{19}F NMR to directly characterize complex exchange topologies with more than one excited state. Examples for multisite ($n > 2$) exchange directly quantified by NMR are generally rare, and include 3-state protein unfolding transitions with folding intermediates using ^{1}H/^{15}N CPMG experiments (Korzhnev et al. 2004c, 2005a, 2007, Neudecker et al. 2006, Tugarinov et al. 2015) or ^{15}N CEST experiments (Lim et al. 2014, Vallurupalli et al. 2019), 3-state RNA and DNA landscapes with transient Watson-Crick-like tautomeric and anionic mispairs using ^{15}N and ^{13}C off-resonance $R_{1\rho}$ experiments (Kimsey et al. 2015, 2018), and a 4-state chaperonin-binding/folding system using ^{15}N DEST and ^{15}N CPMG experiments (Libich et al. 2015). Notably, the detection of distinct states by deconvolution of one-dimensional spectra has been a strength of ^{19}F NMR for challenging systems such as membrane proteins (Kim et al. 2013, Horst et al. 2013, Manglik et al. 2015, Ye et al. 2018, 2016, Eddy et al. 2016, Sušac et al. 2018, Huang et al. 2020, 2021, Frei et al. 2020), and ^{19}F CPMG (Manglik et al. 2015), ^{19}F saturation transfer (Manglik et al. 2015, Kim et al. 2017, Heidari et al. 2019) and ZZ-exchange experiments (Horst et al. 2013, Huang et al. 2020) have been used to verify and quantify the dynamic nature of these systems.

Here we show that exchange scenarios with up to four states can be quantified with ^{19}F NMR in favourable cases. To this end, we used the strengths of five different ^{19}F experiments, the combination of which has two important features: First, the experiments bridge the NMR exchange timescales from slow to fast exchange. Second, the off-resonance experiments (CEST, $R_{1\rho}$) allow for the faithfull characterization of more than one excited state. We note that ^{19}F NMR generally profits from the large chemical shift dispersion of fluorine probes, although it comes at the cost of large chemical shift anisotropies (CSA) and thus increased linewidths (Kitevski-LeBlanc and Prosser 2012). When it comes to experiments that probe biomolecular dynamics, a larger chemical shift difference between two conformational states has the specific advantage, that it leads to more pronounced relaxation dispersion profiles (CPMG, on-resonance $R_{1\rho}$) and the possibility to separate excited states based on their resonance frequency (CEST, off-resonance $R_{1\rho}$). In our case of the PAR-complex, a difference between GS and ES2 of $\Delta\omega_F$ = 2.52 ppm = $1184 \cdot 2\pi$ Hz puts the exchange with $k_{ex} = 1982$ Hz into the intermediate exchange regime which is perfectly suited for relaxation dispersion studies. At the same time, the exchange between GS and ES3 (free state) with $\Delta\omega_F$ = 3.34 ppm = $1570 \cdot 2\pi$ Hz is in the

slow exchange, despite its exchange constant of $\sim 800\,s^{-1}$.

The ^{19}F CEST experiments turned out to be particularly powerful for the ligand:riboswitch complex studied here, and aided in the characterization of exchange rates from below 1 Hz to over 2000 Hz. Conformational dynamics of nucleic acids have been characterized previously using ^{13}C CEST on C8 and C1′ carbons (Zhao et al. 2014, 2017, Liu et al. 2021), ^{15}N CEST on A-N1/N3/N7, G-N1,N7 and U-N3 nitrogens (Zhao et al. 2020, Liu et al. 2021) and ^{1}H CEST on purine H2 and H8, pyrimidine H6, formylcytosine H7, and $^{1}H^{N}$ imino protons (Dubini et al. 2020, Liu et al. 2021, Wang et al. 2021). Apart from the sugar carbon C1′, these experiments focus on probes in the nucleobases, which are sensitive reporters of canonical and non-canonical base-pairing interactions and can provide structural information about the excited state. In principle, the A-F2 probe shares these advantages, although correlative information of structure and chemical shift is still sparse. Importantly, a number of alternative ways to include ^{19}F probes in nucleic acids have been developed, including 5-fluoropyrimidines (Horowitz et al. 1977, Hennig et al. 2007, Puffer et al. 2009), ribose F2′ labeling (Kreutz et al. 2005), 5′-fluoromonophosphate and 5′-fluorodiphosphate labeling (Baranowski et al. 2020), trifluorothymidine (Gmeiner et al. 1991), trifluoromethylated purine ribonucleotides (Chrominski et al. 2020), 2′-O-trifluoromethylated ribonucleotides (Himmelstoß et al. 2020) and [^{19}F,^{13}C] pyrimidine labeling for ^{19}F-^{13}C TROSY experiments (Nußbaumer et al. 2020). We thus anticipate that the combination of different ^{19}F labeling techniques with the set of ^{19}F experiments used here will aid the characterization of complex systems involving nucleic acids.

7. Discussion and Outlook

Structural biology is changing dramatically. The technological advancement in protein structure prediction by AlphaFold (Jumper et al. 2021) is already disruptive on its own, and integrative modeling of AlphaFold predictions together with experimental cryo-EM data and other techniques promises to elucidate the architecture of molecular machines on a new level. In this light, the capacity of NMR to solve biomolecular structures becomes secondary. Instead, one exciting future direction is given by the characterization of energy landscapes and their alteration upon changes in the system. Past NMR studies have revealed fundamental mechanisms, such as the vulnerability of DNA towards fidelity checkpoint evasion and misincorporation of nucleotides due to excited states that are sparsely populated (Kimsey et al. 2015, 2018). At the same time, research has successfully been applied to specific systems, such as the tyrosine-protein kinase Abl, for which NMR experiments revealed the role of distinct conformations and the alteration of the energy landscape in oncogenic mutants (Xie et al. 2020). Other examples include the studies of assembly pathways for chaperone function (Toyama et al. 2021, Harkness et al. 2021), chaperonin:ligand systems (Libich et al. 2015) or the influence of editing alterations such as 5-formylcytosine (Dubini et al. 2020) or N^6-methyladenosine (m^6A) (Liu et al. 2021).

The work presented in this dissertation expands existing NMR methodology by adding ^{19}F on-resonance and off-resonance $R_{1\rho}$ as well as quantitative ^{19}F CEST experiments and by validating these experiments on a two-state folding model system (chapter 4), on multi-site exchanging riboswitch:ligand systems (chapter 6), on the double-heptameric 360 kDa half-proteasome (chapter 4) and on the 5′-3′ exoribonuclease Xrn2 (chapter 5). Previous studies have demonstrated that ^{19}F NMR is a valuable tool to assess and quantify conformational changes in challenging systems such as GPCRs (Liu et al. 2012, Manglik et al. 2015) or to guide cryo-EM structure solution by the identification of sparsely sampled conformations (Huang et al. 2020). A bottleneck in the application of ^{19}F CPMG relaxation dispersion experiments to high-molecular weight assemblies has been the need to use short CPMG times in order to retain a quantifyable signal in the presence of fast transverse relaxation. This limitation in turn establishes a lower limit for the CPMG frequencies that can be measured. Since these low frequency data can carry substantial

information about the exchange process, the limitation is a severe one. Our ^{19}F $R_{1\rho}$ experiments do not suffer in the same manner from this limitation and aid the characterization of dynamics in these situations, although fast relaxation and signal broadening of course remains a serious issue and optimization of ^{19}F-labeling schemes for large biomolecular machines is certainly helpful. Aside from applications to large complexes, the possibility to perform rotating frame relaxation with low spin-lock fields has the additional advantage that full exchange parameter sets can be retrieved from measurements at a single static magnetic field B_0.

The molecular weight boundaries of solution-state NMR have been pushed significantly by the development of advanced strategies for $^{13}CH_3$ methyl labeling in a perdeuterated background (Schütz and Sprangers 2020). The depletion of external protons in conjunction with destructive interferences of dipolar interactions within the methyl group (Tugarinov et al. 2003, Ollerenshaw et al. 2003) gives rise to relatively small transverse relaxation rate constants for certain density matrix elements. Regarding ^{1}H-^{13}C correlation, this methyl-TROSY effect is exploited in an optimal way in the HMQC experiment, and HMQC-based experiments are valuable tools to study dynamics in high molecular weight systems. Here, I applied $^{1}H^{13}C$ HMQC, $^{1}H^{13}C$ MQ-CPMG and ^{13}C SQ-CPMG experiments to the 5'-3' exoribonuclease Xrn2 (chapter 5), which allowed to characterize dynamics of the apo-protein and to derive information about conformational changes induced by slowly degraded substrates. Xrn2 is among the largest single chain proteins for which dynamics have been characterized using solution state NMR methods. The presence of localized motions in Xrn2 was corroborated by ^{19}F CPMG and $R_{1\rho}$ experiments on site-specifically introduced trifluoromethyl probes. Importantly, the use of ^{19}F experiments also allowed to record triplicate CPMG datasets on samples of catalytically active Xrn2 bound to substrates within hours. Although the substrates are added in excess, their cumulative degradation over time is too fast to enable pseudo-3D CPMG experiments on methyl groups, which typically take at least 12 hours for proteins of this size. The combination of static structures derived from X-ray crystallography, cryo-EM or even *in silico* prediction with complementary isotope labeling techniques such as $^{13}CH_3$ methyl group and CF_3 trifluoromethyl group labeling thus represents an attractive avenue of exploration for NMR.

Finally, an important result of this dissertation is the principle proof, that ^{19}F off-resonance experiments can be used to characterize complex exchange situations with more than one excited state (chapter 6). A fundamental problem of CPMG and on-resonance $R_{1\rho}$ experiments in this case is, that contributions from different exchange processes are not directly separable and the profiles can often be reasonably explained with a two-state fit. In prin-

ciple, this problem can be solved by subjecting different fitting models to rigorous statistical testing. Off-resonance experiments offer a more direct way to verify the existence of two or more excited states: as long as these states are separated by a sufficent chemical shift difference $\Delta\omega$, they will give rise to distinct signals in the profile. In my dissertation, I established ^{19}F off-resonance $R_{1\rho}$ and ^{19}F CEST experiments as methods that can unambiguously provide evidence in such a situation. With the aid of these experiments, exchange scenarios with up to four states could be quantified in different ligand:NEO-riboswitch samples. It should be noted, that the high chemical shift sensitivity of the fluorine nucleus to changes in its local environment benefits off-resonance experiments, although these benefits are partially counteracted by the high relaxation rate constants usually encountered for ^{19}F probes.

In summary, in this thesis I developed and applied NMR methods that are able to identify and quantify dynamics in proteins and RNA. The information obtained in this manner can complement static structural knowledge and thereby enhance our understanding of how molecular machines function.

Bibliography

D. Abergel and A. G. Palmer. On the use of the stochastic liouville equation in nuclear magnetic resonance: Application to R 1ρ relaxation in the presence of exchange. *Concepts in Magnetic Resonance Part A: Bridging Education and Research*, 19(2):134–148, 2003. doi: 10.1002/cmr.a.10091.

D. Abergel and A. G. Palmer. A Markov Model for Relaxation and Exchange in NMR Spectroscopy. *The Journal of Physical Chemistry B*, 109(11):4837–4844, Mar. 2005. ISSN 1520-6106, 1520-5207. doi: 10.1021/jp0458304. URL https://pubs.acs.org/doi/10.1021/jp0458304.

M. H. Abobeih, J. Randall, C. E. Bradley, H. P. Bartling, M. A. Bakker, M. J. Degen, M. Markham, D. J. Twitchen, and T. H. Taminiau. Atomic-scale imaging of a 27-nuclear-spin cluster using a quantum sensor. *Nature*, 576(7787):411–415, Dec. 2019. ISSN 0028-0836, 1476-4687. doi: 10.1038/s41586-019-1834-7. URL http://www.nature.com/articles/s41586-019-1834-7.

A. Abragam. *The principles of nuclear magnetism*. The international series of monographs on physics. Clarendon Pr, Oxford, repr edition, 1986. ISBN 978-0-19-851236-3 978-0-19-852014-6.

R. J. Abraham, A. D. Jones, M. A. Warne, R. Rittner, and C. F. Tormena. Conformational analysis. Part 27. NMR, solvation and theoretical investigation of conformational isomerism in fluoro- and 1,1-difluoroacetone. *Journal of the Chemical Society, Perkin Transactions 2*, (4):533, 1996. ISSN 0300-9580, 1364-5471. doi: 10.1039/p29960000533. URL http://xlink.rsc.org/?DOI=p29960000533.

G. Abramov, A. Velyvis, E. Rennella, L. E. Wong, and L. E. Kay. A methyl-TROSY approach for NMR studies of high-molecular-weight DNA with application to the nucleosome core particle. *Proceedings of the National Academy of Sciences*, 117(23):12836–12846, June 2020. ISSN 0027-8424, 1091-6490. doi: 10.1073/pnas.2004317117. URL http://www.pnas.org/lookup/doi/10.1073/pnas.2004317117.

V. Agarwal, Z. D. Miles, J. M. Winter, A. S. Eustáquio, A. A. El Gamal, and B. S. Moore. Enzymatic Halogenation and Dehalogenation Reactions: Pervasive and Mechanistically Diverse. *Chemical Reviews*, 117(8):5619–5674, Apr. 2017. ISSN 0009-2665, 1520-6890. doi: 10.1021/acs.chemrev.6b00571. URL https://pubs.acs.org/doi/10.1021/acs.chemrev.6b00571.

B. M. Akiyama, H. M. Laurence, A. R. Massey, D. A. Costantino, X. Xie, Y. Yang, P.-Y. Shi, J. C. Nix, J. D. Beckham, and J. S. Kieft. Zika virus produces noncoding RNAs using a multi-pseudoknot structure that confounds a cellular exonuclease. *Science*, 354(6316):1148–1152, Dec. 2016. ISSN 0036-8075, 1095-9203. doi: 10.1126/science.aah3963. URL https://www.sciencemag.org/lookup/doi/10.1126/science.aah3963.

M. Akke and A. G. Palmer. Monitoring macromolecular motions on microsecond to millisecond time scales by R1p-R1 constant relaxation time NMR spectroscopy. *Journal of the American Chemical Society*, 118(4):911–912, 1996. doi: 10.1021/ja953503r.

T. R. Alderson and L. E. Kay. Unveiling invisible protein states with NMR spectroscopy. *Current Opinion in Structural Biology*, 60:39–49, Feb. 2020. ISSN 0959440X. doi: 10.1016/j.sbi.2019.10.008. URL https://linkinghub.elsevier.com/retrieve/pii/S0959440X19301186.

A. Allerhand and E. Thiele. Analysis of Carr—Purcell Spin-Echo NMR Experiments on Multiple-Spin Systems. II. The Effect of Chemical Exchange. *The Journal of Chemical Physics*, 45(3):902–916, Aug. 1966. ISSN 0021-9606, 1089-7690. doi: 10.1063/1.1727703. URL http://aip.scitation.org/doi/10.1063/1.1727703.

D. C. Amberg and A. L. Goldstein. Isolation and characterization of RATI: an essential gene of Saccharomyces cerevisiae required for the efficient nucleocytoplasmic trafficking of mRNA. *Genes & Development*, 6(7):1173–1189, July 1992. ISSN 0890-9369, 1549-5477. doi: 10.1101/gad.6.7.1173. URL http://genesdev.cshlp.org/lookup/doi/10.1101/gad.6.7.1173.

N. J. Anthis and G. M. Clore. Visualizing transient dark states by NMR spectroscopy. *Quarterly Reviews of Biophysics*, 48(1):35–116, Feb. 2015. ISSN 0033-5835, 1469-8994. doi: 10.1017/S0033583514000122. URL https://www.cambridge.org/core/product/identifier/S0033583514000122/type/journal_article.

S. Antic, M. T. Wolfinger, A. Skucha, S. Hosiner, and S. Dorner. General and MicroRNA-Mediated mRNA Degradation Occurs on Ribosome Complexes in Drosophila Cells. *Molecular and Cellular Biology*, 35(13):2309–2320, July 2015. ISSN 0270-7306, 1098-5549. doi: 10.1128/MCB.01346-14. URL https://journals.asm.org/doi/10.1128/MCB.01346-14.

J. M. Aramini, K. Hamilton, L.-C. Ma, G. Swapna, P. G. Leonard, J. E. Ladbury, R. M. Krug, and G. T. Montelione. 19F NMR Reveals Multiple Conformations at the Dimer Interface of the Nonstructural Protein 1 Effector Domain from Influenza A Virus. *Structure*, 22(4):515–525, Apr. 2014. ISSN 09692126. doi: 10.1016/j.str.2014.01.010. URL https://linkinghub.elsevier.com/retrieve/pii/S0969212614000380.

J. R. Arnold and J. Fisher. Structural Equilibria in RNA as Revealed by ^{19} NMR. *Journal of Biomolecular Structure and Dynamics*, 17(5):843–856, Apr. 2000. ISSN 0739-1102, 1538-0254. doi: 10.1080/07391102.2000.10506573. URL http://www.tandfonline.com/doi/abs/10.1080/07391102.2000.10506573.

M. J. Audin, G. Dorn, S. A. Fromm, K. Reiss, S. Schütz, M. K. Vorländer, and R. Sprangers. The archaeal exosome: Identification and quantification of site-specific motions that correlate with Cap and RNA binding. *Angewandte Chemie - International Edition*, 52(32):8312–8316, 2013. doi: 10.1002/anie.201302811.

R. Auer, P. Neudecker, D. R. Muhandiram, P. Lundström, D. F. Hansen, R. Konrat, and L. E. Kay. Measuring the Signs of ^{1} H $^{\alpha}$ Chemical Shift Differences Between Ground and Excited Protein States by Off-Resonance Spin-Lock $R_{1\rho}$ NMR Spectroscopy. *Journal of the American Chemical Society*, 131(31):10832–10833, Aug. 2009. ISSN 0002-7863, 1520-5126. doi: 10.1021/ja904315m. URL https://pubs.acs.org/doi/10.1021/ja904315m.

A. M. Awwad and M. McKeague. Riboswitches and synthetic aptamers: a head-to-head comparison. *Aptamers*, 2:1–10, 2018. URL http://japtamers.co.uk/riboswitches-and-synthetic-aptamers-a-head-to-head-comparison/.

A. D. Bain and J. A. Cramer. Optimal NMR measurements for slow exchange in two-site and three-site systems. *The Journal of Physical Chemistry*, 97(12):2884–2887, Mar. 1993. ISSN 0022-3654, 1541-5740. doi: 10.1021/j100114a010. URL https://pubs.acs.org/doi/abs/10.1021/j100114a010.

Bibliography

A. J. Baldwin. An exact solution for R2,eff in CPMG experiments in the case of two site chemical exchange. *Journal of Magnetic Resonance*, 244:114–124, July 2014. ISSN 10907807. doi: 10.1016/j.jmr.2014.02.023. URL https://linkinghub.elsevier.com/retrieve/pii/S1090780714000743.

A. J. Baldwin and L. E. Kay. NMR spectroscopy brings invisible protein states into focus. *Nature Chemical Biology*, 5(11):808–814, Nov. 2009. ISSN 1552-4450, 1552-4469. doi: 10.1038/nchembio.238. URL http://www.nature.com/articles/nchembio.238.

A. J. Baldwin and L. E. Kay. Measurement of the signs of methyl 13C chemical shift differences between interconverting ground and excited protein states by R 1ρ : an application to αB-crystallin. *Journal of Biomolecular NMR*, 53(1):1–12, May 2012. ISSN 0925-2738, 1573-5001. doi: 10.1007/s10858-012-9617-6. URL http://link.springer.com/10.1007/s10858-012-9617-6.

A. J. Baldwin, T. L. Religa, D. F. Hansen, G. Bouvignies, and L. E. Kay. 13CHD2 Methyl group probes of millisecond time scale exchange in proteins by 1H relaxation dispersion: An application to proteasome gating residue dynamics. *Journal of the American Chemical Society*, 132(32):10992–10995, 2010. doi: 10.1021/ja104578n.

H.-L. Bao, T. Ishizuka, T. Sakamoto, K. Fujimoto, T. Uechi, N. Kenmochi, and Y. Xu. Characterization of human telomere RNA G-quadruplex structures in vitro and in living cells using 19F NMR spectroscopy. *Nucleic Acids Research*, 45(9):5501–5511, May 2017. ISSN 0305-1048, 1362-4962. doi: 10.1093/nar/gkx109. URL https://academic.oup.com/nar/article-lookup/doi/10.1093/nar/gkx109.

M. R. Baranowski, M. Warminski, J. Jemielity, and J. Kowalska. 5'-fluoro(di)phosphate-labeled oligonucleotides are versatile molecular probes for studying nucleic acid secondary structure and interactions by 19F NMR. *Nucleic Acids Research*, 48(15):8209–8224, Sept. 2020. ISSN 0305-1048, 1362-4962. doi: 10.1093/nar/gkaa470. URL https://academic.oup.com/nar/article/48/15/8209/5854145.

I. Bertini, S. Ciurli, A. Dikiy, R. Gasanov, C. Luchinat, G. Martini, and N. Safarov. High-Field NMR Studies of Oxidized Blue Copper Proteins: The Case of Spinach Plastocyanin. *Journal of the American Chemical Society*, 121(10):2037–2046, Mar. 1999. ISSN 0002-7863, 1520-5126. doi: 10.1021/ja983833m. URL https://pubs.acs.org/doi/10.1021/ja983833m.

F. Bloch. Nuclear Induction. *Physical Review*, 70(7-8):460–474, Oct. 1946. ISSN 0031-899X. doi: 10.1103/PhysRev.70.460. URL https://link.aps.org/doi/10.1103/PhysRev.70.460.

D. D. Boehr, D. McElheny, H. J. Dyson, and P. E. Wrightt. The dynamic energy landscape of dihydrofolate reductase catalysis. *Science*, 313(5793):1638–1642, 2006. doi: 10.1126/science.1130258.

A. Boeszoermenyi, S. Chhabra, A. Dubey, D. L. Radeva, N. T. Burdzhiev, C. D. Chanev, O. I. Petrov, V. M. Gelev, M. Zhang, C. Anklin, H. Kovacs, G. Wagner, I. Kuprov, K. Takeuchi, and H. Arthanari. Aromatic 19 F- 13 C TROSY: a background-free approach to probe biomolecular structure, function, and dynamics. *Nature Methods*, 16(4):333–340, 2019. ISSN 4159201903. doi: 10.1038/s41592-019-0334-x. URL http://dx.doi.org/10.1038/s41592-019-0334-x.

J. R. Bothe, Z. W. Stein, and H. M. Al-Hashimi. Evaluating the uncertainty in exchange parameters determined from off-resonance R1ρ relaxation dispersion for systems in fast exchange. *Journal of Magnetic Resonance*, 244:18–29, July 2014. ISSN 10907807. doi: 10.1016/j.jmr.2014.04.010. URL https://linkinghub.elsevier.com/retrieve/pii/S1090780714001177.

A. Boussebayle, D. Torka, S. Ollivaud, J. Braun, C. Bofill-Bosch, M. Dombrowski, F. Groher, K. Hamacher, and B. Suess. Next-level riboswitch development—implementation of Capture-SELEX facilitates identification of a new synthetic riboswitch. *Nucleic Acids Research*, 47(9):4883–4895, May 2019. ISSN 0305-1048, 1362-4962. doi: 10.1093/nar/gkz216. URL https://academic.oup.com/nar/article/47/9/4883/5430835.

G. Bouvignies and L. E. Kay. A 2D 13C-CEST experiment for studying slowly exchanging protein systems using methyl probes: An application to protein folding. *Journal of Biomolecular NMR*, 53(4):303–310, 2012. doi: 10.1007/s10858-012-9640-7.

G. Brändén and R. Neutze. Advances and challenges in time-resolved macromolecular crystallography. *Science*, 373(6558):eaba0954, Aug. 2021. ISSN 0036-8075, 1095-9203. doi: 10.1126/science.aba0954. URL https://www.science.org/doi/10.1126/science.aba0954.

U. Brath, M. Akke, D. Yang, L. E. Kay, and F. A. A. Mulder. Functional Dynamics of Human FKBP12 Revealed by Methyl ^{13} C Rotating Frame Relaxation Dispersion NMR Spectroscopy. *Journal of the American Chemical Society*, 128(17):5718–5727, May 2006. ISSN 0002-7863, 1520-5126. doi: 10.1021/ja0570279. URL https://pubs.acs.org/doi/10.1021/ja0570279.

M. Brauer and B. D. Sykes. 19F Nuclear Magnetic Resonance Studies of Selectively Fluorinated Derivatives of G-and F-Actin. *Biochemistry*, 25(8):2187–2191, 1986. doi: 10.1021/bi00356a050.

H. Y. Carr and E. M. Purcell. Effects of Diffusion on Free Precession in Nuclear Magnetic Resonance Experiments. *Physical Review*, 94(3):630–638, May 1954. ISSN 0031-899X. doi: 10.1103/PhysRev.94.630. URL https://link.aps.org/doi/10.1103/PhysRev.94.630.

J. Carver and R. Richards. A general two-site solution for the chemical exchange produced dependence of T2 upon the carr-Purcell pulse separation. *Journal of Magnetic Resonance (1969)*, 6(1):89–105, Jan. 1972. ISSN 00222364. doi: 10.1016/0022-2364(72)90090-X. URL https://linkinghub.elsevier.com/retrieve/pii/002223647290090X.

J. Cavanagh, editor. *Protein NMR spectroscopy: principles and practice*. Academic Press, Amsterdam ; Boston, 2nd ed edition, 2007. ISBN 978-0-12-164491-8. OCLC: ocm70218044.

A. Ceccon, V. Tugarinov, and G. M. Clore. Quantitative Exchange NMR-Based Analysis of Huntingtin–SH3 Interactions Suggests an Allosteric Mechanism of Inhibition of Huntingtin Aggregation. *Journal of the American Chemical Society*, 143(25):9672–9681, June 2021. ISSN 0002-7863, 1520-5126. doi: 10.1021/jacs.1c04786. URL https://pubs.acs.org/doi/10.1021/jacs.1c04786.

J. H. Chang, S. Xiang, K. Xiang, J. L. Manley, and L. Tong. Structural and biochemical studies of the 5′ → 3′ exoribonuclease Xrn1. *Nature Structural & Molecular Biology*, 18(3):270–276, Mar. 2011. ISSN 1545-9993, 1545-9985. doi: 10.1038/nsmb.1984. URL http://www.nature.com/articles/nsmb.1984.

S. Chatterjee and H. Großhans. Active turnover modulates mature microRNA activity in Caenorhabditis elegans. *Nature*, 461(7263):546–549, Sept. 2009. ISSN 0028-0836, 1476-4687. doi: 10.1038/nature08349. URL http://www.nature.com/articles/nature08349.

I. Chernyakov, J. M. Whipple, L. Kotelawala, E. J. Grayhack, and E. M. Phizicky. Degradation of several hypomodified mature tRNA species in Saccharomyces cerevisiae is mediated by Met22 and the 5′-3′ exonucleases Rat1 and Xrn1. *Genes & Development*, 22(10):1369–1380, May 2008. ISSN 0890-9369. doi: 10.1101/gad.1654308. URL http://www.genesdev.org/cgi/doi/10.1101/gad.1654308.

M. Chrominski, M. R. Baranowski, S. Chmielinski, J. Kowalska, and J. Jemielity. Synthesis of Trifluoromethylated Purine Ribonucleotides and Their Evaluation as ^{19} F NMR Probes. *The Journal of Organic Chemistry*, 85(5):3440–3453, Mar. 2020. ISSN 0022-3263, 1520-6904. doi: 10.1021/acs.joc.9b03198. URL https://pubs.acs.org/doi/10.1021/acs.joc.9b03198.

C. Z. Chung, L. E. Seidl, M. R. Mann, and I. U. Heinemann. Tipping the balance of RNA stability by 3' editing of the transcriptome. *Biochimica et Biophysica Acta (BBA) - General Subjects*, 1861(11):2971–2979, Nov. 2017. ISSN 03044165. doi: 10.1016/j.bbagen.2017.05.003. URL https://linkinghub.elsevier.com/retrieve/pii/S0304416517301472.

H. S. Chung, K. McHale, J. M. Louis, and W. A. Eaton. Single-molecule fluorescence experiments determine protein folding transition path times. *Science*, 335(6071):981–984, 2012. doi: 10.1126/science.1215768.

P. Chyży, M. Kulik, S. Re, Y. Sugita, and J. Trylska. Mutations of N1 Riboswitch Affect its Dynamics and Recognition by Neomycin Through Conformational Selection. *Frontiers in Molecular Biosciences*, 8:633130, Feb. 2021. ISSN 2296-889X. doi: 10.3389/fmolb.2021.633130. URL https://www.frontiersin.org/articles/10.3389/fmolb.2021.633130/full.

B. Clouet-d'Orval, D. K. Phung, P. S. Langendijk-Genevaux, and Y. Quentin. Universal RNA-degrading enzymes in Archaea: Prevalence, activities and functions of β-CASP ribonucleases. *Biochimie*, 118:278–285, Nov. 2015. ISSN 03009084. doi: 10.1016/j.biochi.2015.05.021. URL https://linkinghub.elsevier.com/retrieve/pii/S0300908415001716.

P. B. Crowley, C. Kyne, and W. B. Monteith. Simple and inexpensive incorporation of 19F-Tryptophan for protein NMR spectroscopy. *Chemical Communications*, 48(86):10681–10683, 2012. doi: 10.1039/c2cc35347d.

K. S. Cujia, J. M. Boss, K. Herb, J. Zopes, and C. L. Degen. Tracking the precession of single nuclear spins by weak measurements. *Nature*, 571(7764):230–233, July 2019. ISSN 0028-0836, 1476-4687. doi: 10.1038/s41586-019-1334-9. URL http://www.nature.com/articles/s41586-019-1334-9.

M. A. Danielson and J. J. Falke. Use of 19F NMR to Probe Protein Structure and Conformational Changes. *Annual Review of Biophysics and Biomolecular Structure*, 25(1):163–195, June 1996. ISSN 1056-8700, 1545-4266. doi: 10.1146/annurev.bb.25.060196.001115. URL https://www.annualreviews.org/doi/10.1146/annurev.bb.25.060196.001115.

L. Davidson, A. Kerr, and S. West. Co-transcriptional degradation of aberrant pre-mRNA by Xrn2: Degradation of aberrant pre-mRNA by Xrn2. *The EMBO Journal*, 31(11):2566–2578, May 2012. ISSN 02614189. doi: 10.1038/emboj.2012.101. URL http://emboj.embopress.org/cgi/doi/10.1038/emboj.2012.101.

F. Delaglio, S. Grzesiek, G. Vuister, G. Zhu, J. Pfeifer, and A. Bax. NMRPipe: A multidimensional spectral processing system based on UNIX pipes. *Journal of Biomolecular NMR*, 6(3), Nov. 1995. ISSN 0925-2738, 1573-5001. doi: 10.1007/BF00197809. URL http://link.springer.com/10.1007/BF00197809.

B. Dichtl. Lithium toxicity in yeast is due to the inhibition of RNA processing enzymes. *The EMBO Journal*, 16(23):7184–7195, Dec. 1997. ISSN 14602075. doi: 10.1093/emboj/16.23.7184. URL http://emboj.embopress.org/cgi/doi/10.1093/emboj/16.23.7184.

S. Djebali, C. A. Davis, A. Merkel, A. Dobin, T. Lassmann, A. Mortazavi, A. Tanzer, J. Lagarde, W. Lin, F. Schlesinger, C. Xue, G. K. Marinov, J. Khatun, B. A. Williams, C. Zaleski, J. Rozowsky, M. Röder, F. Kokocinski, R. F. Abdelhamid, T. Alioto, I. Antoshechkin, M. T. Baer, N. S. Bar, P. Batut, K. Bell, I. Bell,

S. Chakrabortty, X. Chen, J. Chrast, J. Curado, T. Derrien, J. Drenkow, E. Dumais, J. Dumais, R. Duttagupta, E. Falconnet, M. Fastuca, K. Fejes-Toth, P. Ferreira, S. Foissac, M. J. Fullwood, H. Gao, D. Gonzalez, A. Gordon, H. Gunawardena, C. Howald, S. Jha, R. Johnson, P. Kapranov, B. King, C. Kingswood, O. J. Luo, E. Park, K. Persaud, J. B. Preall, P. Ribeca, B. Risk, D. Robyr, M. Sammeth, L. Schaffer, L.-H. See, A. Shahab, J. Skancke, A. M. Suzuki, H. Takahashi, H. Tilgner, D. Trout, N. Walters, H. Wang, J. Wrobel, Y. Yu, X. Ruan, Y. Hayashizaki, J. Harrow, M. Gerstein, T. Hubbard, A. Reymond, S. E. Antonarakis, G. Hannon, M. C. Giddings, Y. Ruan, B. Wold, P. Carninci, R. Guigó, and T. R. Gingeras. Landscape of transcription in human cells. *Nature*, 489(7414):101–108, Sept. 2012. ISSN 0028-0836, 1476-4687. doi: 10.1038/nature11233. URL `http://www.nature.com/articles/nature11233`.

C. Dong, F. Huang, H. Deng, C. Schaffrath, J. B. Spencer, D. O'Hagan, and J. H. Naismith. Crystal structure and mechanism of a bacterial fluorinating enzyme. 427:5, 2004.

R. C. A. Dubini, A. Schön, M. Müller, T. Carell, and P. Rovó. Impact of 5-formylcytosine on the melting kinetics of DNA by 1H NMR chemical exchange. *Nucleic Acids Research*, 48(15):8796–8807, Sept. 2020. ISSN 0305-1048, 1362-4962. doi: 10.1093/nar/gkaa589. URL `https://academic.oup.com/nar/article/48/15/8796/5870335`.

E. Duchardt-Ferner, J. E. Weigand, O. Ohlenschläger, S. R. Schmidtke, B. Suess, and J. Wöhnert. Highly Modular Structure and Ligand Binding by Conformational Capture in a Minimalistic Riboswitch. *Angewandte Chemie International Edition*, 49(35):6216–6219, Aug. 2010. ISSN 14337851. doi: 10.1002/anie.201001339. URL `http://doi.wiley.com/10.1002/anie.201001339`.

E. Duchardt-Ferner, S. R. Gottstein-Schmidtke, J. E. Weigand, O. Ohlenschläger, J.-P. Wurm, C. Hammann, B. Suess, and J. Wöhnert. What a Difference an OH Makes: Conformational Dynamics as the Basis for the Ligand Specificity of the Neomycin-Sensing Riboswitch. *Angewandte Chemie International Edition*, 55 (4):1527–1530, Jan. 2016. ISSN 14337851. doi: 10.1002/anie.201507365. URL `http://doi.wiley.com/10.1002/anie.201507365`.

M. Dwidar, Y. Seike, S. Kobori, C. Whitaker, T. Matsuura, and Y. Yokobayashi. Programmable Artificial Cells Using Histamine-Responsive Synthetic Riboswitch. *Journal of the American Chemical Society*, 141(28): 11103–11114, July 2019. ISSN 0002-7863, 1520-5126. doi: 10.1021/jacs.9b03300. URL `https://pubs.acs.org/doi/10.1021/jacs.9b03300`.

J. D. Eaton and S. West. Termination of Transcription by RNA Polymerase II: BOOM! *Trends in Genetics*, 36(9): 664–675, Sept. 2020. ISSN 01689525. doi: 10.1016/j.tig.2020.05.008. URL `https://linkinghub.elsevier.com/retrieve/pii/S0168952520301256`.

M. T. Eddy, T. Didenko, R. C. Stevens, and K. Wüthrich. β 2 -Adrenergic Receptor Conformational Response to Fusion Protein in the Third Intracellular Loop. *Structure*, 24(12):2190–2197, Dec. 2016. ISSN 09692126. doi: 10.1016/j.str.2016.09.015. URL `https://linkinghub.elsevier.com/retrieve/pii/S0969212616303069`.

C. Eichmüller and N. R. Skrynnikov. A New Amide Proton R1ρ Experiment Permits Accurate Characterization of Microsecond Time-scale Conformational Exchange. *Journal of Biomolecular NMR*, 32(4):281–293, Aug. 2005. ISSN 0925-2738, 1573-5001. doi: 10.1007/s10858-005-0658-y. URL `http://link.springer.com/10.1007/s10858-005-0658-y`.

E. Z. Eisenmesser, O. Millet, W. Labeikovsky, D. M. Korzhnev, M. Wolf-Watz, D. A. Bosco, J. J. Skalicky, L. E. Kay, and D. Kern. Intrinsic dynamics of an enzyme underlies catalysis. *Nature*, 438(7064):117–121, 2005. doi: 10.1038/nature04105.

A. D. Ellington and J. W. Szostak. In vitro selection of RNA molecules that bind specific ligands. *Nature*, 346 (6287):818–822, Aug. 1990. ISSN 0028-0836, 1476-4687. doi: 10.1038/346818a0. URL http://www.nature.com/articles/346818a0.

P. Emsley, B. Lohkamp, W. G. Scott, and K. Cowtan. Features and development of *Coot*. *Acta Crystallographica Section D Biological Crystallography*, 66(4):486–501, Apr. 2010. ISSN 0907-4449. doi: 10.1107/S0907444910007493. URL https://onlinelibrary.wiley.com/doi/10.1107/S0907444910007493.

R. R. Ernst, G. Bodenhausen, and A. Wokaun. *Principles of nuclear magnetic resonance in one and two dimensions*. Number 14 in The international series of monographs on chemistry. Clarendon Pr, Oxford, repr edition, 2004. ISBN 978-0-19-855647-3.

N. A. Farrow, O. Zhang, J. D. Forman-Kay, and L. E. Kay. A heteronuclear correlation experiment for simultaneous determination of 15N longitudinal decay and chemical exchange rates of systems in slow equilibrium. *Journal of Biomolecular NMR*, 4(5):727–734, 1994. doi: 10.1007/BF00404280.

N. L. Fawzi, J. Ying, D. A. Torchia, and G. M. Clore. Kinetics of Amyloid β Monomer-to-Oligomer Exchange by NMR Relaxation. *Journal of the American Chemical Society*, 132(29):9948–9951, July 2010. ISSN 0002-7863, 1520-5126. doi: 10.1021/ja1048253. URL https://pubs.acs.org/doi/10.1021/ja1048253.

N. L. Fawzi, J. Ying, R. Ghirlando, D. A. Torchia, and G. M. Clore. Atomic-resolution dynamics on the surface of amyloid-β protofibrils probed by solution NMR. *Nature*, 480(7376):268–272, Dec. 2011. ISSN 0028-0836, 1476-4687. doi: 10.1038/nature10577. URL https://www.nature.com/articles/nature10577.

N. L. Fawzi, J. Ying, D. A. Torchia, and G. M. Clore. Probing exchange kinetics and atomic resolution dynamics in high-molecular-weight complexes using dark-state exchange saturation transfer NMR spectroscopy. *Nature Protocols*, 7(8):1523–1533, Aug. 2012. ISSN 1754-2189, 1750-2799. doi: 10.1038/nprot.2012.077. URL https://www.nature.com/articles/nprot.2012.077.

N. L. Fawzi, D. S. Libich, J. Ying, V. Tugarinov, and G. M. Clore. Characterizing Methyl-Bearing Side Chain Contacts and Dynamics Mediating Amyloid β Protofibril Interactions Using $^{13}\mathrm{C}_{\mathrm{methyl}}$ -DEST and Lifetime Line Broadening. *Angewandte Chemie International Edition*, 53(39):10345–10349, Sept. 2014. ISSN 14337851. doi: 10.1002/anie.201405180. URL https://onlinelibrary.wiley.com/doi/10.1002/anie.201405180.

S. Forsén and R. A. Hoffman. Study of Moderately Rapid Chemical Exchange Reactions by Means of Nuclear Magnetic Double Resonance. *The Journal of Chemical Physics*, 39(11):2892–2901, Dec. 1963. ISSN 0021-9606, 1089-7690. doi: 10.1063/1.1734121. URL http://aip.scitation.org/doi/10.1063/1.1734121.

J. S. Fraser, M. W. Clarkson, S. C. Degnan, R. Erion, D. Kern, and T. Alber. Hidden alternative structures of proline isomerase essential for catalysis. *Nature*, 462(7273):669–673, Dec. 2009. ISSN 0028-0836, 1476-4687. doi: 10.1038/nature08615. URL http://www.nature.com/articles/nature08615.

H. Frauenfelder, S. Sligar, and P. Wolynes. The energy landscapes and motions of proteins. *Science*, 254 (5038):1598–1603, Dec. 1991. ISSN 0036-8075, 1095-9203. doi: 10.1126/science.1749933. URL https://www.sciencemag.org/lookup/doi/10.1126/science.1749933.

J. N. Frei, R. W. Broadhurst, M. J. Bostock, A. Solt, A. J. Y. Jones, F. Gabriel, A. Tandale, B. Shrestha, and D. Nietlispach. Conformational plasticity of ligand-bound and ternary GPCR complexes studied by 19F NMR of the β1-adrenergic receptor. *Nature Communications*, 11(1):669, Dec. 2020. ISSN 2041-1723. doi: 10.1038/s41467-020-14526-3. URL http://www.nature.com/articles/s41467-020-14526-3.

A.-L. Fuchs, J. P. Wurm, A. Neu, and R. Sprangers. Molecular basis of the selective processing of short mRNA substrates by the DcpS mRNA decapping enzyme. *Proceedings of the National Academy of Sciences*, 117(32):19237–19244, Aug. 2020. ISSN 0027-8424, 1091-6490. doi: 10.1073/pnas.2009362117. URL http://www.pnas.org/lookup/doi/10.1073/pnas.2009362117.

R. Furter. Expansion of the genetic code: Site-directed p-fluoro-phenylalanine incorporation in Escherichia coli: In vivo site-directed analogue incorporation. *Protein Science*, 7(2):419–426, Feb. 1998. ISSN 09618368. doi: 10.1002/pro.5560070223. URL https://onlinelibrary.wiley.com/doi/10.1002/pro.5560070223.

L. Gasse, D. Flemming, and E. Hurt. Coordinated Ribosomal ITS2 RNA Processing by the Las1 Complex Integrating Endonuclease, Polynucleotide Kinase, and Exonuclease Activities. *Molecular Cell*, 60(5):808–815, Dec. 2015. ISSN 10972765. doi: 10.1016/j.molcel.2015.10.021. URL https://linkinghub.elsevier.com/retrieve/pii/S1097276515008126.

T. H. Geerlings, J. C. Vos, and H. A. Raué. The final step in the formation of 25S rRNA in Saccharomyces cerevisiae is performed by 5′ → 3′ exonucleases. *RNA*, 6(12):1698–1703, Dec. 2000. ISSN 13558382. doi: 10.1017/S1355838200001540. URL http://www.journals.cambridge.org/abstract_S1355838200001540.

J. Gerig. Fluorine NMR of proteins. *Progress in Nuclear Magnetic Resonance Spectroscopy*, 26:293–370, Jan. 1994. ISSN 00796565. doi: 10.1016/0079-6565(94)80009-X. URL https://linkinghub.elsevier.com/retrieve/pii/007965659480009X.

I. P. Gerothanassis. Methods of avoiding the effects of acoustic ringing in pulsed fourier transform nuclear magnetic resonance spectroscopy. *Progress in Nuclear Magnetic Resonance Spectroscopy*, 19(3):267–329, 1987. doi: 10.1016/0079-6565(87)80005-5.

W. H. Gmeiner, R. T. Pon, and J. W. Lown. Synthesis, annealing properties, fluorine-19 NMR characterization, and detection limits of a trifluorothymidine-labeled antisense oligodeoxyribonucleotide 21 mer'. *The Journal of Organic Chemistry*, 56(11):3602–3608, May 1991. ISSN 0022-3263, 1520-6904. doi: 10.1021/jo00011a028. URL https://pubs.acs.org/doi/abs/10.1021/jo00011a028.

A. B. Gopalan, T. Yuwen, L. E. Kay, and P. Vallurupalli. A methyl 1H double quantum CPMG experiment to study protein conformational exchange. *Journal of Biomolecular NMR*, 72(1-2):79–91, 2018. ISSN 1085801802. doi: 10.1007/s10858-018-0208-z. URL http://dx.doi.org/10.1007/s10858-018-0208-z.

S. R. Gottstein-Schmidtke, E. Duchardt-Ferner, F. Groher, J. E. Weigand, D. Gottstein, B. Suess, and J. Wöhnert. Building a stable RNA U-turn with a protonated cytidine. *RNA*, 20(8):1163–1172, Aug. 2014. ISSN 1355-8382, 1469-9001. doi: 10.1261/rna.043083.113. URL http://rnajournal.cshlp.org/lookup/doi/10.1261/rna.043083.113.

D. Grate and C. Wilson. Inducible regulation of the S. cerevisiae cell cycle mediated by an RNA aptamer–ligand complex. *Bioorganic & Medicinal Chemistry*, 9(10):2565–2570, Oct. 2001. ISSN 09680896. doi: 10.1016/S0968-0896(01)00031-1. URL https://linkinghub.elsevier.com/retrieve/pii/S0968089601000311.

M. Guenneugues, P. Berthault, and H. Desvaux. A Method for DeterminingB1Field Inhomogeneity. Are the Biases Assumed in Heteronuclear Relaxation Experiments Usually Underestimated? *Journal of Magnetic Resonance*, 136(1):118–126, Jan. 1999. ISSN 10907807. doi: 10.1006/jmre.1998.1590. URL https://linkinghub.elsevier.com/retrieve/pii/S1090780798915907.

P. Güntert and L. Buchner. Combined automated NOE assignment and structure calculation with CYANA. *Journal of Biomolecular NMR*, 62(4):453–471, Aug. 2015. ISSN 0925-2738, 1573-5001. doi: 10.1007/s10858-015-9924-9. URL http://link.springer.com/10.1007/s10858-015-9924-9.

H. Gustmann, A.-L. J. Segler, D. B. Gophane, A. J. Reuss, C. Grünewald, M. Braun, J. E. Weigand, S. T. Sigurdsson, and J. Wachtveitl. Structure guided fluorescence labeling reveals a two-step binding mechanism of neomycin to its RNA aptamer. *Nucleic Acids Research*, 47(1):15–28, Jan. 2019. ISSN 0305-1048, 1362-4962. doi: 10.1093/nar/gky1110. URL https://academic.oup.com/nar/article/47/1/15/5193333.

E. L. Hahn. Spin Echoes. *Physical Review*, 80(4):580–594, Nov. 1950. ISSN 0031-899X. doi: 10.1103/PhysRev.80.580. URL https://link.aps.org/doi/10.1103/PhysRev.80.580.

G. Haimovich, M. Choder, R. H. Singer, and T. Trcek. The fate of the messenger is pre-determined: A new model for regulation of gene expression. *Biochimica et Biophysica Acta (BBA) - Gene Regulatory Mechanisms*, 1829(6-7):643–653, June 2013. ISSN 18749399. doi: 10.1016/j.bbagrm.2013.01.004. URL https://linkinghub.elsevier.com/retrieve/pii/S1874939913000084.

C. Hammann, D. G. Norman, and D. M. J. Lilley. Dissection of the ion-induced folding of the hammerhead ribozyme using 19F NMR. *Proceedings of the National Academy of Sciences*, 98(10):5503–5508, May 2001. ISSN 0027-8424, 1091-6490. doi: 10.1073/pnas.091097498. URL http://www.pnas.org/cgi/doi/10.1073/pnas.091097498.

A. L. Hansen, E. N. Nikolova, A. Casiano-negroni, and H. M. Al-hashimi. Extending the Range of μs-ms Chemical Exchange Detected in Labeled and Unlabeled Nucleic Acids by Selective Carbon R. *Cell*, 319: 48109–48109, 2009.

A. L. Hansen, P. Lundström, A. Velyvis, and L. E. Kay. Quantifying Millisecond Exchange Dynamics in Proteins by CPMG Relaxation Dispersion NMR Using Side-Chain ^{1} H Probes. *Journal of the American Chemical Society*, 134(6):3178–3189, Feb. 2012. ISSN 0002-7863, 1520-5126. doi: 10.1021/ja210711v. URL https://pubs.acs.org/doi/10.1021/ja210711v.

A. L. Hansen, G. Bouvignies, and L. E. Kay. Probing slowly exchanging protein systems via 13Cα-CEST: monitoring folding of the Im7 protein. *Journal of Biomolecular NMR*, 55(3):279–289, Mar. 2013. ISSN 0925-2738, 1573-5001. doi: 10.1007/s10858-013-9711-4. URL http://link.springer.com/10.1007/s10858-013-9711-4.

D. F. Hansen and J. J. Led. Determination of the geometric structure of the metal site in a blue copper protein by paramagnetic NMR. *Proceedings of the National Academy of Sciences*, 103(6):1738–1743, Feb. 2006. ISSN 0027-8424, 1091-6490. doi: 10.1073/pnas.0507179103. URL http://www.pnas.org/cgi/doi/10.1073/pnas.0507179103.

D. F. Hansen, P. Vallurupalli, P. Lundström, P. Neudecker, and L. E. Kay. Probing Chemical Shifts of Invisible States of Proteins with Relaxation Dispersion NMR Spectroscopy: How Well Can We Do? *Journal of the American Chemical Society*, 130(8):2667–2675, Feb. 2008. ISSN 0002-7863, 1520-5126. doi: 10.1021/ja078337p. URL https://pubs.acs.org/doi/10.1021/ja078337p.

R. W. Harkness, Y. Toyama, Z. A. Ripstein, H. Zhao, A. I. M. Sever, Q. Luan, J. P. Brady, P. L. Clark, P. Schuck, and L. E. Kay. Competing stress-dependent oligomerization pathways regulate self-assembly of the periplasmic protease-chaperone DegP. *Proceedings of the National Academy of Sciences*, 118(32): e2109732118, Aug. 2021. ISSN 0027-8424, 1091-6490. doi: 10.1073/pnas.2109732118. URL http://www.pnas.org/lookup/doi/10.1073/pnas.2109732118.

I. Harvey, P. Garneau, and J. Pelletier. Inhibition of translation by RNA–small molecule interactions. *RNA*, 8(4):452–463, Apr. 2002. ISSN 13558382. doi: 10.1017/S135583820202633X. URL http://www.journals.cambridge.org/abstract_S135583820202633X.

Z. Heidari, I. M. Chrisman, M. D. Nemetchek, S. J. Novick, A.-L. Blayo, T. Patton, D. E. Mendes, P. Diaz, T. M. Kamenecka, P. R. Griffin, and T. S. Hughes. Definition of functionally and structurally distinct repressive states in the nuclear receptor PPARγ. *Nature Communications*, 10(1):5825, Dec. 2019. ISSN 2041-1723. doi: 10.1038/s41467-019-13768-0. URL http://www.nature.com/articles/s41467-019-13768-0.

M. Helgstrand, T. Härd, and P. Allard. Simulations of NMR pulse sequences during equilibrium and non-equilibrium chemical exchange. *Journal of Biomolecular NMR*, 18(1):49–63, 2000. ISSN 09252738. doi: 10.1023/A:1008309220156.

U. A. Hellmich, N. Pfleger, and C. Glaubitz. ^{19} F-MAS NMR on Proteorhodopsin: Enhanced Protocol for Site-Specific Labeling for General Application to Membrane Proteins. *Photochemistry and Photobiology*, 85(2):535–539, Mar. 2009. ISSN 00318655, 17511097. doi: 10.1111/j.1751-1097.2008.00498.x. URL http://doi.wiley.com/10.1111/j.1751-1097.2008.00498.x.

M. Hennig, L. G. Scott, E. Sperling, W. Bermel, and J. R. Williamson. Synthesis of 5-Fluoropyrimidine Nucleotides as Sensitive NMR Probes of RNA Structure. *Journal of the American Chemical Society*, 129(48):14911–14921, Dec. 2007. ISSN 0002-7863, 1520-5126. doi: 10.1021/ja073825i. URL https://pubs.acs.org/doi/10.1021/ja073825i.

Y. Henry, H. Wood, J. Morrissey, E. Petfalski, S. Kearsey, and D. Tollervey. The 5′ end of yeast 5.8S rRNA is generated by exonucleases from an upstream cleavage site. *The EMBO Journal*, 13(10):2452–2463, May 1994. ISSN 02614189. doi: 10.1002/j.1460-2075.1994.tb06530.x. URL https://onlinelibrary.wiley.com/doi/10.1002/j.1460-2075.1994.tb06530.x.

K. Henzler-Wildman and D. Kern. Dynamic personalities of proteins. *Nature*, 450(7172):964–972, Dec. 2007. ISSN 0028-0836, 1476-4687. doi: 10.1038/nature06522. URL http://www.nature.com/articles/nature06522.

R. B. Hill, C. Bracken, W. F. DeGrado, and A. G. Palmer. Molecular Motions and Protein Folding: Characterization of the Backbone Dynamics and Folding Equilibrium of α_2 D Using ^{13} C NMR Spin Relaxation. *Journal of the American Chemical Society*, 122(47):11610–11619, Nov. 2000. ISSN 0002-7863, 1520-5126. doi: 10.1021/ja001129b. URL https://pubs.acs.org/doi/10.1021/ja001129b.

M. Himmelstoß, K. Erharter, E. Renard, E. Ennifar, C. Kreutz, and R. Micura. 2′- *O* -Trifluoromethylated RNA – a powerful modification for RNA chemistry and NMR spectroscopy. *Chemical Science*, 11(41):11322–11330, 2020. ISSN 2041-6520, 2041-6539. doi: 10.1039/D0SC04520A. URL http://xlink.rsc.org/?DOI=D0SC04520A.

J. Hoang and R. S. Prosser. Conformational Selection and Functional Dynamics of Calmodulin: A 19F Nuclear Magnetic Resonance Study. *Biochemistry*, 53(36):5727–5736, 2014. doi: 10.1021/bi500679c.

T. A. Hoek, D. Khuperkar, R. G. Lindeboom, S. Sonneveld, B. M. Verhagen, S. Boersma, M. Vermeulen, and M. E. Tanenbaum. Single-Molecule Imaging Uncovers Rules Governing Nonsense-Mediated mRNA Decay. *Molecular Cell*, 75(2):324–339.e11, July 2019. ISSN 10972765. doi: 10.1016/j.molcel.2019.05.008. URL https://linkinghub.elsevier.com/retrieve/pii/S1097276519303612.

S. A. Hollingsworth and R. O. Dror. Molecular Dynamics Simulation for All. *Neuron*, 99(6):1129–1143, Sept. 2018. ISSN 08966273. doi: 10.1016/j.neuron.2018.08.011. URL https://linkinghub.elsevier.com/retrieve/pii/S0896627318306846.

J. Horowitz, J. Ofengand, W. E. Daniel, and M. Cohn. 19F nuclear magnetic resonance of 5-fluorouridine-substituted tRNA1Val from Escherichia coli. *Journal of Biological Chemistry*, 252(12):4418–4420, June 1977. ISSN 00219258. doi: 10.1016/S0021-9258(17)40283-3. URL https://linkinghub.elsevier.com/retrieve/pii/S0021925817402833.

R. Horst, J. J. Liu, R. C. Stevens, and K. Wüthrich. β_2 -Adrenergic Receptor Activation by Agonists Studied with ^{19}F NMR Spectroscopy. *Angewandte Chemie International Edition*, 52(41):10762–10765, Oct. 2013. ISSN 14337851. doi: 10.1002/anie.201305286. URL https://onlinelibrary.wiley.com/doi/10.1002/anie.201305286.

W. Hu, T. J. Sweet, S. Chamnongpol, K. E. Baker, and J. Coller. Co-translational mRNA decay in Saccharomyces cerevisiae. *Nature*, 461(7261):225–229, Sept. 2009. ISSN 0028-0836, 1476-4687. doi: 10.1038/nature08265. URL http://www.nature.com/articles/nature08265.

S. K. Huang, A. Pandey, D. P. Tran, N. L. Villanueva, A. Kitao, R. K. Sunahara, A. Sljoka, and R. S. Prosser. Delineating the conformational landscape of the adenosine A2A receptor during G protein coupling. *Cell*, 184(7):1884–1894.e14, Apr. 2021. ISSN 00928674. doi: 10.1016/j.cell.2021.02.041. URL https://linkinghub.elsevier.com/retrieve/pii/S0092867421002300.

Y. Huang, X. Wang, G. Lv, A. M. Razavi, G. H. M. Huysmans, H. Weinstein, C. Bracken, D. Eliezer, and O. Boudker. Use of paramagnetic 19F NMR to monitor domain movement in a glutamate transporter homolog. *Nature Chemical Biology*, 16(9):1006–1012, Sept. 2020. ISSN 1552-4450, 1552-4469. doi: 10.1038/s41589-020-0561-6. URL http://www.nature.com/articles/s41589-020-0561-6.

M. P. Hui, P. L. Foley, and J. G. Belasco. Messenger RNA Degradation in Bacterial Cells. *Annual Review of Genetics*, 48(1):537–559, Nov. 2014. ISSN 0066-4197, 1545-2948. doi: 10.1146/annurev-genet-120213-092340. URL https://www.annualreviews.org/doi/10.1146/annurev-genet-120213-092340.

T. I. Igumenova and A. G. Palmer. Off-resonance TROSY-selected R1ρ experiment with improved sensitivity for medium- and high-molecular-weight proteins. *Journal of the American Chemical Society*, 128(25):8110–8111, 2006. doi: 10.1021/ja061692f.

R. Ishima and D. A. Torchia. Estimating the time scale of chemical exchange of proteins from measurements of transverse relaxation rates in solution. *Journal of Biomolecular NMR*, 14(4):369–372, Aug. 1999. ISSN 1573-5001. doi: 10.1023/A:1008324025406. URL https://doi.org/10.1023/A:1008324025406.

R. Ishima and D. A. Torchia. Extending the range of amide proton relaxation dispersion experiments in proteins using a constant-time relaxation-compensated CPMG approach. *Journal of Biomolecular NMR*, 25(3):243–248, 2003. ISSN 09252738. doi: 10.1023/A:1022851228405. URL http://link.springer.com/10.1023/A:1022851228405.

R. Ishima, P. T. Wingfield, S. J. Stahl, J. D. Kaufman, and D. A. Torchia. Using Amide ^{1}H and ^{15}N Transverse Relaxation To Detect Millisecond Time-Scale Motions in Perdeuterated Proteins: Application to HIV-1 Protease. *Journal of the American Chemical Society*, 120(40):10534–10542, Oct. 1998. ISSN 0002-7863, 1520-5126. doi: 10.1021/ja981546c. URL https://pubs.acs.org/doi/10.1021/ja981546c.

R. Ishima, J. M. Louis, and D. A. Torchia. Transverse ^{13} C Relaxation of CHD $_2$ Methyl Isotopmers To Detect Slow Conformational Changes of Protein Side Chains. *Journal of the American Chemical Society*, 121(49): 11589–11590, Dec. 1999. ISSN 0002-7863, 1520-5126. doi: 10.1021/ja992836b. URL https://pubs.acs.org/doi/10.1021/ja992836b.

R. Ishima, J. Baber, J. M. Louis, and D. A. Torchia. Carbonyl carbon transverse relaxation dispersion measurements and ms-μs timescale motion in a protein hydrogen bond network. *Journal of Biomolecular NMR*, 29(2):187–198, June 2004. ISSN 0925-2738. doi: 10.1023/B:JNMR.0000019249.50306.5d. URL http://link.springer.com/10.1023/B:JNMR.0000019249.50306.5d.

J. C. Jackson, J. T. Hammill, and R. A. Mehl. Site-specific incorporation of a 19F-amino acid into proteins as an NMR probe for characterizing protein structure and reactivity. *Journal of the American Chemical Society*, 129(5):1160–1166, 2007. doi: 10.1021/ja064661t.

K. Januszyk and C. D. Lima. The eukaryotic RNA exosome. *Current Opinion in Structural Biology*, 24:132–140, Feb. 2014. ISSN 0959440X. doi: 10.1016/j.sbi.2014.01.011. URL https://linkinghub.elsevier.com/retrieve/pii/S0959440X14000128.

J. Jeener, B. H. Meier, P. Bachmann, and R. R. Ernst. Investigation of exchange processes by two-dimensional NMR spectroscopy. *The Journal of Chemical Physics*, 71(11):4546–4553, Dec. 1979. ISSN 0021-9606, 1089-7690. doi: 10.1063/1.438208. URL http://aip.scitation.org/doi/10.1063/1.438208.

J. Jen. Chemical exchange and nmr T2 relaxation—The multisite case. *Journal of Magnetic Resonance (1969)*, 30(1):111–128, Apr. 1978. ISSN 00222364. doi: 10.1016/0022-2364(78)90229-9. URL https://linkinghub.elsevier.com/retrieve/pii/0022236478902299.

T. H. Jensen, A. Jacquier, and D. Libri. Dealing with Pervasive Transcription. *Molecular Cell*, 52(4):473–484, Nov. 2013. ISSN 10972765. doi: 10.1016/j.molcel.2013.10.032. URL https://linkinghub.elsevier.com/retrieve/pii/S1097276513007983.

L. Jiang, A. Majumdar, W. Hu, T. Jaishree, W. Xu, and D. J. Patel. Saccharide–RNA recognition in a complex formed between neomycin B and an RNA aptamer. *Structure*, 7(7):817–S7, July 1999. ISSN 09692126. doi: 10.1016/S0969-2126(99)80105-1. URL https://linkinghub.elsevier.com/retrieve/pii/S0969212699801051.

M. Jinek, S. M. Coyle, and J. A. Doudna. Coupled 5′ Nucleotide Recognition and Processivity in Xrn1-Mediated mRNA Decay. *Molecular Cell*, 41(5):600–608, Mar. 2011. ISSN 10972765. doi: 10.1016/j.molcel.2011.02.004. URL https://linkinghub.elsevier.com/retrieve/pii/S1097276511000876.

M. A. Juen, C. H. Wunderlich, F. Nußbaumer, M. Tollinger, G. Kontaxis, R. Konrat, D. F. Hansen, and C. Kreutz. Excited States of Nucleic Acids Probed by Proton Relaxation Dispersion NMR Spectroscopy. *Angewandte Chemie - International Edition*, 55(39):12008–12012, 2016. doi: 10.1002/anie.201605870.

J. Jumper, R. Evans, A. Pritzel, T. Green, M. Figurnov, O. Ronneberger, K. Tunyasuvunakool, R. Bates, A. Žídek, A. Potapenko, A. Bridgland, C. Meyer, S. A. A. Kohl, A. J. Ballard, A. Cowie, B. Romera-Paredes, S. Nikolov, R. Jain, J. Adler, T. Back, S. Petersen, D. Reiman, E. Clancy, M. Zielinski, M. Steinegger, M. Pacholska, T. Berghammer, S. Bodenstein, D. Silver, O. Vinyals, A. W. Senior, K. Kavukcuoglu, P. Kohli, and D. Hassabis. Highly accurate protein structure prediction with AlphaFold. *Nature*, 596 (7873):583–589, Aug. 2021. ISSN 0028-0836, 1476-4687. doi: 10.1038/s41586-021-03819-2. URL https://www.nature.com/articles/s41586-021-03819-2.

W. Kabsch. *XDS*. *Acta Crystallographica Section D Biological Crystallography*, 66(2):125–132, Feb. 2010. ISSN 0907-4449. doi: 10.1107/S0907444909047337. URL https://onlinelibrary.wiley.com/doi/10.1107/S0907444909047337.

L. E. Kay, L. K. Nicholson, F. Delaglio, A. Bax, and D. Torchia. Pulse sequences for removal of the effects of cross correlation between dipolar and chemical-shift anisotropy relaxation mechanisms on the measurement of heteronuclear T1 and T2 values in proteins. *Journal of Magnetic Resonance (1969)*, 97(2):359–375, Apr. 1992. ISSN 00222364. doi: 10.1016/0022-2364(92)90320-7. URL https://linkinghub.elsevier.com/retrieve/pii/0022236492903207.

R. Keller. *The computer aided resonance assignment tutorial*. Cantina Verl., Goldau, 2004. ISBN 978-3-85600-112-4. OCLC: 1107012833.

M. Kenna. An Essential Yeast Gene with Homology to the Exonuclease- Encoding XRNJ/KEM1 Gene Also Encodes a Protein with Exoribonuclease Activity. *MOL. CELL. BIOL.*, 13:10, 1993.

M. Kim, N. J. Krogan, L. Vasiljeva, O. J. Rando, E. Nedea, J. F. Greenblatt, and S. Buratowski. The yeast Rat1 exonuclease promotes transcription termination by RNA polymerase II. *Nature*, 432(7016):517–522, Nov. 2004. ISSN 0028-0836, 1476-4687. doi: 10.1038/nature03041. URL http://www.nature.com/articles/nature03041.

T. H. Kim, K. Y. Chung, A. Manglik, A. L. Hansen, R. O. Dror, T. J. Mildorf, D. E. Shaw, B. K. Kobilka, and R. S. Prosser. The role of ligands on the equilibria between functional states of a G protein-coupled receptor. *Journal of the American Chemical Society*, 135(25):9465–9474, 2013. doi: 10.1021/ja404305k.

T. H. Kim, P. Mehrabi, Z. Ren, A. Sljoka, C. Ing, A. Bezginov, L. Ye, R. Pomès, R. S. Prosser, and E. F. Pai. The role of dimer asymmetry and protomer dynamics in enzyme catalysis. *Science*, 355(6322):eaag2355, Jan. 2017. ISSN 0036-8075, 1095-9203. doi: 10.1126/science.aag2355. URL https://www.sciencemag.org/lookup/doi/10.1126/science.aag2355.

I. J. Kimsey, K. Petzold, B. Sathyamoorthy, Z. W. Stein, and H. M. Al-Hashimi. Visualizing transient Watson-Crick-like mispairs in DNA and RNA duplexes. *Nature*, 519(7543):315–320, 2015. doi: 10.1038/nature14227. URL http://dx.doi.org/10.1038/nature14227.

I. J. Kimsey, E. S. Szymanski, W. J. Zahurancik, A. Shakya, Y. Xue, C.-C. Chu, B. Sathyamoorthy, Z. Suo, and H. M. Al-Hashimi. Dynamic basis for dG•dT misincorporation via tautomerization and ionization. *Nature*, 554(7691):195–201, Feb. 2018. ISSN 0028-0836, 1476-4687. doi: 10.1038/nature25487. URL http://www.nature.com/articles/nature25487.

J. L. Kitevski-LeBlanc and R. S. Prosser. Current applications of 19F NMR to studies of protein structure and dynamics. *Progress in Nuclear Magnetic Resonance Spectroscopy*, 62:1–33, 2012. doi: 10.1016/j.pnmrs.2011.06.003. URL http://dx.doi.org/10.1016/j.pnmrs.2011.06.003.

J. L. Kitevski-Leblanc, J. Hoang, W. Thach, S. T. Larda, and R. S. Prosser. 19F NMR studies of a desolvated near-native protein folding intermediate. *Biochemistry*, 52(34):5780–5789, 2013. doi: 10.1021/bi4010057.

I. R. Kleckner and M. P. Foster. An introduction to NMR-based approaches for measuring protein dynamics. *Biochimica et Biophysica Acta (BBA) - Proteins and Proteomics*, 1814(8):942–968, Aug. 2011. ISSN 15709639. doi: 10.1016/j.bbapap.2010.10.012. URL https://linkinghub.elsevier.com/retrieve/pii/S1570963910002864.

D. M. Korzhnev, N. R. Skrynnikov, O. Millet, D. A. Torchia, and L. E. Kay. An NMR experiment for the accurate measurement of heteronuclear spin-lock relaxation rates. *Journal of the American Chemical Society*, 124(36):10743–10753, 2002. doi: 10.1021/ja0204776.

D. M. Korzhnev, V. Y. Orekhov, F. W. Dahlquist, and L. E. Kay. Off-resonance R1ρ relaxation outside of the fast exchange limit: An experimental study of a cavity mutant of T4 lysozyme. *Journal of Biomolecular NMR*, 26(1):10, 2003. ISSN 09252738. doi: https://doi.org/10.1023/A:1023039902737. URL `http://link.springer.com/10.1023/A:1023039902737`.

D. M. Korzhnev, K. Kloiber, V. Kanelis, V. Tugarinov, and L. E. Kay. Probing Slow Dynamics in High Molecular Weight Proteins by Methyl-TROSY NMR Spectroscopy: Application to a 723-Residue Enzyme. *Journal of the American Chemical Society*, 126(12):3964–3973, 2004a. doi: 10.1021/ja039587i.

D. M. Korzhnev, K. Kloiber, and L. E. Kay. Multiple-Quantum Relaxation Dispersion NMR Spectroscopy Probing Millisecond Time-Scale Dynamics in Proteins: Theory and Application. *Journal of the American Chemical Society*, 126(23):7320–7329, June 2004b. ISSN 0002-7863, 1520-5126. doi: 10.1021/ja049968b. URL `https://pubs.acs.org/doi/10.1021/ja049968b`.

D. M. Korzhnev, X. Salvatella, M. Vendruscolo, A. A. Di Nardo, A. R. Davidson, C. M. Dobson, and L. E. Kay. Low-populated folding intermediates of Fyn SH3 characterized by relaxation dispersion NMR. *Nature*, 430(6999):586–590, July 2004c. ISSN 0028-0836, 1476-4687. doi: 10.1038/nature02655. URL `http://www.nature.com/articles/nature02655`.

D. M. Korzhnev, P. Neudecker, A. Mittermaier, V. Y. Orekhov, and L. E. Kay. Multiple-site exchange in proteins studied with a suite of six NMR relaxation dispersion experiments: An application to the folding of a Fyn SH3 domain mutant. *Journal of the American Chemical Society*, 127(44):15602–15611, 2005a. doi: 10.1021/ja054550e.

D. M. Korzhnev, V. Y. Orekhov, and L. E. Kay. Off-resonance R1ρ NMR studies of exchange dynamics in proteins with low spin-lock fields: An application to a fyn SH3 domain. *Journal of the American Chemical Society*, 127(2):713–721, 2005b. doi: 10.1021/ja0446855.

D. M. Korzhnev, T. L. Religa, P. Lundström, A. R. Fersht, and L. E. Kay. The Folding Pathway of an FF domain: Characterization of an On-pathway Intermediate State Under Folding Conditions by 15N, 13Cα and 13C-methyl Relaxation Dispersion and 1H/2H-exchange NMR Spectroscopy. *Journal of Molecular Biology*, 372(2):497–512, Sept. 2007. ISSN 00222836. doi: 10.1016/j.jmb.2007.06.012. URL `https://linkinghub.elsevier.com/retrieve/pii/S0022283607007942`.

H. Koss, M. Rance, and A. G. Palmer. General Expressions for Carr-Purcell-Meiboom-Gill Relaxation Dispersion for N-Site Chemical Exchange. *Biochemistry*, 57(31):4753–4763, 2018. doi: 10.1021/acs.biochem.8b00370.

H. Koss, M. Rance, and A. G. Palmer. Algebraic expressions for Carr-Purcell-Meiboom-Gill relaxation dispersion for N-site chemical exchange. *Journal of Magnetic Resonance*, 321:106846, Dec. 2020. ISSN 10907807. doi: 10.1016/j.jmr.2020.106846. URL `https://linkinghub.elsevier.com/retrieve/pii/S1090780720301646`.

S. A. Kotler, V. Tugarinov, T. Schmidt, A. Ceccon, D. S. Libich, R. Ghirlando, C. D. Schwieters, and G. M. Clore. Probing initial transient oligomerization events facilitating Huntingtin fibril nucleation at atomic resolution by relaxation-based NMR. *Proceedings of the National Academy of Sciences*, 116(9):3562–3571, Feb.

2019. ISSN 0027-8424, 1091-6490. doi: 10.1073/pnas.1821216116. URL http://www.pnas.org/lookup/doi/10.1073/pnas.1821216116.

W. Kremer, B. Schuler, S. Harrieder, M. Geyer, W. Gronwald, C. Welker, R. Jaenicke, and H. R. Kalbitzer. Solution NMR structure of the cold-shock protein from the hyperthermophilic bacterium *Thermotoga maritima*: Solution NMR structure of Csp from *T. maritima*. *European Journal of Biochemistry*, 268(9):2527–2539, May 2001. ISSN 00142956. doi: 10.1046/j.1432-1327.2001.02127.x. URL http://doi.wiley.com/10.1046/j.1432-1327.2001.02127.x.

M. Krepl, J. Vögele, H. Kruse, E. Duchardt-Ferner, J. Wöhnert, and J. Sponer. An intricate balance of hydrogen bonding, ion atmosphere and dynamics facilitates a seamless uracil to cytosine substitution in the U-turn of the neomycin-sensing riboswitch. *Nucleic Acids Research*, 46(13):6528–6543, July 2018. ISSN 0305-1048, 1362-4962. doi: 10.1093/nar/gky490. URL https://academic.oup.com/nar/article/46/13/6528/5035167.

C. Kreutz, H. Kählig, R. Konrat, and R. Micura. Ribose 2'- *F* Labeling: A Simple Tool for the Characterization of RNA Secondary Structure Equilibria by ^{19} F NMR Spectroscopy. *Journal of the American Chemical Society*, 127(33):11558–11559, Aug. 2005. ISSN 0002-7863, 1520-5126. doi: 10.1021/ja052844u. URL https://pubs.acs.org/doi/10.1021/ja052844u.

M. Kulik, T. Mori, Y. Sugita, and J. Trylska. Molecular mechanisms for dynamic regulation of N1 riboswitch by aminoglycosides. *Nucleic Acids Research*, Sept. 2018. ISSN 0305-1048, 1362-4962. doi: 10.1093/nar/gky833. URL https://academic.oup.com/nar/advance-article/doi/10.1093/nar/gky833/5103949.

A. Łabno, R. Tomecki, and A. Dziembowski. Cytoplasmic RNA decay pathways - Enzymes and mechanisms. *Biochimica et Biophysica Acta (BBA) - Molecular Cell Research*, 1863(12):3125–3147, Dec. 2016. ISSN 01674889. doi: 10.1016/j.bbamcr.2016.09.023. URL https://linkinghub.elsevier.com/retrieve/pii/S0167488916302531.

C. J. Langeberg, W. R. W. Welch, J. V. McGuire, A. Ashby, A. D. Jackson, and E. G. Chapman. Biochemical Characterization of Yeast Xrn1. *Biochemistry*, 59(15):1493–1507, Apr. 2020. ISSN 0006-2960, 1520-4995. doi: 10.1021/acs.biochem.9b01035. URL https://pubs.acs.org/doi/10.1021/acs.biochem.9b01035.

M. Larkin, G. Blackshields, N. Brown, R. Chenna, P. McGettigan, H. McWilliam, F. Valentin, I. Wallace, A. Wilm, R. Lopez, J. Thompson, T. Gibson, and D. Higgins. Clustal W and Clustal X version 2.0. *Bioinformatics*, 23(21):2947–2948, Nov. 2007. ISSN 1367-4803, 1460-2059. doi: 10.1093/bioinformatics/btm404. URL https://academic.oup.com/bioinformatics/article-lookup/doi/10.1093/bioinformatics/btm404.

C. Y. Lee. The roles of endonucleolytic cleavage and exonucleolytic digestion in the 5'-end processing of S. cerevisiae box C/D snoRNAs. *RNA*, 9(11):1362–1370, Nov. 2003. ISSN 1355-8382. doi: 10.1261/rna.5126203. URL http://www.rnajournal.org/cgi/doi/10.1261/rna.5126203.

W. Lee, M. Tonelli, and J. L. Markley. NMRFAM-SPARKY: enhanced software for biomolecular NMR spectroscopy. *Bioinformatics*, 31(8):1325–1327, Apr. 2015. ISSN 1460-2059, 1367-4803. doi: 10.1093/bioinformatics/btu830. URL https://academic.oup.com/bioinformatics/article-lookup/doi/10.1093/bioinformatics/btu830.

C. Lento and D. J. Wilson. Subsecond Time-Resolved Mass Spectrometry in Dynamic Structural Biology. *Chemical Reviews*, page acs.chemrev.1c00222, July 2021. ISSN 0009-2665, 1520-6890. doi: 10.1021/acs.chemrev.1c00222. URL https://pubs.acs.org/doi/10.1021/acs.chemrev.1c00222.

D. S. Libich, V. Tugarinov, and G. M. Clore. Intrinsic unfoldase/foldase activity of the chaperonin GroEL directly demonstrated using multinuclear relaxation-based NMR. *Proceedings of the National Academy of Sciences*, 112(29):8817–8823, July 2015. ISSN 0027-8424, 1091-6490. doi: 10.1073/pnas.1510083112. URL http://www.pnas.org/lookup/doi/10.1073/pnas.1510083112.

J. Liebau, M. Tersa, B. Trastoy, J. Patrick, A. Rodrigo-Unzueta, F. Corzana, T. Sparrman, M. E. Guerin, and L. Mäler. Unveiling the activation dynamics of a fold-switch bacterial glycosyltransferase by 19F NMR. *Journal of Biological Chemistry*, 295(29):9868–9878, July 2020. ISSN 00219258. doi: 10.1074/jbc.RA120.014162. URL https://linkinghub.elsevier.com/retrieve/pii/S0021925817489290.

D. Liebschner, P. V. Afonine, M. L. Baker, G. Bunkóczi, V. B. Chen, T. I. Croll, B. Hintze, L.-W. Hung, S. Jain, A. J. McCoy, N. W. Moriarty, R. D. Oeffner, B. K. Poon, M. G. Prisant, R. J. Read, J. S. Richardson, D. C. Richardson, M. D. Sammito, O. V. Sobolev, D. H. Stockwell, T. C. Terwilliger, A. G. Urzhumtsev, L. L. Videau, C. J. Williams, and P. D. Adams. Macromolecular structure determination using X-rays, neutrons and electrons: recent developments in *Phenix*. *Acta Crystallographica Section D Structural Biology*, 75(10):861–877, Oct. 2019. ISSN 2059-7983. doi: 10.1107/S2059798319011471. URL https://onlinelibrary.wiley.com/doi/10.1107/S2059798319011471.

J. Lim, T. Xiao, J. Fan, and D. Yang. An Off-Pathway Folding Intermediate of an Acyl Carrier Protein Domain Coexists with the Folded and Unfolded States under Native Conditions. *Angewandte Chemie International Edition*, 53(9):2358–2361, Feb. 2014. ISSN 14337851. doi: 10.1002/anie.201308512. URL https://onlinelibrary.wiley.com/doi/10.1002/anie.201308512.

B. Liu, H. Shi, A. Rangadurai, F. Nussbaumer, C.-C. Chu, K. A. Erharter, D. A. Case, C. Kreutz, and H. M. Al-Hashimi. A quantitative model predicts how m6A reshapes the kinetic landscape of nucleic acid hybridization and conformational transitions. *Nature Communications*, 12(1):5201, Dec. 2021. ISSN 2041-1723. doi: 10.1038/s41467-021-25253-8. URL https://www.nature.com/articles/s41467-021-25253-8.

J. J. Liu, R. Horst, V. Katritch, R. C. Stevens, K. Wuthrich, and K. Wüthrich. Biased Signaling Pathways in. *Science (New York, N.Y.)*, 1106(March):1106–1111, 2012. doi: 10.1126/science.1215802. URL http://www.ncbi.nlm.nih.gov/pubmed/22267580%0Ahttp://www.pubmedcentral.nih.gov/articlerender.fcgi?artid=PMC3292700%0Ahttp://www.sciencemag.org/cgi/doi/10.1126/science.1215802.

D. C. Lohman, D. R. Edwards, and R. Wolfenden. Catalysis by Desolvation: The Catalytic Prowess of SAM-Dependent Halide-Alkylating Enzymes. *Journal of the American Chemical Society*, 135(39):14473–14475, Oct. 2013. ISSN 0002-7863, 1520-5126. doi: 10.1021/ja406381b. URL https://pubs.acs.org/doi/10.1021/ja406381b.

J. P. Loria, M. Rance, and A. G. Palmer. A Relaxation-Compensated Carr-Purcell-Meiboom-Gill Sequence for Characterizing Chemical Exchange by NMR Spectroscopy. *Journal of the American Chemical Society*, 121(10):2331–2332, Mar. 1999a. ISSN 0002-7863, 1520-5126. doi: 10.1021/ja983961a. URL https://pubs.acs.org/doi/10.1021/ja983961a.

J. P. Loria, M. Rance, and A. G. Palmer. A TROSY CPMG sequence for characterizing chemical exchange in large proteins. *Journal of Biomolecular NMR*, 15(2):151–155, 1999b. ISSN 09252738. doi: 10.1023/A:1008355631073. URL http://link.springer.com/10.1023/A:1008355631073.

M. Lu, R. Ishima, T. Polenova, and A. M. Gronenborn. 19F NMR relaxation studies of fluorosubstituted tryptophans. *Journal of Biomolecular NMR*, 73(8-9):401–409, 2019. ISSN 0123456789. doi: 10.1007/s10858-019-00268-y. URL https://doi.org/10.1007/s10858-019-00268-y.

B. Luke, A. Panza, S. Redon, N. Iglesias, Z. Li, and J. Lingner. The Rat1p 5′ to 3′ Exonuclease Degrades Telomeric Repeat-Containing RNA and Promotes Telomere Elongation in Saccharomyces cerevisiae. *Molecular Cell*, 32(4):465–477, Nov. 2008. ISSN 10972765. doi: 10.1016/j.molcel.2008.10.019. URL https://linkinghub.elsevier.com/retrieve/pii/S1097276508007594.

P. Lundström and M. Akke. Microsecond Protein Dynamics Measured by 13Cα Rotating-Frame Spin Relaxation. *ChemBioChem*, 6(9):1685–1692, Sept. 2005a. ISSN 14394227. doi: 10.1002/cbic.200500086. URL https://onlinelibrary.wiley.com/doi/10.1002/cbic.200500086.

P. Lundström and M. Akke. Off-resonance rotating-frame amide proton spin relaxation experiments measuring microsecond chemical exchange in proteins. *Journal of Biomolecular NMR*, 32(2):163–173, 2005b. doi: 10.1007/s10858-005-5027-3.

P. Lundström, P. Vallurupalli, T. L. Religa, F. W. Dahlquist, and L. E. Kay. A single-quantum methyl 13C-relaxation dispersion experiment with improved sensitivity. *Journal of Biomolecular NMR*, 38(1):79–88, 2007. doi: 10.1007/s10858-007-9149-7.

P. Lundström, D. F. Hansen, and L. E. Kay. Measurement of carbonyl chemical shifts of excited protein states by relaxation dispersion NMR spectroscopy: comparison between uniformly and selectively 13C labeled samples. *Journal of Biomolecular NMR*, 42(1):35–47, Sept. 2008. ISSN 0925-2738, 1573-5001. doi: 10.1007/s10858-008-9260-4. URL http://link.springer.com/10.1007/s10858-008-9260-4.

P. Lundström, D. F. Hansen, P. Vallurupalli, and L. E. Kay. Accurate Measurement of Alpha Proton Chemical Shifts of Excited Protein States by Relaxation Dispersion NMR Spectroscopy. *Journal of the American Chemical Society*, 131(5):1915–1926, Feb. 2009a. ISSN 0002-7863, 1520-5126. doi: 10.1021/ja807796a. URL https://pubs.acs.org/doi/10.1021/ja807796a.

P. Lundström, H. Lin, and L. E. Kay. Measuring 13Cβ chemical shifts of invisible excited states in proteins by relaxation dispersion NMR spectroscopy. *Journal of Biomolecular NMR*, 44(3):139–155, July 2009b. ISSN 0925-2738, 1573-5001. doi: 10.1007/s10858-009-9321-3. URL http://link.springer.com/10.1007/s10858-009-9321-3.

Z. Luz and S. Meiboom. Nuclear Magnetic Resonance Study of the Protolysis of Trimethylammonium Ion in Aqueous Solution—Order of the Reaction with Respect to Solvent. *The Journal of Chemical Physics*, 39 (2):366–370, July 1963. ISSN 0021-9606, 1089-7690. doi: 10.1063/1.1734254. URL http://aip.scitation.org/doi/10.1063/1.1734254.

A. Manglik, T. H. Kim, M. Masureel, C. Altenbach, Z. Yang, D. Hilger, M. T. Lerch, T. S. Kobilka, F. S. Thian, W. L. Hubbell, R. S. Prosser, and B. K. Kobilka. Structural insights into the dynamic process of β2-adrenergic receptor signaling. *Cell*, 161(5):1101–1111, 2015. doi: 10.1016/j.cell.2015.04.043. URL http://dx.doi.org/10.1016/j.cell.2015.04.043.

F. Massi, E. Johnson, C. Wang, M. Rance, and A. G. Palmer. NMR R1ρ Rotating-Frame Relaxation with Weak Radio Frequency Fields. *Journal of the American Chemical Society*, 126(7):2247–2256, 2004. doi: 10.1021/ja038721w.

E. Matei and A. M. Gronenborn. 19F Paramagnetic Relaxation Enhancement: A Valuable Tool for Distance Measurements in Proteins. *Angewandte Chemie - International Edition*, 55(1):150–154, 2016. doi: 10.1002/anie.201508464.

S. Matsumoto, S. Ishida, M. Araki, T. Kato, K. Terayama, and Y. Okuno. Extraction of protein dynamics information from cryo-EM maps using deep learning. *Nature Machine Intelligence*, 3(2):153–160, Feb. 2021. ISSN 2522-5839. doi: 10.1038/s42256-020-00290-y. URL http://www.nature.com/articles/s42256-020-00290-y.

H. Mazal and G. Haran. Single-molecule FRET methods to study the dynamics of proteins at work. *Current Opinion in Biomedical Engineering*, 12:8–17, Dec. 2019. ISSN 24684511. doi: 10.1016/j.cobme.2019.08.007. URL https://linkinghub.elsevier.com/retrieve/pii/S2468451119300261.

H. M. McConnell. Reaction Rates by Nuclear Magnetic Resonance. *The Journal of Chemical Physics*, 28(3): 430–431, Mar. 1958. ISSN 0021-9606, 1089-7690. doi: 10.1063/1.1744152. URL http://aip.scitation.org/doi/10.1063/1.1744152.

A. J. McCoy, R. W. Grosse-Kunstleve, P. D. Adams, M. D. Winn, L. C. Storoni, and R. J. Read. *Phaser* crystallographic software. *Journal of Applied Crystallography*, 40(4):658–674, Aug. 2007. ISSN 0021-8898. doi: 10.1107/S0021889807021206. URL https://onlinelibrary.wiley.com/doi/10.1107/S0021889807021206.

S. Meiboom and D. Gill. Modified Spin-Echo Method for Measuring Nuclear Relaxation Times. *Review of Scientific Instruments*, 29(8):688–691, Aug. 1958. ISSN 0034-6748, 1089-7623. doi: 10.1063/1.1716296. URL http://aip.scitation.org/doi/10.1063/1.1716296.

T. S. Miki and H. Großhans. The multifunctional RNase XRN2. *Biochemical Society Transactions*, 41(4):825–830, Aug. 2013. ISSN 0300-5127, 1470-8752. doi: 10.1042/BST20130001. URL https://portlandpress.com/biochemsoctrans/article/41/4/825/67095/The-multifunctional-RNase-XRN2.

T. S. Miki, H. Richter, S. Rüegger, and H. Großhans. PAXT-1 Promotes XRN2 Activity by Stabilizing It through a Conserved Domain. *Molecular Cell*, 53(2):351–360, 2014a. doi: 10.1016/j.molcel.2014.01.001.

T. S. Miki, S. Rüegger, D. Gaidatzis, M. B. Stadler, and H. Großhans. Engineering of a conditional allele reveals multiple roles of XRN2 in Caenorhabditis elegans development and substrate specificity in microRNA turnover. *Nucleic Acids Research*, 42(6):4056–4067, Apr. 2014b. ISSN 1362-4962, 0305-1048. doi: 10.1093/nar/gkt1418. URL https://academic.oup.com/nar/article/42/6/4056/2438405.

V. Z. Miloushev and A. G. Palmer. R1ρ relaxation for two-site chemical exchange: General approximations and some exact solutions. *Journal of Magnetic Resonance*, 177(2):221–227, 2005. doi: 10.1016/j.jmr.2005.07.023.

G. T. Montelione and G. Wagner. 2D Chemical Exchange NMR Spectroscopy by Proton-Detected Heteronuclear Correlation. *Journal of the American Chemical Society*, 111(8):3096–3098, 1989. ISSN 0002786318911. doi: 10.1021/ja00190a072.

P. B. Moore. How Should We Think About the Ribosome? *Annual Review of Biophysics*, 41(1):1–19, June 2012. ISSN 1936-122X, 1936-1238. doi: 10.1146/annurev-biophys-050511-102314. URL http://www.annualreviews.org/doi/10.1146/annurev-biophys-050511-102314.

G. A. Morris and R. Freeman. Enhancement of nuclear magnetic resonance signals by polarization transfer. *Journal of the American Chemical Society*, 101(3):760–762, Jan. 1979. ISSN 0002-7863, 1520-5126. doi: 10.1021/ja00497a058. URL https://pubs.acs.org/doi/abs/10.1021/ja00497a058.

F. A. Mulder, R. A. De Graaf, R. Kaptein, and R. Boelens. An Off-resonance Rotating Frame Relaxation Experiment for the Investigation of Macromolecular Dynamics Using Adiabatic Rotations. *Journal of Magnetic Resonance*, 131(2):351–357, 1998. doi: 10.1006/jmre.1998.1380.

F. A. Mulder, A. Mittermaier, B. Hon, F. W. Dahlquist, and L. E. Kay. Studying excited states of proteins by NMR spectroscopy. *Nature Structural Biology*, 8(11):932–935, 2001. doi: 10.1038/nsb1101-932.

F. A. A. Mulder and M. Akke. Carbonyl13C transverse relaxation measurements to sample protein backbone dynamics. *Magnetic Resonance in Chemistry*, 41(10):853–865, Oct. 2003. ISSN 0749-1581, 1097-458X. doi: 10.1002/mrc.1252. URL https://onlinelibrary.wiley.com/doi/10.1002/mrc.1252.

A. Neu, U. Neu, A.-L. Fuchs, B. Schlager, and R. Sprangers. An excess of catalytically required motions inhibits the scavenger decapping enzyme. *Nature Chemical Biology*, 11(9):697–704, Sept. 2015. ISSN 1552-4450, 1552-4469. doi: 10.1038/nchembio.1866. URL http://www.nature.com/articles/nchembio.1866.

P. Neudecker, D. M. Korzhnev, and L. E. Kay. Assessment of the Effects of Increased Relaxation Dispersion Data on the Extraction of 3-site Exchange Parameters Characterizing the Unfolding of an SH3 Domain. *Journal of Biomolecular NMR*, 34(3):129–135, Mar. 2006. ISSN 0925-2738, 1573-5001. doi: 10.1007/s10858-006-0001-2. URL http://link.springer.com/10.1007/s10858-006-0001-2.

P. Neudecker, P. Robustelli, A. Cavalli, P. Walsh, P. Lundstrom, A. Zarrine-Afsar, S. Sharpe, M. Vendruscolo, and L. E. Kay. Structure of an Intermediate State in Protein Folding and Aggregation. *Science*, 336(6079):362–366, Apr. 2012. ISSN 0036-8075, 1095-9203. doi: 10.1126/science.1214203. URL https://www.sciencemag.org/lookup/doi/10.1126/science.1214203.

E. N. Nikolova, E. Kim, A. A. Wise, P. J. O'Brien, I. Andricioaei, and H. M. Al-Hashimi. Transient Hoogsteen base pairs in canonical duplex DNA. *Nature*, 470(7335):498–504, 2011. doi: 10.1038/nature09775. URL http://dx.doi.org/10.1038/nature09775.

E. N. Nikolova, F. L. Gottardo, and H. M. Al-Hashimi. Probing Transient Hoogsteen Hydrogen Bonds in Canonical Duplex DNA Using NMR Relaxation Dispersion and Single-Atom Substitution. *Journal of the American Chemical Society*, 134(8):3667–3670, Feb. 2012. ISSN 0002-7863, 1520-5126. doi: 10.1021/ja2117816. URL https://pubs.acs.org/doi/10.1021/ja2117816.

F. Nußbaumer, R. Plangger, M. Roeck, and C. Kreutz. Aromatic ^{19}F–^{13}C TROSY—[^{19}F, ^{13}C]-Pyrimidine Labeling for NMR Spectroscopy of RNA. *Angewandte Chemie International Edition*, 59(39):17062–17069, Sept. 2020. ISSN 1433-7851, 1521-3773. doi: 10.1002/anie.202006577. URL https://onlinelibrary.wiley.com/doi/10.1002/anie.202006577.

M. Olejniczak. The bulge region of HIV-1 TAR RNA binds metal ions in solution. *Nucleic Acids Research*, 30 (19):4241–4249, Oct. 2002. ISSN 13624962. doi: 10.1093/nar/gkf541. URL https://academic.oup.com/nar/article-lookup/doi/10.1093/nar/gkf541.

J. E. Ollerenshaw, V. Tugarinov, and L. E. Kay. Methyl TROSY: Explanation and experimental verification. *Magnetic Resonance in Chemistry*, 41(10):843–852, 2003. doi: 10.1002/mrc.1256.

V. Y. Orekhov, D. M. Korzhnev, and L. E. Kay. Double- and Zero-Quantum NMR Relaxation Dispersion Experiments Sampling Millisecond Time Scale Dynamics in Proteins. *Journal of the American Chemical Society*, 126(6):1886–1891, 2004. doi: 10.1021/ja038620y.

R. Otten, J. Villali, D. Kern, and F. A. A. Mulder. Probing Microsecond Time Scale Dynamics in Proteins by Methyl ^{1}H Carr-Purcell-Meiboom-Gill Relaxation Dispersion NMR Measurements. Application to Activation of the Signaling Protein NtrC ^{r}. *Journal of the American Chemical Society*, 132(47):17004–17014, Dec. 2010. ISSN 0002-7863, 1520-5126. doi: 10.1021/ja107410x. URL https://pubs.acs.org/doi/10.1021/ja107410x.

J. H. Overbeck, W. Kremer, and R. Sprangers. A suite of 19F based relaxation dispersion experiments to assess biomolecular motions. *Journal of Biomolecular NMR*, 74(12):753–766, Dec. 2020. ISSN 0925-2738, 1573-5001. doi: 10.1007/s10858-020-00348-4. URL http://link.springer.com/10.1007/s10858-020-00348-4.

K. Packer and K. Wright. The use of single-spin operator basis sets in the N.M.R. spectroscopy of scalar-coupled spin systems. *Molecular Physics*, 50(4):797–813, Nov. 1983. ISSN 0026-8976, 1362-3028. doi: 10.1080/00268978300102691. URL http://www.tandfonline.com/doi/abs/10.1080/00268978300102691.

A. M. Page, K. Davis, C. Molineux, R. D. Kolodner, and A. W. Johnson. Mutational analysis of exoribonuclease I from Saccharomyces cerevisiae. *Nucleic Acids Research*, 26(16):3707–3716, Aug. 1998. ISSN 0305-1048, 1362-4962. doi: 10.1093/nar/26.16.3707. URL https://academic.oup.com/nar/article-lookup/doi/10.1093/nar/26.16.3707.

A. G. Palmer and H. Koss. Chemical Exchange. In *Methods in Enzymology*, volume 615, pages 177–236. Elsevier, 2019. ISBN 978-0-12-816762-5. doi: 10.1016/bs.mie.2018.09.028. URL https://linkinghub.elsevier.com/retrieve/pii/S0076687918303914.

A. G. Palmer and F. Massi. Characterization of the dynamics of biomacromolecules using rotating-frame spin relaxation NMR spectroscopy. *Chemical Reviews*, 106(5):1700–1719, 2006. doi: 10.1021/cr0404287.

A. G. Palmer, C. D. Kroenke, and J. Patrick Loria. Nuclear Magnetic Resonance Methods for Quantifying Microsecond-to-Millisecond Motions in Biological Macromolecules. In *Methods in Enzymology*, volume 339, pages 204–238. Elsevier, 2001. ISBN 978-0-12-182240-8. doi: 10.1016/S0076-6879(01)39315-1. URL https://linkinghub.elsevier.com/retrieve/pii/S0076687901393151.

A. G. Palmer, M. J. Grey, and C. Wang. Solution NMR Spin Relaxation Methods for Characterizing Chemical Exchange in High-Molecular-Weight Systems. In *Methods in Enzymology*, volume 394, pages 430–465. Elsevier, 2005. ISBN 978-0-12-182799-1. doi: 10.1016/S0076-6879(05)94018-4. URL https://linkinghub.elsevier.com/retrieve/pii/S0076687905940184.

V. Pelechano, W. Wei, and L. M. Steinmetz. Widespread Co-translational RNA Decay Reveals Ribosome Dynamics. *Cell*, 161(6):1400–1412, June 2015. ISSN 00928674. doi: 10.1016/j.cell.2015.05.008. URL https://linkinghub.elsevier.com/retrieve/pii/S0092867415005565.

D. Perl, C. Welker, T. Schindler, K. Schröder, M. A. Marahiel, R. Jaenicke, and F. X. Schmid. Conservation of rapid two-state folding in mesophilic, thermophilic and hyperthermophilic cold shock proteins. *Nature Structural Biology*, 5(3):229–235, Mar. 1998. ISSN 1072-8368. doi: 10.1038/nsb0398-229. URL http://www.nature.com/doifinder/10.1038/nsb0398-229.

K. Pervushin, R. Riek, G. Wider, and K. Wüthrich. Attenuated T2 relaxation by mutual cancellation of dipole–dipole coupling and chemical shift anisotropy.pdf. *Proceedings of the National Academy of Sciences of the United States of America*, 94(November):12366–12371, 1997.

E. Petfalski, T. Dandekar, Y. Henry, and D. Tollervey. Processing of the Precursors to Small Nucleolar RNAs and rRNAs Requires Common Components. *Molecular and Cellular Biology*, 18(3):1181–1189, Mar. 1998. ISSN 0270-7306, 1098-5549. doi: 10.1128/MCB.18.3.1181. URL https://journals.asm.org/doi/10.1128/MCB.18.3.1181.

E. F. Pettersen, T. D. Goddard, C. C. Huang, E. C. Meng, G. S. Couch, T. I. Croll, J. H. Morris, and T. E. Ferrin. UCSF ChimeraX : Structure visualization for researchers,

educators, and developers. *Protein Science*, 30(1):70–82, Jan. 2021. ISSN 0961-8368, 1469-896X. doi: 10.1002/pro.3943. URL https://onlinelibrary.wiley.com/doi/10.1002/pro.3943.

M. Pfender, P. Wang, H. Sumiya, S. Onoda, W. Yang, D. B. R. Dasari, P. Neumann, X.-Y. Pan, J. Isoya, R.-B. Liu, and J. Wrachtrup. High-resolution spectroscopy of single nuclear spins via sequential weak measurements. *Nature Communications*, 10(1):594, Dec. 2019. ISSN 2041-1723. doi: 10.1038/s41467-019-08544-z. URL http://www.nature.com/articles/s41467-019-08544-z.

N. Popovych, S. Sun, R. H. Ebright, and C. G. Kalodimos. Dynamically driven protein allostery. *Nature Structural & Molecular Biology*, 13(9):831–838, Sept. 2006. ISSN 1545-9993, 1545-9985. doi: 10.1038/nsmb1132. URL http://www.nature.com/articles/nsmb1132.

W. Pornsiriwong, G. M. Estavillo, K. X. Chan, E. E. Tee, D. Ganguly, P. A. Crisp, S. Y. Phua, C. Zhao, J. Qiu, J. Park, M. T. Yong, N. Nisar, A. K. Yadav, B. Schwessinger, J. Rathjen, C. I. Cazzonelli, P. B. Wilson, M. Gilliham, Z.-H. Chen, and B. J. Pogson. A chloroplast retrograde signal, 3'-phosphoadenosine 5'-phosphate, acts as a secondary messenger in abscisic acid signaling in stomatal closure and germination. *eLife*, 6:e23361, Mar. 2017. ISSN 2050-084X. doi: 10.7554/eLife.23361. URL https://elifesciences.org/articles/23361.

B. Puffer, C. Kreutz, U. Rieder, M.-O. Ebert, R. Konrat, and R. Micura. 5-Fluoro pyrimidines: labels to probe DNA and RNA secondary structures by 1D 19 F NMR spectroscopy. *Nucleic Acids Research*, 37(22):7728–7740, Dec. 2009. ISSN 1362-4962, 0305-1048. doi: 10.1093/nar/gkp862. URL https://academic.oup.com/nar/article-lookup/doi/10.1093/nar/gkp862.

M. R. Puno, E.-M. Weick, M. Das, and C. D. Lima. SnapShot: The RNA Exosome. *Cell*, 179(1):282–282.e1, Sept. 2019. ISSN 00928674. doi: 10.1016/j.cell.2019.09.005. URL https://linkinghub.elsevier.com/retrieve/pii/S0092867419310116.

L.-H. Qu, A. Henras, Y.-J. Lu, H. Zhou, W.-x. Zhou, Y.-Q. Zhu, J. Zhao, Y. Henry, M. Caizergues-Ferrer, and J.-P. Bachellerie. Seven Novel Methylation Guide Small Nucleolar RNAs Are Processed from a Common Polycistronic Transcript by Rat1p and RNase III in Yeast. *Molecular and Cellular Biology*, 19(2):1144–1158, Feb. 1999. ISSN 0270-7306, 1098-5549. doi: 10.1128/MCB.19.2.1144. URL https://journals.asm.org/doi/10.1128/MCB.19.2.1144.

M. Rabani, R. Raychowdhury, M. Jovanovic, M. Rooney, D. J. Stumpo, A. Pauli, N. Hacohen, A. F. Schier, P. J. Blackshear, N. Friedman, I. Amit, and A. Regev. High-Resolution Sequencing and Modeling Identifies Distinct Dynamic RNA Regulatory Strategies. *Cell*, 159(7):1698–1710, Dec. 2014. ISSN 00928674. doi: 10.1016/j.cell.2014.11.015. URL https://linkinghub.elsevier.com/retrieve/pii/S0092867414014469.

A. Rangadurai, E. S. Szymaski, I. J. Kimsey, H. Shi, and H. M. Al-Hashimi. Characterizing micro-to-millisecond chemical exchange in nucleic acids using off-resonance R1ρ relaxation dispersion. *Progress in Nuclear Magnetic Resonance Spectroscopy*, 112-113:55–102, June 2019. ISSN 00796565. doi: 10.1016/j.pnmrs.2019.05.002. URL https://linkinghub.elsevier.com/retrieve/pii/S0079656519300123.

A. Rangadurai, H. Shi, and H. M. Al-Hashimi. Extending the Sensitivity of CEST NMR Spectroscopy to Micro-to-Millisecond Dynamics in Nucleic Acids Using High-Power Radio-Frequency Fields. *Angewandte Chemie International Edition*, 59(28):11262–11266, July 2020. ISSN 1433-7851, 1521-3773. doi: 10.1002/anie.202000493. URL https://onlinelibrary.wiley.com/doi/10.1002/anie.202000493.

F. Rastinejad, C. Evilia, and P. Lu. [23] Studies of nucleic acids and their protein interactions by 19F NMR. In *Methods in Enzymology*, volume 261, pages 560–575. Elsevier, 1995. ISBN 978-0-12-182162-3. doi: 10.1016/S0076-6879(95)61025-1. URL https://linkinghub.elsevier.com/retrieve/pii/S0076687995610251.

H. N. Raum, M. Dreydoppel, and U. Weininger. Conformational exchange of aromatic side chains by 1H CPMG relaxation dispersion. *Journal of Biomolecular NMR*, 72(1-2):105–114, 2018. ISSN 1085801802. doi: 10.1007/s10858-018-0210-5. URL http://dx.doi.org/10.1007/s10858-018-0210-5.

H. N. Raum, J. Schörghuber, M. Dreydoppel, R. J. Lichtenecker, and U. Weininger. Site-selective 1H/2H labeling enables artifact-free 1H CPMG relaxation dispersion experiments in aromatic side chains. *Journal of Biomolecular NMR*, 73(10-11):633–639, 2019. ISSN 0123456789. doi: 10.1007/s10858-019-00275-z. URL https://doi.org/10.1007/s10858-019-00275-z.

J. G. Reddy, S. Pratihar, D. Ban, S. Frischkorn, S. Becker, C. Griesinger, and D. Lee. Simultaneous determination of fast and slow dynamics in molecules using extreme CPMG relaxation dispersion experiments. *Journal of Biomolecular NMR*, 70(1):1–9, 2018. ISSN 0123456789. doi: 10.1007/s10858-017-0155-0. URL http://dx.doi.org/10.1007/s10858-017-0155-0.

T. L. Religa, R. Sprangers, and L. E. Kay. Dynamic Regulation of Archaeal Proteasome Gate Opening As Studied by TROSY NMR. 328:6, 2010.

E. Rennella, R. Huang, A. Velyvis, and L. E. Kay. 13CHD2-CEST NMR spectroscopy provides an avenue for studies of conformational exchange in high molecular weight proteins. *Journal of Biomolecular NMR*, 63 (2):187–199, 2015. doi: 10.1007/s10858-015-9974-z.

E. Rennella, A. K. Schuetz, and L. E. Kay. Quantitative measurement of exchange dynamics in proteins via 13C relaxation dispersion of 13CHD2-labeled samples. *Journal of Biomolecular NMR*, 65(2):59–64, 2016. doi: 10.1007/s10858-016-0038-9.

H. Richter, I. Katic, H. Gut, and H. Großhans. Structural basis and function of XRN2 binding by XTB domains. *Nature Structural & Molecular Biology*, 23(2):164–171, Feb. 2016. ISSN 1545-9993, 1545-9985. doi: 10.1038/nsmb.3155. URL http://www.nature.com/articles/nsmb.3155.

G. Robinson, P. W. Kuchel, B. E. Chapman, D. M. Doddrell, and M. G. Irving. A simple procedure for selective inversion of NMR resonances for spin transfer enzyme kinetic measurements. *Journal of Magnetic Resonance (1969)*, 63(2):314–319, June 1985. ISSN 00222364. doi: 10.1016/0022-2364(85)90321-X. URL https://linkinghub.elsevier.com/retrieve/pii/002223648590321X.

P. Rovó. Recent advances in solid-state relaxation dispersion techniques. *Solid State Nuclear Magnetic Resonance*, 108:101665, Aug. 2020. ISSN 09262040. doi: 10.1016/j.ssnmr.2020.101665. URL https://linkinghub.elsevier.com/retrieve/pii/S0926204020300278.

N. Salvi, A. Abyzov, and M. Blackledge. Atomic resolution conformational dynamics of intrinsically disordered proteins from NMR spin relaxation. *Progress in Nuclear Magnetic Resonance Spectroscopy*, 102-103:43–60, Nov. 2017. ISSN 00796565. doi: 10.1016/j.pnmrs.2017.06.001. URL https://linkinghub.elsevier.com/retrieve/pii/S0079656517300213.

M. Sattler, J. Schleucher, and C. Griesinger. Heteronuclear multidimensional NMR experiments for the structure determination of proteins in solution employing pulsed field gradients. *Progress in Nuclear Magnetic Resonance Spectroscopy*, 34(2):93–158, 1999. doi: 10.1016/S0079-6565(98)00025-9.

P. Schanda and B. Brutscher. Very fast two-dimensional NMR spectroscopy for real-time investigation of dynamic events in proteins on the time scale of seconds. *Journal of the American Chemical Society*, 127(22): 8014–8015, 2005. doi: 10.1021/ja051306e.

J. Schlagnitweit, E. Steiner, H. Karlsson, and K. Petzold. Efficient Detection of Structure and Dynamics in Unlabeled RNAs: The SELOPE Approach. *Chemistry - A European Journal*, 24(23):6067–6070, 2018. doi: 10.1002/chem.201800992.

M. Schmid and T. H. Jensen. Controlling nuclear RNA levels. *Nature Reviews Genetics*, 19(8):518–529, Aug. 2018. ISSN 1471-0056, 1471-0064. doi: 10.1038/s41576-018-0013-2. URL `http://www.nature.com/articles/s41576-018-0013-2`.

C. Schmidt, E. Kowalinski, V. Shanmuganathan, Q. Defenouillère, K. Braunger, A. Heuer, M. Pech, A. Namane, O. Berninghausen, M. Fromont-Racine, A. Jacquier, E. Conti, T. Becker, and R. Beckmann. The cryo-EM structure of a ribosome–Ski2-Ski3-Ski8 helicase complex. *Science*, 354(6318):1431–1433, Dec. 2016. ISSN 0036-8075, 1095-9203. doi: 10.1126/science.aaf7520. URL `https://www.science.org/doi/10.1126/science.aaf7520`.

B. Schuler, W. Kremer, H. R. Kalbitzer, and R. Jaenicke. Role of entropy in protein thermostability: Folding kinetics of a hyperthermophilic cold shock protein at high temperatures using 19F NMR. *Biochemistry*, 41 (39):11670–11680, 2002a. doi: 10.1021/bi026293l.

B. Schuler, E. A. Lipman, and W. A. Eaton. Probing the free-energy surface for protein folding with single-molecule fluorescence spectroscopy. *Nature*, 419(6908):743–747, 2002b. doi: 10.1038/nature01060.

S. Schütz and R. Sprangers. Methyl TROSY spectroscopy: A versatile NMR approach to study challenging biological systems. *Progress in Nuclear Magnetic Resonance Spectroscopy*, 116:56–84, Feb. 2020. ISSN 00796565. doi: 10.1016/j.pnmrs.2019.09.004. URL `https://linkinghub.elsevier.com/retrieve/pii/S0079656519300470`.

L. G. Scott, B. H. Geierstanger, J. R. Williamson, and M. Hennig. Enzymatic Synthesis and ^{19} F NMR Studies of 2-Fluoroadenine-Substituted RNA. *Journal of the American Chemical Society*, 126(38):11776–11777, Sept. 2004. ISSN 0002-7863, 1520-5126. doi: 10.1021/ja047556x. URL `https://pubs.acs.org/doi/10.1021/ja047556x`.

O. Shalem, O. Dahan, M. Levo, M. R. Martinez, I. Furman, E. Segal, and Y. Pilpel. Transient transcriptional responses to stress are generated by opposing effects of mRNA production and degradation. *Molecular Systems Biology*, 4(1):4, Jan. 2008. ISSN 1744-4292, 1744-4292. doi: 10.1038/msb.2008.59. URL `https://onlinelibrary.wiley.com/doi/10.1038/msb.2008.59`.

D. E. Shaw, P. Maragakis, K. Lindorff-larsen, S. Piana, Y. Shan, and W. Wriggers. Atomic-Level Characterization. 330(October):341–347, 2010.

Y. Shen and A. Bax. Protein backbone and sidechain torsion angles predicted from NMR chemical shifts using artificial neural networks. *Journal of Biomolecular NMR*, 56(3):227–241, July 2013. ISSN 0925-2738, 1573-5001. doi: 10.1007/s10858-013-9741-y. URL `http://link.springer.com/10.1007/s10858-013-9741-y`.

T. Shobuike. The dhp1+ gene, encoding a putative nuclear 5'->3' exoribonuclease, is required for proper chromosome segregation in fission yeast. *Nucleic Acids Research*, 29(6):1326–1333, Mar. 2001. ISSN

13624962. doi: 10.1093/nar/29.6.1326. URL https://academic.oup.com/nar/article-lookup/doi/10.1093/nar/29.6.1326.

N. R. Skrynnikov, F. A. Mulder, B. Hon, F. W. Dahlquist, and L. E. Kay. Probing slow time scale dynamics at methyl-containing side chains in proteins by relaxation dispersion NMR measurements: Application to methionine residues in a cavity mutant of T4 lysozyme. *Journal of the American Chemical Society*, 123(19): 4556–4566, 2001. doi: 10.1021/ja004179p.

F. Sochor, R. Silvers, D. Müller, C. Richter, B. Fürtig, and H. Schwalbe. 19F-labeling of the adenine H2-site to study large RNAs by NMR spectroscopy. *Journal of Biomolecular NMR*, 64(1):63–74, Jan. 2016. ISSN 0925-2738, 1573-5001. doi: 10.1007/s10858-015-0006-9. URL http://link.springer.com/10.1007/s10858-015-0006-9.

J. A. Solinger, D. Pascolini, and W.-D. Heyer. Active-Site Mutations in the Xrn1p Exoribonuclease of *Saccharomyces cerevisiae* Reveal a Specific Role in Meiosis. *Molecular and Cellular Biology*, 19(9):5930–5942, Sept. 1999. ISSN 0270-7306, 1098-5549. doi: 10.1128/MCB.19.9.5930. URL https://journals.asm.org/doi/10.1128/MCB.19.9.5930.

M.-G. Song and M. Kiledjian. 3′ Terminal oligo U-tract-mediated stimulation of decapping. *RNA*, 13(12): 2356–2365, Dec. 2007. ISSN 1355-8382, 1469-9001. doi: 10.1261/rna.765807. URL http://rnajournal.cshlp.org/lookup/doi/10.1261/rna.765807.

O. Sørensen, G. Eich, M. Levitt, G. Bodenhausen, and R. Ernst. Product operator formalism for the description of NMR pulse experiments. *Progress in Nuclear Magnetic Resonance Spectroscopy*, 16:163–192, Jan. 1984. ISSN 00796565. doi: 10.1016/0079-6565(84)80005-9. URL https://linkinghub.elsevier.com/retrieve/pii/0079656584800059.

R. Sprangers and L. E. Kay. Quantitative dynamics and binding studies of the 20S proteasome by NMR. *Nature*, 445(7128):618–622, 2007. doi: 10.1038/nature05512.

N. Stein. *CHAINSAW* : a program for mutating pdb files used as templates in molecular replacement. *Journal of Applied Crystallography*, 41(3):641–643, June 2008. ISSN 0021-8898. doi: 10.1107/S0021889808006985. URL https://onlinelibrary.wiley.com/doi/10.1107/S0021889808006985.

E. Steiner, J. Schlagnitweit, P. Lundström, and K. Petzold. Capturing Excited States in the Fast-Intermediate Exchange Limit in Biological Systems Using1H NMR Spectroscopy. *Angewandte Chemie - International Edition*, 55(51):15869–15872, 2016. doi: 10.1002/anie.201609102.

A. Stevens. Purification and characterization of a Saccharomyces cerevisiae exoribonuclease which yields 5′-mononucleotides by a 5′ leads to 3′ mode of hydrolysis. *Journal of Biological Chemistry*, 255(7):3080–3085, Apr. 1980. ISSN 00219258. doi: 10.1016/S0021-9258(19)85855-6. URL https://linkinghub.elsevier.com/retrieve/pii/S0021925819858556.

A. Stevens and T. L. Poole. 5′-Exonuclease-2 of Saccharomyces cerevisiae. *Journal of Biological Chemistry*, 270 (27):16063–16069, July 1995. ISSN 00219258. doi: 10.1074/jbc.270.27.16063. URL https://linkinghub.elsevier.com/retrieve/pii/S0021925817488284.

G. Stoecklin and O. Mühlemann. RNA decay mechanisms: Specificity through diversity. *Biochimica et Biophysica Acta (BBA) - Gene Regulatory Mechanisms*, 1829(6-7):487–490, June 2013. ISSN 18749399. doi: 10.1016/j.bbagrm.2013.04.002. URL https://linkinghub.elsevier.com/retrieve/pii/S1874939913000655.

S. Sugano, T. Shobuike, T. Takeda, A. Sugino, and H. Ikeda. Molecular analysis of the dhp1 + gene of Schizosaccharomyces pombe: an essential gene that has homology to the DST 2 and RAT 1 genes of Saccharomyces cerevisiae. *Molecular and General Genetics MGG*, 243(1):1–8, Jan. 1994. ISSN 0026-8925, 1432-1874. doi: 10.1007/BF00283869. URL http://link.springer.com/10.1007/BF00283869.

L. Sušac, M. T. Eddy, T. Didenko, R. C. Stevens, and K. Wüthrich. A $_{2a}$ adenosine receptor functional states characterized by ^{19} F-NMR. *Proceedings of the National Academy of Sciences*, 115(50):12733–12738, Dec. 2018. ISSN 0027-8424, 1091-6490. doi: 10.1073/pnas.1813649115. URL http://www.pnas.org/lookup/doi/10.1073/pnas.1813649115.

P. Tesina, E. Heckel, J. Cheng, M. Fromont-Racine, R. Buschauer, L. Kater, B. Beatrix, O. Berninghausen, A. Jacquier, T. Becker, and R. Beckmann. Structure of the 80S ribosome–Xrn1 nuclease complex. *Nature Structural & Molecular Biology*, 26(4):275–280, Apr. 2019. ISSN 1545-9993, 1545-9985. doi: 10.1038/s41594-019-0202-5. URL http://www.nature.com/articles/s41594-019-0202-5.

M. Tollinger, N. R. Skrynnikov, F. A. A. Mulder, J. D. Forman-Kay, and L. E. Kay. Slow Dynamics in Folded and Unfolded States of an SH3 Domain. *Journal of the American Chemical Society*, 123(46):11341–11352, Nov. 2001. ISSN 0002-7863, 1520-5126. doi: 10.1021/ja011300z. URL https://pubs.acs.org/doi/10.1021/ja011300z.

J. R. Tolman and K. Ruan. NMR Residual Dipolar Couplings as Probes of Biomolecular Dynamics. *Chemical Reviews*, 106(5):1720–1736, May 2006. ISSN 0009-2665, 1520-6890. doi: 10.1021/cr040429z. URL https://pubs.acs.org/doi/10.1021/cr040429z.

Y. Toyama, R. W. Harkness, T. Y. T. Lee, J. T. Maynes, and L. E. Kay. Oligomeric assembly regulating mitochondrial HtrA2 function as examined by methyl-TROSY NMR. *Proceedings of the National Academy of Sciences*, 118(11):e2025022118, Mar. 2021. ISSN 0027-8424, 1091-6490. doi: 10.1073/pnas.2025022118. URL http://www.pnas.org/lookup/doi/10.1073/pnas.2025022118.

O. Trott and A. G. Palmer. R 1ρ relaxation outside of the fast-exchange limit. *Journal of Magnetic Resonance*, 154(1):157–160, 2002. doi: 10.1006/jmre.2001.2466.

C. Tuerk and L. Gold. Systematic Evolution of Ligands by Exponential Enrichment: RNA Ligands to Bacteriophage T4 DNA Polymerase. *Science*, 249(4968):505–510, Aug. 1990. ISSN 0036-8075, 1095-9203. doi: 10.1126/science.2200121. URL https://www.science.org/doi/10.1126/science.2200121.

V. Tugarinov and L. E. Kay. Separating degenerate 1H transitions in methyl group probes for single-quantum 1H-CPMG relaxation dispersion NMR spectroscopy. *Journal of the American Chemical Society*, 129(30):9514–9521, 2007. doi: 10.1021/ja0726456.

V. Tugarinov, P. M. Hwang, J. E. Ollerenshaw, and L. E. Kay. Cross-correlated relaxation enhanced 1H-13C NMR spectroscopy of methyl groups in very high molecular weight proteins and protein complexes. *Journal of the American Chemical Society*, 125(34):10420–10428, 2003. doi: 10.1021/ja030153x.

V. Tugarinov, D. S. Libich, V. Meyer, J. Roche, and G. M. Clore. The Energetics of a Three-State Protein Folding System Probed by High-Pressure Relaxation Dispersion NMR Spectroscopy. *Angewandte Chemie - International Edition*, 54(38):11157–11161, 2015. doi: 10.1002/anie.201505416.

S.-R. Tzeng and C. G. Kalodimos. Allosteric inhibition through suppression of transient conformational states. *Nature Chemical Biology*, 9(7):462–465, July 2013. ISSN 1552-4450, 1552-4469. doi: 10.1038/nchembio.1250. URL http://www.nature.com/articles/nchembio.1250.

P. Vallurupalli and L. E. Kay. Probing Slow Chemical Exchange at Carbonyl Sites in Proteins by Chemical Exchange Saturation Transfer NMR Spectroscopy. *Angewandte Chemie International Edition*, 52(15):4156–4159, Apr. 2013. ISSN 14337851. doi: 10.1002/anie.201209118. URL https://onlinelibrary.wiley.com/doi/10.1002/anie.201209118.

P. Vallurupalli, G. Bouvignies, and L. E. Kay. Studying "Invisible" Excited Protein States in Slow Exchange with a Major State Conformation. *Journal of the American Chemical Society*, 134(19):8148–8161, May 2012. ISSN 0002-7863, 1520-5126. doi: 10.1021/ja3001419. URL https://pubs.acs.org/doi/10.1021/ja3001419.

P. Vallurupalli, N. Chakrabarti, R. Pomès, and L. E. Kay. Atomistic picture of conformational exchange in a t4 lysozyme cavity mutant: An experiment-guided molecular dynamics study. *Chemical Science*, 7(6):3602–3613, 2016. doi: 10.1039/c5sc03886c.

P. Vallurupalli, V. P. Tiwari, and S. Ghosh. A Double-Resonance CEST Experiment to Study Multistate Protein Conformational Exchange: An Application to Protein Folding. *Journal of Physical Chemistry Letters*, 10(11):3051–3056, 2019. doi: 10.1021/acs.jpclett.9b00985.

F. Van De Ven and C. Hilbers. A simple formalism for the description of multiple-pulse experiments. Application to a weakly coupled two-spin () system. *Journal of Magnetic Resonance (1969)*, 54(3):512–520, Oct. 1983. ISSN 00222364. doi: 10.1016/0022-2364(83)90331-1. URL https://linkinghub.elsevier.com/retrieve/pii/0022236483903311.

F. J. M. v. d. Ven. *Multidimensional NMR in liquids: basic principles and experimental methods*. VCH, New York, 1995. ISBN 978-0-471-18594-9 978-1-56081-665-2.

M. Wang and D. G. Pestov. 5'-end surveillance by Xrn2 acts as a shared mechanism for mammalian pre-rRNA maturation and decay. *Nucleic Acids Research*, 39(5):1811–1822, Mar. 2011. ISSN 1362-4962, 0305-1048. doi: 10.1093/nar/gkq1050. URL https://academic.oup.com/nar/article-lookup/doi/10.1093/nar/gkq1050.

Y. Wang, G. Han, X. Jiang, T. Yuwen, and Y. Xue. Chemical shift prediction of RNA imino groups: application toward characterizing RNA excited states. *Nature Communications*, 12(1):1595, Dec. 2021. ISSN 2041-1723. doi: 10.1038/s41467-021-21840-x. URL http://www.nature.com/articles/s41467-021-21840-x.

R. K. Wangsness and F. Bloch. The Dynamical Theory of Nuclear Induction. *Physical Review*, 89(4):728–739, Feb. 1953. ISSN 0031-899X. doi: 10.1103/PhysRev.89.728. URL https://link.aps.org/doi/10.1103/PhysRev.89.728.

K. Ward, A. Aletras, and R. Balaban. A New Class of Contrast Agents for MRI Based on Proton Chemical Exchange Dependent Saturation Transfer (CEST). *Journal of Magnetic Resonance*, 143(1):79–87, Mar. 2000. ISSN 10907807. doi: 10.1006/jmre.1999.1956. URL https://linkinghub.elsevier.com/retrieve/pii/S1090780799919560.

D. Wassenberg, C. Welker, and R. Jaenicke. Thermodynamics of the unfolding of the cold-shock protein from Thermotoga maritima. *Journal of Molecular Biology*, 289(1):187–193, 1999. doi: 10.1006/jmbi.1999.2772.

J. E. Weigand, M. Sanchez, E.-B. Gunnesch, S. Zeiher, R. Schroeder, and B. Suess. Screening for engineered neomycin riboswitches that control translation initiation. *RNA*, 14(1):89–97, 2008. ISSN 1355-8382. doi: 10.1261/rna.772408. URL http://www.rnajournal.org/cgi/doi/10.1261/rna.772408.

J. E. Weigand, S. R. Gottstein-Schmidtke, S. Demolli, F. Groher, E. Duchardt-Ferner, J. Wöhnert, and B. Suess. Sequence Elements Distal to the Ligand Binding Pocket Modulate the Efficiency of a Synthetic Riboswitch. *ChemBioChem*, 15(11):1627–1637, July 2014. ISSN 14394227. doi: 10.1002/cbic.201402067. URL `http://doi.wiley.com/10.1002/cbic.201402067`.

U. Weininger, Z. Liu, D. D. McIntyre, H. J. Vogel, and M. Akke. Specific 12CβD212C γD2S13CεHD2 isotopomer labeling of methionine to characterize protein dynamics by 1H and 13C NMR relaxation dispersion. *Journal of the American Chemical Society*, 134(45):18562–18565, 2012a. doi: 10.1021/ja309294u.

U. Weininger, M. Respondek, and M. Akke. Conformational exchange of aromatic side chains characterized by L-optimized TROSY-selected 13C CPMG relaxation dispersion. *Journal of Biomolecular NMR*, 54(1):9–14, Sept. 2012b. ISSN 0925-2738, 1573-5001. doi: 10.1007/s10858-012-9656-z. URL `http://link.springer.com/10.1007/s10858-012-9656-z`.

U. Weininger, A. T. Blissing, J. Hennig, A. Ahlner, Z. Liu, H. J. Vogel, M. Akke, and P. Lundström. Protein conformational exchange measured by 1H R 1ρ relaxation dispersion of methyl groups. *Journal of Biomolecular NMR*, 57(1):47–55, 2013. doi: 10.1007/s10858-013-9764-4.

U. Weininger, U. Brath, K. Modig, K. Teilum, and M. Akke. Off-resonance rotating-frame relaxation dispersion experiment for 13C in aromatic side chains using L-optimized TROSY-selection. *Journal of Biomolecular NMR*, 59(1):23–29, May 2014. ISSN 0925-2738, 1573-5001. doi: 10.1007/s10858-014-9826-2. URL `http://link.springer.com/10.1007/s10858-014-9826-2`.

G. Werstuck. Controlling Gene Expression in Living Cells Through Small Molecule-RNA Interactions. *Science*, 282(5387):296–298, Oct. 1998. doi: 10.1126/science.282.5387.296. URL `https://www.sciencemag.org/lookup/doi/10.1126/science.282.5387.296`.

S. West, N. Gromak, and N. J. Proudfoot. Human 5′ $\rightarrow$ 3′ exonuclease Xrn2 promotes transcription termination at co-transcriptional cleavage sites. *Nature*, 432(7016):522–525, Nov. 2004. ISSN 0028-0836, 1476-4687. doi: 10.1038/nature03035. URL `http://www.nature.com/articles/nature03035`.

M. Wolf-Watz, V. Thai, K. Henzler-Wildman, G. Hadjipavlou, E. Z. Eisenmesser, and D. Kern. Linkage between dynamics and catalysis in a thermophilic-mesophilic enzyme pair. *Nature Structural & Molecular Biology*, 11(10):945–949, Oct. 2004. ISSN 1545-9993, 1545-9985. doi: 10.1038/nsmb821. URL `http://www.nature.com/articles/nsmb821`.

J. P. Wurm, I. Holdermann, J. H. Overbeck, P. H. O. Mayer, and R. Sprangers. Changes in conformational equilibria regulate the activity of the Dcp2 decapping enzyme. *Proceedings of the National Academy of Sciences*, 114(23):6034–6039, June 2017. ISSN 0027-8424, 1091-6490. doi: 10.1073/pnas.1704496114. URL `http://www.pnas.org/lookup/doi/10.1073/pnas.1704496114`.

J. P. Wurm, S. Sung, A. C. Kneuttinger, E. Hupfeld, R. Sterner, M. Wilmanns, and R. Sprangers. Molecular basis for the allosteric activation mechanism of the heterodimeric imidazole glycerol phosphate synthase complex. *Nature Communications*, 12(1):2748, Dec. 2021. ISSN 2041-1723. doi: 10.1038/s41467-021-22968-6. URL `http://www.nature.com/articles/s41467-021-22968-6`.

S. Xiang, A. Cooper-Morgan, X. Jiao, M. Kiledjian, J. L. Manley, and L. Tong. Structure and function of the 5′$\rightarrow$3′ exoribonuclease Rat1 and its activating partner Rai1. *Nature*, 458(7239):784–788, Apr. 2009. ISSN 0028-0836, 1476-4687. doi: 10.1038/nature07731. URL `http://www.nature.com/articles/nature07731`.

T. Xie, T. Saleh, P. Rossi, and C. G. Kalodimos. Conformational states dynamically populated by a kinase determine its function. *Science*, 370(6513):eabc2754, Oct. 2020. ISSN 0036-8075, 1095-9203. doi: 10.1126/science.abc2754. URL https://www.science.org/doi/10.1126/science.abc2754.

L. Ye, N. Van Eps, M. Zimmer, O. P. Ernst, and R. Scott Prosser. Activation of the A 2A adenosine G-protein-coupled receptor by conformational selection. *Nature*, 533(7602):265–268, 2016. doi: 10.1038/nature17668. URL http://dx.doi.org/10.1038/nature17668.

L. Ye, C. Neale, A. Sljoka, B. Lyda, D. Pichugin, N. Tsuchimura, S. T. Larda, R. Pomès, A. E. García, O. P. Ernst, R. K. Sunahara, and R. S. Prosser. Mechanistic insights into allosteric regulation of the A2A adenosine G protein-coupled receptor by physiological cations. *Nature Communications*, 9(1):1372, Dec. 2018. ISSN 2041-1723. doi: 10.1038/s41467-018-03314-9. URL http://www.nature.com/articles/s41467-018-03314-9.

T. Yuwen and L. E. Kay. Longitudinal relaxation optimized amide 1H-CEST experiments for studying slow chemical exchange processes in fully protonated proteins. *Journal of Biomolecular NMR*, 67(4):295–307, Apr. 2017. ISSN 0925-2738, 1573-5001. doi: 10.1007/s10858-017-0104-y. URL http://link.springer.com/10.1007/s10858-017-0104-y.

T. Yuwen and L. E. Kay. Revisiting 1HN CPMG relaxation dispersion experiments: a simple modification can eliminate large artifacts. *Journal of Biomolecular NMR*, 73(10-11):641–650, 2019. ISSN 0123456789. doi: 10.1007/s10858-019-00276-y. URL https://doi.org/10.1007/s10858-019-00276-y.

T. Yuwen, P. Vallurupalli, and L. E. Kay. Enhancing the Sensitivity of CPMG Relaxation Dispersion to Conformational Exchange Processes by Multiple-Quantum Spectroscopy. *Angewandte Chemie*, 128(38):11662–11666, 2016. doi: 10.1002/ange.201605843.

T. Yuwen, R. Huang, and L. E. Kay. Probing slow timescale dynamics in proteins using methyl 1H CEST. *Journal of Biomolecular NMR*, 68(3):215–224, 2017. ISSN 0123456789. doi: 10.1007/s10858-017-0121-x.

T. Yuwen, R. Huang, P. Vallurupalli, and L. E. Kay. A Methyl-TROSY-Based 1H Relaxation Dispersion Experiment for Studies of Conformational Exchange in High Molecular Weight Proteins. *Angewandte Chemie - International Edition*, 58(19):6250–6254, 2019. doi: 10.1002/anie.201900241.

Z. Zhang, J. Vögele, K. Mráziková, H. Kruse, X. Cang, J. Wöhnert, M. Krepl, and J. Šponer. Phosphorothioate Substitutions in RNA Structure Studied by Molecular Dynamics Simulations, QM/MM Calculations, and NMR Experiments. *The Journal of Physical Chemistry B*, 125(3):825–840, Jan. 2021. ISSN 1520-6106, 1520-5207. doi: 10.1021/acs.jpcb.0c10192. URL https://pubs.acs.org/doi/10.1021/acs.jpcb.0c10192.

B. Zhao, A. L. Hansen, and Q. Zhang. Characterizing slow chemical exchange in nucleic acids by carbon CEST and low spin-lock field R 1ρ NMR spectroscopy. *Journal of the American Chemical Society*, 136(1):20–23, 2014. doi: 10.1021/ja409835y.

B. Zhao, S. L. Guffy, B. Williams, and Q. Zhang. An excited state underlies gene regulation of a transcriptional riboswitch. *Nature Chemical Biology*, 13(9):968–974, Sept. 2017. ISSN 1552-4450, 1552-4469. doi: 10.1038/nchembio.2427. URL http://www.nature.com/articles/nchembio.2427.

B. Zhao, J. T. Baisden, and Q. Zhang. Probing excited conformational states of nucleic acids by nitrogen CEST NMR spectroscopy. *Journal of Magnetic Resonance*, 310:106642, Jan. 2020. ISSN 10907807. doi: 10.1016/j.jmr.2019.106642. URL https://linkinghub.elsevier.com/retrieve/pii/S1090780719302812.

D. Zigáčková and Š. Vaňáčová. The role of 3′ end uridylation in RNA metabolism and cellular physiology. *Philosophical Transactions of the Royal Society B: Biological Sciences*, 373(1762):20180171, Dec. 2018. ISSN 0962-8436, 1471-2970. doi: 10.1098/rstb.2018.0171. URL `https://royalsocietypublishing.org/doi/10.1098/rstb.2018.0171`.

A. Appendix

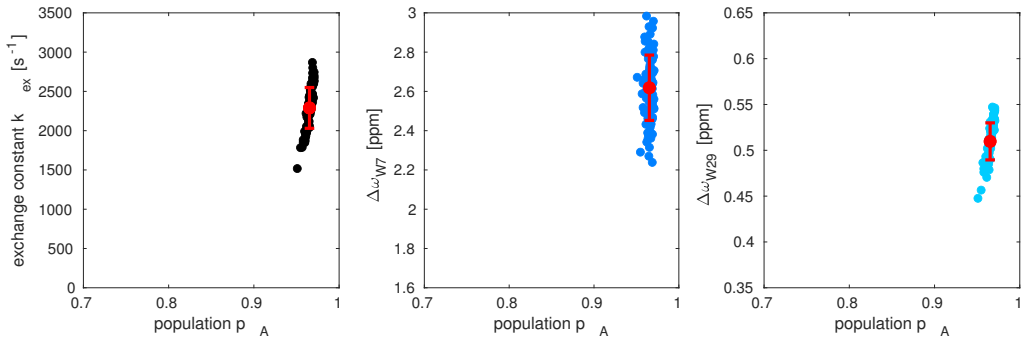

Figure A.1.: Monte Carlo simulation for on-resonance $R_{1\rho}$ experiments of 5FW-labeled TmCsp at 344 K and 500 MHz

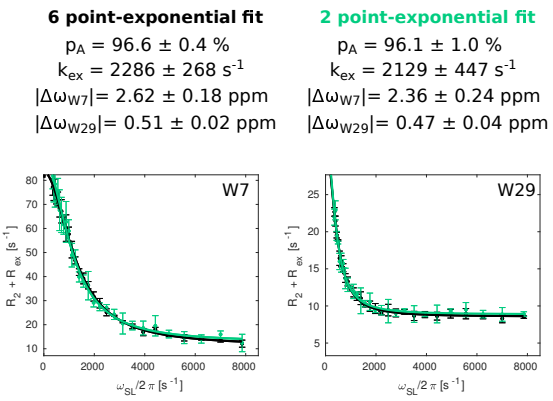

Figure A.2.: Comparison of on-resonance $R_{1\rho}$ profiles from 6-point and 2-point exponential fits

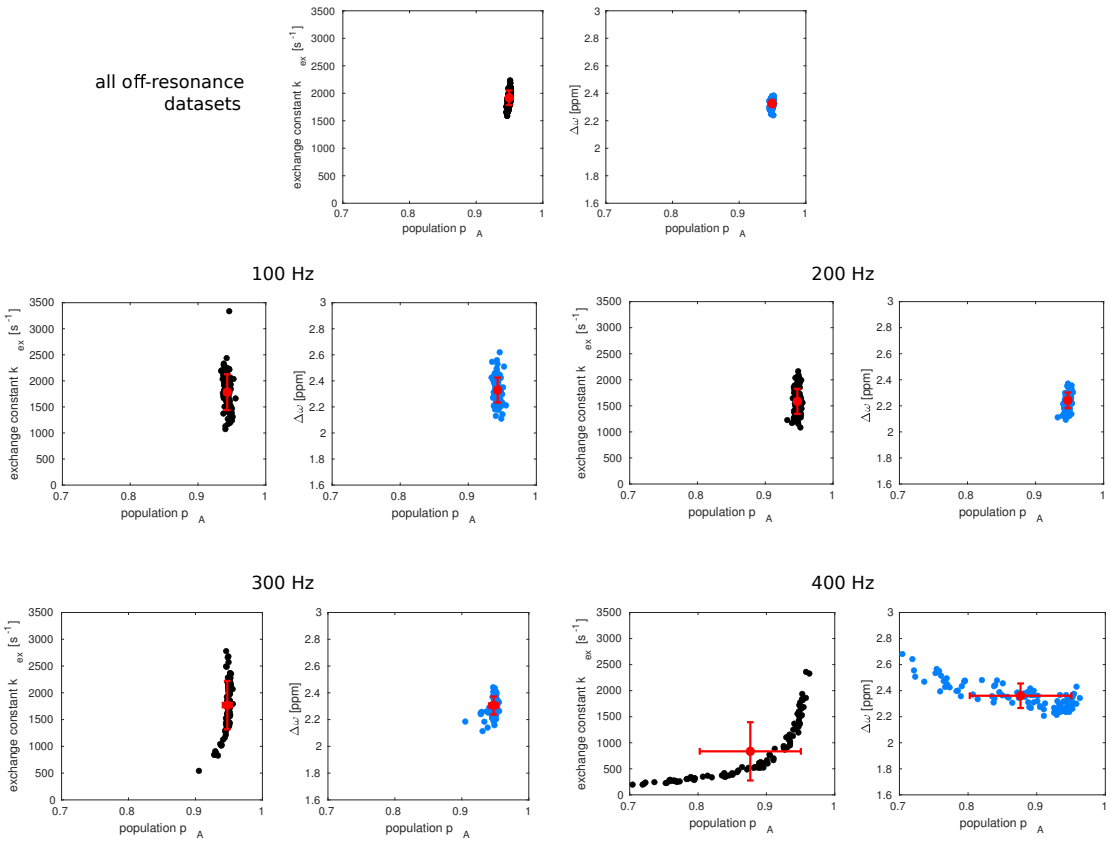

Figure A.3.: Monte Carlo simulation for off-resonance $R_{1\rho}$ experiments of 5FW-labeled TmCsp at 344 K and spin lock powers of 100-400 Hz at 500 MHz

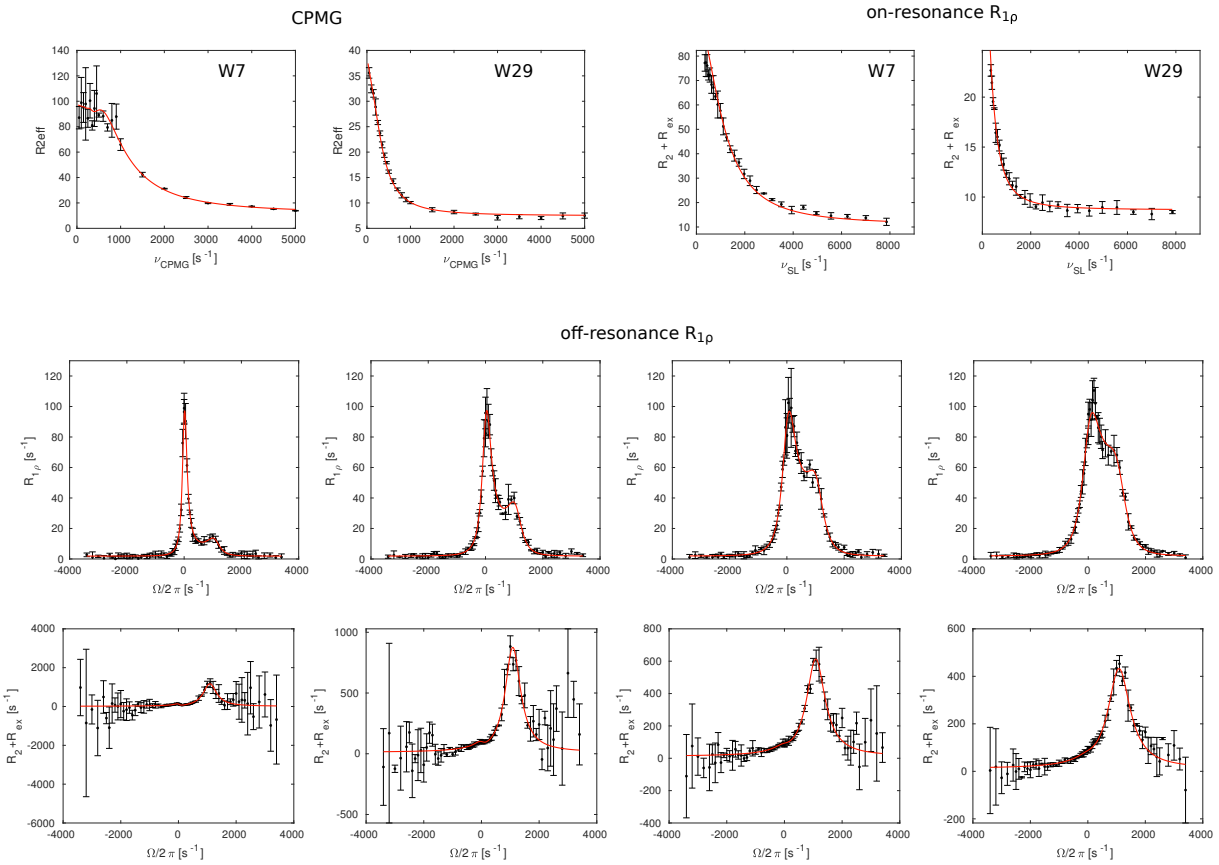

Figure A.4.: Global fit of ^{19}F data from 5FW-labeled TmCsp Shown are ^{19}F CPMG, on-resonance $R_{1\rho}$ and off-resonance $R_{1\rho}$ experimental data (black) with the global fit (red line)

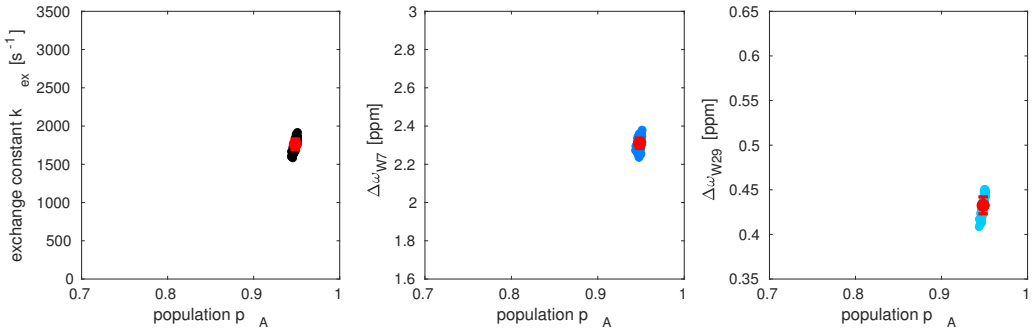

Figure A.5.: Monte Carlo simulation for a global fit of ^{19}F data from 5FW-labeled TmCsp Shown are correlation plots of the exchange constant k_{ex} with population p_A as well as the chemical shift differences $\Delta\omega_{W7}$ and $\Delta\omega_{W29}$ with p_A

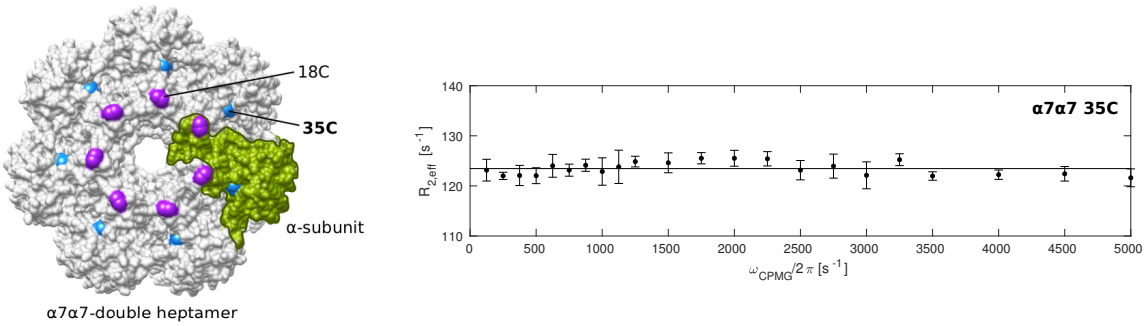

Figure A.6.: CPMG experiment of the BTFA-labeled $\alpha_7\alpha_7$ 35C mutant

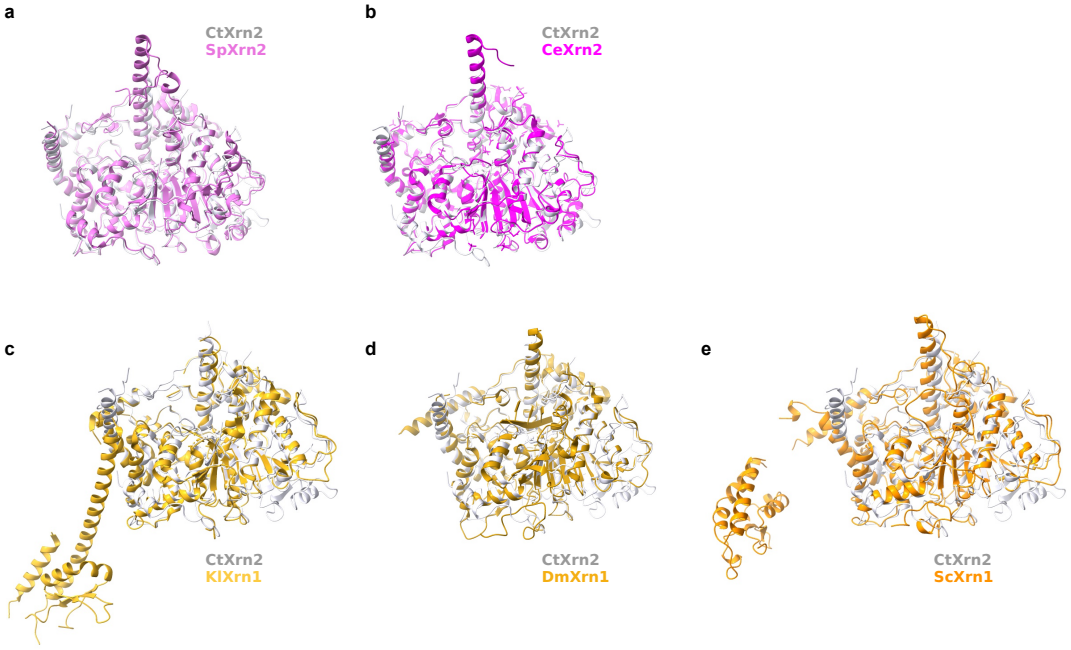

Figure A.7.: Structural comparison of CtXrn2 with homologeous proteins Overlay of the CtXrn2 structure solved in this study with (A) SpXrn2 (PDB: 3FQD), (B) CeXrn2 (PDB: 5FIR), (C) KlXrn1 (PDB: 3PIE), (D) DmXrn1 (PDB: 2Y35) and (E) ScXrn1 (PDB: 6Q8Y). The r.m.s.d. values for a pruned set of residues as obtained by the ChimeraX matchmaker command is included for all matches. For clarity, the C-terminal PAZ, KOW, SH3 and WH domains are omitted in the Xrn1 structures.

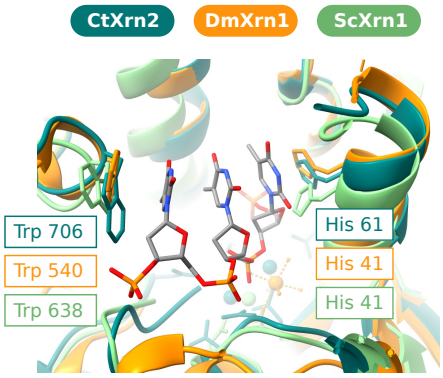

Figure A.8.: Comparison of the His-Trp stacking sandwich In the CtXrn2 structure solved in this study (dark green), the His-Trp pair (His61-Trp706) is similarly positioned as in the DmXrn1 structure (orange, PDB 2Y35, shown with the DNA pseudosubstrate) and the ScXrn1 structure (light green, PDB 6Q8Y, shown without the RNA substrate for clarity).

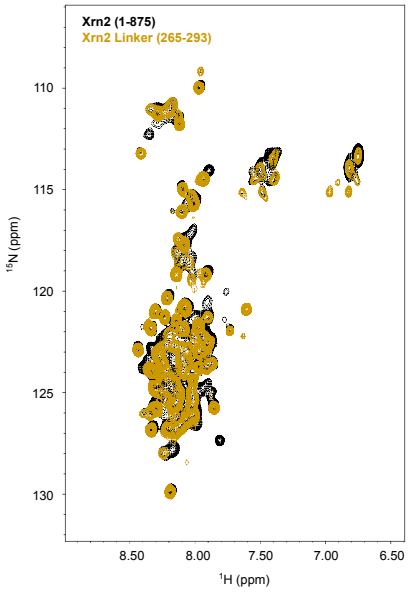

Figure A.9.: ^{1}H-^{15}N TROSY spectra of Xrn2 (1-875) and Xrn2 Linker (265-293) Due to the high molecular weight of Xrn2, only ^{1}H-^{15}N correlations from flexible parts of the protein are visible in the ^{1}H-^{15}N TROSY spectra, whereas the ^{1}H-^{15}N resonances in the protein core are broadened beyond detection. The ^{1}H-^{15}N spectrum from the Xrn2 linker region (residues 265-293) largely overlaps with the spectrum from Xrn2 (1-875), proving that the linker region in Xrn2 is flexible in the full length context.

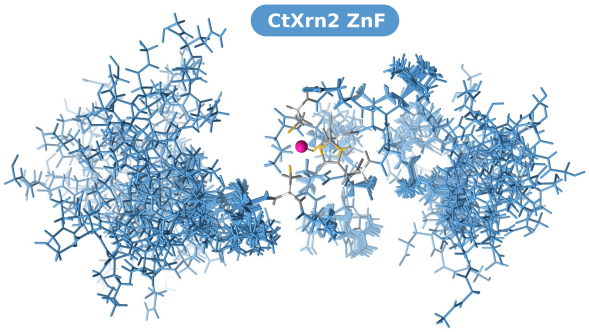

Figure A.10.: NMR structural bundle of the Xrn2 zinc finger (ZnF) Shown are the 20 lowest energy structures from the structure calculation. The Zn^{2+} ion is shown in pink, the coordinating CCHC residues are shown in grey/yellow. The core of the ZnF is well defined, the regions N- and C- terminal to the ZnF are highly flexible, which ensures that the ZnF can be embedded into the Xrn2 core.

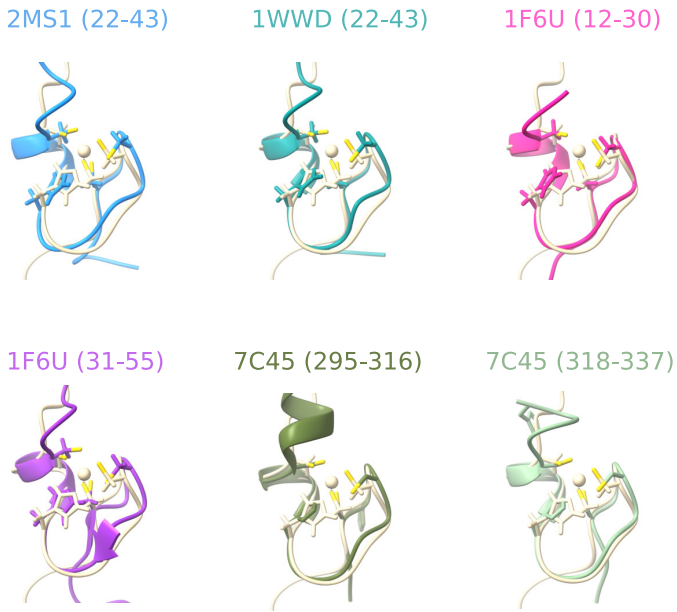

Figure A.11.: Comparison of the Xrn2 zinc finger with known CCHC zinc finger structures The zinc finger of Xrn2 adopts the same fold as other known CCHC zinc fingers, exemplified here by zinc fingers from the nucleocapsid protein of MLV (PDB 2MS1, 1WWD), from the nucleocapsid protein of HIV-1 (PDB 1F6U) and from RNase D (PDB 7C45).

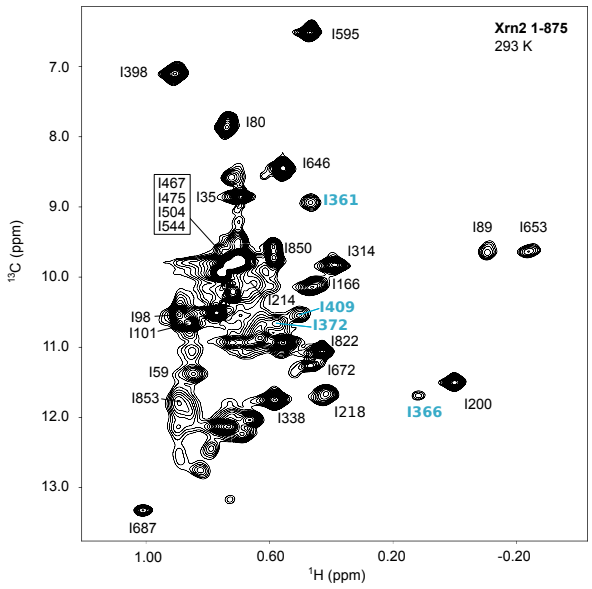

Figure A.12.: ^{1}H-^{13}C methyl TROSY spectrum of Xrn2 at 293 K Highlighted in blue are residues, that could only be assigned at 293 K, but not at 313 K, due to strong exchange broadening at the elevated temperature.

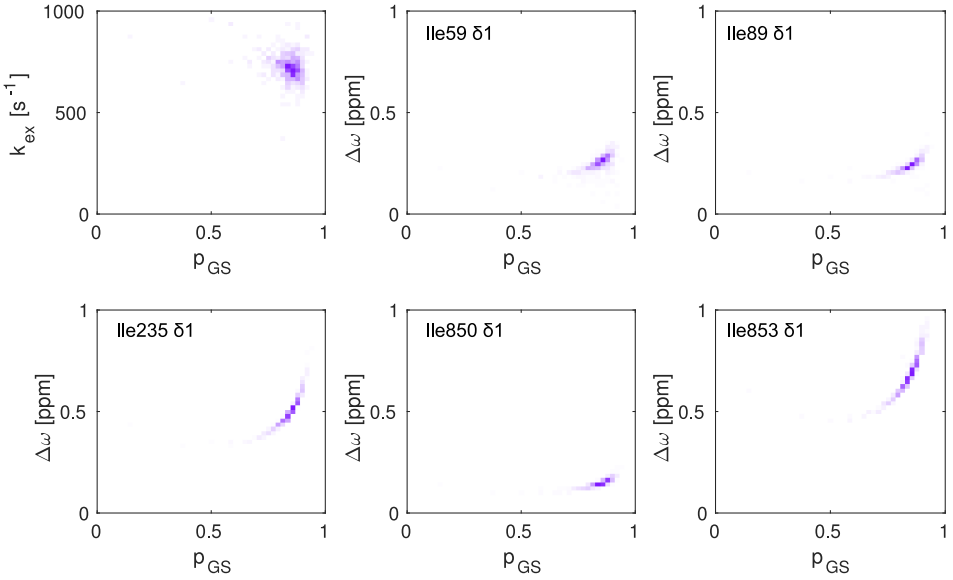

Figure A.13.: Distribution of fit parameters obtained from Monte Carlo trials Subplots show the distribution of the exchange constant k_{ex} as well as the carbon chemical shift differences $|\Delta\omega_C|$ for the isoleucine residues, against the ground state population p_{GS}. The distributions are based on a global fit of two RD experiments (SQ and MQ) for the 5 indicated residues at 3 magnetic field strengths (500, 600 and 800 MHz proton frequency).

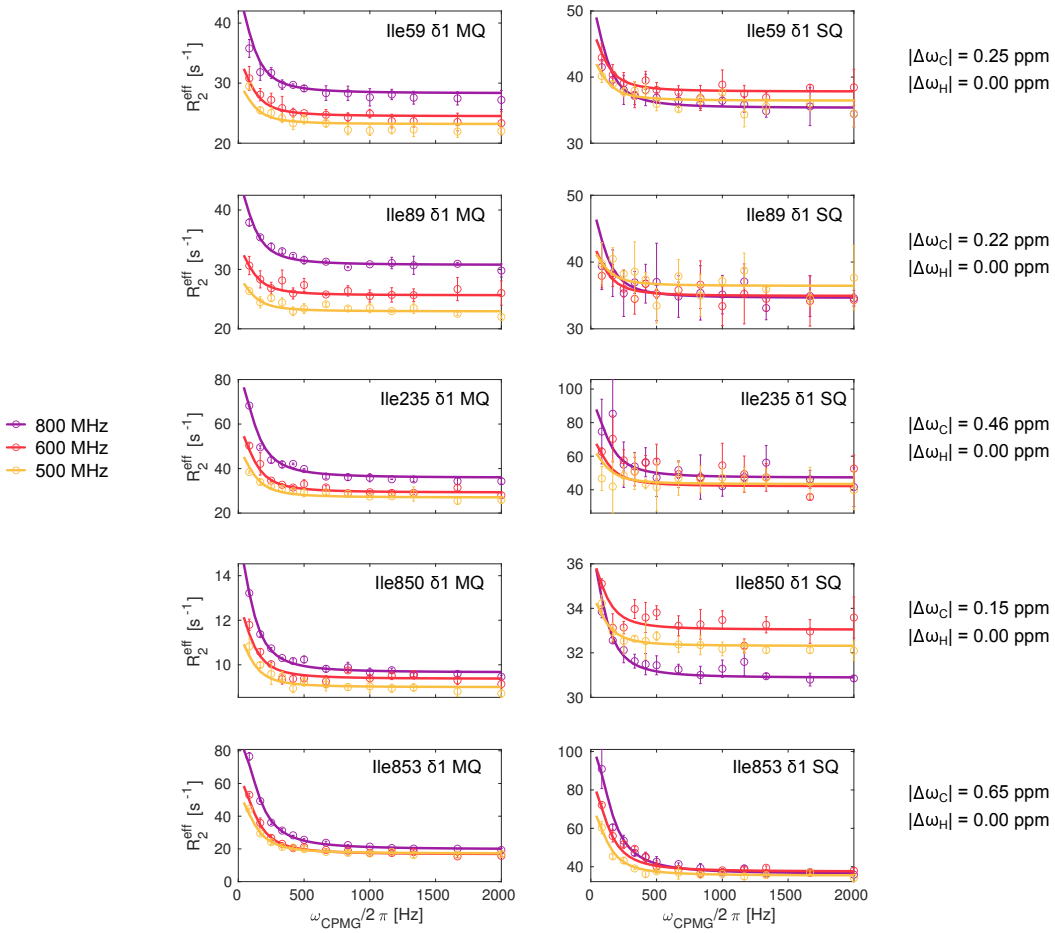

Figure A.14.: [^{13}C SQ and ^{1}H-^{13}C MQ CPMG data of Xrn2 at 313 K The largest chemical shift differences between ground state and excited state were obtained for Ile853 ($\Delta\omega_C = 0.65$ ppm) and Ile235 ($\Delta\omega_C = 0.46$ ppm). For those residues the relative values of $\Delta\omega$ and k_{ex}, that define the NMR timescale, are comparable in size and places the motion in the intermediate exchange regime. It is generally possible to extract information on the populations and the chemical shift differences, when the dynamics are not in the fast exchange limit. However, when we applied a Monte Carlo procedure in order to extract errors for the fitting parameters, we still found a considerable spread in the solution space, with a characteristic interdependence of p_{GS} and the particular chemical shift differences (figure A.13) given by a residue-dependent constant $\Phi_{ex} = p_{GS}p_{ES}\Delta\omega^2$. Of note, even when the lower limit of $|\Delta\omega| = 2 \cdot \Phi_{ex}^{1/2}$ is considered, the exchange still remains in the intermediate regime for Ile853.

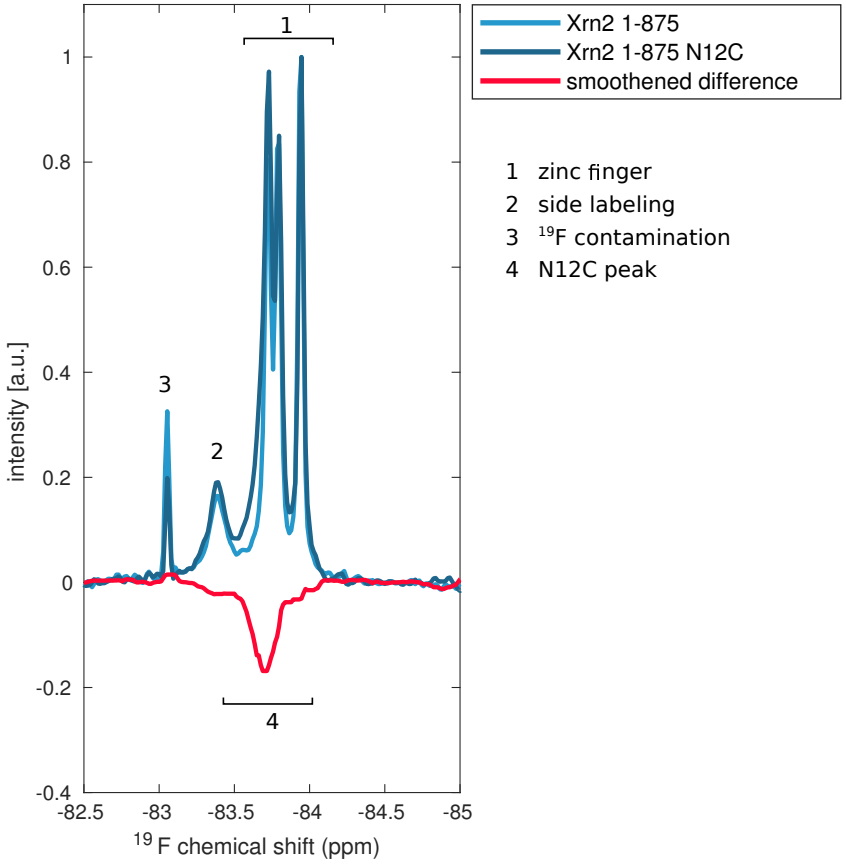

Figure A.15.: Initial ^{19}F spectra of BTFA-labeled Xrn2 1-875 and Xrn2 1-875 N12C We labeled both wild type Xrn2 as well as the Xrn2 N12C mutant for 30′ at 30 °C. Both spectra show three strong peaks (labeled ′1′) between between -83.7 and -84.0 ppm, which we attributed to the three zinc finger cysteine residues in the supposedly flexible loop 265-295, as well as a broad peak at -83.4 ppm (labeled ′2′) and a sharp peak at -83.0 ppm (labeled ′3′). A difference spectrum (Spectrum Xrn2 1-875 minus spectrum Xrn2 1-875 N12C) revealed a clear additional peak well above the noise level around -83.7 ppm, which we attributed to the ^{19}F labeled additional cysteine at position 12 (labeled ′4′). CPMG spectra of both samples showed the distinct presence of relaxation dispersion in the N12C sample. To be able to accurately quantify those dispersion we removed the ZnF from the protein (to eliminate the resonances labeled ′1′), we reduced labeling times to 30′ incubation at 4 °C (to eliminate the resonance labeled ′2′) and we purified the labeled enzyme via size exclusion chromatography (to eliminate the resonance labeled ′4′). The resulting ^{19}F spectrum shows a single resonance at -83.78 ppm (Figure 5.6).

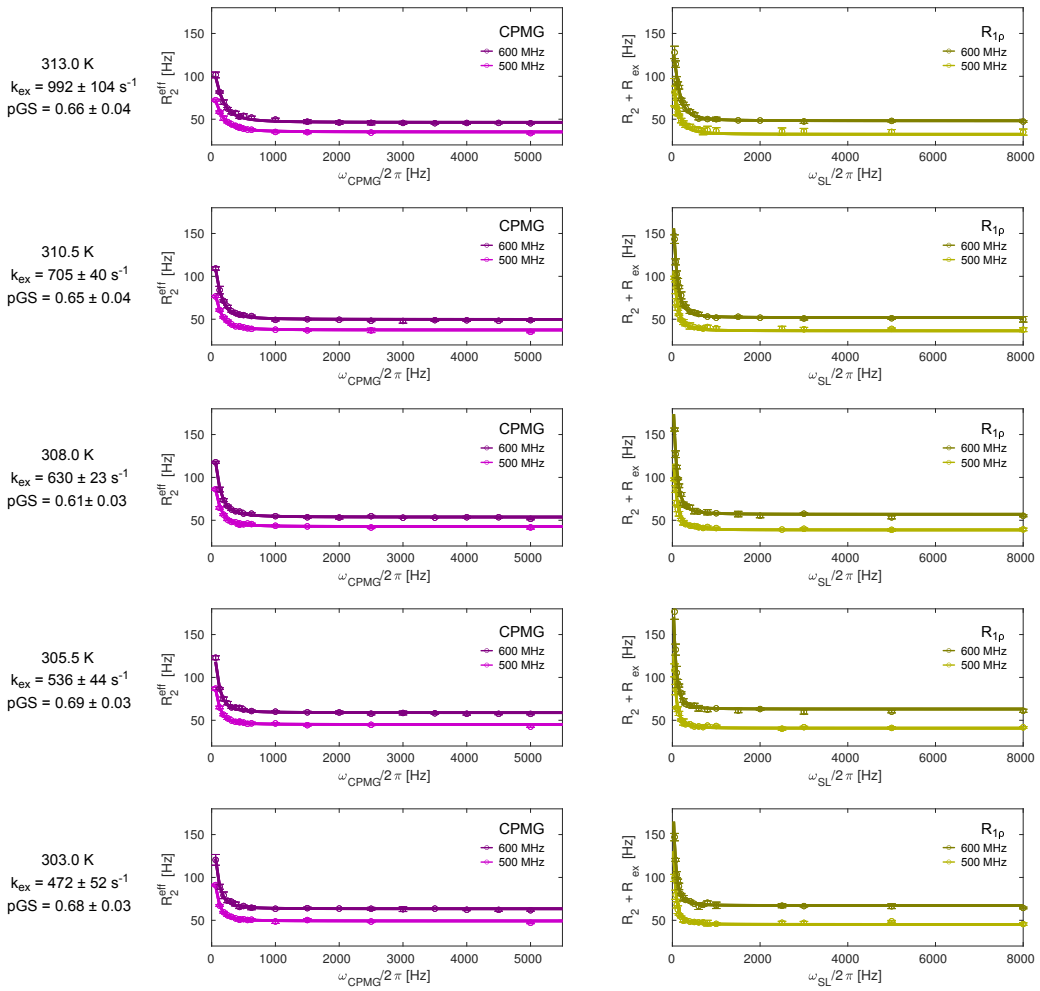

Figure A.16.: Temperature dependent ^{19}F relaxation dispersion. ^{19}F CPMG (left) and $R_{1\rho}$ relaxation (right) dispersion of CtXrn2 1-875 ΔZnF N12C^{BTFA} at temperatures between 303 K and 313 K and 1H Larmor frequencies of 500 MHz and 600 MHz. Fit parameters of the global fit and separate fits of CPMG and $R_{1\rho}$ datasets are included in table A.3.

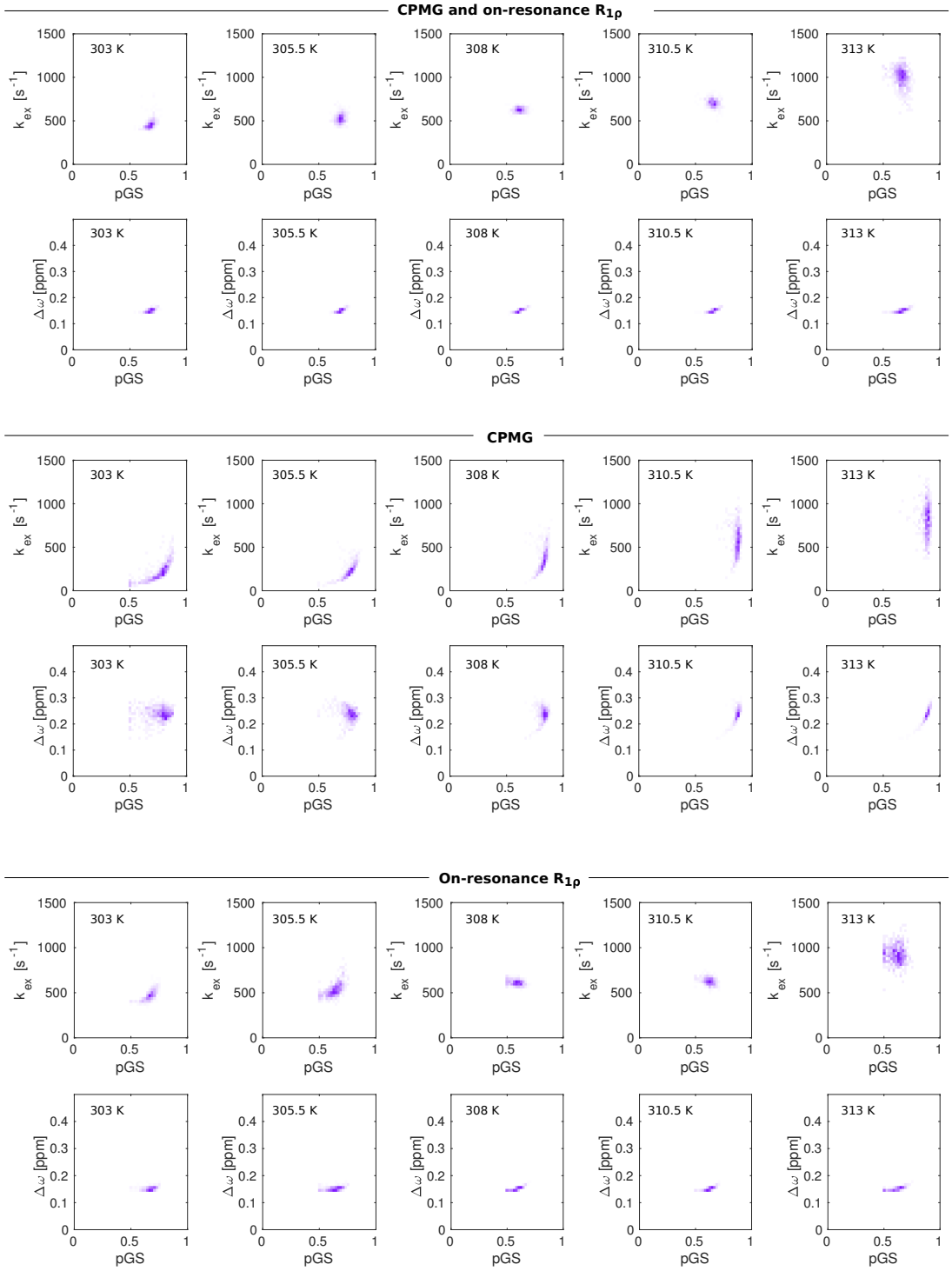

Figure A.17.: Monte Carlo trials of ^{19}F CPMG and $R_{1\rho}$ relaxation dispersion data Distribution of fit parameters obtained from MC simulations, where ^{19}F CPMG and $R_{1\rho}$ relaxation data was fitted simultaneously (top), or where either only the ^{19}F CPMG (middle) or $R_{1\rho}$ relaxation data (bottom) was fitted. Note the large increase in the uncertainty when only one data set is used in for fitting.

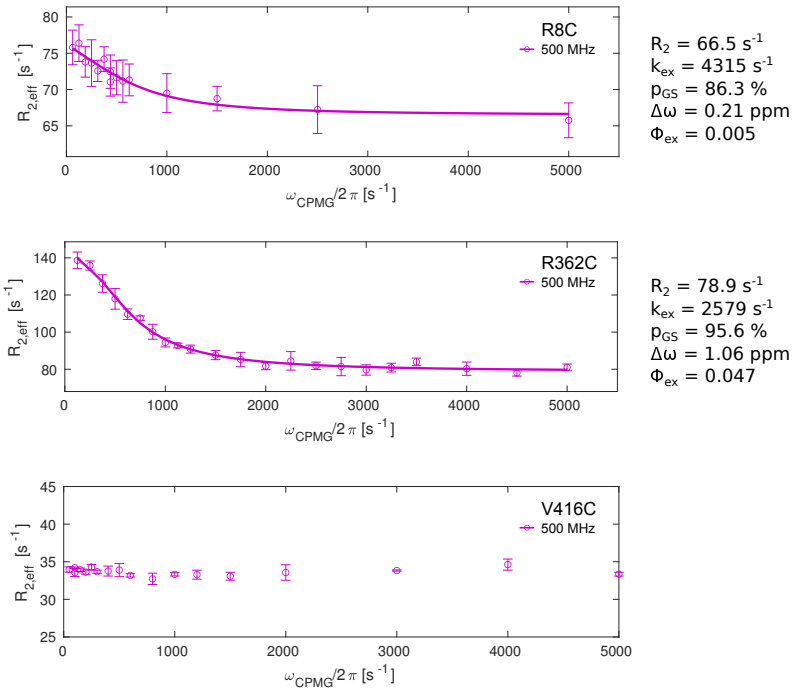

Figure A.18.: ^{19}F CPMG profiles of additional BTFA-labeled Xrn2 cysteine mutants Relaxation dispersions were observed for ^{19}F probes attached to artificially introduced cysteine residues in (R8C) or next to (R362C) the α1-helix, but not at a more remote labeling site (V416C). Note that the fitting parameters are not very accurate as only CPMG data at one temperature and one field strength has been used.

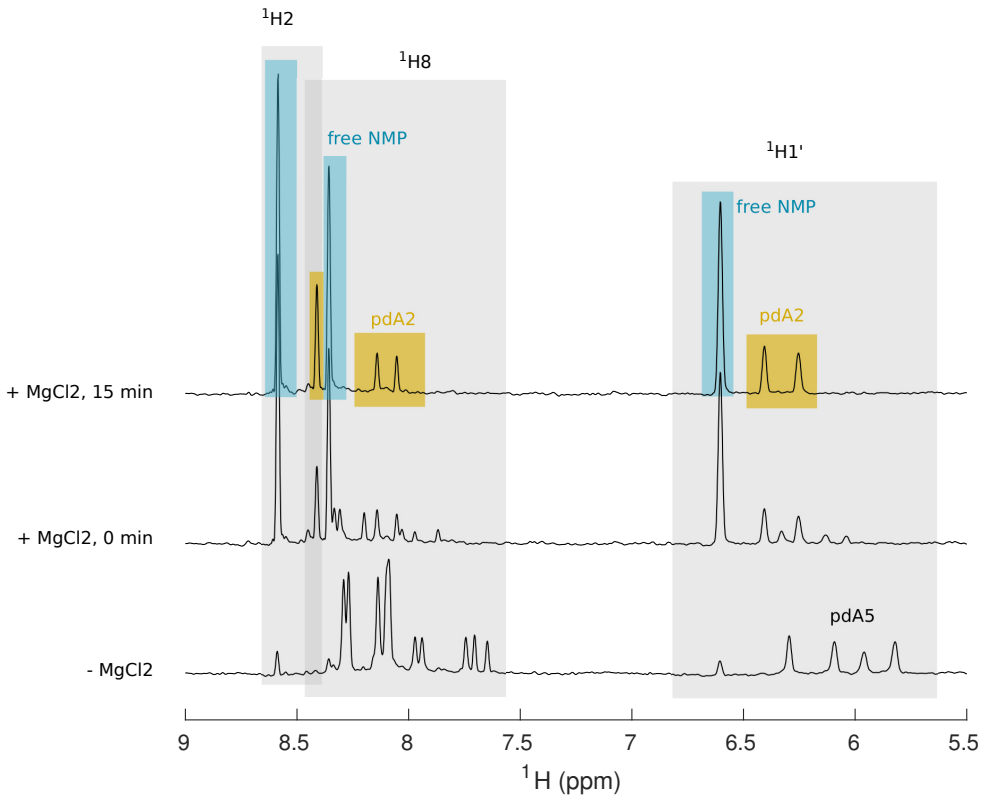

Figure A.19.: ^{1}H spectra of pdA5 degradation by Xrn2 200 µM pdA5 were added to 50 µM Xrn2 in the absence of catalytically important magnesium ions (bottom spectra). The H1′ sugar proton resonances in pdA5 are clearly visible around 6 ppm. pdA5 is not degraded by Xrn2 under these conditions. Upon addition of magnesium the turnover of pdA5 into pdA2 and free nucleotides is initiated (middle spectrum). Within 15 minutes, the pdA5 is completely degraded (top spectrum).

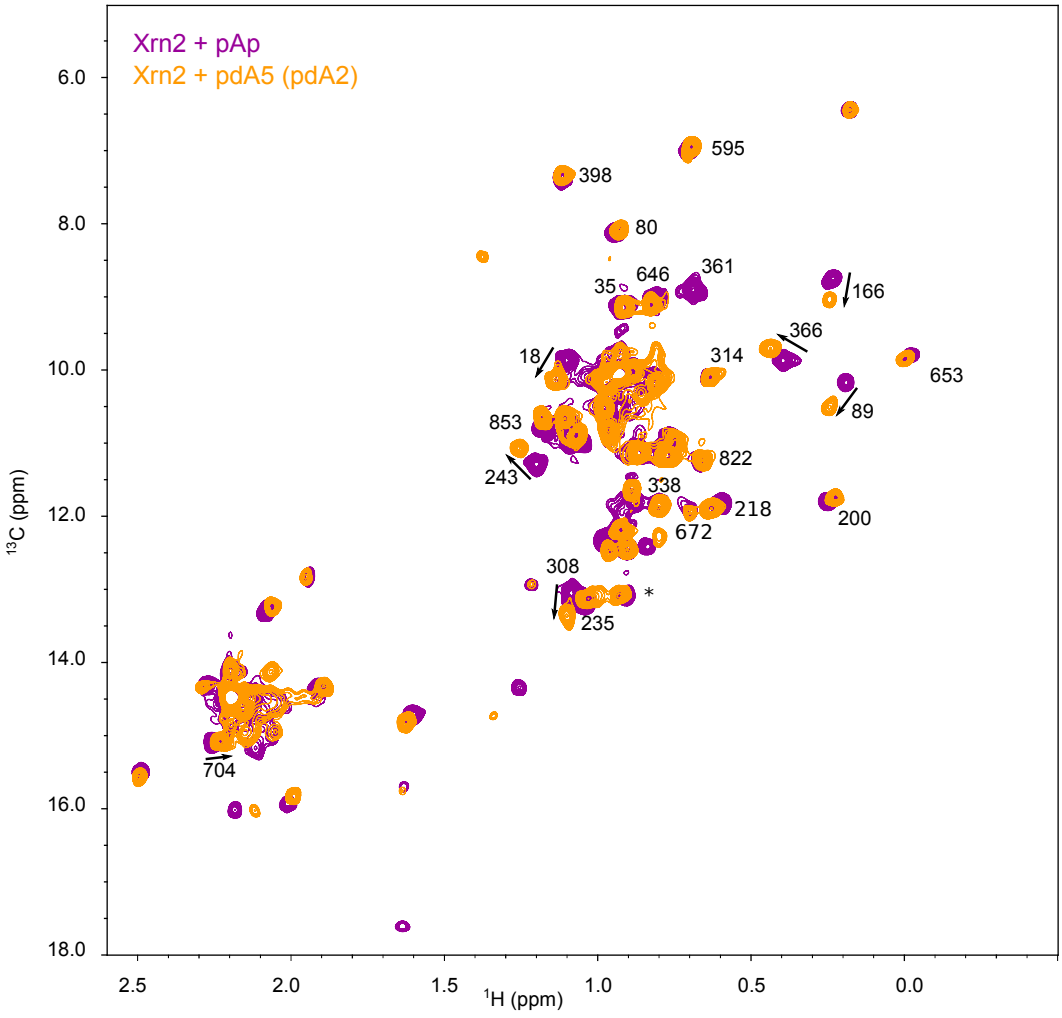

Figure A.20.: pAp and pdA2 induce the same global conformational change in Xrn2. Overlay of the ^{1}H-^{13}C HMQC methyl-TROSY spectra in the presence of pAp (purple) and pdA2 (orange, produced by partial degradation of pdA5), recorded at 18.8 T and 313 K. Resonances of residues that display a different chemical shift in the pAp and pdA2 states are labeled.

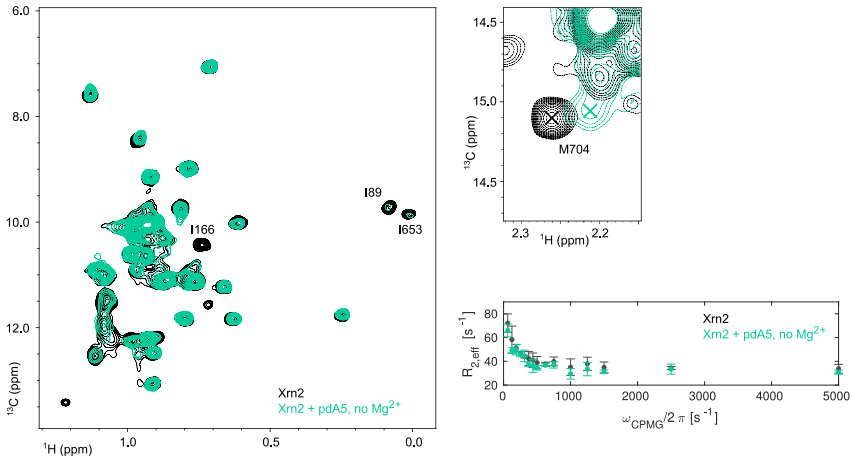

Figure A.21.: In the absence of Mg^{2+} ions pdA5 interacts with the RNA binding groove, but does not induce the active conformation in Xrn2 Overlay of the ^{1}H-^{13}C HMQC methyl-TROSY spectra of the apo state (black) and after addition of pdA5 (green), recorded at 18.8 T and 313 K. CSPs of M704 (right panel) clearly report on the interaction of pdA5 with the RNA binding groove. The absence of significant CSPs around the active site (as observed in the presence of Mg^{2+}; figure 5.7G) indicates that the stable active conformation is not formed. Binding of the pseudosubstrate in the absence of Mg^{2+} does not change the dynamics of the α1-helix (as observed in the presence of Mg^{2+}; figure 5.7H), as shown by the overlay of CPMG data.

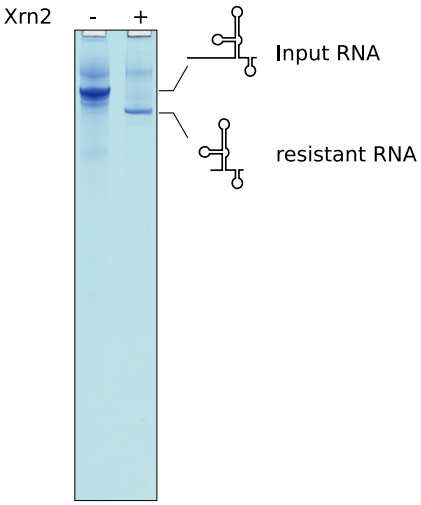

Figure A.22.: Xrn2 degrades the unstructured 5′-region of the xrRNA until it encounters the degradation-resistant pseudoknot structure The substrate RNA (table A.1) carries an unfolded sequence at the 5′-end, followed by the pseudoknot structure. The linear 5′-end is rapidly degraded, but further degradation is sterically blocked by the pseudoknot, giving rise to an Xrn2 resistant RNA fragment that can be detected by urea polyacrylamide gel electrophoresis after the NMR measurement.

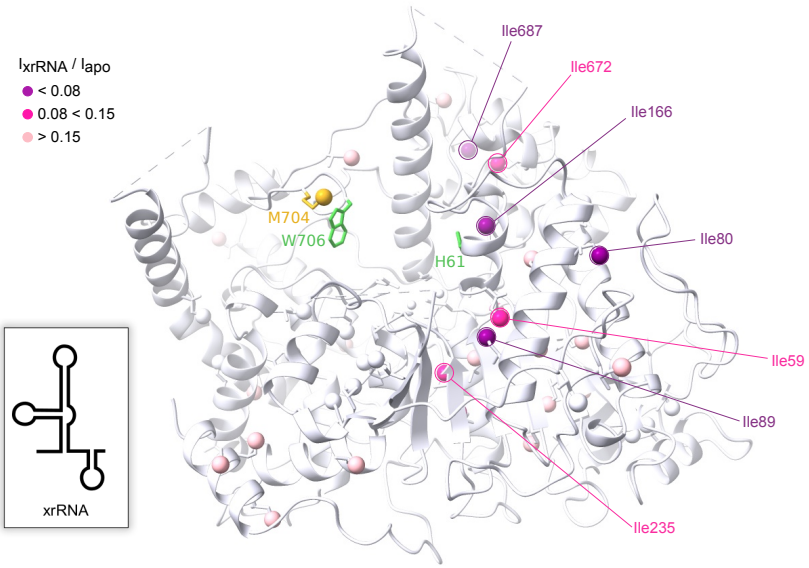

Figure A.23.: Intensity changes in Xrn2 Ileδ1-methyl groups upon addition of xrRNA The addition of xrRNA to Xrn2 results in a significant overall decrease of the signal intensities, presumably due to an increase in the rotational correlation time and due to the introduction of a large number of protons from the xrRNA. The decrease is particularly strong between the α3-helix and the active site.

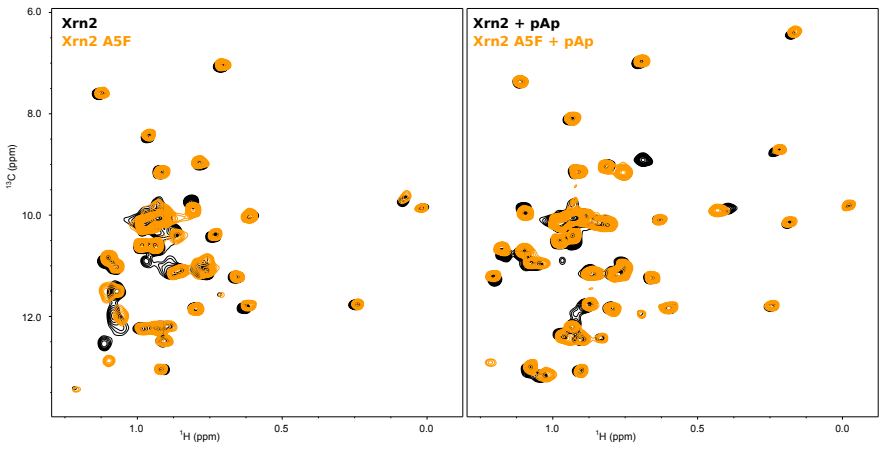

Figure A.24.: The A5F mutation does not interfere with the Xrn2 structure or with the binding of the substrate to Xrn2 Left: HMQC spectra of Xrn2 WT (black) and Xrn2 A5F (orange). The introduction of the A5F mutation causes CSPs close to the site of mutation. The overall structure of Xrn2 is not effected by the mutation. Right: HMQC spectra of the Xrn2 WT:pAp complex (black) and Xrn2 A5F:pAp complex (orange). As above, minor chemical shift perturbations are visible around the N-terminal α1-helix, that are due to the point mutation. The overall structural of the active state is, however, maintained in the presence of the A5F mutation.

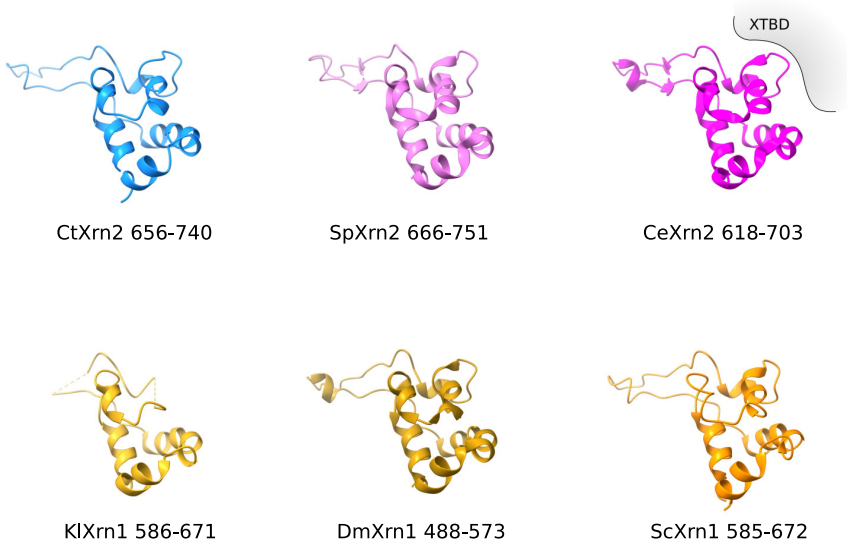

Figure A.25.: The PBS (PAXT-1 – binding segment) of CtXrn2 (blue) is folded For clarity, only the Xrn2 PBS is visualized. For comparison, the PBS from S. pombe Xrn2 (orchid, PDB 3FQD), C. elegans Xrn2 (magenta, with the XTBD binding site indicated, PDB 5FIR), K. lactis Xrn1 (yellow, PDB 3PIE), D. melanogaster Xrn1 (gold, PDB 2Y35) and S. cerevisiae Xrn1 (orange, PDB 6Q8Y) are shown.

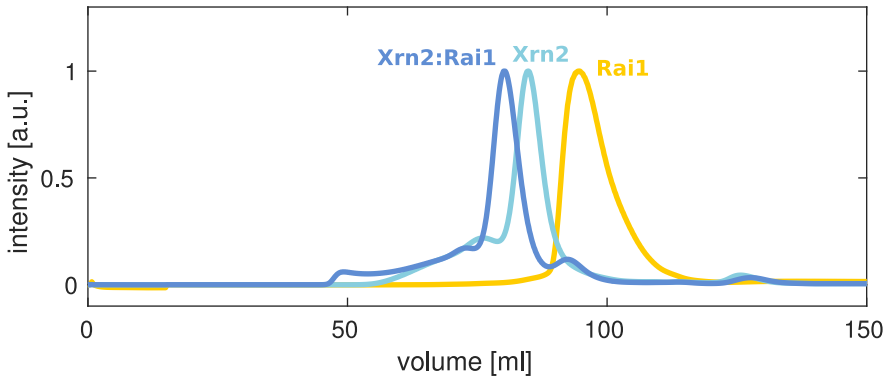

Figure A.26.: Xrn2 and Rai1 from Chaetomium thermophilum form a stable complex Shown are three exemplary size exclusion chromatography (SEC) runs of Rai1 (yellow), Xrn2 (light blue) and the Xrn2:Rai1 complex (blue). Xrn2 and Rai1 form a complex that elutes earlier than Xrn2 or Rai1 alone.

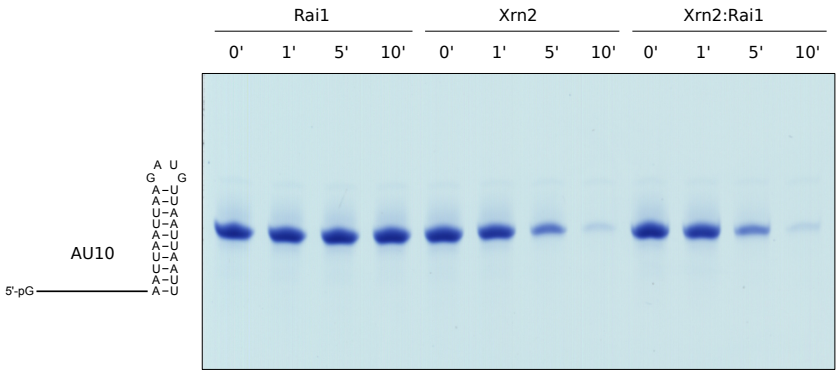

Figure A.27.: CtRai1 does not degrade monophosphorylated RNA and does not enhance the exoribonucleolytic activity of CtXrn2 A monophosphorylated AU10 RNA (12 µM) is not degraded by Rai1 (10 nM) (lanes 1 to 4). This RNA is, however degraded readily by Xrn2 (lanes 5-8). The rate of RNA degradation is not effected by the addition of Rai1 (lanes 9 to 12). This implies that Rai1 does not influence CtXrn2 activity in C. thermophilum, as was observed for the S. pombe proteins.

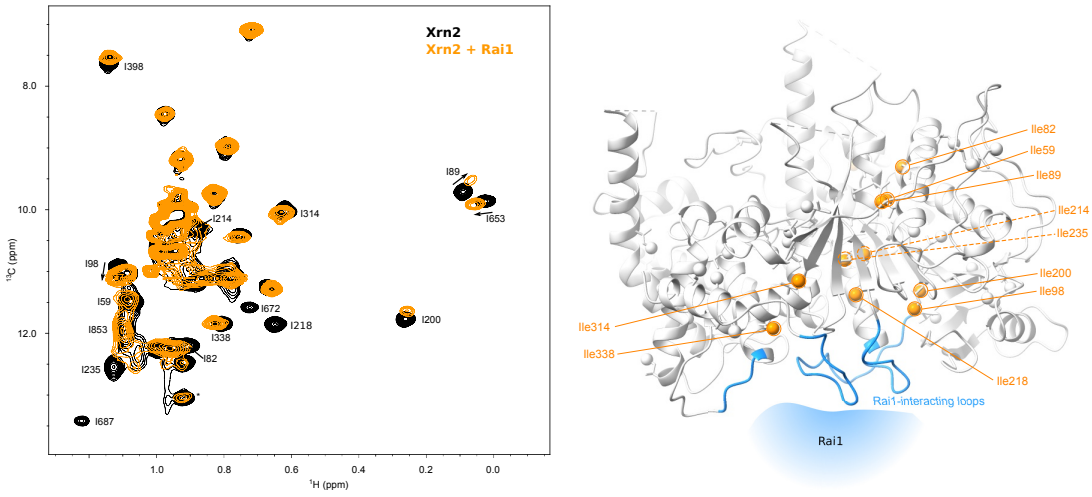

Figure A.28.: Changes in the Xrn2 enzyme spread from the Rai1 interface along the central β-sheet. Left: the HMQC spectrum of Ileδ1-[$^{13}CH_3$] and Metϵ-[$^{13}CH_3$] methyl labeled Xrn2 in the absence (black) and presence (orange) of unlabeled, protonated Rai1. Right: Structure of Xrn2 with Ileδ1 methyl groups, which show pronounced changes in the HMQC spectrum, highlighted in orange, and the putative Rai1 interaction surface, inferred from the Structure of the Xrn2:Rai1 complex in S. pombe (PDB 3FQD), highlighted in blue. CSPs upon Rai1 interaction reach from the Rai1 binding site towards a region that is remote from the active site.

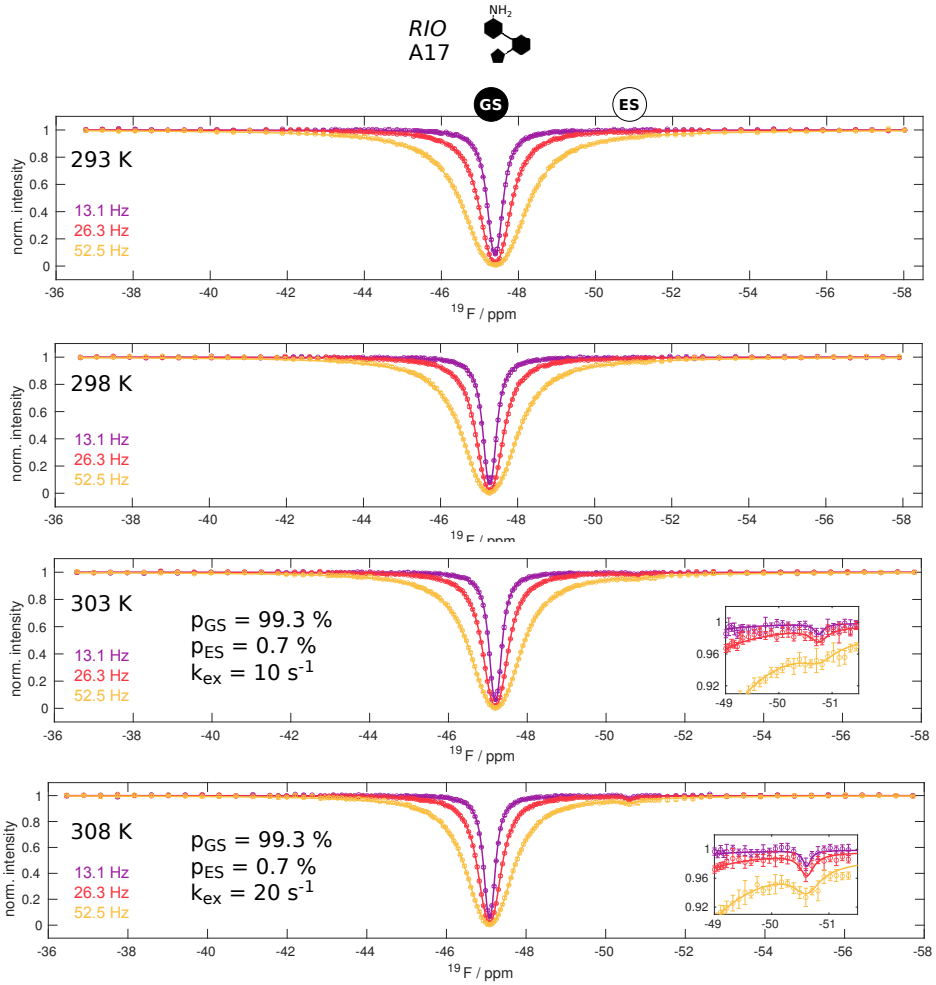

Figure A.29.: CEST data for the RIO-bound riboswitch at 293 K to 308 K CEST profiles at 293 K, 298 K, 303 K and 308 K from A17 at B1 fields of 13.1 Hz, 26.3 Hz and 52.5 Hz with data (circles with errorbars) and the fit from the no-exchange (293 K, 298 K) and 2-state exchange (303 K, 308 K) model (solid line). The resonance positions of GS and ES are indicated above the CEST spectra. The insets show a zoom of the CEST profiles in the region of the ES.

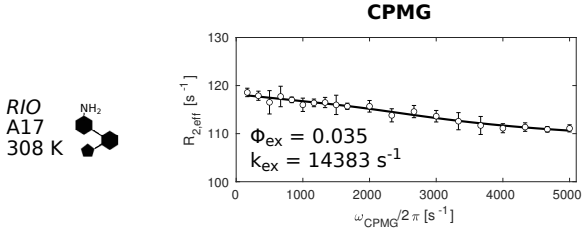

Figure A.30.: CPMG data for the RIO-bound riboswitch at 308 K

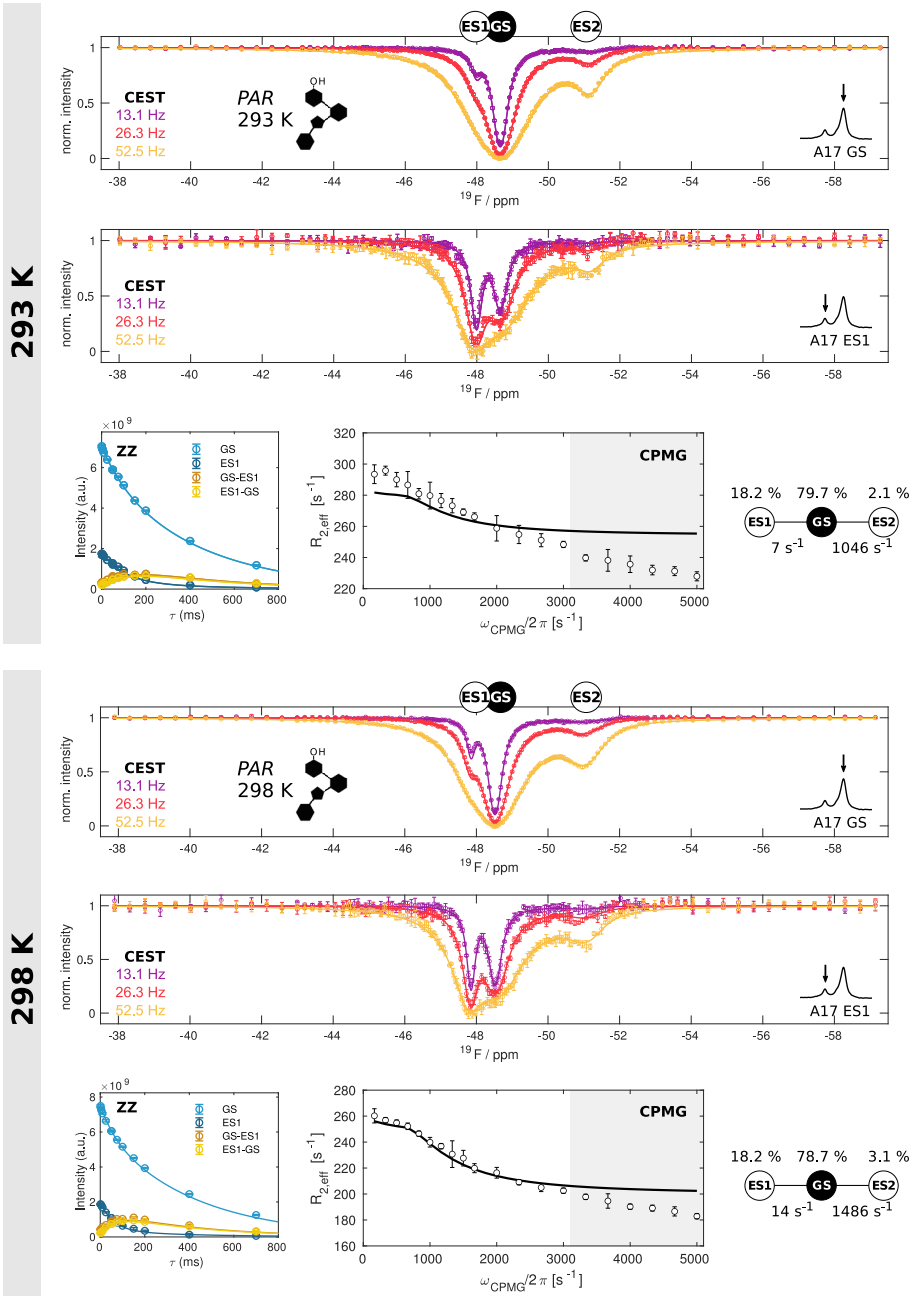

Figure A.31.: CEST, ZZ-exchange and CPMG data for the PAR-bound riboswitch at 293 K and 298 K Top: CEST profiles, ZZ-exchange data and CPMG curve of the A17F2 resonance at 293 K, together with the parameters obtained by a least-square fitting routine. Bottom: CEST profiles, ZZ-exchange data and CPMG curve of the A17F2 resonance at 298 K, together with the parameters obtained by a least-square fitting routine.

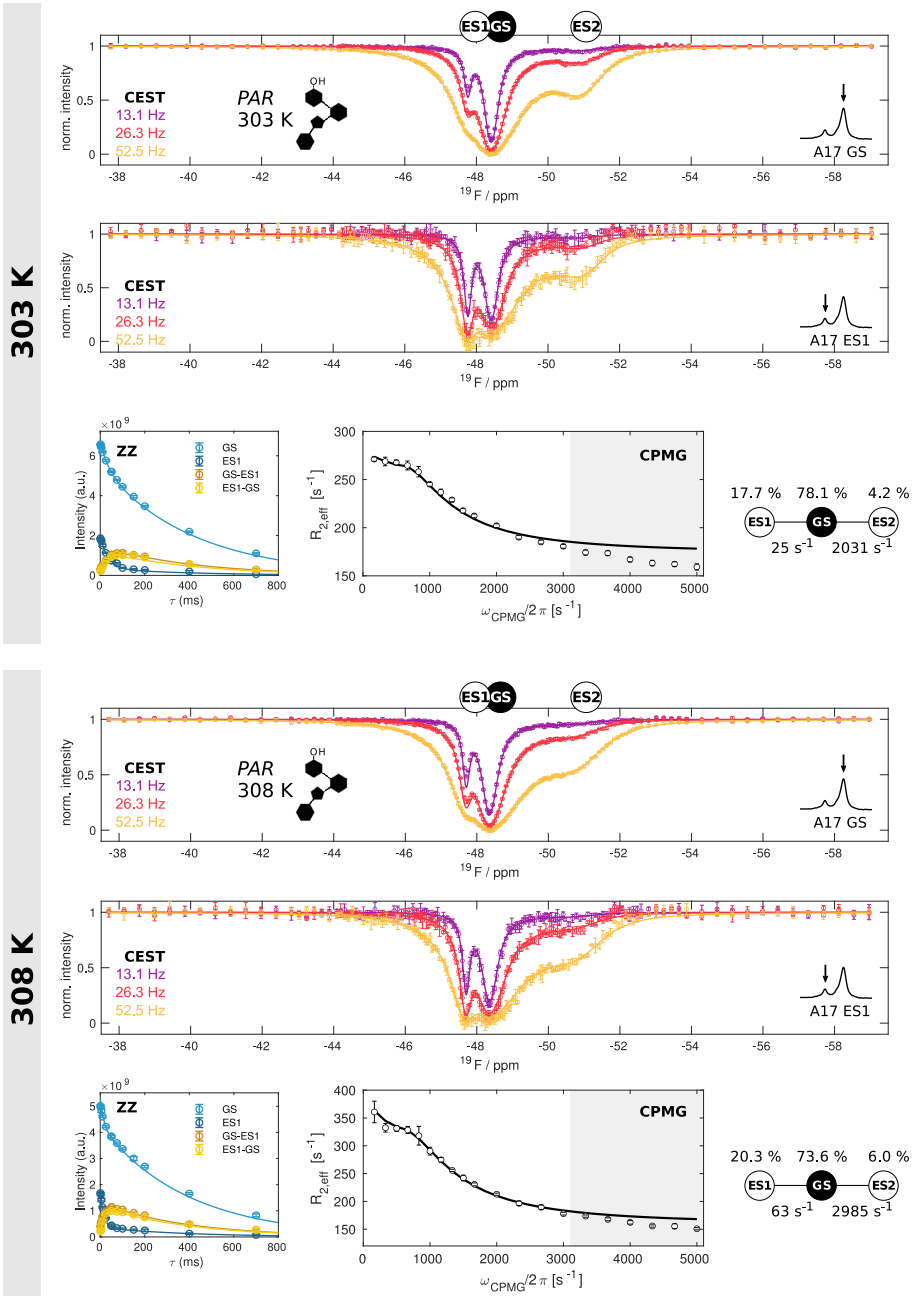

Figure A.32.: CEST, ZZ-exchange and CPMG data for the PAR-bound riboswitch at 303 K and 308 K Top: CEST profiles, ZZ-exchange data and CPMG curve of the A17F2 resonance at 303 K, together with the parameters obtained by a least-square fitting routine. Bottom: CEST profiles, ZZ-exchange data and CPMG curve of the A17F2 resonance at 308 K, together with the parameters obtained by a least-square fitting routine.

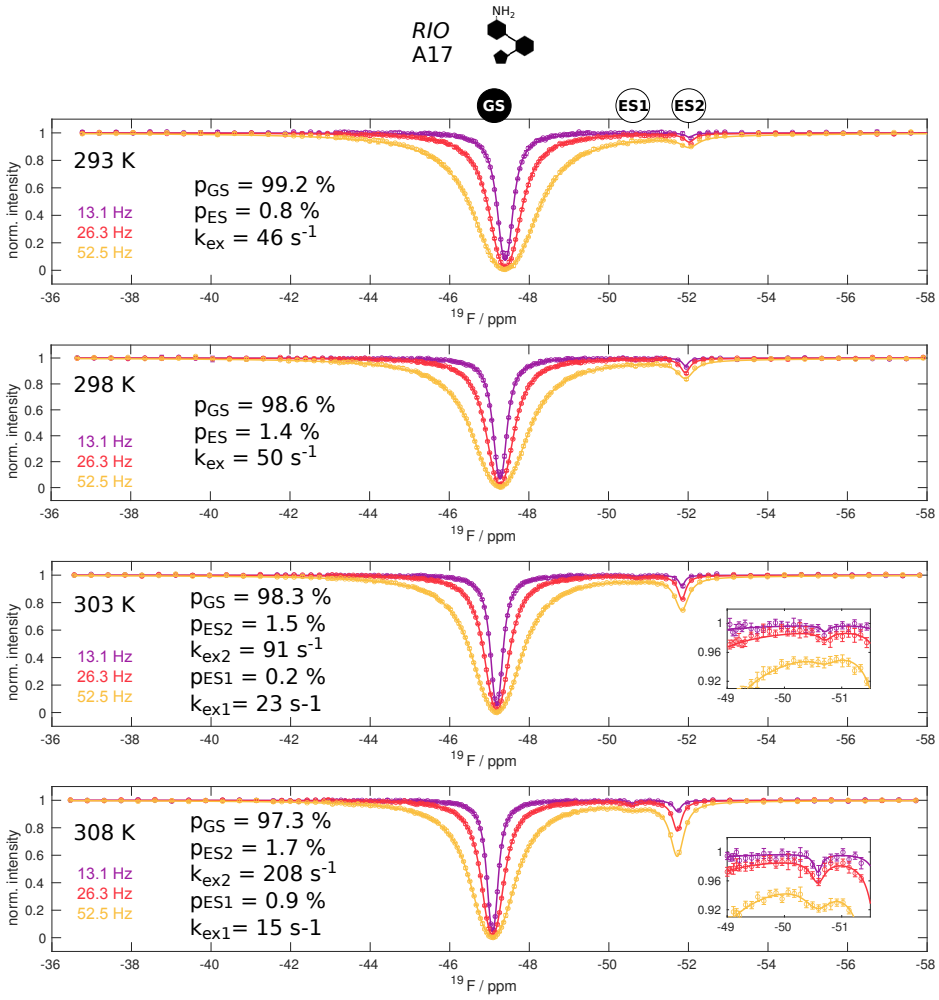

Figure A.33.: CEST data for the unsaturated RIO-bound riboswitch CEST profiles at 293 K, 298 K, 303 K and 308 K from A17 at B1 fields of 13.1 Hz, 26.3 Hz and 52.5 Hz with data (circles with errorbars) and the fit from the 2-state (293 K, 298 K) and 3-state (303 K, 308 K) exchange model (solid line). The resonance positions of GS, ES1 and ES2 are indicated above the CEST spectra. The insets show a zoom of the CEST profiles in the region of the ES.

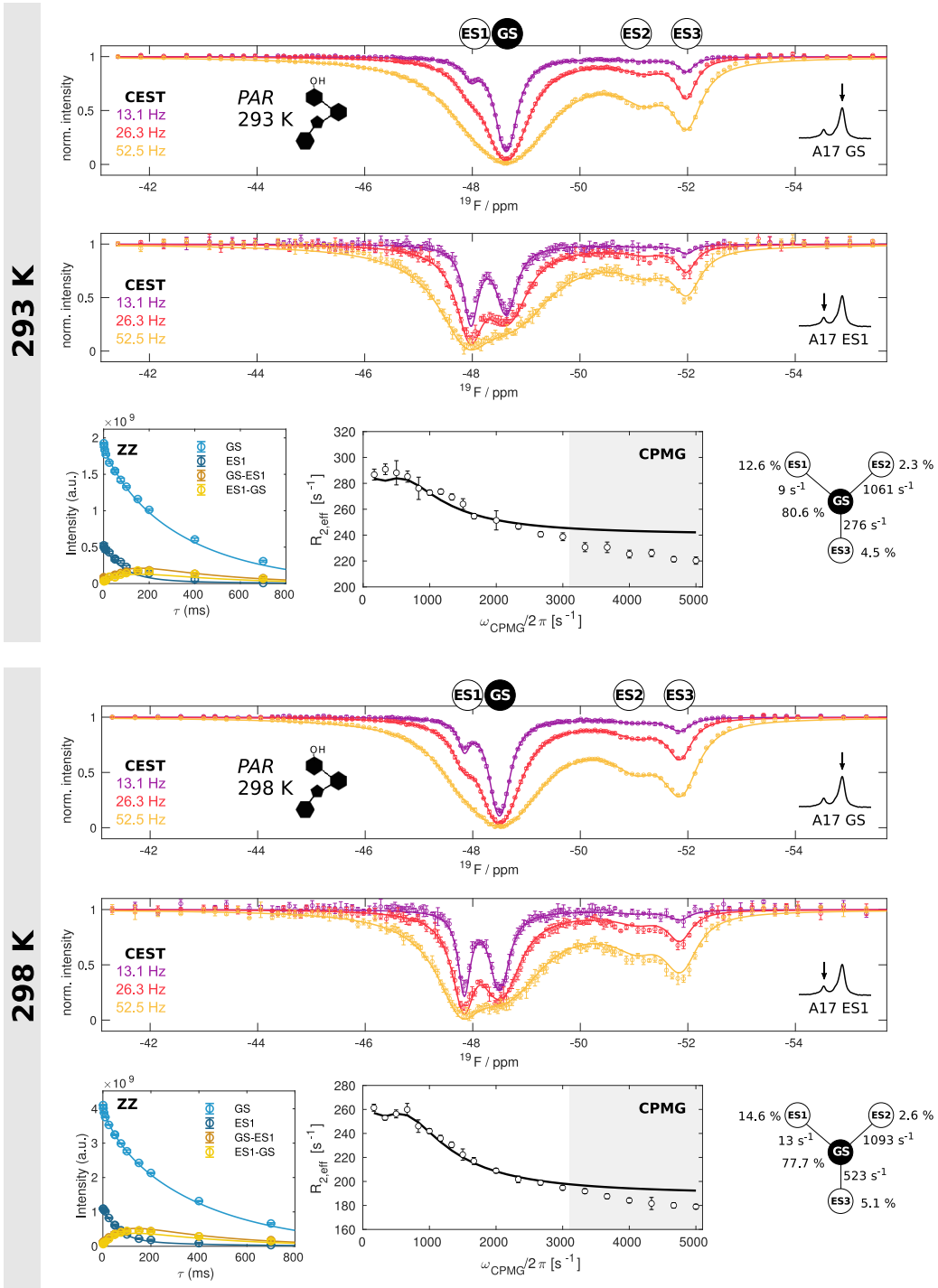

Figure A.34.: CEST, ZZ-exchange and CPMG data for the unsaturated PAR-bound riboswitch Top: CEST profiles, ZZ-exchange data and CPMG curve of the A17F2 resonance at 293 K, together with the parameters obtained by a least-square fitting routine. Bottom: CEST profiles, ZZ-exchange data and CPMG curve of the A17F2 resonance at 298 K, together with the parameters obtained by a least-square fitting routine.

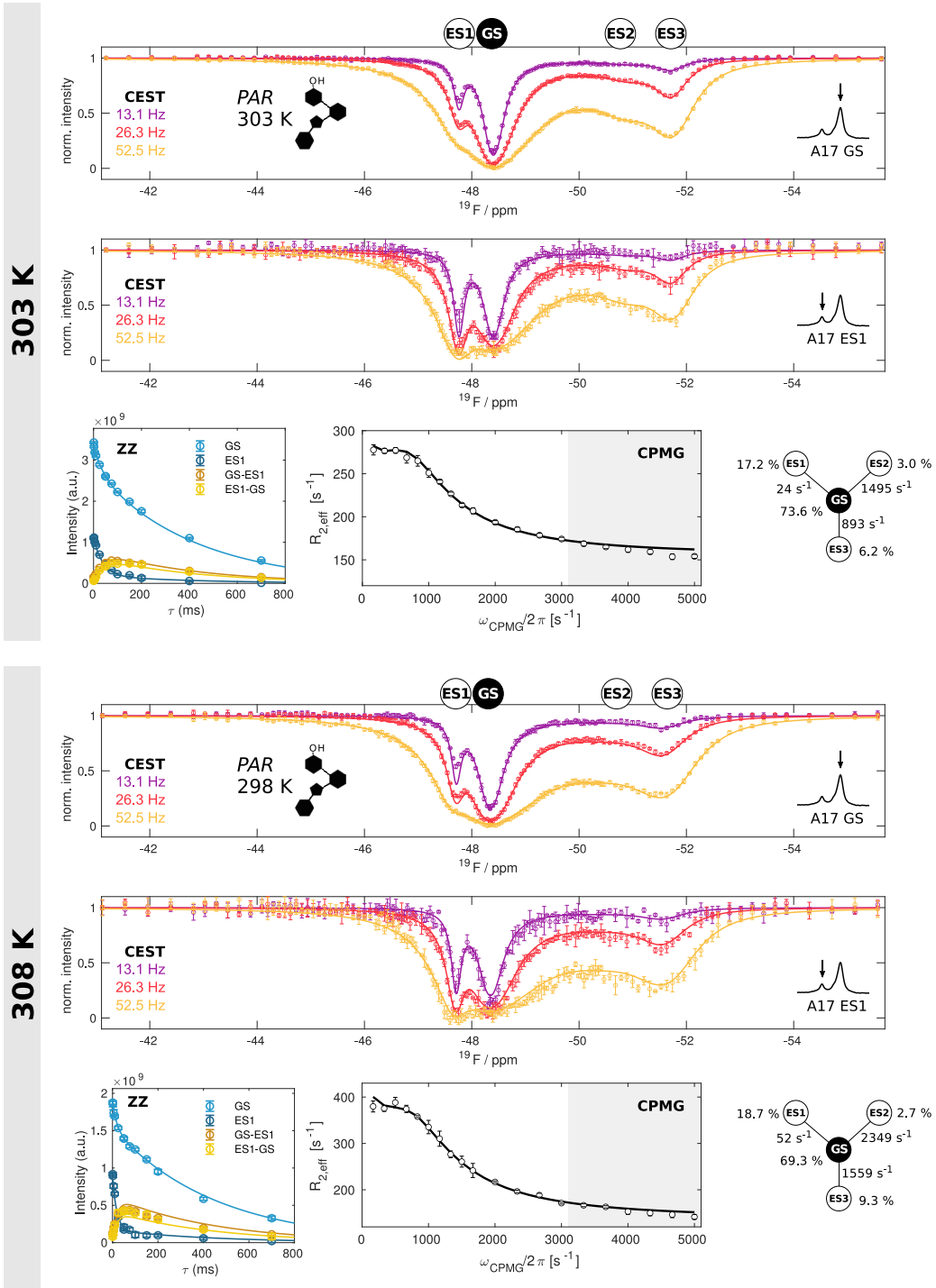

Figure A.35.: CEST, ZZ-exchange and CPMG data for the unsaturated PAR-bound riboswitch Top: CEST profiles, ZZ-exchange data and CPMG curve of the A17F2 resonance at 303 K, together with the parameters obtained by a least-square fitting routine. Bottom: CEST profiles, ZZ-exchange data and CPMG curve of the A17F2 resonance at 308 K, together with the parameters obtained by a least-square fitting routine

RNA	IVT primer sequence	RNA sequence	Internal RNA primer reference
5mer RNA	5′-CTTCTTTCTTCCCTTCCTTCCTCTCACTCCTATAGTGAGTCGTATTACG-3′	5′-GGAGUGAGAGGAAGGAAGGGAAGAAAGAAG-3′ ⟶ 5′-GGAGU-3′ after RNase A cleavage	8
10mer RNA	5′-CTTCTTTCTTCCCTTCCTTCACTCTCCTCCTATAGTGAGTCGTATTACG-3′	5′-GGAGGAGAGUGAAGGAAGGGAAGAAAGAAG-3′ ⟶ 5′-GGAGGAGAGU-3′ after RNase A cleavage	9
AU10	5′-AATTAATTAACATCTTAATTAATTATCTCCTTATTCTAATTCCTATAGTGAGTCGTATTACG-3′	5′-GGAAUUAGAAUAAGGAGAUAAUUAAUUAAGAUGUUAAUUAAUU-3′	110
GC8	5′-GGCCGGCCTTGCGGCCGGCCATCTCCTTATTCTAATTCCTATAGTGAGTCGTATTACG-3′	5′-GGAAUUAGAAUAAGGAGAUGGCCGGCCGCAAGGCCGGCC-3′	187
GC10	5′-CCGGCCGGCCTTGCGGCCGGCCGGATCTCCTTATTCTAATTCCTATAGTGAGTCGTATTACG-3′	5′-GGAAUUAGAAUAAGGAGAUCCGGCCGGCCGCAAGGCCGGCCGG-3′	111
GC12	5′-CCCCGGCCGGCCTTGCGGCCGGCCGGGGATCTCCTTATTCTAATTCCTATAGTGAGTCGTATTACG-3′	5′-GGAAUUAGAAUAAGGAGAUCCCCGGCCGGCCGCAAGGCCGGCCGGGG-3′	151
GC14	5′-CCCCGGCCGGCCCCTTGCGGGGCCGGCCGGGGATCTCCTTATTCTAATTCCTATAGTGAGTCGTATTACG-3′	5′-GGAAUUAGAAUAAGGAGAUCCCCGGCCGGCCCCGCAAGGGGCCGGCCGGGG-3′	152
ZIKV xrRNA	5′-CCCACTTTCGTGGGGGGGTTACAGGCTGCACAGCTTTCCCCAAACTGTGGCGACTTTCGCCGGCCTGACAACACTAAAATTGGTGCTTACAACACTCCCTATAGTGAGTCGTATTACG-3′	5′-GGGAGUGUUGUAAGCACCAAUUUUAGUGUUGUCAGGCCGGCGAAAGUCGCCACAGUUUGGGGAAAGCUGUGCAGCCUGUAACCCCCCCACGAAAGUGGG-3′	186

Table A.1.: RNA Sequences used in exoribonuclease degradation and binding assays

Construct	Tag and cleavage site	Internal reference
TmCsp	N-His6-GB1-TEV	#2093
CtXrn2 1-875	C-His6	#1683
CtXrn2 1-875 Δ263-300	C-His6	#1821
CtXrn2 265-293	N-His6-GB1-TEV	#1820
CtXrn2 1-875 A5F	C-His6	#2331
CtXrn2 1-875 Δ263-300 N12C A5F	C-His6	#2316
CtXrn2 422-571	N-His6-TEV	#1764
CtXrn2 1-875 Δ263-300 N12C	C-His6	#1913
CtXrn2 1-875 Δ263-300 R8C	C-His6	#1982
CtXrn2 1-875 Δ263-300 R362C	C-His6	#1967
CtXrn2 1-875 Δ263-300 V416C	C-His6	#1955

Table A.2.: Constructs used in this thesis Isoleucine mutants are provided separately in table A.4

		CPMG	$R_{1\rho}$	CPMG + $R_{1\rho}$
303 K	p_{GS}	0.746 ± 0.091	0.663 ± 0.045	0.676 ± 0.030
	k_{ex} [s^{-1}]	236 ± 102	475 ± 52	472 ± 52
305.5 K	p_{GS}	0.761 ± 0.057	0.629 ± 0.054	0.689 ± 0.027
	k_{ex} [s^{-1}]	248 ± 82	539 ± 68	536 ± 44
308 K	p_{GS}	0.817 ± 0.032	0.581 ± 0.043	0.614 ± 0.033
	k_{ex} [s^{-1}]	386 ± 121	614 ± 27	630 ± 23
310.5	p_{GS}	0.854 ± 0.035	0.618 ± 0.039	0.651 ± 0.035
	k_{ex} [s^{-1}]	581 ± 145	629 ± 35	705 ± 40
313 K	p_{GS}	0.872 ± 0.030	0.605 ± 0.056	0.655 ± 0.044
	k_{ex} [s^{-1}]	816 ± 175	919 ± 91	992 ± 104
	$\lvert\Delta\omega\rvert$ [ppm]	0.237 ± 0.024	0.154 ± 0.005	0.154 ± 0.0050

Table A.3.: Fit parameters from global fit of relaxation dispersion data from 303 K to 313 K (figure A.16). For each temperature, the ground state population p_{GS} as well as the exchange constant k_{ex} are given for a global fit of (1) CPMG data, (2) $R_{1\rho}$ data and (3) combined CPMG + $R_{1\rho}$ data. The common absolute chemical shift difference $|\Delta\omega|$ is given in the last line.

Construct	Tag	Internal database reference	Assigned (313 K)	Assigned (313 K, pAp)
CtXrn2 1-875 I3M	C-His6	#1985		x
CtXrn2 1-875 Δ435-568 I17V	C-His6	#1854		x
CtXrn2 1-875 Δ435-568 I18V	C-His6	#1831		x
CtXrn2 1-875 Δ435-568 I27V	C-His6	#1929	x	x
CtXrn2 1-875 Δ435-568 I35V	C-His6	#1924	x	x
CtXrn2 1-875 I59V	C-His6	#1810	x	x
CtXrn2 1-875 Δ435-568 I80V	C-His6	#1920	x	x
CtXrn2 1-875 Δ435-568 I82V	C-His6	#1921	x	
CtXrn2 1-875 Δ435-568 I89V	C-His6	#1856	x	x
CtXrn2 1-875 Δ435-568 I98V	C-His6	#1875	x	x
CtXrn2 1-875 Δ435-568 I101V	C-His6	#1925	x	x
CtXrn2 1-875 Δ435-568 I166V	C-His6	#1825	x	x
CtXrn2 1-875 Δ435-568 I175V	C-His6	#1922	x	x
CtXrn2 1-875 Δ435-568 I200V	C-His6	#1926	x	x
CtXrn2 1-875 Δ435-568 I201V	C-His6	#1876	x	
CtXrn2 1-875 Δ435-568 I214V	C-His6	#1894	x	x
CtXrn2 1-875 Δ435-568 I218V	C-His6	#1940	x	x
CtXrn2 1-875 Δ435-568 I235V	C-His6	#1927	x	x
CtXrn2 1-875 Δ435-568 I243V	C-His6	#1947		x
CtXrn2 1-875 Δ435-568 I308V	C-His6	#1877		x
CtXrn2 1-875 Δ435-568 I314V	C-His6	#1937	x	x
CtXrn2 1-875 Δ435-568 I338V	C-His6	#1928	x	x
CtXrn2 1-875 Δ435-568 I361V	C-His6	#1855		x
CtXrn2 1-875 Δ435-568 I366V	C-His6	#1862		x
CtXrn2 1-875 Δ435-568 I372V	C-His6	#1860		x
CtXrn2 1-875 Δ435-568 I379V	C-His6	#1930	x	x
CtXrn2 1-875 Δ435-568 I398V	C-His6	#1948	x	x
CtXrn2 1-875 Δ435-568 I409V	C-His6	#1826		x
CtXrn2 1-875 Δ435-568 (ΔI467 ΔI475 ΔI504 ΔI544)	C-His6	#1823	x	x
CtXrn2 1-875 Δ435-568 I595V	C-His6	#1949	x	x
CtXrn2 1-875 Δ435-568 I646V	C-His6	#1859	x	x
CtXrn2 1-875 Δ435-568 I653V	C-His6	#1878	x	x
CtXrn2 1-875 Δ435-568 I672V	C-His6	#1879	x	x
CtXrn2 1-875 Δ435-568 I687V	C-His6	#1931	x	x
CtXrn2 1-875 Δ435-568 I688V	C-His6	#1941	x	
CtXrn2 1-875 I697V	C-His6	#1812	x	
CtXrn2 1-875 Δ435-568 I715V	C-His6	#1832		
CtXrn2 1-875 Δ435-568 I748V	C-His6	#1938	(x)	
CtXrn2 1-875 Δ435-568 I759V	C-His6	#1932	(x)	
CtXrn2 1-875 Δ435-568 I790V	C-His6	#1942	x	
CtXrn2 1-875 Δ435-568 I817V	C-His6	#1880	(x)	
CtXrn2 1-875 Δ435-568 I822V	C-His6	#1950	x	x
CtXrn2 1-875 Δ435-568 I850V	C-His6	#1939	x	x
CtXrn2 1-875 Δ435-568 I852V	C-His6	#1951	x	x
CtXrn2 1-875 Δ435-568 I853V	C-His6	#1827	x	x
CtXrn2 1-875 Δ263-300 M704C	C-His6	#1956	x	x

Table A.4.: Xrn2 assignment mutants Single-point mutants of Xrn2 used to assign individual Ileδ1 methyl group resonances as well as the M704ϵ methyl group resonance. Resonances marked with an *x* have been assigned. Resonances from I748, I759 and I817 could only be assigned to a set of three peaks and are marked with an *(x)*